

BOSTON UNIVERSITY
GRADUATE SCHOOL OF ARTS AND SCIENCES

Dissertation

SEARCH FOR TECHNIPARTICLES AT DØ RUN II

by

LORENZO FELIGIONI

Laurea, Università' degli Studi di Perugia, 1999

Submitted in partial fulfillment of the
requirements for the degree of
Doctor of Philosophy

2006

Approved by

First Reader

Meenakshi Narain, Ph.D.
Associate Professor of Physics

Second Reader

James P. Miller, Ph.D.
Professor of Physics

Acknowledgments

I would like to thank my advisor, Prof. Meenakshi Narain, for giving me the opportunity to work on many interesting projects during my years at DØ and for her support since the beginning of my experience at Boston University. I would also like to thank Prof. Yogendra Srivastava, who encouraged me to pursue this Ph.D.

I would like to express my appreciation to my friends, without whom this journey would have been far less interesting: Rob, Wei, Claudio, Giancarlo, Stefano, Michel, Ludovic, Paul, Jovan, Sameet, Vishal and Pradeep. Thank you to Melinda for always being there, and to my parents for their unwavering support.

SEARCH FOR TECHNIPARTICLES AT DØ RUN II

(Order No.)

LORENZO FELIGIONI

Boston University Graduate School of Arts and Sciences, 2006

Major Professor: Meenakshi Narain, Associate Professor of Physics

ABSTRACT

Technicolor theory (TC) accomplishes the necessary electroweak symmetry breaking responsible for the mass of the elementary particles. TC postulates the existence of a new $SU(N_{TC})$ gauge theory. Like QCD the exchange of gauge bosons causes the existence of a non-vanishing chiral condensate which dynamically breaks the $SU(N_{TC})_L \times SU(N_{TC})_R$ symmetry. This gives rise to $N_{TC}^2 - 1$ Nambu-Goldstone Bosons. Three of these Goldstone Bosons become the longitudinal components of the W^\pm and Z which therefore acquire mass; the remaining ones are new particles (technihadrons) that can be produced at the high energy colliders and detected.

The Technicolor Straw Man Model (TCSM) is a version of the dynamical symmetry breaking with a large number of technifermions and a relative low value of their masses. One of the processes predicted by the TCSM is $q\bar{q} \rightarrow V_T \rightarrow W\pi_T$, where V_T is the Technicolor equivalent of the QCD vector meson and π_T is the equivalent of the pion. W is the electroweak gauge boson of the Standard Model.

This dissertation describes the search for $W\pi_T$ with the DØ detector, a multi-purpose particle detector located at one of the collision points of the Tevatron accelerator situated in Batavia, IL. The final state considered for this thesis is a W boson that decays to electron and neutrino plus a π_T that decays into $b\bar{c}$ or $b\bar{b}$, depending on the charge of the initial technivector meson produced.

In the $D\bar{0}$ detector this process will appear as a narrow cluster of energy deposits in the electromagnetic calorimeter with an associated track reconstructed in the tracking detector. The undetected neutrino from the decay of the W boson will be seen as missing momentum. The fragmentation of the quarks from the decay of the π_T will produce two jets of collimated particles. Events where a b -quark is produced are selected by requesting at least one jet to be associated with a secondary vertex of interaction produced by the decay of B -meson (b -tagging).

In the absence of an excess over the Standard Model prediction for the final state considered in this analysis, we compute a 95% Confidence Level upper limit on the techniparticle production cross section for the V_T mass range: $190 \text{ GeV}/c^2 \leq m(V_T) \leq 220 \text{ GeV}/c^2$.

Contents

1	Introduction	1
2	Technicolor Theory	4
2.1	The Standard Model of Particle Physics	4
2.2	Gauge Theory of the Electroweak Interactions	7
2.3	The Higgs Mechanism	10
2.4	Technicolor	10
2.4.1	Extended Technicolor	12
2.4.2	Low-Scale Technicolor	13
2.4.3	Technihadron Production and Decay	14
2.5	Technicolor at Hadron Colliders	15
2.5.1	Previous Searches	15
2.5.2	Technicolor at DØ Run II	16
3	Experimental Apparatus	24
3.1	The Tevatron Accelerator	24
3.2	The DØ Detector	25
3.2.1	The Tracking System	27
3.2.2	The DØ Calorimeter	30
3.2.3	The Muon System	34

3.2.4	The Luminosity Monitor	36
3.2.5	The DØ Trigger System	37
4	Event Reconstruction	40
4.1	Event Reconstruction	40
4.2	Track and Vertex Reconstruction	41
4.2.1	The Alternative Algorithm (AA)	42
4.2.2	The Histogramming Track Finder Algorithm (HTF)	43
4.2.3	Track Selection	43
4.2.4	Primary Vertex	44
4.2.5	Probabilistic Primary Vertex Selection	45
4.3	Jet Reconstruction	46
4.3.1	Introduction	46
4.3.2	The DØ Run II Cone Jet Algorithm	48
4.3.3	Calculation of Jet Variables	51
4.3.4	Jet Identification	51
4.3.5	Jet Energy Scale	52
4.4	Electron Identification	54
4.4.1	Electron Definition	57
4.5	Muon Identification	60
4.6	Missing Energy	62
4.7	The Event Simulation	63
5	<i>b</i>-tagging Performance with the DØ detector	65
5.1	The Vertex Algorithm	66
5.1.1	Primary Vertex	66
5.1.2	Secondary Vertex	67
5.2	<i>b</i> -tagging in data	70

5.2.1	Data Sample Selection	70
5.2.2	Jets Track Requirement: Taggability	71
5.2.3	V_0 Removal and γ -conversion Filter	72
5.3	b -tagging Efficiency: SystemD	73
5.3.1	SystemD Systematic Uncertainties	80
5.3.2	Tagging Efficiency in Monte Carlo Simulated Events	82
5.4	Light-jet tagging Efficiency a.k.a.. Mistag Rate	86
5.4.1	Mistag rate for Data	87
5.4.2	Monte Carlo based Correction to Negative Tag Rate	88
5.4.3	Parameterization of Light-quark Mistag Rate obtained in Data	88
5.4.4	Mistag Systematics	91
5.5	SVT Optimization	96
6	Event Selection	98
6.1	Sample Luminosity	99
6.2	Trigger Selection	100
6.3	Electron Finding Efficiency	100
6.3.1	Calorimeter Electron Reconstruction	103
6.3.2	Electron ID Efficiency	104
6.3.3	Loose to Tight Fake Rate	108
6.4	$W + 2$ jets selection	108
6.4.1	Physics Background	109
6.4.2	QCD-multijet Background	110
6.4.3	Data Yield and Background Estimate	110
6.5	$W + 2$ jets and 1 b -tag selection	110
6.5.1	Physics Background	111
6.5.2	W +jets mistag background:	114

6.5.3	$W + 2$ jets ≥ 1 b -tag: event topology	114
7	Calibration of Parametrized Monte Carlo	128
7.1	Electron Calibration	129
7.1.1	Electron Resolution	129
7.2	Jet Calibration	131
7.3	Object Missing Energy	135
7.4	$W\pi_T$ Search Optimization	139
7.4.1	Systematic Uncertainties	139
8	Final Event Selection and Upper Limits on $W\pi_T$ Production Cross Section	156
8.1	Acceptance for Technicolor signal mass grid	156
8.2	Systematic Uncertainty	178
8.3	Upper Limits on $W\pi_T$ Production Cross Section	181
9	Conclusion and Outlook	201
9.1	Summary	201
9.2	Outlook	201
6	Bibliography	202
7	Curriculum Vitae	213
8	List of publications	213

List of Tables

2.1	The known quarks and leptons [14]. Masses are expressed in GeV except where indicated otherwise.	5
2.2	Quantum numbers for the fermions of the first family. Fermions of the second and third families have the same quantum numbers as the corresponding fermions of the first family.	8
2.3	Decay rates for $V_T \rightarrow G\pi_T$, parameter settings are $M_{V_T} = 210$ GeV, $M_{\pi_T} = 110$ GeV, $M_V = M_A = 100$ GeV, technifermion charges $Q_U + Q_D = 5/3$; $c_\chi = \cos \chi$ and $s_\chi = \sin \chi$ [28].	15
2.4	Cross section times branching ratio for $\rho_T \rightarrow W\pi_T \rightarrow e\nu b\bar{b}(\bar{c})$ production as a function of $M(\pi_T)$, $M(\rho_T)$ and M_V	21
2.5	Cross section times branching ratio for $\rho_T \rightarrow W\pi_T \rightarrow e\nu b\bar{b}(\bar{c})$ production as a function of $M(\pi_T)$, $M(\rho_T)$ and M_V	22
2.6	Cross section times branching ratio for $\rho_T \rightarrow W\pi_T \rightarrow e\nu b\bar{b}(\bar{c})$ production as a function of $M(\pi_T)$, $M(\rho_T)$ and M_V	23
3.1	Comparison between Tevatron parameters for Run II and Run Ib (1993-1995).	26
3.2	Characteristics and deployment of various sensor types in the SMT. i (o) indicates length of the inner (outer) H-disk sensor. SS stands for single-sided, DS double sided and DSDM for double-sided double-metal.	28

4.1	List of cuts for tracks selected for the second pass PV computation, as implemented in RECO.	45
4.2	Overview of different muon types. Categorization based upon which sub-detector is used for the reconstruction.	61
5.1	d0root second pass track selection requirements.	66
5.2	Resolution for d0root and RECO for primary vertices with $ z < 40$ cm [44]. 67	
5.3	SVT tracks selection. The cuts has been tuned to achieve the highest efficiency for 0.1% (loose), 0.5% (medium) and 0.25% light quark mistag rates in the data [71].	68
5.4	SVT setting for the three vertex definitions.	70
5.5	b -tagging efficiency in “ μ +jet” data derived using the SystemD method. Only statistical uncertainty is quoted.	77
5.6	Correlation parameters derived from Monte Carlo.	80
5.7	Sources of systematic uncertainty for SystemD based b -tagging efficiency. Last line is the total systematic uncertainty from all contributions.	82
5.8	Monte Carlo samples used for b -tagging efficiency and mistag rate estimation.	82
5.9	b -tagging efficiency in Monte Carlo.	83
5.10	c -tagging Efficiency in Monte Carlo.	83
5.11	Mistag rates for light quarks in the qcd Monte Carlo samples.	86
5.12	Average value of the heavy flavor correction factor F_{hf} , the positive vs negative tagging rate asymmetry correction factor $F_{\ell\ell}$, and the product of the two for different vertex definitions.	88
5.13	Negative tagging efficiency and the statistical uncertainty in the EM1TRK data sample.	88
5.14	Mistag rates for light quarks in the EM1TRK data sample.	90

5.15	Relative difference ($ \frac{predicted-observed}{observed} $) between the number of observed tags using different <i>EM LowEMF</i> parameterization applied to EM1TRK and QCD data for the three vertex types.	94
5.16	Systematic Uncertainties on the negative tagging rate.	95
5.17	Systematic Uncertainties for the Light Quark mistag rate.	95
6.1	Physics Background Processes. We list their cross sections and number of events generated and processed through DØGeant.	99
6.2	Requirement at Level 1, Level 2 and Level 3 for the v11 single EM trigger list.	101
6.3	Requirement at Level 1, Level 2 and Level 3 for the v12 and v13 single EM trigger list.	102
6.4	Data Sample and Background Estimates after $W + 2$ jets selection. . . .	111
6.5	Data Sample and Background Estimates after $W + 2$ jets ≥ 1 <i>b</i> -tag selection. . . .	115
7.1	Mass points generated with full detector simulation and used for PMCS calibration.	129
7.2	Acceptance for all tuning mass points after requesting one central electron to be present in the event in both PMCS and DØGeant; r is the ratio of the acceptances in DØGeant and PMCS.	134
7.3	Resolution parameters for the PMCS jet categories.	134
7.4	Acceptance for all tuning mass points after requesting one central electron and two jets to be present in the event in both PMCS and DØGeant; r is the ratio of the acceptances in DØGeant and PMCS.	135
7.5	Acceptance for all tuning mass points after requesting one central electron, two jets, $MET_{obj} > 20$ GeV in both PMCS and DØGeant; r is the ratio of the acceptances in DØGeant and PMCS.	153

7.6	Acceptance for all tuning mass points after requesting one central electron,two jets, $MET_{obj} > 20$ GeV, $M_T(W) > 30$ GeV, in both PMCS and DØGeant; r is the ratio of the acceptances in DØGeant and PMCS. . . .	153
7.7	Acceptance for all tuning mass points after requesting one central electron,two jets, $MET_{obj} > 20$ GeV, $M_T(W) > 30$ GeV and at least one b -tagged jet in both PMCS and DØGeant; r is the ratio of the acceptances in DØGeant and PMCS.	154
7.8	Acceptance for all tuning mass points after subsequent cuts on H_T^e , $\Delta\phi(jj)$, $\Delta\phi(e, MET)$, $p_T(jj)$ and $M(jj)$ together with $M(Wjj)$ (mass window cut) in both PMCS (P) and DØGeant (G); r is the ratio of the acceptances in DØGeant and PMCS.	155
7.9	Acceptance after optimization in PMCS (P) and DØGeant (G). The first row shows the effect of cutting on the calorimeter missing energy in DØGeant. A scale factor of 0.905 is applied to PMCS to correct for this cut. The agreement between PMCS and DØGeant after this scale factor is applied, is shown in the last row. The average difference between the two simulations is 5.4%.	155
8.1	Values of optimized cuts using S/\sqrt{B} for topological variable as function of $M(\pi_T)$ and $M(\rho_T)$	159
8.2	Values of optimized cuts using S/\sqrt{B} for topological variable as function of $M(\pi_T)$ and $M(\rho_T)$	160
8.3	Values of optimized cuts using S/\sqrt{B} for topological variable as function of $M(\pi_T)$ and $M(\rho_T)$	161
8.4	Values of optimized cuts using S/\sqrt{B} for $M(\pi_T)$, $M(\rho_T)$ mass window as function of $M(\pi_T)$ and $M(\rho_T)$	162

8.5	Values of optimized cuts using S/\sqrt{B} for $M(\pi_T)$, $M(\rho_T)$ mass window as function of $M(\pi_T)$ and $M(\rho_T)$	163
8.6	Values of optimized cuts using S/\sqrt{B} for $M(\pi_T)$, $M(\rho_T)$ mass window as function of $M(\pi_T)$ and $M(\rho_T)$	164
8.7	Acceptances for $\rho_T \rightarrow W\pi_T \rightarrow e\nu b\bar{b}(\bar{c})$ production as a function of $M(\pi_T)$, $M(\rho_T)$ and M_V . Only statistical uncertainties are reported. . . .	178
8.8	Acceptances for $\rho_T \rightarrow W\pi_T \rightarrow e\nu b\bar{b}(\bar{c})$ production as a function of $M(\pi_T)$, $M(\rho_T)$ and M_V . Only statistical uncertainties are reported. . . .	179
8.9	Acceptances for $\rho_T \rightarrow W\pi_T \rightarrow e\nu b\bar{b}(\bar{c})$ production as a function of $M(\pi_T)$, $M(\rho_T)$ and M_V . Only statistical uncertainties are reported. . . .	180
8.10	Mass points used for the evaluation of the systematic uncertainties. . . .	183
8.11	Ratio between the number of expected background events and the number of expected background events when no jet smearing is applied. The rows represent different series of mass dependent cuts on topological variables. Different columns represent the three different mass points (190,100), (200,115), (220,115) chosen for the evaluation of the systematic uncertainty.	183
8.12	Ratio between the number of expected signal events and the number of expected signal events when no jet smearing is applied. The rows represent different series of mass dependent cuts on topological variables. Different columns represent the three different mass points (190,100), (200,115), (220,115) chosen for the evaluation of the systematic uncertainty.	184
8.13	Ratio between the number of expected background events and the number of expected background events when jet energy scale is increased by σ_{syst} . The rows represent different series of mass dependent cuts on topological variables. Different columns represent the three different mass points (190,100), (200,115), (220,115) chosen for the evaluation of the systematic uncertainty.	185

8.14	Ratio between the number of expected signal events and the number of expected signal events when jet energy scale is increased by σ_{syst} . The rows represent different series of mass dependent cuts on topological variables. Different columns represent the three different mass points (190,100), (200,115), (220,115) chosen for the evaluation of the systematic uncertainty.	186
8.15	Ratio between the number of expected background events and the number of expected background events when jet energy scale is decreased by σ_{syst} . The rows represent different series of mass dependent cuts on topological variables. Different columns represent the three different mass points (190,100), (200,115), (220,115) chosen for the evaluation of the systematic uncertainty.	187
8.16	Ratio between the number of expected signal events and the number of expected signal events when jet energy scale is decreased by σ_{syst} . The rows represent different series of mass dependent cuts on topological variables. Different columns represent the three different mass points (190,100), (200,115), (220,115) chosen for the evaluation of the systematic uncertainty.	188
8.17	Ratio between the number of expected background events and the number of expected background events when b , c and <i>light</i> -tagging efficiencies are increased by σ_{syst} . The rows represent different series of mass dependent cuts on topological variables. Different columns represent the three different mass points (190,100), (200,115), (220,115) chosen for the evaluation of the systematic uncertainty.	189

8.18	Ratio between the number of expected background events and the number of expected background events when b , c and <i>light</i> -tagging efficiencies are decreased by σ_{syst} . The rows represent different series of mass dependent cuts on topological variables. Different columns represent the three different mass points (190,100), (200,115), (220,115) chosen for the evaluation of the systematic uncertainty.	190
8.19	Ratio between the number of expected signal events and the number of expected signal events when b , c and <i>light</i> -tagging efficiencies are increased by σ_{syst} . The rows represent different series of mass dependent cuts on topological variables. Different columns represent the three different mass points (190,100), (200,115), (220,115) chosen for the evaluation of the systematic uncertainty.	191
8.20	Ratio between the number of expected signal events and the number of expected signal events when b , c and <i>light</i> -tagging efficiencies are decreased by σ_{syst} . The rows represent different series of mass dependent cuts on topological variables. Different columns represent the three different mass points (190,100), (200,115), (220,115) chosen for the evaluation of the systematic uncertainty.	192
8.21	Summary of systematic uncertainties for signal and background.	192
8.22	Data yield, background and signal expectation, expected 95% C.L. U.L. and calculated 95% C.L. U.L. on $\rho_T \rightarrow W\pi_T \rightarrow e\nu b\bar{b}(\bar{c})$ cross section using 388 pb ⁻¹ of DØ data after cuts on topological variable as listed in Tables 8.2, 8.3, 8.5 and 8.6 as function of $M(\pi_T)$ and $M(\rho_T)$	198
8.23	Data yield, background and signal expectation, expected 95% C.L. U.L. and calculated 95% C.L. U.L. on $\rho_T \rightarrow W\pi_T \rightarrow e\nu b\bar{b}(\bar{c})$ cross section using 388 pb ⁻¹ of DØ data after cuts on topological variable as listed in Tables 8.2, 8.3, 8.5 and 8.6 as function of $M(\pi_T)$ and $M(\rho_T)$	199

8.24	Data yield, background and signal expectation, expected 95% C.L. U.L. and calculated 95% C.L. U.L. on $\rho_T \rightarrow W\pi_T \rightarrow e\nu b\bar{b}(\bar{c})$ cross section using 388 pb ⁻¹ of DØ data after cuts on topological variable as listed in Tables 8.2, 8.3, 8.5 and 8.6 as function of $M(\pi_T)$ and $M(\rho_T)$	200
8.25	Excluded region at 95% C.L. in the $(M(\rho_T), M(\pi_T))$ plane for $\rho_T \rightarrow W\pi_T \rightarrow e\nu b\bar{b}(\bar{c})$ production with $M_V = 500$ GeV calculated using 388 pb ⁻¹ of DØ data.	200

List of Figures

2.1	Standard Model of Particle Interactions: The basic building blocks of matter are six leptons and six quarks that interact by means of force-carrying particles called bosons [9].	5
2.2	Exclusion region for technihadrons from $\rho_T \rightarrow W\pi_T$ search performed by CDF in Run I [29].	17
2.3	Exclusion regions for the CDF search for $\omega_T \rightarrow \gamma\pi_T$. The inset show the limit for $M(\pi_T) = 120$ GeV [30].	18
2.4	Experimental upper limit at 95% for $D\bar{O}$ for the process $\rho_T \rightarrow ee$ using 125 pb^{-1} of data collected during Run I [32].	19
2.5	Cross section times branching ratio for the process $\rho_T \rightarrow W\pi_T^{0,(\pm)} \rightarrow e\nu_e b\bar{b} (b\bar{c})$ with $M_V = 100$ GeV in the ρ_T, π_T plane. The unit of measure of the iso-cross section curves is pb, K-factor is included. The azure dashed line represents the threshold for $W\pi_T$ production, the green solid line the threshold for $\pi_T\pi_T$ production.	20
3.1	The Tevatron Accelerators [35].	26
3.2	The disk/barrel design of the SMT [36].	28
3.3	Schematic of the CFT. a) axial section of the CFT b) transverse section [38].	29
3.4	The $D\bar{O}$ calorimeter consists of three modules, central and end calorimeter. Each module is divided into Electromagnetic, Fine and Coarse Hadronic [36].	31

3.5	Calorimeter Unit Cell [36].	32
3.6	Schematic view of DØ calorimeter showing the transverse and longitudinal segmentation, the lines indicates the pseudorapidity interval from the center of the detector [36].	33
3.7	Cross section of FPS and CPS scintillator strips [36].	35
3.8	PDT pads viewed from above [39].	36
3.9	Block diagram of the DØ trigger system, the arrows indicates the data flow [40].	38
4.1	Track p_T spectrum for minimum bias and hard-scatter vertices in Monte Carlo simulated events [45].	46
4.2	Collinear sensitivity: pictures <i>a)</i> , <i>b)</i> and <i>c)</i> illustrate possible scenarios where different results of the jet algorithm are obtained depending if e.g. the energy of a seed is split or not between two detector towers. Infrared sensitivity: pictures <i>d)</i> and <i>e)</i> illustrate a possible scenario where the result of the jet algorithm varies depending e.g. on the presence or not of soft gluon radiation [47].	50
4.3	Correction to the measured energy in data as a function of the measured energy (top left), jet η (bottom left) and relative uncertainty (right) [54].	55
4.4	Correction to the measured energy in Monte Carlo as a function of the measured energy (top left), jet η (bottom left) and relative uncertainty (right) [54].	56
5.1	Decay Length Significance Distribution for Monte Carlo light-quark jets (left) and <i>b</i> -jets (right).	69
5.2	Taggability versus jet η (right) and jet p_T (left) for QCD and EM1TRK samples.	72

5.3	Two track invariant mass in QCD data, the left plot shows the K_s and the right plot the Λ peak [43].	73
5.4	Reconstructed γ -conversion in MC vs. radius of the silicon layer (right) and in data vs. z -position of silicon F-disks (left) [43].	74
5.5	$p_T^{rel}(\mu)$: transverse momentum of muon measured with respect to the axis formed by the vectorial sum of the jet axis plus muon momentum [72].	75
5.6	Normalized $p_T^{rel}(\mu)$ distributions in Monte Carlo simulation: muons from light-jets (blue triangles), c -jets (green squares) and b -jets (red dots) [72].	76
5.7	b -tagging efficiency determined from the “ μ +jet” data skim as a function of jet E_T and η for the LOOSE vertex criterion. The red curves represents the $\pm 1\sigma$ from the fit.	78
5.8	b -tagging efficiency determined from the “ μ +jet” data skim as a function of jet E_T and η for the MEDIUM vertex criterion. The red curves represents the $\pm 1\sigma$ from the fit.	78
5.9	b -tagging efficiency determined from the “ μ +jet” data skim as a function of jet E_T and η for the TIGHT vertex criterion. The red curves represents the $\pm 1\sigma$ from the fit.	79
5.10	b -tagging efficiency in Monte Carlo simulated $Z \rightarrow b\bar{b}$ (red circles) and derived using SystemD in a mixtures of light and heavy-flavored jets.	79
5.11	System8 variable β versus jet E_T for all SVT vertex definitions	81
5.12	System8 variable κ_b versus jet E_T for all SVT vertex definitions	81
5.13	System8 variable κ_{cl} versus jet E_T for all SVT vertex definitions	81
5.14	b -tagging efficiency in b -jets from $Z \rightarrow b\bar{b}$ events, both inclusive jets (top) and jets associated with a muon (bottom).	84
5.15	c -tagging efficiency in c -jets from $Z \rightarrow c\bar{c}$ events, both inclusive jets (top) and jets associated with a muon (bottom).	85

5.16	Origin of tracks contributing to negative tag (left) and positive tag (right) in Monte Carlo [73].	87
5.17	The light quark fraction F_{hf} (top plots) and the light quark positive/negative asymmetry $F_{\ell\ell}$ (middle plots) and the combined quark scale factor $F_{hf}\cdot F_{\ell\ell}$ (bottom plots) as a function of jet E_T and η derived from <i>qcd</i> Monte Carlo for the different vertex types.	89
5.18	Negative Tagging rate as a function of jet p_T for the CC (black), ICR (red), and EC (green) calorimeters and for the LOOSE vertex types. The top plots are the negative tagging rates from the low em-fraction jets in the EM1TRK (left) and QCD multi-jet (right) data samples. Their ratio is plotted in the bottom left plot shows. The ratio of the negative tags rate obtained using low em-fraction jets in the EM1TRK data to that obtained in using all the jets in the EM1TRK sample is plotted on the bottom right.	91
5.19	Negative Tagging rate as a function of jet p_T for the CC (black), ICR (red), and EC (green) calorimeters and for the MEDIUM vertex types. The top plots are the negative tagging rates from the low em-fraction jets in the EM1TRK (left) and QCD multi-jet (right) data samples. Their ratio is plotted in the bottom left plot shows. The ratio of the negative tags rate obtained using low em-fraction jets in the EM1TRK data to that obtained in using all the jets in the EM1TRK sample is plotted on the bottom right.	92

5.20	Negative Tagging rate as a function of jet p_T for the CC (black), ICR (red), and EC (green) calorimeters and for the TIGHT vertex types. The top plots are the negative tagging rates from the low em-fraction jets in the EM1TRK (left) and QCD multi-jet (right) data samples. Their ratio is plotted in the bottom left plot shows. The ratio of the negative tags rate obtained using low em-fraction jets in the EM1TRK data to that obtained in using all the jets in the EM1TRK sample is plotted on the bottom right.	93
5.21	Efficiency versus Negative Tagging rate for different SVT definitions. The colored points indicate different cut on the vertex Decay Length Significance $1 \leq dl_{sig} \leq 10$. In the left plot SVT uses tracks with $dca_{sig} \geq 3.0$, $p_T \geq 1$ GeV, $\chi^2 < 10$ and 2 or more (red triangles, MEDIUM SVT) or 3 or more SMT hits (blue triangles). In the right plot SVT use tracks with $dca_{sig} \geq 3.5$, $p_T \geq 1$ GeV, 2 or more SMT hits and $\chi^2 < 3$ and (red triangles) or 3 or $\chi^2 < 10$ more (blue triangles).	96
5.22	Performance of the SVT tagger.	97
6.1	Turn-on curves versus electron p_T for trigger version v11 (left), v12 (center) and v13 (right) [77].	100
6.2	$M(e, trk)$ and $M(e, e)$ for EM1TRK data, two top plots, and Monte Carlo, two bottom plots.	105
6.3	$M(e, Loose)$ and $M(Loose, Loose)$ for EM1TRK data (top plots) and Monte Carlo (bottom plots).	107
6.4	$M(Loose, Tight)$ and $M(Tight, Tight)$ for EM1TRK data (top plots) and Monte Carlo (bottom plots).	117
6.5	Electron fake rate versus p_T estimated in EM1TRK data. The function used for the fit is $f(p_T(e)) = p_0 \exp(-\sqrt{x}) + p_1$	118

6.6	Distributions for electron p_T (left) and object missing energy (right), after $W + 2$ jets selection.	118
6.7	Distribution for W boson transverse mass after $W+2$ jets selection. Object missing energy is used in order to compute $M_T(W)$	119
6.8	Distributions for first and second leading jet p_T (top row), and detector η (bottom row) after $W + 2$ jets selection.	120
6.9	Feynman Diagram for the technipion production and decay.	121
6.10	b -tagging efficiency two-dimensional parametrization (top left) comes from the data derived Muon Jets efficiency times a Monte Carlo derived scale factor (bottom left) which takes into account the different efficiency in pure Muon Jet sample (center left) with respect to the inclusive sample (center right). The bottom right plot shows the Monte Carlo c -tagging needed to derived the c -tagging efficiency parameterization.	122
6.11	Distributions for electron p_T , object missing energy (top row), W boson transverse mass and H_T^e (bottom row) after $W+2 jets \geq 1b-tag$ selection. The yellow histogram represents $W\pi_T$ for $M(\rho_T) = 200$ GeV, $M(\pi_T) = 105$ GeV and $M_V = 100$ GeV. Object missing energy is used in order to compute $M_T(W)$ and H_T^e	123
6.12	Distributions for first and second leading jet p_T (top row), and detector η (bottom row) after $W + 2 jets \geq 1b-tag$ selection. The yellow histogram represents $W\pi_T$ for $M(\rho_T) = 200$ GeV, $M(\pi_T) = 105$ GeV and $M_V = 100$ GeV.	124
6.13	Distributions for p_T and $\Delta\phi$ of the dijet system (top row), dijet and W plus dijet invariant mass (bottom row) after $W+2 jets \geq 1b-tag$ selection. The yellow histogram represents $W\pi_T$ for $M(\rho_T) = 200$ GeV, $M(\pi_T) = 105$ GeV and $M_V = 100$ GeV. Object missing energy is used in order to compute $M(Wjj)$	125

6.14	Distributions for $\Delta\phi$ between the electron and the object missing transverse momentum direction, after $W+2 jets \geq 1b\text{-tag}$ selection. The yellow histogram represents $W\pi_T$ for $M(\rho_T) = 200$ GeV, $M(\pi_T) = 105$ GeV and $M_V = 100$ GeV.	126
6.15	Distributions for $M(jj)$ versus $M(Wjj)$. The colored 2D histogram represents the expected SM background, white squares represent data after $W + 2 jets \geq 1b - tag$ selection.	127
7.1	Efficiency versus ϕ_{loc} for the mass point (200,105). Right plot: black solid histograms represents ϕ_{loc} for the generated electrons, overlaid with the ϕ_{loc} distributions for the generated electrons matched to a reconstructed EM cluster (black circles). In the same plot the red dots represent the generated electrons matched to a Tight electron. Left plot: Efficiency for a generated electron to pass several quality cuts as function of ϕ_{loc}	130
7.2	Energy resolution for DØGeant electrons in different energy bins.	131
7.3	Electron Resolution (left) and Offset (right) estimated from fully simulated events.	132
7.4	Selected events with one reconstructed electron, distributions of the electron transverse momentum for DØGeant (black histogram) and PMCS (red dots).	133
7.5	Selected events with one reconstructed electron and two jets, distributions of the transverse momentum for the leading jet DØGeant (black histogram) and PMCS (red dots).	136
7.6	Selected events with one reconstructed electron and two jets, distributions of the transverse momentum for the second leading jet DØGeant (black histogram) and PMCS (red dots).	137

7.7	Flavour content for jet in events with two jets and one electron for the mass point (200,105) in both charged (left) and neutral state (right). In the upper (lower) plots the first and second leading jet for DØGeant (PMCS) are the solid histogram, red is the b -content, yellow the c -content and grey the <i>light</i> -content. Black dots represent PMCS (DØGeant).	138
7.8	Selected events with one reconstructed electron and two jets, distributions of object missing transverse energy in DØGeant (black histogram) and PMCS (red dots).	140
7.9	H_T^e distributions for events passing the cuts listed in Table 7.7, for DØGeant (solid black histogram), and PMCS (red dots) in arbitrary units. The same distributions are used together with the background in Figure 6.11 to calculate the upper cut on H_T^e maximizing S/\sqrt{B} for (shown in the superimposed curve for both simulations). Optimized cut values are shown in the legend.	142
7.10	H_T^e distributions for events passing the cuts listed in Table 7.7, for DØGeant (solid black histogram), and PMCS (red dots) in arbitrary units. The same distributions are used together with the background in Figure 6.11 to calculate the lower cut on H_T^e maximizing S/\sqrt{B} for (shown in the superimposed curve for both simulations). Optimized cut values are shown in the legend.	143
7.11	$\Delta\phi(jj)$ distributions for events passing the cuts listed in Table 7.7, for DØGeant (solid black histogram), and PMCS (red dots) in arbitrary units. The same distributions are used together with the background in Figure 6.13 to calculate the lower cut on $\Delta\phi(jj)$ maximizing S/\sqrt{B} for (shown in the superimposed curve for both simulations). Optimized cut values are shown in the legend.	144

7.12	$\Delta\phi(e, MET)$ distributions for events passing the cuts listed in Table 7.7, for DØGeant (solid black histogram), and PMCS (red dots) in arbitrary units. The same distributions are used together with the background in Figure 6.14 to calculate the lower cut on $\Delta\phi(e, MET)$ maximizing S/\sqrt{B} for (shown in the superimposed curve for both simulations). Optimized cut values are shown in the legend.	145
7.13	$p_T(jj)$ distributions for events passing the cuts listed in Table 7.7, for DØGeant (solid black histogram), and PMCS (red dots) in arbitrary units. The same distributions are used together with the background in Figure 6.13 to calculate the upper cut on $p_T(jj)$ maximizing S/\sqrt{B} for (shown in the superimposed curve for both simulations). Optimized cut values are shown in the legend.	146
7.14	$M(jj)$ distributions for events passing the cuts listed in Table 7.7, for DØGeant (solid black histogram), and PMCS (red dots) in arbitrary units. The π_T resonance is fitted with a Gaussian in both simulations.	147
7.15	$M(Wjj)$ distributions for events passing the cuts listed in Table 7.7, for DØGeant (solid black histogram), and PMCS (red dots) in arbitrary units. The ρ_T resonance is fitted with a Gaussian in both simulations.	148
7.16	$M(jj)$ distributions for events passing the cuts listed in Table 7.7, for DØGeant (solid black histogram), and PMCS (red dots) in arbitrary units. The same distributions are used together with the background in Figure 6.13 to calculate the lower cut on $M(jj)$ maximizing S/\sqrt{B} for (shown in the superimposed curve for both simulations). Optimized cut values are shown in the legend.	149

7.17	$M(jj)$ distributions for events passing the cuts listed in Table 7.7, for DØGeant (solid black histogram), and PMCS (red dots) in arbitrary units. The same distributions are used together with the background in Figure 6.13 to calculate the upper cut on $M(jj)$ maximizing S/\sqrt{B} for (shown in the superimposed curve for both simulations). Optimized cut values are shown in the legend.	150
7.18	$M(Wjj)$ distributions for events passing the cuts listed in Table 7.7, for DØGeant (solid black histogram), and PMCS (red dots) in arbitrary units. The same distributions are used together with the background in Figure 6.13 to calculate the lower cut on $M(Wjj)$ maximizing S/\sqrt{B} for (shown in the superimposed curve for both simulations). Optimized cut values are shown in the legend.	151
7.19	$M(Wjj)$ distributions for events passing the cuts listed in Table 7.7, for DØGeant (solid black histogram), and PMCS (red dots) in arbitrary units. The same distributions are used together with the background in Figure 6.13 to calculate the upper cut on $M(Wjj)$ maximizing S/\sqrt{B} for (shown in the superimposed curve for both simulations). Optimized cut values are shown in the legend.	152
8.1	Acceptance after baseline cuts for the $190 \leq M(\rho_T) \leq 220$ GeV mass grid region produced with PMCS. Red squares (grey circles) indicate the acceptance for $W\pi_T^{\pm(0)}$	157
8.2	Cut values for the H_T^e window for the $190 \leq M(\rho_T) \leq 220$ GeV mass grid region produced with PMCS. Red squares (grey circles) indicate the cut optimized using $W\pi_T^{\pm(0)}$	165

8.3	Cut values for $p_T(jj)$ for the $190 \leq M(\rho_T) \leq 220$ GeV mass grid region produced with PMCS. Red squares (grey circles) indicate the cut optimized using $W\pi_T^{\pm(0)}$	166
8.4	Cut values for $\Delta\phi(jj)$ for the $190 \leq M(\rho_T) \leq 220$ GeV mass grid region produced with PMCS. Red squares (grey circles) indicate the cut optimized using $W\pi_T^{\pm(0)}$	167
8.5	Cut values for $\Delta\phi(e, MET)$ for the $190 \leq M(\rho_T) \leq 220$ GeV mass grid region produced with PMCS. Red squares (grey circles) indicate the cut optimized using $W\pi_T^{\pm(0)}$	168
8.6	Cut values for the $M(jj)$ window for the $190 \leq M(\rho_T) \leq 220$ GeV mass grid region produced with PMCS. Red squares (grey circles) indicate the cut optimized using $W\pi_T^{\pm(0)}$	169
8.7	Cut values for the $M(Wjj)$ window for the $190 \leq M(\rho_T) \leq 220$ GeV mass grid region produced with PMCS. Red squares (grey circles) indicate the cut optimized using $W\pi_T^{\pm(0)}$	170
8.8	Distribution for H_T^e for $W\pi_T$ produced with $M(\rho_T) = 210$ GeV and $M(\pi_T) = 110$ GeV (azure histogram), SM predicted background (red histogram) and data (black squares) after baseline cuts. The optimized mass window cuts, at $H_T^e = 95$ GeV and $H_T^e = 176$ GeV, are represented with a dotted line.	171
8.9	Distribution for $\Delta\phi(e, MET)$ for $W\pi_T$ produced with $M(\rho_T) = 210$ GeV and $M(\pi_T) = 110$ GeV (azure histogram), SM predicted background (red histogram) and data (black squares) after baseline and H_T^e cuts. The optimized lower cut at $\Delta\phi(e, MET) = 1.6$ is represented with a dotted line.	172

8.10	Distribution for $p_T(jj)$ for $W\pi_T$ produced with $M(\rho_T) = 210$ GeV and $M(\pi_T) = 110$ GeV (azure histogram), SM predicted background (red histogram) and data (black squares) after baseline, H_T^e , $\Delta\phi(e, MET)$ and $\Delta\phi(jj)$ cuts. The optimized upper cut at $p_T(jj) = 57$ GeV is represented with a dotted line.	173
8.11	Distribution for $M(jj)$ for $W\pi_T$ produced with $M(\rho_T) = 210$ GeV and $M(\pi_T) = 110$ GeV (azure histogram), SM predicted background (red histogram) and data (black squares) after baseline, H_T^e , $\Delta\phi(e, MET)$, $\Delta\phi(jj)$ and $p_T(jj)$ cuts. The optimized window cuts at $M(jj) = 72$ GeV and $M(jj) = 132$ GeV are represented with a dotted line.	174
8.12	Distribution for $M(Wjj)$ for $W\pi_T$ produced with $M(\rho_T) = 210$ GeV and $M(\pi_T) = 110$ GeV (azure histogram), SM predicted background (red histogram) and data (black squares) after baseline, H_T^e , $\Delta\phi(e, MET)$, $\Delta\phi(jj)$ and $p_T(jj)$ cuts. The optimized window cuts at $M(Wjj) = 165$ GeV and $M(Wjj) = 255$ GeV are represented with a dotted line.	175
8.13	Distribution of $M(Wjj)$ versus $M(jj)$ for the SM predicted (colored histogram) and data (black dots), after baseline, H_T^e , $\Delta\phi(e, MET)$, $\Delta\phi(jj)$ and $p_T(jj)$ cuts optimized for $W\pi_T$ produced with $M(\rho_T) = 210$ GeV and $M(\pi_T) = 110$ GeV. The optimized mass window cuts are represented with a white dotted line.	176
8.14	Acceptance after all optimized cuts for the $190 \leq M(\rho_T) \leq 220$ GeV mass grid region produced with PMCS. Red squares (grey circles) indicate the acceptance for $W\pi_T^{\pm(0)}$	177
8.15	Summary of relative uncertainties for the background evaluated at the end of the optimization chain for the $190 \leq M(\rho_T) \leq 220$ GeV mass grid region.	193

8.16	Comparison of data events (black dots) and background events (red squares) after all mass-dependent optimized cuts applied. Also shown is the expected $\rho_T \rightarrow W\pi_T \rightarrow e\nu b\bar{b}(\bar{c})$ signal events for $M_V = 100$ GeV (yellow triangles).	194
8.17	Comparison of data events (black dots) and background events (red squares) after all mass-dependent optimized cuts applied. Also shown is the expected $\rho_T \rightarrow W\pi_T \rightarrow e\nu b\bar{b}(\bar{c})$ signal events for $M_V = 100$ GeV (yellow triangles).	195
8.18	95% C.L. U.L. on $\rho_T \rightarrow W\pi_T \rightarrow e\nu b\bar{b}(\bar{c})$ production cross section for the $155 \leq M(\rho_T) \leq 185$ GeV mass grid region. Red squares (blue triangles) represent $W\pi_T$ cross section times branching ratio with $M_V = 100$ ($M_V = 500$). Grey reverse triangles represent the expected 95% C.L. U.L. on the cross section, the yellow circles represent the 95% C.L. U.L. on the cross section with $388 pb^{-1}$ integrated luminosity of $D\bar{O}$ data.	196
8.19	95% C.L. U.L. on $\rho_T \rightarrow W\pi_T \rightarrow e\nu b\bar{b}(\bar{c})$ production cross section for the $190 \leq M(\rho_T) \leq 220$ GeV mass grid region. Red squares (blue triangles) represent $W\pi_T$ cross section times branching ratio with $M_V = 100$ ($M_V = 500$). Grey reverse triangles represent the expected 95% C.L. U.L. on the cross section, the yellow circles represent the 95% C.L. U.L. on the cross section with $388 pb^{-1}$ integrated luminosity of $D\bar{O}$ data.	197

LIST OF ABBREVIATIONS

Abbreviation	The Complete Phrase
AA	Alternative Algorithm
AC	Alternating Current
ADC	Analog to Digital Converter
CC	Central Calorimeter
CL	Confidence Level
CDF	Collider Detector at FermiLab
CFT	Central Fiber Tracker
CH	Coarse Hadronic
CHF	Coarse Hadronic Fraction
CL	Confidence Level
DCA	Distance of Closest Approach
DL	Decay Length
DLS	Decay Length Significance
EDM	Event Data Model
EM	Electromagnetic

LIST OF ABBREVIATIONS - CONTINUED

Abbreviation	The Complete Phrase
EMF	Electromagnetic Fraction
ESB	Electroweak Symmetry Breaking
ETC	Extended Technicolor
eV	Electron Volt
FMI	Fermilab's Main Injector
FPGA	Field Programmable Gate Array
FPS	Forward Preshower
FH	Fine Hadronic
HTF	Histogramming Track Finder
Hz	Hertz
KF	Kalman Filter
L1	Level One
L2	Level Two
MDT	Mini Drift Tube
MIP	Minimum Ionizing Particle

LIST OF ABBREVIATIONS - CONTINUED

Abbreviation	The Complete Phrase
MET	Missing Transverse Energy
PDT	Proportional Drift Tube
PDF	Parton Distribuiton Function
PMCS	Parametrized Monte Carlo Simulation
PV	Primary Vertex
QCD	Quantum Chromodynamics
RF	Radio Frequency
SMT	Silicon MicroStrip Tracker
SM	Standard Model
SC	Scintillation Counter
SV	Secondary Vertex
SVT	Secondary Vertex Algorithm
TC	Technicolor
TC2	Topcolor Assisted Technicolor
TCSM	Technicolor Straw Man Model

LIST OF ABBREVIATIONS - CONTINUED

Abbreviation	The Complete Phrase
TFW	Trigger Framework
UL	Upper Limit
VLPC	Visible Light Photon Counter
WTC	Walking Technicolor

Chapter 1

Introduction

In 1900, during a lecture at the Royal Institution of Great Britain, Lord Kelvin stated that “two clouds” were overshadowing the “beauty and clearness” of the “Dynamical Theory of Heat and Light”. He was referring to two open problems that remained unsolved by what today is called “classical physics”: the interpretation of the result of the Michelson-Morley experiment [1] and the problem of black body radiation [2]. The solutions to these two problems led eventually to the discovery of the two most prominent physics theories of the last century: the theory of Special Relativity [3] and Quantum Mechanics [4]. After the “two clouds” finally dissolved, a new way of thinking about the laws governing the universe was revealed.

Today, the theory that describes the most fundamental interactions of matter is called the Standard Model of particle physics (SM). The SM, introduced at the end of the 60’s [5, 6, 7], succeeded on describing nature by combining the two theories that arose from Lord Kelvin’s “clouds”. In doing so it abandons the classical language of causality by bringing its predictions into the realm of chance described using the language of stochastic processes: statistics. Nowadays, testing the Standard Model involves performing the same experiment multiple times and comparing the frequencies of the resulting phenomena with the SM predictions. Up to now, the agreement between experiments

and prediction has reached a precision of the order of one tenth of a percent.

Notwithstanding a series of successes in predicting experimental results, many theorists are not satisfied from a conceptual point of view with the answers given by the SM. A number of answers to theoretical open questions require the introduction of new particles which, if they exist, would invalidate certain SM predictions. The repeated experiment, in high energy physics, consists of collisions between two sub-atomic particles. From these collisions other particles are produced. If the energy involved in these collisions reaches a level which produces new particles, they may be discovered, or their absence used to invalidate the theory that predicts them.

In the second Chapter of this paper, a brief description of the Standard Model is given, with special attention paid to a question that has interested the physics community for many years: how to describe particles as objects with a mass without destroying the entire SM theoretical implant. In the same chapter it is shown how this can be accomplished via two competing theoretical models, the Higgs model and Technicolor, with particular regard to how Technicolor can be “seen” in the energetic collisions of sub-atomic particles.

Chapter 3 describes the Tevatron circular accelerator, the experimental apparatus used to accelerate and collide protons and anti-protons with a center of mass energy of 1.96 TeV, located at the Fermi National Laboratory in Batavia, IL. These collisions happen at two distinct points in the three-mile long accelerator, where each of the two Fermilab high energy detectors, the Central Detector Fermilab (CDF) and $D\bar{0}$, are located. In the same chapter a description of the $D\bar{0}$ detector, its design principle and an explanation of its basic components is provided. Chapter 4 shows, starting from the signal recorded in the various sub-detectors, how “physics objects” are reconstructed and describes the algorithm used to make the energy and direction of these objects as close as possible to that of the original particles produced in the collision. In Chapter 5 the main algorithm used to discriminate against the background, b -tagging, is introduced.

Also described is the first DØ evaluation of b -tagging efficiency and fake rate. Chapter 6 illustrates the first event selection performed to isolate a sample of events containing Technicolor particles. Chapter 7 deals with the description of the tuning of Fast Monte Carlo used to simulate Technicolor signals at several points of the theory parameter space. Chapter 8 contains the final events selection, the systematic error estimation and the final limits on Technicolor production. Finally, Chapter 9 contains the conclusions and future plans.

Throughout this thesis natural units are used ($\hbar = c = 1$): units of measure for masses, momentum and energy are the same and conventionally chosen to be eV .

Chapter 2

Technicolor Theory

2.1 The Standard Model of Particle Physics

Within the “Standard Model”, elementary particles are considered point-like and structureless. They are divided into two groups depending on their spin, “fermions” with spin $s = \frac{1}{2}$ and “bosons” with integer spin ($s = 0, 1, 2, \dots$)^a.

Fermions are classified into “leptons” and “quarks” depending on their electric charge q and color, $SU(3)$ quantum number. Leptons have integer electric charge while quarks have fractional charge as shown in Table 2.1. To the lepton group belong the longest known particles: the electron e (discovered in 1897 by British physicist J.J. Thompson), the muon μ (discovered in 1937 by J. C. Street and E. C. Stevenson [10]) and the τ (discovered in 1975 at the Stanford Linear Accelerator [11, 12, 13]). The three leptons are associated to other particles in order to form a “generation”: the neutrinos. The three neutrinos are named according to their generation partner: ν_e , ν_μ and ν_τ . Neutrinos don’t carry any electric charge and interact only weakly with ordinary matter, making their detection quite challenging. Because of their elusiveness, at first their existence

^aThe existence of this intrinsic quantum number was first postulated by Pauli in 1924 to explain the existence of a double structure in the spectrum of Alkali metals. After one year George Uhlenbeck and Samuel Goudsmit experimentally interpreted this quantity to be the “spin”: the intrinsic quantized magnetic momentum of a particle [8].

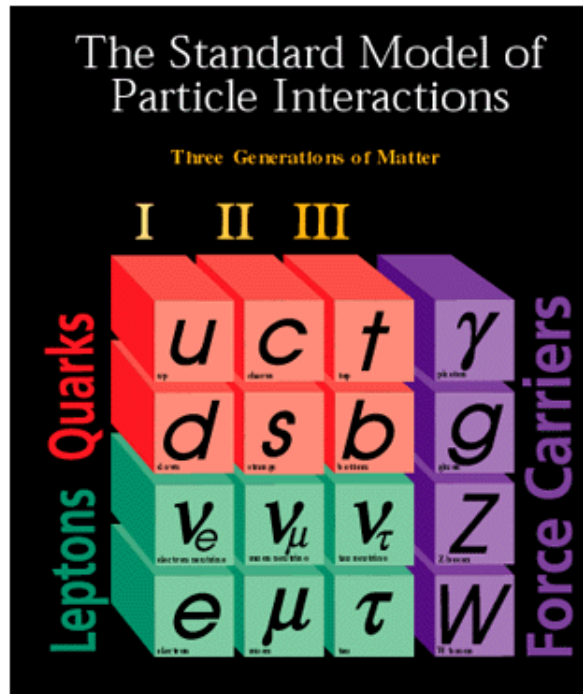


Figure 2.1: Standard Model of Particle Interactions: The basic building blocks of matter are six leptons and six quarks that interact by means of force-carrying particles called bosons [9].

was just postulated by Wolfgang Pauli in order to enforce the law of conservation of momentum in nuclei β decay processes; its name, coined by Enrico Fermi, comes from the Italian for “neutral”. SM particle classification is shown in Figure 2.1.

Quarks come in six different flavors: u , d , s , c , b and t . They carry fractional electric charge and another “color” charge that allows them to interact by means of the Strong Force. Quarks can not be found in Nature as isolated particles but only within colorless clusters: mesons and baryons are composite particles made out of a quark anti-quark

Quarks				Leptons			
$q = 2/3$		$q = -1/3$		$q = -1$		$q = 0$	
u	0.0015-0.004	d	0.004-0.008	e	0.000511	ν_e	< eV
c	1.15-1.35	s	0.080-0.130	μ	0.106	ν_μ	< 190 keV
t	174.3 ± 5.1	b	4.1-4.4	τ	1.777	ν_τ	< 18.2 MeV

Table 2.1: The known quarks and leptons [14]. Masses are expressed in GeV except where indicated otherwise.

pair and three quarks respectively; they both are generally referred to as “hadrons”.

Only with the introduction of particle accelerators could quarks be seen individually. In fact, the Strong Force, responsible for binding quarks into hadrons, becomes weak when it happens at distances of the order of a femtometer (fm^b). These distances are reached in hadron collisions with large momentum transfers; the results of these collisions can be interpreted in terms of constituent of the hadrons: quarks.

It took several decades, and several generations of particle accelerators, from when the first quarks were discovered at SLAC, by looking at the results of electron-proton inelastic scattering, to the 1995 discovery of the heavy top quark with 1.8 TeV center of mass (c.o.m) energy at the Tevatron $p\bar{p}$ accelerator [15, 16].

The SM is a quantum field theory based on the gauge symmetry $SU(3)_C \times SU(2)_L \times U(1)_Y$ [5, 6, 7], where $SU(3)_C$ is the symmetry group of the strong interactions and $SU(2)_L \times U(1)_Y$ is the symmetry group for the electroweak interactions. The eight “gluons” are the gauge bosons of $SU(3)_C$ and are responsible for mediating the strong force. They are massless and electrically neutral but carry color quantum number. The four bosons responsible for the electromagnetic and weak interactions are the massless photon, γ , and the W^\pm and Z bosons with masses of 80.4 and 91.2 GeV [14] and charge $q = \pm 1$ and 0 respectively.

The three SM fermion families can be represented as:

^b1 fm = 10^{-15} m.

$$\begin{aligned}
& \begin{pmatrix} e^- \\ \nu_e \end{pmatrix}_L, \quad e_R^-, \quad \begin{pmatrix} u \\ d \end{pmatrix}_L, \quad u_R, \quad d_R \\
& \begin{pmatrix} \mu^- \\ \nu_\mu \end{pmatrix}_L, \quad \mu_R^-, \quad \begin{pmatrix} c \\ s \end{pmatrix}_L, \quad c_R, \quad s_R \\
& \begin{pmatrix} \tau^- \\ \nu_\tau \end{pmatrix}_L, \quad \tau_R^-, \quad \begin{pmatrix} t \\ d \end{pmatrix}_L, \quad t_R, \quad b_R,
\end{aligned}$$

and the same for their corresponding antiparticles. The subscripts L and R denote left and right-handed particles. Only left-handed particles, and right-handed anti-particles, participate in the weak interaction, leading to the ‘‘Parity’’ violation for the weak interactions.

2.2 Gauge Theory of the Electroweak Interactions

The Electroweak interaction is described by a non-Abelian gauge theory with $SU(2)_L \times U(1)_Y$ symmetry. Non-Abelian gauge theories were first introduced by Yang and Mills in 1954 [17] in order to build a theory of the nuclear interactions invariant under nuclear isospin rotation. In 1961 Glashow proposed them as the solution for the unification of the electromagnetic and weak force [18].

The four bosons associated with the four generators of the symmetry group are: $W_\mu^i, i = 1, 2, 3$ weak bosons of $SU(2)_L$ having $T_i = \frac{\sigma_i}{2}, i = 1, 2, 3$ as generators, and B_μ the hypercharge $\frac{Y}{2}$ boson for $U(1)_Y$. The relation between the hypercharge, the weak isospin and the electric charge is:

$$Q = T_3 + \frac{Y}{2}. \quad (2.1)$$

Fermion	T	T_3	Q	Y
ν_L	$\frac{1}{2}$	$\frac{1}{2}$	0	-1
e_L	$\frac{1}{2}$	$-\frac{1}{2}$	-1	-1
e_R	0	0	-1	-2
u_L	$\frac{1}{2}$	$\frac{1}{2}$	$\frac{2}{3}$	$\frac{1}{3}$
d_L	$\frac{1}{2}$	$-\frac{1}{2}$	$-\frac{1}{3}$	$\frac{1}{3}$
u_R	0	0	$\frac{2}{3}$	$\frac{4}{3}$
u_R	0	0	$-\frac{1}{3}$	$-\frac{2}{3}$

Table 2.2: Quantum numbers for the fermions of the first family. Fermions of the second and third families have the same quantum numbers as the corresponding fermions of the first family.

The fermion quantum numbers are shown in Table 2.2.

The Lagrangian of the Electroweak interactions can be written as:

$$\mathcal{L}_{SM} = \mathcal{L}_f + \mathcal{L}_G \quad (2.2)$$

where:

$$\mathcal{L}_f = \sum_{f=l,q} \bar{f} i \not{D} f, \quad (2.3)$$

is the fermion part and

$$\mathcal{L}_G = -\frac{1}{4} W_{\mu\nu}^i W_i^{\mu\nu} - \frac{1}{4} B_{\mu\nu} B^{\mu\nu} \quad (2.4)$$

is the Lagrangian for the gauge field in term of the field strength tensors:

$$W_{\mu\nu}^i = \partial_\mu W_\nu^i - \partial_\nu W_\mu^i + g\epsilon^{ijk} W_\mu^j W_\nu^k, \quad (2.5)$$

$$B_{\mu\nu} = \partial_\mu B_\nu - \partial_\nu B_\mu. \quad (2.6)$$

It is possible to show that if the covariant derivative is of the form:

$$D_\mu f = (\partial_\mu + ig\vec{T}\vec{W}_\mu + ig'\frac{Y}{2}B_\mu)f \quad (2.7)$$

the Lagrangian \mathcal{L}_{SM} is invariant under the $SU(2)_L \times U(1)_Y$ transformations:

$$\begin{aligned}
f_L &\rightarrow e^{ig\vec{T}\vec{\theta}(x)} f_L \\
f_R &\rightarrow f_R \\
f &\rightarrow e^{ig'\frac{Y}{2}\alpha(x)} f \\
W_\mu^i &\rightarrow W_\mu^i + \partial_\mu\theta^i(x) + g\epsilon^{ijk}\theta^j W_\mu^k \\
B_\mu &\rightarrow B_\mu - \partial_\mu\alpha(x)
\end{aligned} \tag{2.8}$$

The W , Z and electromagnetic fields can be expressed by a linear combination of these fields:

$$\begin{aligned}
W_\mu^\pm &= \frac{1}{\sqrt{2}}(W_\mu^1 \mp iW_\mu^2) \\
Z_\mu &= \cos\theta_w W_\mu^3 - \sin\theta_w B_\mu \\
A_\mu &= \sin\theta_w W_\mu^3 + \cos\theta_w B_\mu,
\end{aligned} \tag{2.9}$$

where θ_w , the electroweak mixing angle is such that:

$$\sin\theta_W = e/g; \quad \cos\theta_W = e/g'. \tag{2.10}$$

Finally any mass term for gauge bosons or fermions is forbidden by the $SU(2)_L \times U(1)_Y$ gauge symmetry. A mechanism is needed that generates masses without destroying the SM symmetries. The mechanism of the Electroweak Symmetry Breaking (ESB) leads naturally to the understanding of the origin of mass for elementary particles. Several theoretical models address this problem as described in the next sections.

2.3 The Higgs Mechanism

The Standard Higgs Model accomplishes the ESB by introducing a fundamental weak doublet of scalar fields, namely the Higgs field,

$$\phi = \begin{pmatrix} \phi^+ \\ \phi^0 \end{pmatrix}, \quad (2.11)$$

and a potential of the form

$$V = \lambda(\phi^\dagger\phi - \frac{1}{2}v^2)^2, \quad (2.12)$$

where λ represents the scalar self coupling. In this representation we can choose the vacuum expectation value of the Higgs field to be:

$$\langle \phi_0 \rangle = \begin{pmatrix} 0 \\ v/\sqrt{2} \end{pmatrix}. \quad (2.13)$$

which breaks both $SU(2)_L$ and $U(1)_Y$ symmetries providing masses to the vector bosons corresponding to the generators of the broken symmetries, the W and Z bosons [19].

2.4 Technicolor

The Higgs Mechanism does not give an explanation of the dynamics responsible for the generation of the mass. Furthermore it presents problems of a deeper nature. The hierarchy problem arises if new physics is present at any higher scale. In this case the mass of the Higgs boson would be unnaturally susceptible to one loop contributions from new heavy particles and an extreme fine tuning would be necessary in order to keep the Higgs light. The triviality problem comes from the fact that λ becomes zero at finite

energy implying that this model is only an effective low-energy theory, valid below some cut-off scale Λ [20].

One possible solution to the triviality and the hierarchy problems together with a dynamical explanation for the ESB is given by Technicolor. Technicolor is a new non-Abelian gauge theory based on Quantum Chromo Dynamics (QCD). It was first formulated by Weinberg and Susskind [21, 22]. The simplest Technicolor model predicts a new strong $SU(N_{TC})$ gauge theory and new fermions, "techniquarks" transforming as fundamentals of the theory:

$$\Psi_L = \begin{pmatrix} U \\ D \end{pmatrix}_L, \quad U_R, D_R. \quad (2.14)$$

Like QCD in the $m_u, m_d \rightarrow 0$ limit, technifermions have a chiral $SU(2)_L \times SU(2)_R$ symmetry. Just as in QCD the "low energy" limit of this gauge theory breaks the chiral symmetry: Technicolor coupling becomes strong, causing technifermions to form condensates,

$$\langle \bar{U}U + \bar{D}D \rangle \neq 0, \quad (2.15)$$

and to break $SU(2)_L \times SU(2)_R$ down to $SU(2)_V$. In the case where the left-handed techniquarks form a weak doublet, and the right-handed techniquarks are a weak singlet, the spontaneous breaking of the chiral symmetry will break as well the weak interactions down to electromagnetism. The Nambu-Goldstone bosons produced by the breaking of the symmetry are called technipions π_T in analogy with the pions of QCD. Three of these technipions are "eaten" and become the longitudinal components of the W and Z which acquire mass in the process. In this simple model

$$M_W = \frac{gF_{TC}}{2} \quad (2.16)$$

F_{TC} being the analog of f_π in QCD.

In order to agree with the observed masses, F_{TC} has to be 246 GeV. Unfortunately this simple version of QCD-scaled Technicolor is incompatible with precision electroweak data and can not accommodate the masses of the fermions. Nonetheless, this simplest version remains a paradigm for dynamical electroweak symmetry breaking theories [23].

2.4.1 Extended Technicolor

Technicolor must be able to produce a mechanism for generating quark and lepton masses. This is achieved by the coupling of Standard Model fermions, the ordinary matter, with the same Technicolor condensates responsible for the W and Z boson masses. The additional gauge field coupling to both SM fermions and Technicolor fermions is postulated in Extended Technicolor Theories (ETC) [24, 25].

Generally in many ETC models Flavor Changing Neutral Currents (FCNC) work against the possibility of generating masses for the heaviest quarks. By imposing a particular dependency of TC coupling constants, "Walking Technicolor" (WTC) [26] makes it possible to enhance those terms in ETC involving technifermion bilinears (mass terms) without dangerously increasing the ordinary fermion coupling responsible for FCNC.

Still WTC does not arrive at masses of the order of the top quark mass. For this reason another gauge interaction, namely, Topcolor assisted Technicolor (TC2) [27] is predicted. Together with all other extensions of the basic Technicolor model, WTC requires a large number N_D of technifermion doublets. Many technifermions are needed to make the coupling constant of Walking Technicolor small. Many also seem to be required in TC2 to generate the hard masses of quarks and leptons, to induce the correct mixing between heavy and light quarks, and to break topcolor symmetry down to ordinary color (via technifermion condensation).

In general the Technicolor scale Λ_{TC} 's value depends on the number of technifermion

doublets $\Lambda_{TC} \sim F_{TC}/\sqrt{N_D}$. For high N_D the lowest lying technihadrons have masses of the order of few hundred GeV. This scenario is usually referred to as Low-Scale Technicolor.

2.4.2 Low-Scale Technicolor

The "Technicolor Straw Man Model" (TCSM) [28] is a model of the Low-Scale Technicolor for collider experiments. In this model color-singlet technifermion bound states are postulated to be vector and pseudo-scalar mesons. Their names come directly from their QCD equivalent: for the vector mesons sector the spin-one isotriplet and its isoscalar partner are called $\rho_T^{\pm,0}$ and ω_T . If isospin is a good approximate symmetry ρ_T and ω_T should be degenerate in mass. The pseudo scalar mesons and lightest technihadrons are $\Pi_T^{\pm,0}$ and $\Pi_T^{0'}$.

In TCSM the isovectors are considered being two-state mixtures of the longitudinal components of the W and Z bosons and the mass-eigenstate pseudo-Goldstone $\pi_T^{\pm,0}$. The form of this mixing can be written as:

$$|\Pi_T \rangle = \cos \chi |\pi_T \rangle + \sin \chi |W_L \rangle . \quad (2.17)$$

Technipions couple to the mass of ordinary SM particles and follow the decay law:

$$\Gamma(\pi_T \rightarrow \bar{f}' f) = \frac{1}{16\pi F_T^2} N_f p_f C_{1f}^2 (m_f + m_{f'})^2 \quad (2.18)$$

$$\Gamma(\pi_T^{0'} \rightarrow gg) = \frac{1}{128\pi F_T^2} \alpha_C^2 C_{1g}^2 N_{TC}^2 p_f M_{\pi_T^{0'}}^3 . \quad (2.19)$$

Where C_{1f} is an ETC factor, N_f the number of colors of fermions, p_f the fermion momentum, α_C the QCD coupling constant and C_{1g}^2 is a Clebsh of order one [28].

2.4.3 Technihadron Production and Decay

In the limit that the electroweak coupling g and g' are set to zero the decay rate to technipions for ρ_T is

$$\Gamma(\rho_T \rightarrow \pi_A \pi_B) = \frac{2\alpha_{\rho_T} \mathcal{C}_{AB}^2 p^3}{3 \hat{s}} \quad (2.20)$$

where p is the momentum of π_T and

$$\mathcal{C}_{AB} = \begin{cases} \sin \chi^2 & \text{for } W_L^+ W_L^- \text{ or } W_L^\pm Z_L \\ \sin \chi \cos \chi & \text{for } W_L^\pm \pi_T^\mp, \text{ or } W_L^\pm \pi_T^0, \pi_T^\pm Z_L \\ \cos \chi^2 & \text{for } \pi_T^+ \pi_T^- \text{ or } \pi_T^\pm \pi_T^0 \end{cases} \quad (2.21)$$

The rate of the isospin-violating decay of the vector meson ω_T into a longitudinally polarized W boson and a technipion can be estimated as

$$\Gamma(\omega_T \rightarrow W_T^\pm \pi_T^\mp) = |\epsilon_{\rho\omega}|^2 \Gamma(\rho_T^0 \rightarrow W_T^\pm \pi_T^\mp), \quad (2.22)$$

where $\epsilon_{\rho\omega}$, the vector meson mixing amplitude is considered to be small based on an analogy with the same quantity in QCD.

The decay rate for any vector technimeson $V_T = \rho_T, \omega_T$ to decay in any transversely polarized gauge boson G plus technipion is :

$$\Gamma(V_T \rightarrow G \pi_T) = \frac{2\alpha V_{TG\pi_T}^2 p^3}{3M_V^2} + \frac{\alpha A_{VG\pi_T}^2 p(3M_G^2 + 2p^2)}{6M_A^2} \quad (2.23)$$

where p the momentum of the gauge boson G , M_V and M_A are mass parameters estimated to be comparable and on the order of several hundred GeV by analogy with QCD. A and V , the coefficients for the vectorial and the axial current, depend upon the charge of the technipions and the number of technicolor doublets present in the theory. These are explicitly calculated for a particular case in Table 2.3.

Process	$V_{V_T G \pi_T}$	$A_{V_T G \pi_T}$	$\Gamma(V_T \rightarrow G \pi_T)$
$\omega_T \rightarrow \gamma \pi_T^0$	c_χ	0	$0.115 c_\chi^2$
$\omega_T \rightarrow \gamma \pi_T^{0'}$	$(Q_U + Q_D)c_{\chi'}$	0	$0.320 c_{\chi'}^2$
$\omega_T \rightarrow Z \pi_T^0$	$c_\chi \cot 2\theta_W$	0	$2.9 \times 10^{-3} c_\chi^2$
$\omega_T \rightarrow Z \pi_T^{0'}$	$-(Q_U + Q_D)c_{\chi'} \tan 2\theta_W$	0	$5.9 \times 10^{-3} c_{\chi'}^2$
$\omega_T \rightarrow W^\pm \pi_T^\mp$	$c_\chi / (2 \sin \theta_W)$	0	$2.4 \times 10^{-2} c_\chi^2$
$\rho_T^0 \rightarrow \gamma \pi_T^0$	$(Q_U + Q_D)c_\chi$	0	$0.320 c_\chi^2$
$\rho_T^0 \rightarrow \gamma \pi_T^{0'}$	$c_{\chi'}$	0	$0.115 c_{\chi'}^2$
$\rho_T^0 \rightarrow Z \pi_T^0$	$-(Q_U + Q_D)c_\chi \tan \theta_W$	0	$5.9 \times 10^{-3} c_\chi^2$
$\rho_T^0 \rightarrow Z \pi_T^{0'}$	$c_{\chi'} \cot 2\theta_W$	0	$2.9 \times 10^{-3} c_{\chi'}^2$
$\rho_T^0 \rightarrow W^\pm \pi_T^\mp$	0	$\pm c_\chi / (2 \sin \theta_W)$	$2.4 \times 10^{-2} c_\chi^2$
$\rho_T^\pm \rightarrow \gamma \pi_T^\pm$	$(Q_U + Q_D)c_\chi$	0	$0.320 c_\chi^2$
$\rho_T^\pm \rightarrow Z \pi_T^\pm$	$-(Q_U + Q_D)c_\chi \tan \theta_W$	$\pm c_\chi / \sin 2\theta_W$	$0.153 c_\chi^2$
$\rho_T^\pm \rightarrow W^\pm \pi_T^0$	0	$\mp c_\chi / (2 \sin \theta_W)$	$0.143 c_\chi^2$
$\rho_T^\pm \rightarrow W^\pm \pi_T^{0'}$	$c_{\chi'} / (2 \sin \theta_W)$	0	$2.4 \times 10^{-2} c_{\chi'}^2$

Table 2.3: Decay rates for $V_T \rightarrow G \pi_T$, parameter settings are $M_{V_T} = 210$ GeV, $M_{\pi_T} = 110$ GeV, $M_V = M_A = 100$ GeV, technifermion charges $Q_U + Q_D = 5/3$; $c_\chi = \cos \chi$ and $s_\chi = \sin \chi$ [28].

2.5 Technicolor at Hadron Colliders

Technicolor particles are predicted to be produced and detected at hadron colliders.

2.5.1 Previous Searches

During the Tevatron run from 1992 to 1996 (Run I) both high energy physics collaborations, CDF and DØ performed searches for Technicolor color singlet sector in their data. The CDF collaboration performed a search for Technicolor in several final states [29, 30]:

$$\begin{aligned}
q\bar{q} \rightarrow W^\pm, Z\gamma &\rightarrow \rho_T^{\pm,0} \rightarrow W_L^\pm \pi_T \rightarrow l^\pm \nu_l b j \\
&\rightarrow W_L^\pm \pi_T, \pi_T \pi_T, Z \pi_T \\
&\rightarrow \omega_T \rightarrow \gamma \pi_T \rightarrow \gamma b j
\end{aligned} \tag{2.24}$$

They published a combined analysis for the lepton plus jets and four jets final states.

In these analysis about 109 pb^{-1} of luminosity were used. In the lepton plus jets analysis, after requiring either one electron or one muon and a substantial amount of missing transverse energy in the event, at least one jet was required to be b -tagged in order to discriminate against W boson produced together with light quarks. Cuts on $\Delta\phi$ between the two jets and p_T of the dijet system were performed in order to discriminate against W boson plus heavy flavored jets and top-quark events. After simultaneous fitting for the existence of ρ_T and π_T resonances, a counting experiment was performed to estimate the excess over SM background prediction. In the absence of a signal 95% C.L. U.L. were derived and are shown in Figure 2.2.

Using 85 pb^{-1} of integrated luminosity CDF also searched for the decay $\omega_T \rightarrow \gamma\pi_T$ using the hypothesis that the technipion decays only into a b anti- b quark pair [30]. They found no excess over the SM background and computed a 95% C.L. exclusion region plot as function of ρ_T and π_T masses as shown in Figure 2.3. In the TC model used by CDF, decays of techni-vector mesons into transversely polarized gauge bosons were not considered [31].

An earlier version of TCSM was used by DØ to perform a search for the Technicolor process $\omega_T, \rho_T \rightarrow e^+e^-$ with 125 pb^{-1} collected in Run I [32]. The analysis consisted of a counting experiment in the dielectron invariant mass spectrum, where the resonance produced by the technivector meson decays should appear. The decay rate into two electrons depends upon the value of the ρ_T and ω_T masses as well as the difference between the technivector meson mass and π_T mass: in case this difference is greater than 100 GeV the decay channel $\rho_T \rightarrow W\pi_T$ would be open with the effect of worsening the limit reached by the analysis as shown in Figure 2.4.

2.5.2 Technicolor at DØ Run II

At the Tevatron, since the beginning of the actual run which started in March 2001 (Run II), the energy of the colliding beam increased from 1.8 TeV up to 1.96 TeV.

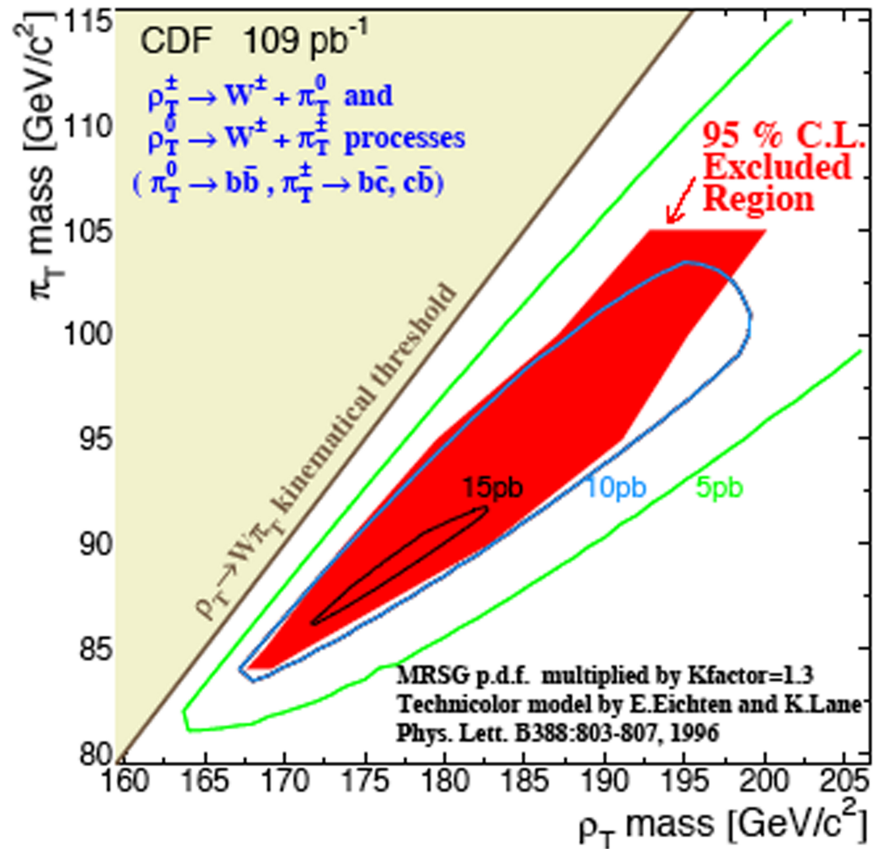


Figure 2.2: Exclusion region for technihadrons from $\rho_T \rightarrow W\pi_T$ search performed by CDF in Run I [29].

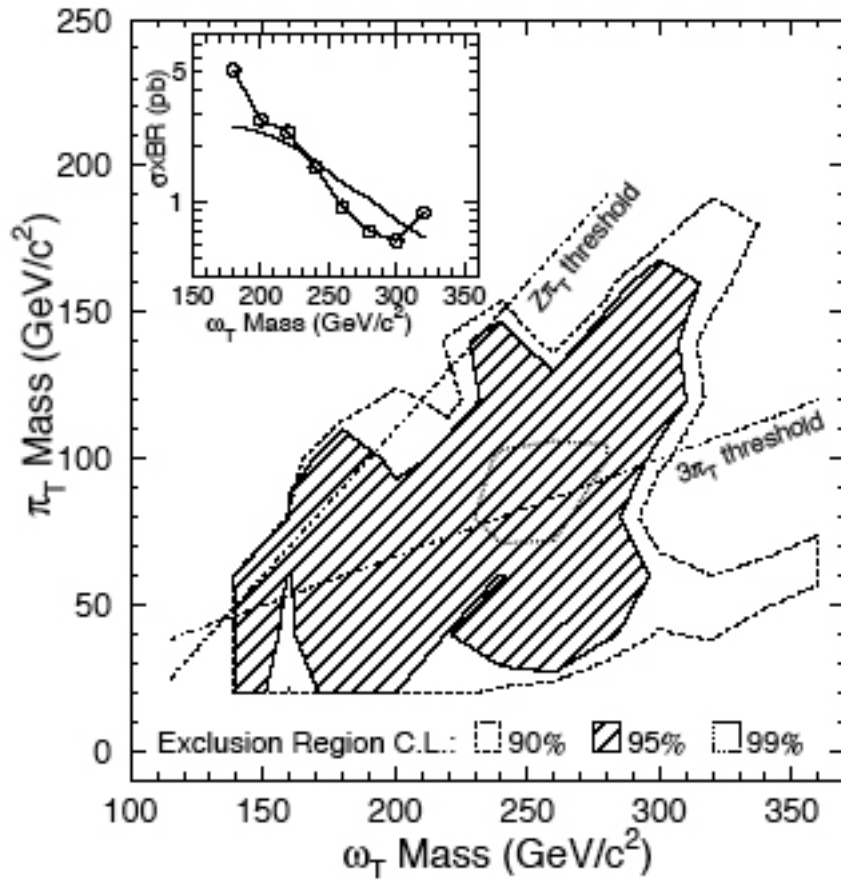


Figure 2.3: Exclusion regions for the CDF search for $\omega_T \rightarrow \gamma\pi_T$. The inset show the limit for $M(\pi_T) = 120 \text{ GeV}$ [30].

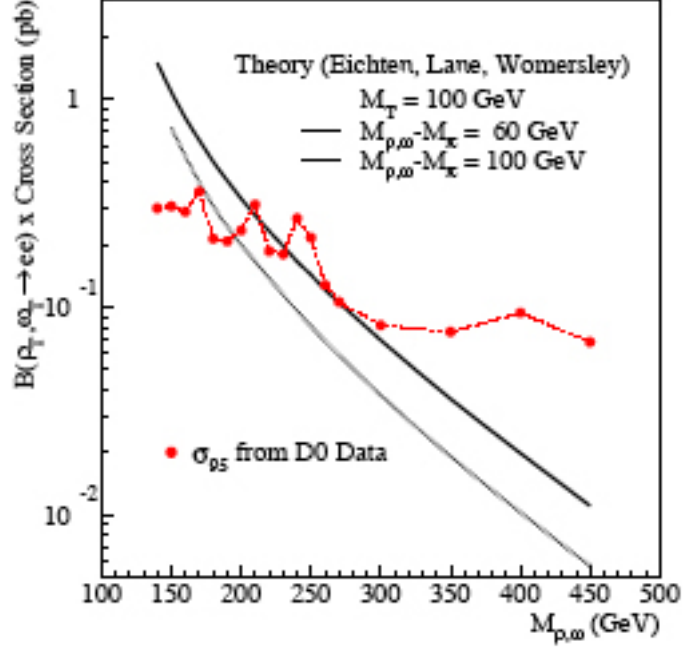


Figure 2.4: Experimental upper limit at 95% for DØ for the process $\rho_T \rightarrow ee$ using 125 pb^{-1} of data collected during Run I [32].

Consequently, changes in the cross section of the produced physics processes are expected. In the last few years a new version of the TCSM has been implemented in the Monte Carlo event generator PYTHIA 6.2 [33]. Changes have been made to the modeling of the $SU(3)_C$ single sector that affect mainly results for e^+e^- colliders. Figure 2.5 shows the cross section times branching ratio for the process $\rho_T \rightarrow W\pi_T^{0,(\pm)} \rightarrow e\nu_e b\bar{b}(b\bar{c})$. The same quantity is listed in Tables 2.4, 2.5 and 2.6 for $155 \leq M(\rho_T) \leq 220$. We use a multiplicative K-factor which is equal to:

$$K = 1 + \frac{\alpha_s}{\pi} \frac{2}{3} \left(1 + \frac{4}{3}\pi^2\right) \simeq 1.3. \quad (2.25)$$

The value of K depends upon the strong coupling constant α_s which itself depends upon the momentum transfer, Q^2 at the collision. For Q^2 of the order of the ρ_T mass of few hundred GeV, K can be considered constantly equal to 1.3 [34].

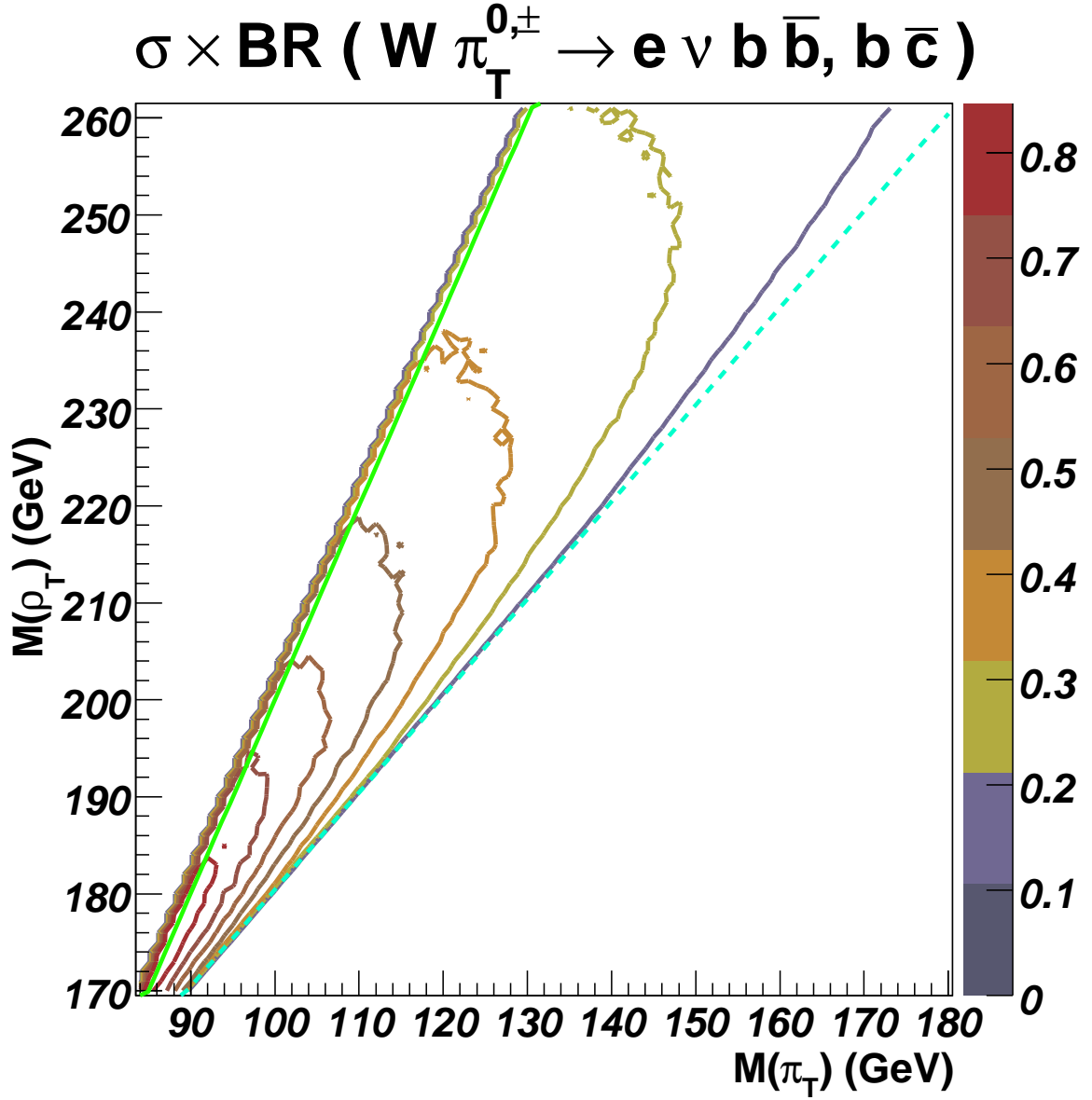


Figure 2.5: Cross section times branching ratio for the process $\rho_T \rightarrow W\pi_T^{0,(\pm)} \rightarrow e\nu_e b\bar{b}$ ($b\bar{c}$) with $M_V = 100$ GeV in the ρ_T , π_T plane. The unit of measure of the iso-cross section curves is pb, K-factor is included. The azure dashed line represents the threshold for $W\pi_T$ production, the green solid line the threshold for $\pi_T\pi_T$ production.

$M(\rho_T)$ (GeV)	$M(\pi_T)$ (GeV)	$\sigma(W\pi_T \rightarrow e\nu_e b\bar{b}(b\bar{c}))$ (pb)			
		$M_V = 100$ GeV		$M_V = 500$ GeV	
		neutral	charged	neutral	charged
155	70	0.092	0.146	0.063	0.1
	75	0.099	0.133	0.066	0.115
160	75	0.129	0.182	0.089	0.157
	80	0.195	0.272	0.31	0.468
165	75	0.124	0.203	0.095	0.165
	80	0.2	0.276	0.164	0.282
	85	0.178	0.218	0.382	0.382
170	80	0.178	0.241	0.138	0.236
	85	0.406	0.376	0.644	0.585
	90	0.145	0.185	0.24	0.24
175	80	0.143	0.216	0.119	0.209
	85	0.244	0.323	0.251	0.372
	90	0.345	0.335	0.586	0.514
	95	0.135	0.159	0.222	0.256
180	85	0.183	0.261	0.165	0.273
	90	0.42	0.383	0.657	0.583
	95	0.305	0.276	0.466	0.452
	100	0.12	0.125	0.178	0.194
185	85	0.123	0.229	0.123	0.23
	90	0.236	0.323	0.275	0.408
	95	0.362	0.349	0.575	0.512
	100	0.267	0.236	0.369	0.382
	105	0.101	0.108	0.165	0.3

Table 2.4: Cross section times branching ratio for $\rho_T \rightarrow W\pi_T \rightarrow e\nu b\bar{b}(b\bar{c})$ production as a function of $M(\pi_T)$, $M(\rho_T)$ and M_V .

$M(\rho_T)$ (GeV)	$M(\pi_T)$ (GeV)	$\sigma(W\pi_T \rightarrow e\nu_e b\bar{b}(b\bar{c}))$ (pb)			
		$M_V = 100$ GeV		$M_V = 500$ GeV	
		neutral	charged	neutral	charged
190	90	0.174	0.257	0.165	0.286
	95	0.325	0.376	0.489	0.564
	100	0.309	0.314	0.506	0.429
	105	0.223	0.228	0.297	0.312
195	90	0.13	0.215	0.114	0.226
	95	0.234	0.288	0.253	0.407
	100	0.254	0.342	0.39	0.558
	105	0.277	0.277	0.402	0.396
	110	0.196	0.18	0.228	0.288
200	95	0.148	0.244	0.143	0.304
	100	0.256	0.328	0.331	0.537
	105	0.234	0.306	0.355	0.481
	110	0.242	0.244	0.31	0.37
	115	0.157	0.17	0.192	0.233
205	95	0.109	0.214	0.112	0.22
	100	0.191	0.253	0.224	0.365
	105	0.221	0.29	0.302	0.486
	110	0.211	0.266	0.293	0.42
	115	0.195	0.214	0.292	0.304
	120	0.14	0.15	0.155	0.203

Table 2.5: Cross section times branching ratio for $\rho_T \rightarrow W\pi_T \rightarrow e\nu b\bar{b}(b\bar{c})$ production as a function of $M(\pi_T)$, $M(\rho_T)$ and M_V .

$M(\rho_T)$ (GeV)	$M(\pi_T)$ (GeV)	$\sigma(W\pi_T \rightarrow e\nu_e b\bar{b}(b\bar{c}))$ (pb)			
		$M_V = 100$ GeV		$M_V = 500$ GeV	
		neutral	charged	neutral	charged
210	100	0.138	0.206	0.141	0.27
	105	0.199	0.281	0.286	0.436
	110	0.192	0.269	0.3	0.402
	115	0.189	0.223	0.28	0.354
	120	0.182	0.195	0.224	0.282
	125	0.12	0.14	0.131	0.169
215	100	0.099	0.194	0.114	0.203
	105	0.156	0.238	0.175	0.346
	110	0.173	0.259	0.255	0.41
	115	0.181	0.234	0.246	0.36
	120	0.156	0.218	0.236	0.326
	125	0.156	0.164	0.193	0.248
	130	0.096	0.119	0.107	0.151
220	105	0.114	0.2	0.128	0.25
	110	0.185	0.231	0.217	0.391
	115	0.167	0.239	0.221	0.379
	120	0.158	0.213	0.22	0.323
	125	0.142	0.192	0.22	0.276
	130	0.134	0.153	0.188	0.195
	135	0.083	0.106	0.096	0.123

Table 2.6: Cross section times branching ratio for $\rho_T \rightarrow W\pi_T \rightarrow e\nu b\bar{b}(b\bar{c})$ production as a function of $M(\pi_T)$, $M(\rho_T)$ and M_V .

Chapter 3

Experimental Apparatus

3.1 The Tevatron Accelerator

Currently, the Tevatron proton anti-proton accelerator is the particle accelerator with the highest center of mass energy anywhere in the world. A schematic of the chain of linear and circular accelerators is represented in Figure 3.1.

In the multi-step acceleration process for the production of the proton and anti-proton beams, the first step happens in the Cockcroft-Walton accelerator. Here hydrogen atoms are immersed in a strong electrostatic field that strips the electrons from their orbits and drifts the ionized nuclei towards a cesium surface. The collision of the protons with the metal knocks H^- ions out of the surface. The same electric field drifts the H^- away from the surface and accelerates them to 750 keV. The accelerated ions are then transferred to the next pre-accelerator machine: the Linear Accelerator (Linac).

The Linac is made of five drift tube cavities and seven side coupled cavities (SCL). In the drift tubes particles are accelerated in the gaps between the tubes and shielded inside the tubes when the electric field changes polarity. At an energy of 116 MeV the ion beam passes to the SCL part of the Linac and is accelerated up to 400 MeV.

After the Linac, the Booster is the first synchrotron in the accelerator chain of Fer-

milab. It is also the smallest one, measuring 474 m of circumference. As soon as the H^- ions enter the Booster they are stripped of the electrons by means of a carbon foil. After being accelerated to 8 GeV the protons go to the Main Injector, a new accelerator for Run II. Fermilab's Main Injector (FMI) was built to replace the old Main Ring accelerator. The FMI performs better in terms of proton intensity than the old accelerator and can operate at the same time at 150 and 120 GeV for both colliding and fixed target experiments. Together with the Recycler, a fixed energy storage ring placed in the same tunnel as the FMI, the FMI constitutes the core of the Tevatron upgrade for Run II.

Protons from the FMI accelerate to the energy of 120 GeV before colliding with a Nickel target in order to create anti-protons. The few anti-protons produced in this process have a wide spread in energy distribution. In the Debuncher, they are made to go through a series of Radio Frequency (RF) electric fields with the effect of reducing their dispersion; this process is also called "stochastic cooling". The anti-protons are then stored in the Accumulator where they are kept until a sufficient amount of anti-protons is transferred from the Debuncher.

When the stack of anti-protons reaches a sufficient size, $\approx 10^{12}$ particles, the 8 GeV beam circulating in the Accumulator is transferred to the FMI, accelerated to 150 GeV and passed through the Tevatron circular accelerator, already loaded with 36 proton bunches. The 6.2 km radius Tevatron uses 774 superconducting dipole magnets in order to accelerate protons and anti-protons, injected at 150 GeV, to beam energies of 980 GeV. Table 3.1 shows the comparison between some Tevatron parameters for Run II and Run Ib.

3.2 The $D\bar{O}$ Detector

$D\bar{O}$ is a multipurpose detector located at one of the interaction points of the Tevatron accelerator. It is sub-divided into three main parts. From the innermost to the outer-

	Run Ib	Run II
Protons/bunch	2.3×10^{11}	2.7×10^{11}
Anti-protons/bunch	5.5×10^{10}	$3. \times 10^{10}$
Total Anti-protons	3.3×10^{11}	1.1×10^{12}
Anti-protons production rate	6.0×10^{11}	1.0×10^{11}
Anti-protons bunches	6	36
Energy	900	1000
Typical Luminosity	0.16×10^{31}	0.86×10^{32}
Bunch Spacing	~ 3500	396
Interaction crossing	2.5	2.3

Table 3.1: Comparison between Tevatron parameters for Run II and Run Ib (1993-1995).

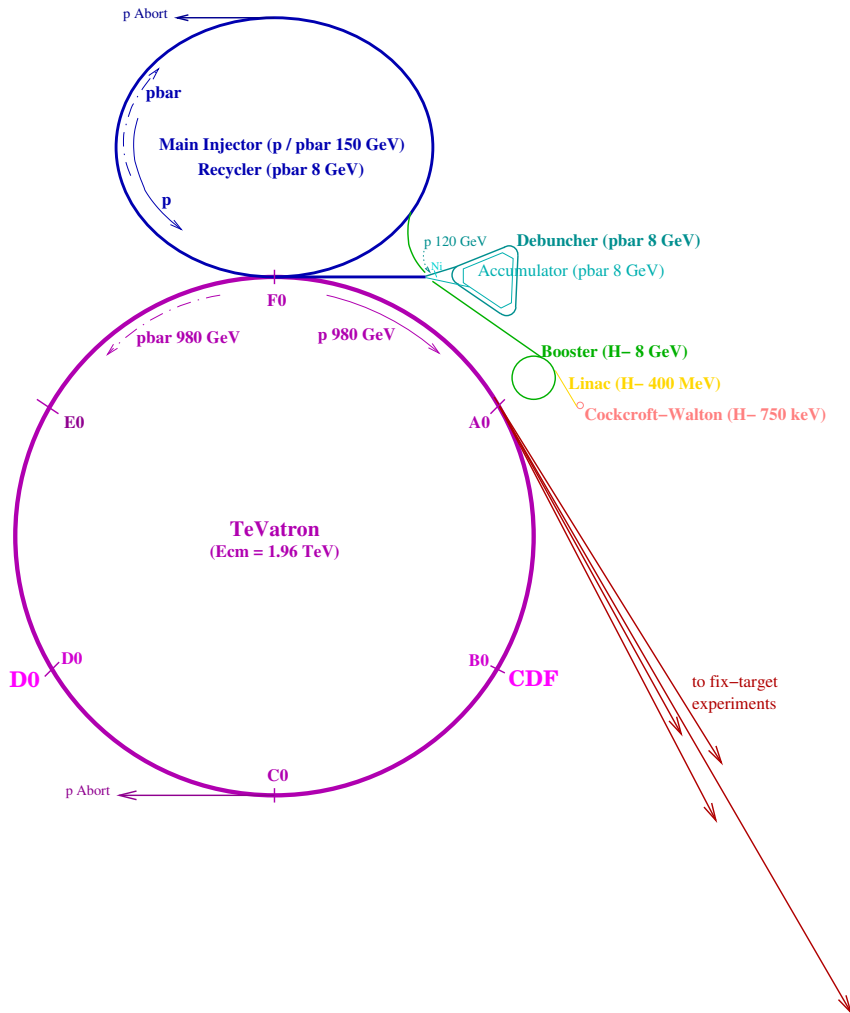


Figure 3.1: The Tevatron Accelerators [35].

most, they are: the tracking system, the uranium liquid-argon calorimeter and the muon spectrometer.

In this section details of the individual constituents of the detector are discussed together with a description of the trigger and the data acquisition systems. We introduce now the coordinate system used to describe the detector: the z -axis is along the proton direction, the angles θ and ϕ are the polar and azimuthal angle, the r coordinate indicates the distance to the z -axis and $\eta = -\ln \tan \theta/2$ is the pseudorapidity, a quantity that approximates the true rapidity $y = 1/2 \ln((E + p_z)/(E - p_z))$ for $mc^2/E \rightarrow 0$.

3.2.1 The Tracking System

The improved Tevatron performances for Run II triggered a series of improvements for the DØ detector [36] in order to fully take advantage of the promised higher luminosity [37]. One of the most important one is the complete replacement of the tracking system. The new tracking system includes the silicon microstrip tracker (SMT) and the central fiber tracker (CFT). The tracking detector is surrounded by a 2.8 m long superconducting solenoid that provides a 2 Tesla axial magnetic field used to determine the momentum of the charged particles.

The Silicon Microstrip Tracker

The SMT is a semiconductor high precision tracking detector. When a charged particle penetrates the detector it produces electron-hole pairs. The typical energy for electron-hole production in Silicon is 3.6 eV. The collection of the charge produced in the detector gives a measure of the position of the incoming particle. In order to avoid multiple Coulomb interactions the thickness of Silicon devices is kept to 300 μm . Implanting a p type strip on the n type bulk gives a single sided detector, adding another n⁺ on the other side gives a double sided detector.

The design of the SMT was driven by several factors: three-dimensional track recon-

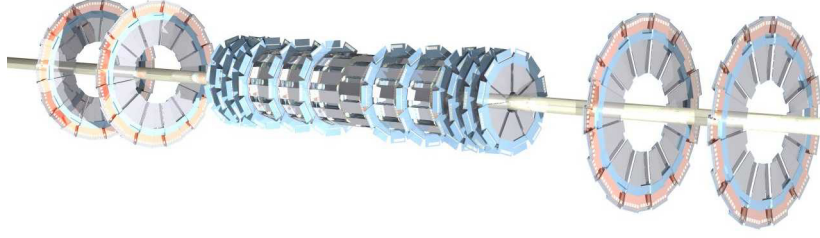


Figure 3.2: The disk/barrel design of the SMT [36].

Module	Type	Layer	Pitch (μm) p/n	Length (cm)	Inner Radius (cm)	Outer Radius (cm)
F-disk	DS		50/62.5	7.93	2.57	9.96
H-disks	SS		40	76.3 ⁱ	9.5	26
			80 readout	63.3 ^o		
Central barrels	DSDM	1,3	50/153.5	12.0	2.715	7.582
	DS	2.4	50/62.5	6.0	4.55	10.51
Outer barrels	SS	1.3	50	6.0	2.715	7.582
	DS	2.4	50/62.5	6.0	4.55	10.51

Table 3.2: Characteristics and deployment of various sensor types in the SMT. *i* (*o*) indicates length of the inner (outer) H-disk sensor. SS stands for single-sided, DS double sided and DSDM for double-sided double-metal.

struction, with vertexing capability and impact parameter resolution of about $30 \mu\text{m}$, radiation hardness to resist the Tevatron luminosity regime and high eta coverage allowing the reconstruction of tracks along the entire interaction region ($\sigma \approx 25 \text{ cm}$). The SMT design consists of six barrel/disk modules supported by a double-walled carbon-fiber/epoxy half cylinder. The cylinder also supports the detector cabling and cooling system and maintains the high precision alignment. Each barrel contains four concentric layers of silicon ladders. A schematic of the SMT is shown in Figure 3.2.

The ladder, the smallest detector unit, consists of two $300 \mu\text{m}$ thick wafers, with size of $6.0 \times 2.1 \text{ cm}$. Layers can be double or single sided, as shown in Table 3.2. At the end of each barrel a disk of twelve double-sided wedge detectors is located (“F-disk”). Three more F-disks are located on each side, not attached to the barrels. In the forward region two larger disks (“H-disks”) provide support for tracking at high η ($\eta > 2.2$).

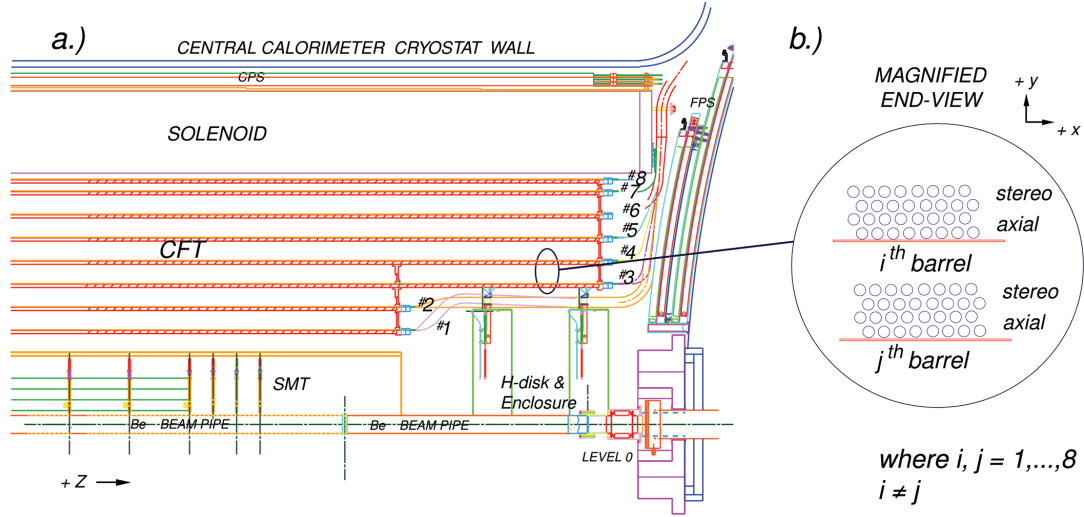


Figure 3.3: Schematic of the CFT. a) axial section of the CFT b) transverse section [38].

The Central Fiber Tracker

Together with the SMT, the Central Fiber Tracker (CFT) enables track reconstruction and momentum measurement for all charged particles within the range $\eta = \pm 1.7$.

The fibers in the CFT are made of scintillating material that absorbs the electromagnetic radiation of the particles and then, in response, fluoresces photons at a characteristic wavelength, releasing the previously absorbed energy.

The basic CFT detection element is the multicladd scintillating fiber. The fiber consists of three layers, the core is made of polystyrene surrounded by a thin acrylic cladding, and then surrounded by fluoro-acrylic cladding. These three materials have indices of refraction of 1.59, 1.49 and 1.42, respectively. The addition of the second cladding increases the light trapping by about 70% with respect to single-clad fibers, and improves the mechanical robustness of the fibers.

A schematic view of the CFT is shown in Figure 3.3. The scintillating fibers have a diameter of $835 \mu\text{m}$ and length of 1.66 or 2.52 m. About 76,800 fibers cover 8 concentric support cylinders occupying the radial space from 20 to 50 cm. On each of the eight supports, two different doublet layers are mounted. In one layer, layer x , the fibers are

parallel to the beam line. The other layer is made of fibers with a tilt of 3 degrees clockwise (anti-clockwise) from the z -axis, layer “u” (“v”). From the smallest radius outward the orientations on the cylinders is xu-xv-xu-xv-xu-xv-xu-xv .

Each scintillating fiber is connected to a clear fiber waveguide that transfers the light to a Visible Light Photon Counter (VLPC). VLPC are high efficiency single photon detectors made of arsenic doped silicon diodes operating at temperatures between 8-10 K. When tested with cosmic rays the CFT showed a doublet hit efficiency of about 99.9% and a resolution of 100 μm . The fast and continuous readout of the CFT detector is processed by the first of the three different DØ trigger levels. The names of the trigger levels are “Level 1”, “Level 2” and “Level 3” as described in Section 3.2.5.

3.2.2 The DØ Calorimeter

DØ calorimeter system consists of three liquid-argon/uranium sampling calorimeters (one central and two end caps), as shown in Figure 3.4. In addition the intercryostat detector, made of a series of scintillating tiles, fills the gaps between the cryostats.

The calorimeter is used to measure the energy of the particles produced in the proton anti-proton collisions. Almost all particles, except muons and neutrinos, lose their energy through radiation and collisions inside the calorimeter. Each calorimeter module is divided in three sections, the inner Electromagnetic (EM) section, the Fine Hadronic (FH) and the outer Coarse Hadronic (CH) section.

High energetic electrons and photons produce electromagnetic showers when interacting with the heavy uranium nuclei. Their energy loss follows the law:

$$\frac{dE}{E} = -\frac{dx}{X_0}. \quad (3.1)$$

The radiation length X_0 for Uranium is 3.2 mm. In order to ensure that showers from high energetic particles are properly contained, the EM section of the calorimeter is

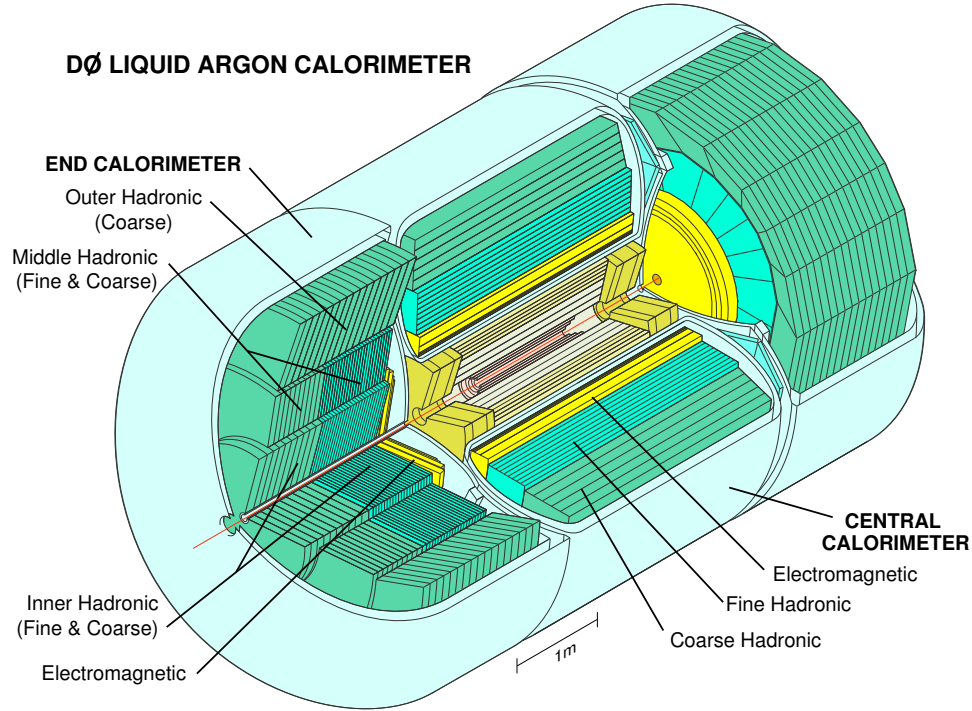


Figure 3.4: The DØ calorimeter consists of three modules, central and end calorimeter. Each module is divided into Electromagnetic, Fine and Coarse Hadronic [36].

about $21 X_0$ thick. Hadrons interact via the strong force with the uranium nuclei. The scale of their interaction is given by the absorption length λ , which for the short range nature of the strong interaction is bigger than the same quantity for EM particles. Both the FH and CH have a thickness of 3.2λ .

The DØ calorimeter is a *sampling* calorimeter, this means that only the fraction of the shower energy absorbed in the active material is measured, whereas part of the energy hadrons lose to break apart the Uranium nuclei is not detected. The basic calorimeter module is the “unit cell”, as shown in the schematic in Figure 3.5. Inside the cell the electron-ion pairs produced by the ionization of the liquid argon drift to the grounded absorber plates (cathodes) or to the readout pads (anodes) kept at 2 to 2.5 kV. A readout pad consists of two layers of G10 plastics covered by highly resistive carbon-loaded epoxy. In the inner surface a plastic sheet is copper-coated and milled into the pattern necessary for the precision readout. Each calorimeter cell has size of 0.1×0.1 in $\Delta\phi \times \Delta\eta$. In

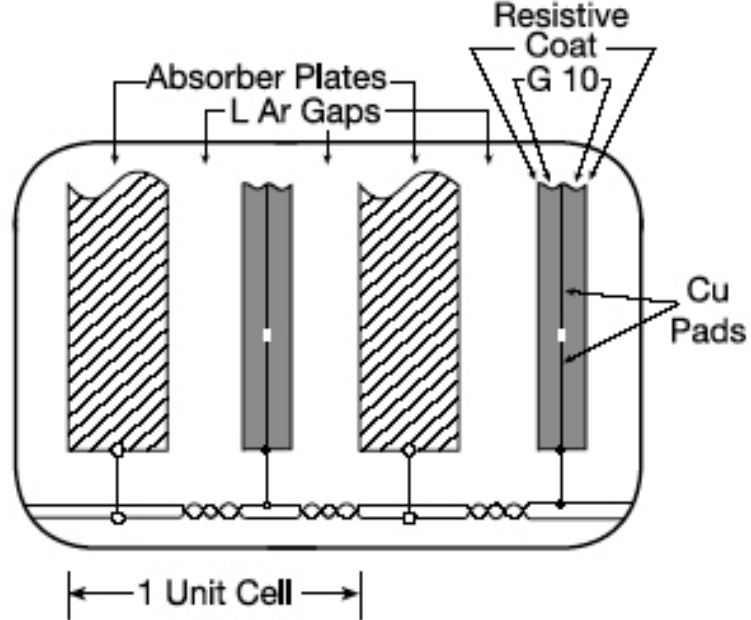


Figure 3.5: Calorimeter Unit Cell [36].

the third layer, where the shower maximum for electrons with p_T of 20 GeV is located, the EM section has a finer segmentation of 0.05×0.05 . Cells are arranged to form pseudo-projective towers as shown in Figure 3.6.

Calorimeter electronics

There are about 47,000 readout channels connected to the calorimeter readout system.

The readout is done in three stages:

1. Signals from the calorimeter cells are transported to the pre-amplifiers located in the cryostats;
2. Signals are transported in the baseline subtractor boards (BLS). Here they are kept for about $4 \mu s$, until a trigger is available. The BLSs provide a fast analog trigger sum signal for Level 1 and Level 2 calorimeter triggers and at the same time perform signal shaping and baseline subtraction prior to the digitalization;

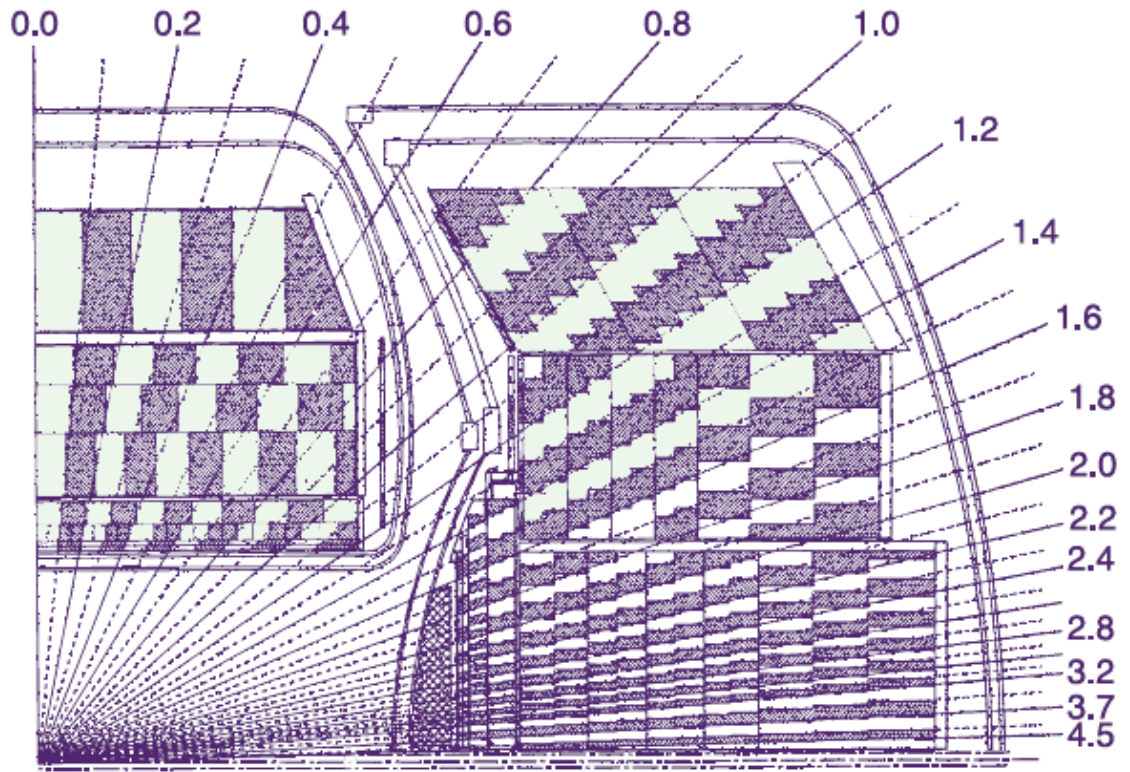


Figure 3.6: Schematic view of DØ calorimeter showing the transverse and longitudinal segmentation, the lines indicates the pseudorapidity interval from the center of the detector [36].

3. The signal is sent to the Analog to Digital Converter (ADC) and enter the Level 3 trigger system and data acquisition system.

Preshower Detectors

The preshower detector, divided into three systems, one at low and two at high pseudorapidity, is made of extruding polystyrene plastic, a scintillating material. The fast read out makes its usage possible in the trigger system; the energy measurement provides shower shape information that helps identify electromagnetic objects.

The Central Preshower (CPS) is located in the 51 mm gap between the solenoid and the electromagnetic calorimeter. At the center of each strip a wavelength-shifting fiber is located and it is read out using VLPC. In the CPS, the three layers of 1280 strips, covering up to a pseudorapidity η of 1.3, are arranged in an axial u - v geometry in order to match the CFT geometry for Level 1 triggering purposes. A cross section of the scintillator strips is shown in Figure 3.7.

The two Forward Preshowers (FPS) consist of two layers of scintillating fibers mounted on the edge of the end calorimeter cryostat. The two layers are separated by a $2X_0$ -thick lead absorber. The first minimum ionizing particle (MIP) layer covers the pseudorapidity region $1.5 < |\eta| < 2.5$.

3.2.3 The Muon System

Muons, once produced in the proton anti-proton collisions, travel through all material in the calorimeter without being stopped. They can be detected using the tracking detector and the mass spectrometer located in the outer part of the detector: the Muon System. The Muon System is divided in the central muon system, with a coverage up to $|\eta| < 1$, and the forward muon system that extends the coverage up to $|\eta| < 2$.

At the core of the central muon system there is a 109 cm thick toroid magnet, shaped as a square annulus, with its inner surface located at 318 cm from the beam line. The

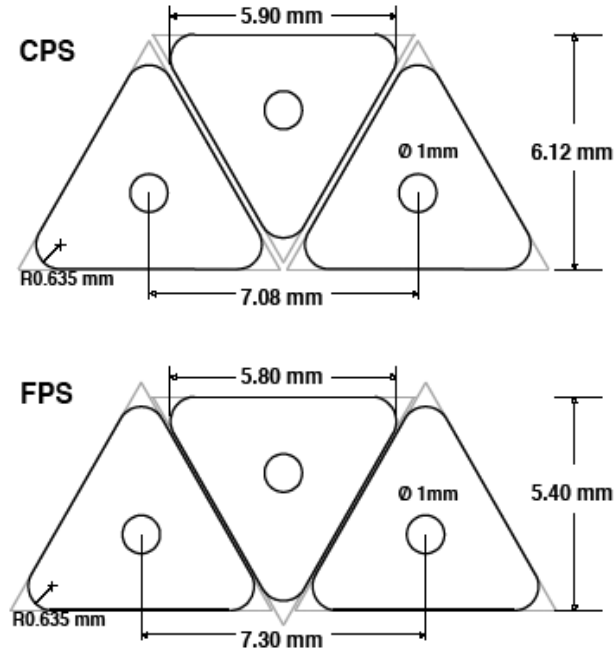


Figure 3.7: Cross section of FPS and CPS scintillator strips [36].

toroid is surrounded by proportional drift chambers and scintillator detectors. Three layers of proportional drift tubes (PDT), for a total of 164 chambers, cover almost 55% of the central muon system, while close to 90% is covered by at least two layers [36]. The chamber size is typically $2.8 \times 5.6 \text{ m}^2$ wide and 10.1 cm in height. Each PDT layer has three decks of cells oriented along the toroid magnetic field in order to detect the muon bend coordinate. In Figure 3.8 the anode wire together with the segmented geometry of the vernier cathode is shown [39]. For every hit, the drift time inside a cell, the ΔT between hits in two neighboring cells and the quantity of charge in both cathode and anode are recorded.

A layer of scintillation counters covers the inner part of the PDT, the A- ϕ counters. Their name comes from the ϕ segmentation of about 4.5 deg that matches the central fiber tracker trigger segmentation. The A- ϕ counters are a fast detector used for triggering on muons, rejecting out-of-time backscatter as well as identifying low p_T muons that do not penetrate the toroid. The Cosmic cap and bottom counters are scintillators

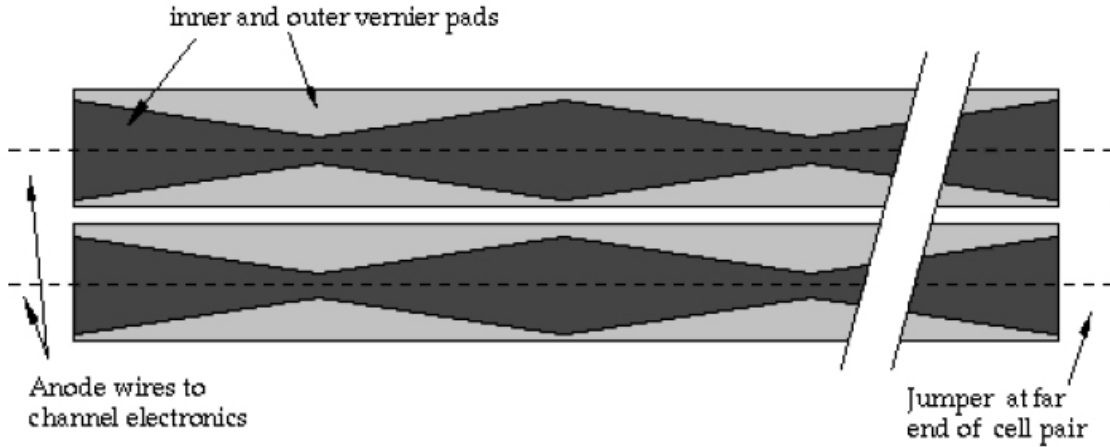


Figure 3.8: PDT pads viewed from above [39].

located on the outer side of the central muon PDT and provide a fast time signal that allows to discriminate against cosmic ray background.

In the forward muon system the same role of the PDT is played by the mini drift tubes (MDT). Three layers of MDT, namely A, B and C-layer, have three (B and C-layer) or four decks of tubes. Each tube consists of eight cells having $9.4 \times 9.4 \text{ mm}^2$ of cross section and an anode wire at the center. The maximum drift time depends upon the angle of the incident particle and varies from 40 to 60 ns. Even though the momentum resolution of the MDT is only 20% for muon below 40 GeV, its usage is very important for particles with $1.6 \leq \eta \leq 2.0$ that are not fully covered by the CFT. Three layers of finely segmented scintillating counters are installed next to the three MDT layers. Their ϕ segmentation is also 4.5 deg and η goes from 0.07 to 0.12.

3.2.4 The Luminosity Monitor

In order to determine the amount of luminosity \mathcal{L} recorded, DØ uses the detection of $p\bar{p}$ inelastic scattering with a dedicated device, the Luminosity Monitor (LM). The total

luminosity is obtained with the formula:

$$\mathcal{L} = \frac{f\bar{N}_{LM}}{\sigma_{LM}}, \quad (3.2)$$

where f is the beam crossing frequency, \bar{N}_{LM} the average number of interactions per beam crossing and σ_{LM} is the effective cross section for the process.

The LM detector consists of two arrays of twenty-four plastic scintillators located at the ends of the calorimeter, with pseudorapidity coverage range $2.7 < |\eta| < 4.4$.

In order to discriminate against the beam halo, the z position of the vertex is calculated from the time of flight: $z = (c/2)(t_- - t_+)$, where t_{\pm} is the time of flight of particles hitting the detector at ± 140 cm. Cutting on $|z| < 100$ cm eliminates the background at $z \approx \pm 140$ cm.

3.2.5 The DØ Trigger System

Three stages of trigger are implemented in the DØ trigger system to identify interesting events to be recorded. The first stage (Level 1) processes all the events coming from the $p\bar{p}$ collision at 1.7 MHz through a series of hardware trigger elements reducing the event rates to 1.6 kHz. At this rate events are processed to Level 2 that brings the rate to 1 kHz. The last stage, Level 3, is a collection of software tools, installed on computer farms that filter the Level 2 output and bring the rate to the final 50 Hz that will be fully reconstructed.

The Trigger Framework (TFW) has a fundamental role in both Level 1 and Level 2 decision making. The Run II TFW consists of 9U 400 mm cards; it makes use of field programmable gate array (FPGE) technology to implement different functions. The TFW receives “AND-OR” terms from different parts of the experiment and combines them to form 128 “physics” triggers. It controls and sets prescale for any “physics” trigger and runs lower level commands for diagnostics. Figure 3.9 shows a schematic of

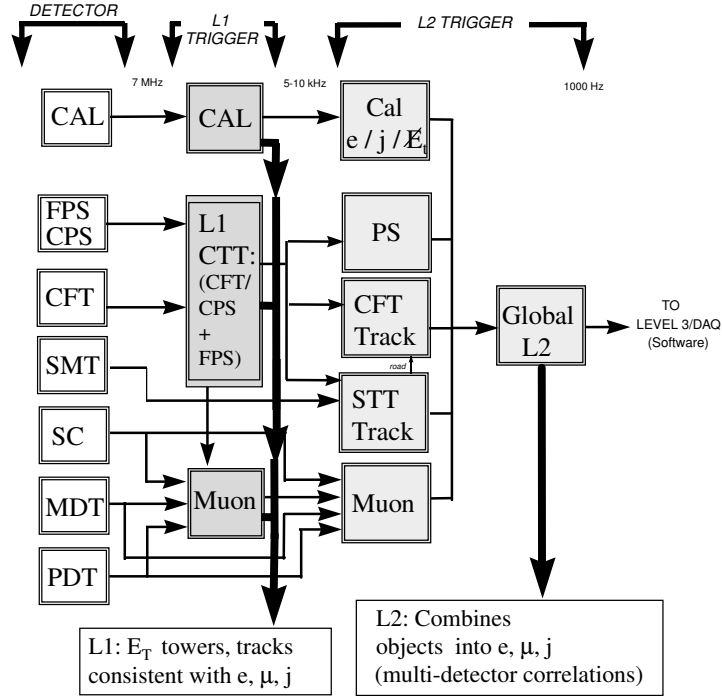


Figure 3.9: Block diagram of the DØ trigger system, the arrows indicates the data flow [40].

the components of the DØ trigger.

The calorimeter trigger (L1Cal) uses the energy deposition clustered in calorimeter towers of size of $\Delta\phi \times \Delta\eta = 0.2 \times 0.2$. After subtracting pedestals, the tower energies are processed to give E_T information. The EM E_T and the total E_T (EM+H) of the event are used alone or in combination in order to trigger on local variables (i.e. presence of EM or EM+H towers with energy above some preset threshold value) or global variables (i.e. $\sum E_T$ and missing transverse energy).

The Level 1 central track trigger (L1CTT) provides fast track information by processing hits from the CFT and the preshower detectors, CPS and FPS. This information is then used at Level 1, for the L2 track trigger system and for finding muons. The L1Muon uses central tracks from L1CTT to match hits on the scintillator counters and to match track-stubs from the wire chambers.

Level 2 triggers consist of a set of preprocessing engines, based on the detector subsys-

tems, and a global set of tools and filters (L2Global). The L2Global worker establishes correlations among L1 and L2 objects and issues the final L2 accept. Among the L2 preprocessors:

- L2Cal uses coarse calorimeter tower clustering to define jets, electrons and photons; it also calculates missing transverse energy;
- L2Muon makes use of timing and calibration information to improve the quality of the muon candidates;
- L2STT uses L1CTT tracks to define region of the detector, called roads, where SMT hits should be looked for. The results of the fits of SMT hits together with hits in the outermost and innermost CFT layer are sent to L2Global;
- L2CTT can be run in two modes, with or without input from STT. In the latter, L1CTT uses L1 readout information to refine the track p_T measurement; the track ϕ_{em} at the third layer of the EM calorimeter is calculated in this stage.

The software based Level 3 trigger performs a partial reconstruction of physics objects. At this level a series of software algorithms (filter tools) perform cuts on the event physics objects and their relations. At a rate of 50 Hz the events are sent to the host cluster to be recorded.

Chapter 4

Event Reconstruction

4.1 Event Reconstruction

The software used for reconstructing objects for physics analysis is the $D\bar{O}$ Offline Reconstruction Program (RECO). It processes either collider events or simulated events produced with the $D\bar{O}$ simulation software. First, for each event the Event Data Model (EDM) organizes the detector information by storing them in chunks. More layers of chunks are produced later once RECO processes the detector information.

As a first step RECO unpacks individual data blocks, associates electronics channels with physical detector elements and applies detector specific calibration constants. Second in the chain of the process for RECO is clustering hits produced by charged particles in the tracking detector in order to produce tracks. The tracks are stored in a specific chunk and used for reconstructing the primary vertex of interaction, i.e. the three-dimensional collision point for the proton and anti-proton that generated the recorded event. The energy deposited into the inner calorimeter is used to reconstruct electrons and photons. The cones of activated hadronic calorimeter cells are used to reconstruct the energy of incoming “jets” of hadrons, and last the imbalance in event momentum is used in order to detect neutrinos. Finally, information from each of the

preceding reconstruction steps are combined in order to produce “objects” for physics analysis. As explained later in this section tracks that are not associated with the PV are used to reconstruct secondary vertices of interaction (SV) indicating the possibility of the production and decay of B-mesons.

RECO is designed to produce two output formats: the Data Summary Tape (DST) containing extensive information necessary to perform any physics analysis, and the Thumbnail (TMB) containing a summary of the objects stored in the DST and designed to be one tenth the DST size, which is about 15 Kb per event. In addition to these two, TMBTree is a ROOT based ntuple reproducing the TMB data structure and accessible from ROOT [41].

4.2 Track and Vertex Reconstruction

The signal coming from the energy deposition of charged particles in the tracking detector is digitized and processed in order to account for detector anisotropy and electronic noise, respectively by applying an offset and gain and by removing a pedestal to each strip readout. The trajectory of the particle can be identified by a series of contiguous hits through the SMT and CFT detectors. Elaborate tracking algorithms are used in order to take into account the detector inefficiencies, i.e. missing hits in adjacent sub-detector system, and fake hits due to noise fluctuations above the pedestal cut an ADC level of 8 counts.

The first part of the tracking reconstruction process consists of identifying clusters of sub-detector components (strip for the SMT and fibers for the CFT) with a readout passing a certain threshold value. In the SMT, the position of the centroid of the cluster \bar{n} is given by the average of the strip positions weighted by their pulse intensities. Axial and stereo hits are combined resulting in three dimensional coordinates for the centroids. The CFT cluster algorithm is a standard nearest neighbor algorithm: it starts from an

activated fiber and goes on adding all the neighboring hit fibers until a non-hit fiber is found. The number of ADC-counts needed to activate a fiber varies with the length of the fiber itself, longer fibers lose more light therefore have smaller activation thresholds. The position assigned to the cluster is the middle point between the innermost and the outermost hits.

DØ uses two different algorithms in order to fit the cluster positions to tracks: the Alternative Algorithm (AA) and the Histogramming Track Finder (HTF) [42].

4.2.1 The Alternative Algorithm (AA)

The Alternative Algorithm is based on the method of pattern recognition. It starts building Track Hypotheses from any inner SMT hits and any other pair of SMT hits that satisfy the following requirement:

- The second hits must be in a following layer;
- The difference in their axial angle $\Delta\phi < 0.08$ radians;

The third hit should also belong to a following layer provided that:

- The radius of the circle passing through all three hits measures less than 30 cm;
- It has a minimum distance with respect to the beam spot (*dca*) of 2.5 cm;
- The χ^2 of the fit is less than 16.

After any Track Hypothesis is extrapolated to the next layer all hits in given window are associated with the original Hypothesis, the track is then refit and kept as Track Hypothesis if it passes the χ^2 cut. Missing detector hits, “misses”, are categorized as “inside misses” (misses between any two hits of the Track Hypothesis), “forward” and “backward” misses (misses for forward or backward track extrapolation). Misses are very important in order to reject poorly reconstructed trucks.

4.2.2 The Histogramming Track Finder Algorithm (HTF)

The Histogramming Track Finder algorithm is run in parallel to the AA algorithm in order to find Track Hypotheses. The HTF working principle consists of building histograms with quantities derived from detector hit positions and finding local histogram maxima corresponding to true tracks. This technique is generally less CPU consuming than any pattern recognition based algorithm.

Particle trajectories in the transverse plane can be characterized by the three parameters (ρ, dca, ϕ) :

- The radius of curvature $\rho = qB/p_T$ where q is the particle charge, B is the magnetic field and p_T the transverse momentum);
- Dca is the distance of closest approach to the beam axis;
- ϕ is the azimuthal angle.

The HTF working principle can be described by considering the case of tracks from particles produced directly in the $p\bar{p}$ collision: $dca \approx 0$. For this case any hit in the *coordinate space* (x, y) can be mapped to a line in the *parameter space* (ρ, ϕ) (Hough transform) [43]. Any detector hit makes to a line in the *parameter space*. Lines originating from hits belonging to the same tracks intersect at the same point, and result in a local maximum in the discretized *parameter space*.

If only a few hits are present it may not be simple to distinguish the local maximum. More sophisticated approaches that make use of templates and a Kalman Filter technique in order to discriminate against noise are then used.

4.2.3 Track Selection

After all Track Hypotheses are identified by the two algorithms, a selection of tracks, satisfying the requirements below, is kept:

- Hits must be found in at least four detectors;
- Tracks must not have more than three inside misses;
- Tracks must not have more than 6 forward or backward misses;
- Not more than two inside misses in the SMT;
- $N_{hits}/5 \geq N_{miss}$.

At the end the total number of axial hits and the total number of shared axial hits used by the Track Hypothesis are computed. Only tracks passing more requirements based on the shared hits:

- $N_{shared} \leq 2/3N_{tot}$;
- $N_{shared} \leq 1/3N_{tot}$ or $N_{tot} - N_{shared} > 3$;
- Plus a few more strong conditions for short tracks and misses.

are kept in the final collection of tracks.

4.2.4 Primary Vertex

Primary Vertices (PV) are formed by fitting a collection of tracks with small impact parameter to a three-dimensional point inside the detector. PV's are very important in order to understand the collision point and to reconstruct other event quantities. They are second in the reconstruction chain, after tracks.

The PV fit follows a “tear-down” procedure: after all tracks are fitted to a PV, tracks with χ^2 contribution to the fit greater than 10 are removed. Only after the total χ^2 of the PV fit becomes less than 10, the algorithm stops removing tracks.

All tracks excluded by the PV fit are refitted with the same criteria: it's very likely that one event has multiple PV's. There are two sources for multiple PV: fake and “Minimum bias” vertices. The first ones are artifacts of the detector resolution and track

Track Variable	cut
p_T	$\geq 0.5 \text{ GeV}$
SMT hits	$\geq 2 \text{ (DATA)} \geq 0 \text{ (Monte Carlo)}$
dca/σ_{dca}	≤ 5.0

Table 4.1: List of cuts for tracks selected for the second pass PV computation, as implemented in RECO.

misidentification. “Minimum bias” vertices are generated by low momentum transfer $p\bar{p}$ interactions. The PV algorithm is run twice, the first time tracks are selected with a loose dca significance cut, $dca/\sigma_{dca} < 100$ where the dca is calculated with respect to a nominal beam position passing by the z -axis of the detector. The collection of PV’s formed by the first pass is fitted to a straight line that better represents the actual beam position; this is used in order to calculate the dca for tracks used in the second pass of PV fits. The second pass track selection is indicated in Table 4.1 [44].

4.2.5 Probabilistic Primary Vertex Selection

The hard-scatter interaction is identified among the collection of reconstructed PV’s also containing minimum bias vertices, by using a probabilistic approach. $P(p_T)$, where p_T is the track transverse momentum, is a probability distribution function derived from Monte Carlo. As shown in Figure 4.1 the p_T of tracks forming the vertex is a powerful discriminator between “hard-scatter” and minimum bias vertices. $P(p_T)$ has the form:

$$P(p_T) = \frac{\int_{\log_{10}(p_t)}^{\infty} F(p_t) dp_T}{\int_{\log_{10}(0.5)}^{\infty} F(p_t) dp_T} \quad (4.1)$$

where $F(p_T)$ is the minimum bias track p_T distribution shown in Figure 4.1.

The total probability for a vertex to originate from a minimum bias interaction is given by the formula:

$$P_{min\ bias} = \Pi \sum_{k=0}^{N-1} -\frac{\ln(\Pi)^k}{k!}, \quad (4.2)$$

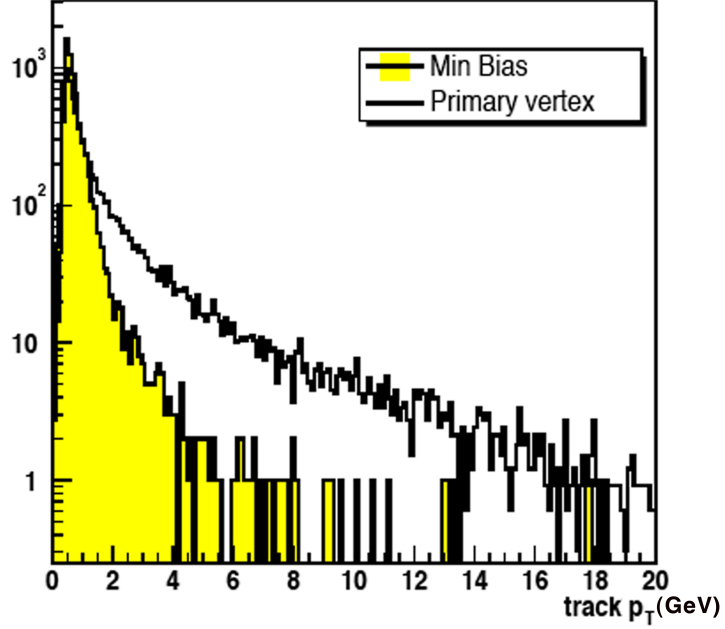


Figure 4.1: Track p_T spectrum for minimum bias and hard-scatter vertices in Monte Carlo simulated events [45].

where Π is the product of the single probabilities of the N tracks belonging to the PV vertex. In each event the PV with minimum $P_{min\ bias}$ is taken as the hard-scatter vertex [45].

4.3 Jet Reconstruction

4.3.1 Introduction

Due to the confinement of color, highly energetic partons (quarks and gluons) produced by the Tevatron proton and anti-proton collisions generate collimated streams of colorless hadrons, the so-called jets, of total energy equivalent to that of the original parton. To cluster final-state particles and to reconstruct kinematic quantities of the jet, jet algorithms are needed. Jet algorithms can be defined at several levels, corresponding to the different types of objects used as input:

- At detector level, when using energy deposits in the calorimeter or charged particles reconstructed in the tracking system;
- At particle level, when using stable particles in Monte Carlo simulated events;
- At parton level, when using partons in Monte Carlo simulated events.

Perturbative QCD (pQCD) succeeds in predicting the existence and behavior of jets, provided that the jet algorithm ensures collinear and infrared safety [46]:

- *Collinear Safety*: The algorithm should be insensitive to the splitting of a parton in two collinear ones of same total energy or to the splitting of some energy deposit between several calorimeter towers;
- *Infrared Safety*: The algorithm should be insensitive to the presence of a soft parton or a low energy deposit in the event.

The other most important attributes that a jet algorithm should possess in order to ensure consistency among experimental measurements and theoretical predictions are [47]:

- *Invariance under Boosts*: The algorithm should be independent upon of boosts of the colliding partons center of mass frame;
- *Boundary Stability*: Jet kinematic quantities should exhibit boundaries (due to the total energy-momentum conservation) insensitive to the details of the final state;
- *Order Independence*: The algorithm should find the same jets at parton, particle and detector level.

4.3.2 The DØ Run II Cone Jet Algorithm

Several types of jet algorithms can be employed at the Tevatron [48], but here only the DØ Run II cone jet algorithm [49] with $R_{cone} = 0.5$ will be considered.

Objects are clustered into a cone jet if their angular distance ΔR to the axis of the geometrical cone defining the jet is smaller than the radius R_{cone} . $\Delta R = \sqrt{\Delta Y^2 + \Delta\varphi^2}$ will be used here, where Y is the rapidity and φ the azimuth. The first step in a cone jet algorithm is to find all stable cones, also called proto-jets, in a given event. A cone is defined as stable if the kinematical combination of all objects (partons, particles or energy towers) inside this cone results in a proto-jet whose momentum is aligned with the geometrical cone axis. Since any given object can belong to more than one proto-jet, a second step, usually designed as merging/splitting, is generally needed to attribute each object to a unique jet.

Since finding all stable cones in any given event is a problem for which no analytical solution exists, an iterative procedure in several steps is followed:

- Start from a given position, also called a seed, of the cone axis;
- Calculate the proto-jet candidate direction from the objects inside this cone;
- Replace the cone axis by the newly calculated proto-jet direction;
- Iterate the two previous steps unless or until the two directions coincide;
- Repeat this procedure for all possible seeds.

Such a procedure can a priori be guaranteed of finding all stable cones in any given event, but only if all points on a fine enough grid in (η, φ) are used as seeds, in which case the algorithm is called “seedless”. Since this option is much too CPU-time consuming, usual cone jet algorithms only search stable cones from seeds corresponding to objects above a certain threshold in transverse momentum.

In $D\bar{O}$ since the granularity of the calorimeter is very fine, all calorimeter cells must first be combined in pseudo-projective towers, as seen from the nominal interaction point, of approximate size $\Delta\phi \times \Delta\eta = 0.1 \times 0.1$. This is done by summing their 4-momenta, after having assigned a 4-momentum $p^{cell} = (E^{cell}, \mathbf{p}^{cell})$ to each cell, where E^{cell} is the energy measured in the detector, and p^{cell} represents the direction between the primary vertex and center of the cell, with $E^{cell} = |\mathbf{p}^{cell}|$. The so-formed towers are the objects used for clustering by the algorithm. Since the number of towers per event is still very important on average, a simple cone algorithm, which clusters towers uniquely in cones of size $R_{cone} = 0.3$, without any iteration and starting from the most energetic ones, is used in a preliminary step to form preclusters. Preclusters are then used as seeds by the $D\bar{O}$ Run II Cone algorithm.

Calorimeter noise, due to many sources, e.g. isolated activated cells (“hot cells”), sometimes enters the clustering process with the consequence of creating “fake” jets. In some cases, such noise can be identified prior to clustering and jet formation. In particular, when hot cells are generated by fluctuations of the electronic noise that survive the pedestal subtraction at 2.5σ , where σ_{ped} is the pedestal width measured for each cell, the NADA [50] algorithm is used to identify them by looking at the sum of the energy deposited in the neighboring cells $E_{cube} = \sum E_{cell}$. If then E_{cube} is less than a certain threshold value, the cell is removed. In a further step, an algorithm called t42 [51] suppresses cells whose measured energy is below $4 \sigma_{ped}$ and which do not have a neighbor cell with more than $4 \sigma_{ped}$ of measured energy. In addition, a special treatment is applied to CH cells when forming preclusters: if the highest energy cell from a tower used as a seed for precluster formation is part of CH, its energy is first subtracted to that of the tower before entering the normal procedure. This procedure has been shown to prevent efficiently the formation of fake jets, most of which coming from the Coarse Hadronic part of the calorimeter, with a negligible loss of good jets.

In general, seed-based algorithms are not collinear and infrared safe, as illustrated

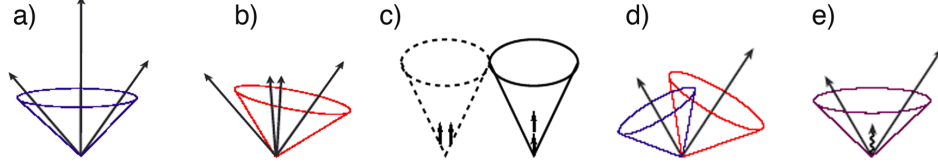


Figure 4.2: Collinear sensitivity: pictures *a)*, *b)* and *c)* illustrate possible scenarios where different results of the jet algorithm are obtained depending if e.g. the energy of a seed is split or not between two detector towers. Infrared sensitivity: pictures *d)* and *e)* illustrate a possible scenario where the result of the jet algorithm varies depending e.g. on the presence or not of soft gluon radiation [47].

in Figure 4.2. Pictures *a)*, *b)* and *c)* show two examples of collinear unsafety, when the two partons or energy deposits resulting from the splitting are below the seed threshold: Figures 4.2 *a)* and *b)* show how a different proto-jet can be found and Figure 4.2 *c)* shows how a jet can be missed, in case of collinear splitting. Pictures *d)* and *e)* show an example of infrared unsafety, where either two separate jets or a single jet merging the two previous ones can be found, depending on the presence of a soft parton.

As regards jet reconstruction inefficiency due to energy splitting between two towers, it was shown in Run I that the main parameter controlling this inefficiency was the E_T threshold on towers used to form seeds, $E_T^{min\ tower}$. With a value of $E_T^{min\ tower} = 1$ GeV, the Run I algorithm was proved to be 100% efficient for jets of p_T above 15 GeV. In Run II, a value of $E_T^{min\ tower} = 0.5$ GeV is used, such that, even if the calibration changed between Run I and Run II, the algorithm should be even more efficient.

In order to avoid collinear and infrared unsafety, midpoints are also used as starting points for clustering [52], in addition to usual seeds. In principle, all midpoints defined by directions equal to $p_i + p_j$, $p_i + p_j + p_k$ etc, where i , j , k , etc. represent all possible seeds should be used. However, to save computing time, following Run II Jet Physics workshop recommendations [47], only midpoints between pairs of already found proto-jets are used as seeds.

Finally, the proto-jets which share some energy are treated in the merging/splitting

step. For any pair of proto-jets, if the lower E_T proto-jet shares more than 50% of its energy with the other proto-jet, both are merged, otherwise the energy of each shared tower is attributed exclusively to the proto-jet to which it is closest in ΔR . The objects formed when the merging/splitting step is finished are called jets and only those with $p_T > p_T^{min}$ are kept, where $p_T^{min} = 8$ GeV for version p14 of the RECO software.

4.3.3 Calculation of Jet Variables

Each cell inside the cone jet contributes to build the jet four-momentum. The 4-momentum of a jet is first obtained from the sum of the 4-momenta of all cells.

$$p^J = (E^J, \mathbf{p}^J) = \sum_{i \subset J} (E^i, p_x^i, p_y^i, p_z^i), \quad (4.3)$$

The jet kinematic properties are then defined by the following usual set of equations:

$$p_T^J = \sqrt{(p_x^J)^2 + (p_y^J)^2} \quad (4.4)$$

$$\phi^J = \tan^{-1} \frac{p_y^J}{p_x^J}, \quad \theta^J = \cot^{-1} \frac{p_z^J}{p_T^J}. \quad (4.5)$$

Jets which contain at least two cells can acquire mass if the 3-momenta of the cells are not collinear. This happens most of the time since the detector has a projective geometry only with respect to its center.

4.3.4 Jet Identification

Several quantities are used after jet reconstruction in order to further suppress fake jets:

- To remove isolated electromagnetic particle, a cut on the maximal fraction of energy deposited in the electromagnetic (EMF) part of the calorimeter is placed:
EMF < 0.95;

- To remove some problematic noise jets, a cut on the minimal EMF is also placed $0.05 < \text{EMF}$;
- Jets having 90% or more of their energy in one tower are removed;
- The ratio of the highest cell energy and the next-to-highest cell energy (HotF) has a cut of $\text{HotF} < 10$;
- To avoid cluster around hot cell in the coarse hadronic calorimeter, a cut on the fraction of the energy deposited in the coarse hadronic calorimeter (CHF) is applied at $\text{CHF} < 0.4$;
- Since the trigger readout uses a different electronic chain, it is sensitive to different electronic noise than the normal readout. Matching the L1 readout energy of a jet with its normal energy has thus proved to be the most efficient way to distinguish between fake and good jets. Using the scalar sum of the trigger towers L1SET of a jet, a cut is applied at
 1. $\text{L1SET}/(p_T(\text{jet})(1-\text{CHF})) > 0.4$ in the CC and EC;
 2. $\text{L1SET}/(p_T(\text{jet})(1-\text{CHF})) > 0.2$ in the ICD.

4.3.5 Jet Energy Scale

The DØ calorimeter being of the sampling type, it measures only part of the energy of the original particles. It was designed to have almost equal response to electromagnetic particles, R_{em} , and to hadrons R_h in Run I. Calorimeters with exactly equal response to electrons and hadrons are called “compensating”^a. In Run II, however, due to the reduction of the electronic signal integration time, it was expected to see an increase of

^aAn ideal compensating calorimeter will have the ratio between the hadronic and electromagnetic response $e/h = 1$.

the ratio e/h above its Run I value, hence a lower relative response of hadrons compared to electrons.

Even though it is possible to measure R_{em} with a certain precision by using a clean sample of $Z \rightarrow e^+e^-$ events, R_h measurement is more challenging due to the fact that only part of hadron energy is measured. In general the relation between the original jet energy at the particle level and the measured energy (as in Equation 4.3) can be written as:

$$E_{jet}^{particle} = \frac{E_{jet}^{meas} - E_O(\mathcal{R}, \eta, \mathcal{L})}{R_{cone}(\mathcal{R}, \eta, E) R_{jet}(\mathcal{R}, \eta, E, \phi)} \quad (4.6)$$

where:

1. E_{jet}^{meas} corresponds to the sum of the energy deposited in the cells;
2. $E_O(\mathcal{R}, \eta, \mathcal{L})$ is an offset due to calorimeter noise and pile-up energy from previous interactions. It depends on the direction of the jet, the luminosity and it is estimated using the jet cone angular area $\pi\mathcal{R}^2$;
3. R_{cone} takes into account the energy deposited outside the cone, due to the finite size of energy showering in the calorimeter even for a single particle;
4. R_{jet} is the response of the hadronic calorimeter.

R_{jet} is calculated from events where one photon and one jet are produced. At particle level the total transverse momentum of the event is, on average,

$$\mathbf{p}_T^\gamma + \mathbf{p}_T^{jet} = 0. \quad (4.7)$$

When measured in the calorimeter this quantity can be different from zero. By measuring

the missing transverse energy in the event

$$-\vec{E}_T = - \sum_{E^{cell} > 0} \mathbf{p}_T^{cell} = R_{em} \mathbf{p}_T^\gamma + R_{had} \mathbf{p}_T^{jet} \quad (4.8)$$

and by introducing the quantity:

$$\vec{E}_T^{EMcorr} = E_T - (1 - R_{em}) \mathbf{p}_T^\gamma \quad (4.9)$$

the response R_{had} can be written as:

$$R_{had} = 1 + \frac{\vec{E}_T^{EMcorr} \cdot \mathbf{n}_T^\gamma}{p_T^\gamma} \quad (4.10)$$

where \mathbf{n}_T^γ represents the direction of the photon. This method for estimating R_{jet} is called the Missing E_T Projection Fraction Method [53]. The correction to the measured energy for both DATA and Monte Carlo simulated events is shown in Figure 4.3 and Figure 4.4 together with an estimation of the systematic uncertainty.

4.4 Electron Identification

The first step towards the identification of electrons is the reconstruction of clusters of activated cells in the EM calorimeter using a simple Cone Algorithm. These clusters are built around calorimeter towers formed by contiguous cells in the four EM calorimeter layers plus the first FH layer. Only clusters with energy greater than 1.5 GeV are used to seed the reconstruction of the final electron candidates, the ‘‘EM cluster’’. EM clusters are formed by adding all the towers within a cone of size $R = 0.5$.

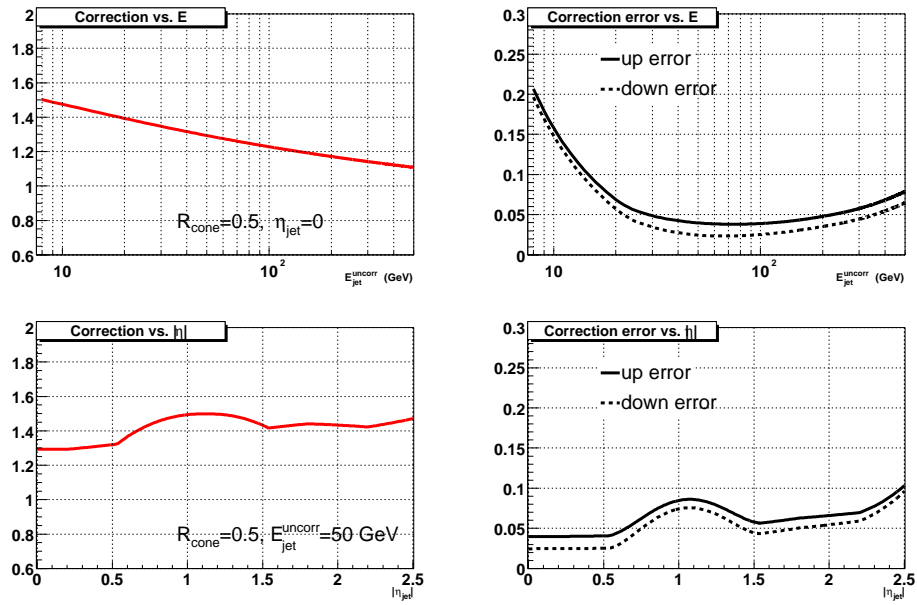


Figure 4.3: Correction to the measured energy in data as a function of the measured energy (top left), jet η (bottom left) and relative uncertainty (right) [54].

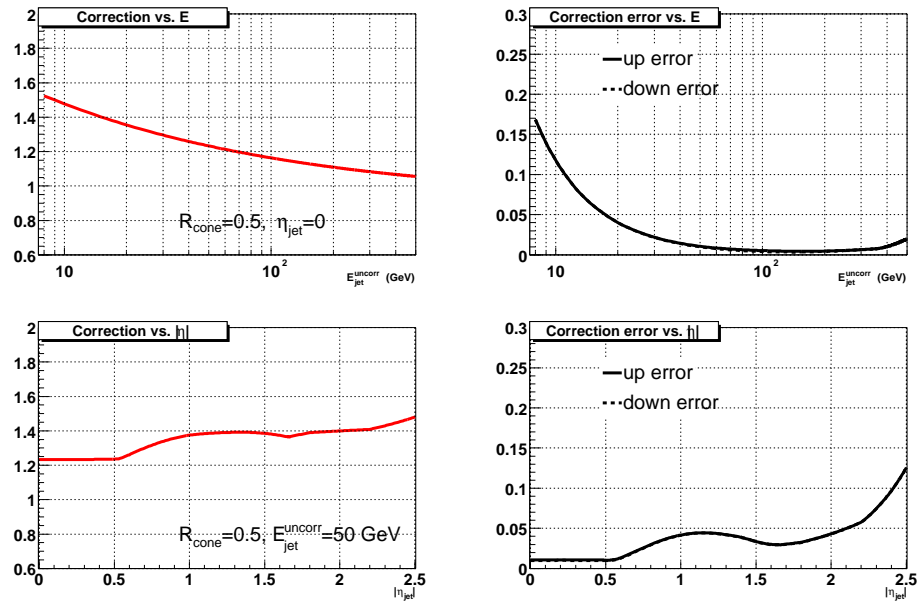


Figure 4.4: Correction to the measured energy in Monte Carlo as a function of the measured energy (top left), jet η (bottom left) and relative uncertainty (right) [54].

4.4.1 Electron Definition

Several quantities can be used to discriminate between signal electrons and their sources of background: γ 's and π 's. What follows is a list of cuts on cluster variables that are used to define “Loose” and “Tight” electrons.

- The Isolation is defined as

$$Isolation = \frac{E_{tot}(0.4) - E_{EM}(0.2)}{E_{EM}(0.2)}, \quad (4.11)$$

where $E_{tot}(0.4)$ is the total energy within a cone of radius $R = 0.4$ and $E_{EM}(0.2)$ is the EM energy in a cone of radius 0.2. Electrons tend to be very localized in comparison to pions which tend to produce a larger cone size. For this reason a cut on $Isolation < 0.15$ is applied;

- In order to discriminate against photons, that don't interact with the tracking detector by being electrically neutral, a track is requested to be in the proximity of the EM cluster. The matching criteria is based upon a spatial and momentum χ^2 :

$$\chi_{match}^2 = \left(\frac{\delta\phi}{\sigma_\phi}\right)^2 + \left(\frac{\delta z}{\sigma_z}\right)^2 + \left(\frac{E_T/p_T - 1}{\sigma_{E_t/p_t}}\right)^2; \quad (4.12)$$

- Electrons lose all their energy in the EM part of the calorimeter, therefore a cut on the fraction of the energy deposited in this part of the calorimeter (f_{EM}) is applied to any EM cluster: $f_{EM} > 0.9$;
- The transverse and longitudinal shower shape profile is used in order to improve the discrimination between electrons and pions. For each detector tower, two correlation matrices are built using Monte Carlo simulated electrons [55]. For two

shower shape variables x_i and x_j this has the form:

$$M_{ij} = \frac{1}{N} \sum_{n=1}^N (x_i^n - \bar{x}_i)(x_j^n - \bar{x}_j) \quad (4.13)$$

where N is the number of the reference electrons. The two matrices use 7 and 8 variables, respectively:

- The fraction of the total energy deposited in the four EM layers;
- The total energy deposited;
- The vertex z position;
- the shower shape in the ϕ direction;

The second matrix also includes:

- The shower shape in the z direction;

In order to keep only electrons that have shape consistent with the candidate electrons an upper cut on hmN , defined as:

$$hmN = \sum_{ij}^N (x'_i - \bar{x}_i) H_{ij} (x'_j - \bar{x}_j), \quad (4.14)$$

where $H = M^{-1}$, is applied:

- $hm7 < 30$;
- $hm8 < 75$;
- A further step in discriminating against background is taken by using a likelihood function based on several Monte Carlo distributions [56, 57]. The quantities used are:
 - electron η_{DET} ;

- f_{EM} ;
- $hm7$;
- Ratio between the calorimeter p_T and the matched track p_T ;
- dca of the matched track;
- χ^2 probability for the fit of the matched track;
- Number of tracks in a radius R of 0.05 around (and including) the matched track;
- Total p_T of the tracks in a radius R of 0.04 around (but not including) the matched track;

For each electron candidate, with \mathbf{x}_e as vector of likelihood variables, $P_{sig}(\mathbf{x}_e)$ represents the probabilities that the candidate is a real electron and $P_{back}(\mathbf{x}_e)$ that is a fake electron. No correlations among single variable are assumed, the total probability is then just the product of the individual probabilities. The discriminant:

$$\mathcal{L}(\mathbf{x}_e) = \frac{P_{sig}(\mathbf{x}_e)}{P_{sig}(\mathbf{x}_e) + P_{back}(\mathbf{x}_e)} \quad (4.15)$$

tends towards 1 for real electrons, whereas it is close to 0 for background. When no tracks are found the likelihood values is set to -1. All electrons are required to have $\mathcal{L} \geq 0$;

Other quantities used for the Loose electrons are:

- $p_T > 20$ GeV;
- $\eta_{DET} < 1.1$;

Tight electron are defined to have $\mathcal{L} > 0.4$.

4.5 Muon Identification

Muons can be identified using three independent DØ sub-detectors. The external muon spectrometer with its extended pseudo-rapidity coverage up to $\eta < 2$ provides unambiguous muon identification: muons identified using this detector are called “local muons”. Muon tracks can be detected with high efficiency in the tracking detector, a local muon matched to a track is called a “central” track-matched muon. In principle even the calorimeter can help. A muon can be identified by its minimum ionizing particle (MIP) signature. However, this capability is not yet implemented in the actual muon identification algorithm due to the low efficiency $\approx 50\%$.

Reconstructed muons are classified according to their “type” and “quality”. The type corresponds uniquely to the number of external layers used for the reconstruction: $nseg$. The absolute value of $nseg$ can be equal to 1, 2 or 3, which respectively indicates that the local muon is made of A-layer only hits, B or C-layer only hits or by hits from all three layers. A negative value of $nseg$ means that the muon could not be matched to any track as shown in Table 4.2.

Muons are also categorized according to their quality: “Tight”, “Medium” or “Loose” muons are defined below.

- **Tight Muon**

- $|nseg| = 3$;
- At least two A layer wire hits;
- At least one A layer scintillator hit;
- At least three BC layer wire hits;
- At least one BC layer scintillator hit;
- A converged local fit;

- $|nseg| = 3$ **Medium**

$nseg$	Muon Type	Central track matching algorithm	MTC matching criterion
3	Central Track + local muon track (A, B and C-layer)	Muon to central if local track converged. Central to muon otherwise	$\Delta\eta, \Delta\phi$ between MTC and central track extrapolated to calorimeter
2	Central Track + BC only	Central to muon	as above
1	Central Track + A only	Central to muon	as above
0	Central Track + muon hit or central track + MTC	Central to muon	as above
- 1	A segment only	no match	$\Delta\eta, \Delta\phi$ between MTC and A-layer segment
- 2	BC segment only	no match	$\Delta\eta, \Delta\phi$ between MTC and BC-layer segment
- 3	local muon track (A + BC)	no match	$\Delta\eta, \Delta\phi$ between local muon track at A-layer

Table 4.2: Overview of different muon types. Categorization based upon which sub-detector is used for the reconstruction.

- $|nseg| = 3$;
- At least two A layer wire hits;
- At least one A layer scintillator hit;
- At least two BC layer wire hits;
- At least one BC layer scintillator hit;
- $|nseg| = 3$ **Loose** is allowed to fail one of the $|nseg| = 3$ **Medium** requirements;
- $|nseg| = 2$ **Medium**
 - $|nseg| = 2$;

- At least two BC layer wire hits;
- At least one BC layer scintillator hit;
- $|\eta_{DET}| < 1.6$
- $|nseg| = 2$ **Loose** does not have any $|\eta_{DET}|$ cut;
- $|nseg| = 1$ **Medium**;
 - $|nseg| = 1$;
 - At least two A layer wire hits;
 - At least one scintillator hit;
 - $|\eta_{DET}| < 1.6$
- $|nseg| = 1$ **Loose** does not have any $|\eta_{DET}|$ cut;

4.6 Missing Energy

The missing transverse energy (MET) is the signature for neutrinos in the DØ calorimeter. Its calculation combines information from many sub-detectors: calorimeter, the tracking system (for PV determination), and the muon detector (for the muon correction to the event energy).

By defining the x and y component of the visible energy of the detector as

$$E_{vis}^{x,y} = \sum_{cells} E_i^{x,y} \quad (4.16)$$

the calorimeter missing transverse energy components are defined as the negative of E_{vis} : $\not{E}_x = -E_{vis}^x$ and $\not{E}_y = -E_{vis}^y$. The total MET is then $\not{E}_T = \sqrt{(\not{E}_x)^2 + (\not{E}_y)^2}$ [58].

In order to be used in the analysis the missing energy has to be corrected at several steps [59]. First, cells from CH are not part of the MET reconstruction due to their higher

noise component. A correction is used to compensate for CH jets that pass quality cuts and therefore considered signal and not noise. MET is corrected for the jet energy scale of good jets. Bad jets are also contributing to the MET, therefore they are removed from the visible energy, i.e. added back to the missing transverse energy. Lastly the muon calorimeter energy deposition as MIP is estimated and again subtracted from the visible energy.

4.7 The Event Simulation

Cross sections for all physics processes originating from the $p\bar{p}$ interactions can be estimated numerically. Among the many software packages available the most comprehensive Monte Carlo based event generator is PYTHIA [60]. PYTHIA (version 6.202) is part of the DØ simulation software and is used to calculate the four momenta of the particles resulting from the $p\bar{p}$ collision. The parton distribution functions (PDF) CTEQ5L parametrize the momentum distribution of quarks and gluons within the nuclei and then gives an estimation of the center of mass energy. PYTHIA also simulates the hadronization and fragmentation of quarks into colorless jets of hadrons.

For some events with many partons in the final state the ALPGEN event generator [61] is also used. ALPGEN, in fact, performs a complete leading order calculation of $qq \rightarrow W + \leq 4$ jets processes. ALPGEN is interfaced to PYTHIA to handle the parton hadronization process.

After the flow of generated particles has been stored in a chunk, the detector response is produced by DØGSTAR [62] (DØ Simulation of the Total Apparatus Response), a software package based on GEANT [63] that simulates hits in the tracking detector (DØsim) together with pile-up effects and noise (DØraw). RECO is run after the full detector simulation.

The Parameterized Monte Carlo Simulation (PMCS) [64] runs on the PYTHIA output

to simulate the detector response and the reconstruction effects. PMCS, also known as “Fast Monte Carlo”, smears the generated particle four-momenta with energy dependent resolution function derived either from data or from the full detector resolution, therefore reducing the cpu-time used per event.

Chapter 5

b-tagging Performance with the DØ detector

Identifying calorimeter jets generated by the hadronization of *b*-quarks (a.k.a. *b*-tagging) is a powerful discriminator against the background for many interesting physics processes: for example, when top quarks are produced, because of their large mass, they decay immediately into a *b*-quark and a *W* boson. Identifying *b*-quarks is then fundamental in order to distinguish $t\bar{t}$ and single top production from QCD multi-jet background. In the realm of searches for new physics *b*-tagging again plays a key role. The Higgs boson, if it exists and has a mass lower than 135 GeV, would decay mainly into $b\bar{b}$ [65]; SUSY and Technicolor also predict an excess of events with *b*-quarks over the SM expectation.

Mesons containing *b*-quarks, i.e. *B*-mesons, have higher lifetime when compared to other light-flavored mesons. Monte Carlo simulations show that the distance in the transverse plane between the PV and the point where *B*-meson decays, L_{xy} , has a mean value of ≈ 3 mm, furthermore 70% of events with $L_{xy} > 1$ mm have at least 2 tracks with $dca/\sigma(dca) > 3.0$. Due to the high resolution of the silicon detector, these tracks are excluded from the PV finding algorithm, they can be identified and used in order to reconstruct the point in space where the *B*-hadrons have decayed: the Secondary Vertex

of interaction [66].

5.1 The Vertex Algorithm

The package `d0root` [67] is an object-oriented package based on the ROOT [68] analysis software. A series of Kalman Filter based algorithms (KF) [69, 70] are implemented in `d0root` with the purpose of fitting tracks into a vertex. KF not only allows the reconstruction of the vertex position, it also refits the track parameters with the constraint that they have to pass through the vertex.

5.1.1 Primary Vertex

KF-based fits can be run recursively and are therefore more time efficient when compared to the Least χ^2 method, as implemented in RECO^a. Apart from this difference in the fitting technique used, both `d0root` and RECO use the same two-pass method and minimum bias probability based selection, as discussed in Section 4.2.4. Differences can be found in the track selection, tighter in `d0root` as shown in Table 5.1, and in the track z -clustering applied in `d0root` to better distinguish between different vertices in the same event.

Track Variable	cut
p_T	$\geq 0.5 \text{ GeV}$
SMT hits	≥ 2
dca/σ_{dca}	≤ 3.0

Table 5.1: `d0root` second pass track selection requirements.

RECO and `d0root` performances have been compared on the same set of multi-jet 5000 data events: the reconstructed efficiency is slightly better (`d0root` finds PV in

^aIn the Least χ^2 method all tracks are fitted globally, in a single step, requiring the inversion of matrices with dimensionality equal to the number of tracks. KF, instead, fits track information adding one track at a time, and the dimension of the matrices to be inverted is reduced to the number of parameters to be estimated.

98% of the time, while RECO has 97% efficiency) and the resolutions in the transverse directions are shown in Table 5.2.

	σ_x (μm)	σ_y (μm)
d0root	38 ± 5	38 ± 5
RECO	35 ± 1	35 ± 1

Table 5.2: Resolution for d0root and RECO for primary vertices with $|z| < 40$ cm [44].

5.1.2 Secondary Vertex

The Secondary Vertex Algorithm (SVT) uses tracks with high impact parameter in order to fit the position of the decay of heavy-flavored hadrons.

Track-jet Reconstruction

Before tracks are fitted to a secondary vertex they are clustered to form track-jets. Only tracks belonging to track-jets will be used by the SVT algorithm. Track-jets are reconstructed with the following algorithm [66]:

1. **Z Pre-clustering:**

- Sort track by p_T ;
- Recalculate dca and dca_z with respect to the closest PV;
- Cluster tracks having $\Delta z < 2$ cm by looping in descending order of track p_T .

2. **Track Selection:** after pre-clustering, tracks passing the following cuts are selected:

- Number of SMT hits > 2 ;
- $p_T > 0.5$ GeV;
- $dca < 0.15$ cm;

- $|dca_z| < 0.4$ cm;

3. Jet Clustering:

- Selected tracks are clustered around a seed track with $p_T > 1$ GeV using a simple cone jet algorithm.

Secondary Vertex Fit

Only tracks forming track-jets and passing the cuts listed in Table 5.3 are used by the SVT. Three vertex definitions are developed and analyzed, in order to have different working points in terms of efficiency versus mistag rate [71]. This will be discussed in Section 5.5.

The SVT is used in *Build-Up* modality: the first step consists of finding seed vertices by fitting all combinations of pairs of selected tracks among the tracks making track-jets. After keeping only vertices with good χ^2 , it attempts to add tracks pointing to the seed vertex, rejecting those tracks with χ^2 contribution to the vertex fit greater than 10. If the track is accepted the vertex parameters are re-fitted including the new track. This is repeated until there are no more tracks available in the track-jet. Only vertices with total $\chi^2 < 100$ are kept.

Variable	LOOSE	MEDIUM	TIGHT
IP significance of tracks \geq	3.0	3.5	3.5
track $\chi^2 <$	10	10	3
p_T of tracks $>$	1.0 GeV	1.0 GeV	1.0 GeV
Number of SMT hits \geq	2	2	2
r-phi dca of tracks (cm) \geq	0.15	0.15	0.15
z dca of tracks (cm) \geq	0.4	0.4	0.4
track-to-vertex $\chi^2 \leq$	15	15	15

Table 5.3: SVT tracks selection. The cuts has been tuned to achieve the highest efficiency for 0.1% (loose), 0.5% (medium) and 0.25% light quark mistag rates in the data [71].

Fake tracks and tracks produced by short-living hadrons could still have a finite

probability of forming vertices. After the vertex is reconstructed other cuts on vertex quantities are applied to reduce the contributions of these sources of noise. The vertex decay length $|L_{xy}|$ is defined as the vector going from the Primary Vertex to the Secondary Vertex: $|L_{xy}| = |\vec{r}_{SV} - \vec{r}_{PV}|$. Cutting on this quantity is fundamental in order to further reduce background. Unfortunately not only B -hadrons have finite values for $\langle |L_{xy}| \rangle$: for some light-flavored hadrons like K_s and Λ $\langle |L_{xy}| \rangle \approx 2.5$ cm. Other cuts are applied to the vertex *collinearity*, the inner product of \vec{L}_{xy} and the momentum of the Secondary Vertex defined as the vectorial sum of the momenta of all attached tracks, and to the vertex Decay Length Significance $|L_{xy}|/\sigma_{L_{xy}}$. A summary of the cuts to the vertex quantities is shown in Table 5.4. Figure 5.1 shows the difference in Decay Length Significance distributions for vertices found inside jets for Monte Carlo light flavored and b -jets.

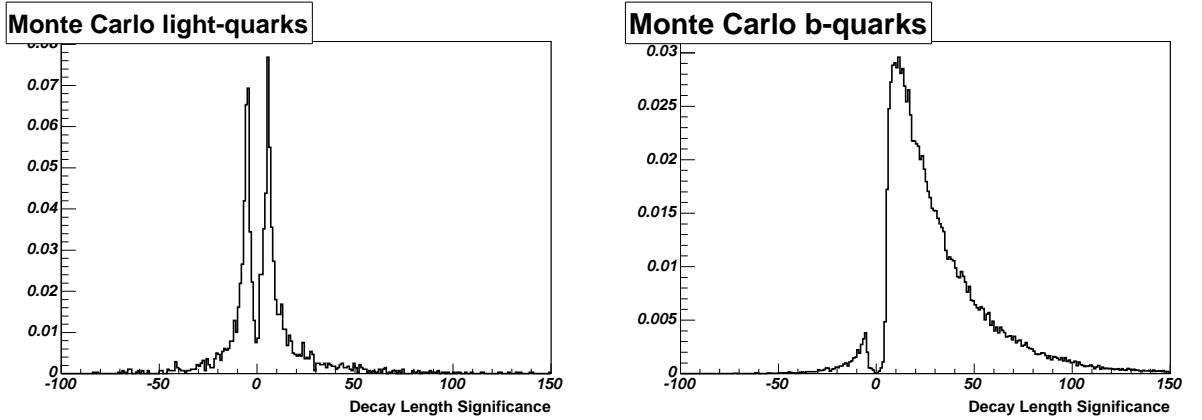


Figure 5.1: Decay Length Significance Distribution for Monte Carlo light-quark jets (left) and b -jets (right).

A jet is called “positively tagged” if there is at least one Secondary Vertex with positive Decay Length Significance within a ΔR of 0.5 with respect to the jet axis. A “negatively tagged” jet has no positive tag associated and at least one Secondary Vertex with negative Decay Length Significance within 0.5 in ΔR with respect to the jet axis. In general unless explicitly specified a tagged jet is understood to be positively tagged.

Variable	LOOSE	MEDIUM	TIGHT
vertex $\chi^2 <$	100	100	100
vertex collinearity \geq	0.9	0.9	0.9
vertex decay length \leq	2.6 cm	2.6 cm	2.6 cm
minimum track multiplicity \geq	2	2	2
<i>b</i>-jet criterion - signed decay length significance \geq	5.0	6.0	7.0

Table 5.4: SVT setting for the three vertex definitions.

5.2 *b*-tagging in data

We establish the *b*-tagging efficiency and light-quark tagging fake rates (mistag) using data. In both cases we have to identify topologies where either heavy or light quarks are predominantly produced and then make use of algorithms that extract the flavor composition together with the uncertainties of this estimation.

5.2.1 Data Sample Selection

In order to evaluate the efficiency of tagging *b*-quarks we analyze “Muon-Jets” events, i.e. events where a muon and a jet are detected to be close to each other; the exact definition is described in Section 5.3. *B*-hadrons semi-leptonic decay to a final state with muon has a branching fraction of 10.95%, for light quarks the same quantity is much smaller. Therefore the existence of a muon and a jet close to each other is a good signature that the jet is produced by the hadronization of a *b*-quark. These events are important for the estimation of the *b*-tagging efficiency. For the mistag evaluation, generic dijet-events, where the *b*-quark content is of order of few percent, are used.

- **μ +jet Data Sample:** The skim requires one muon, inside a ΔR of 0.5 with a jet.

Further requirements applied for this study are:

- One medium muon, $p_T > 4$ GeV;

- Two good jets, $p_T > 15$ GeV;
- Good run quality.

This selection leads to a total of 1.1×10^7 events.

- **EM1TRK Data Sample:** The EM1TRK skim requires the presence of one electron with $E_T > 8$ GeV and one track with $p_T > 5$ GeV within $\Delta\phi = 0.1$ of the EM cluster. Further cuts are:

- Missing $E_T < 10$ GeV;
- Two jets, $p_T > 15$ GeV;
- Good run quality.

We analyze a total of 7.3×10^6 events passing these cuts.

- **QCD Data Sample:** Events passing any jet-trigger, plus the following requirements:

- Two good jets, $p_T > 15$ GeV;
- Good run quality.

This selection leads to a sample of 1.6×10^6 events.

5.2.2 Jets Track Requirement: Taggability

Differences in tracking efficiency and fake jets generated by calorimeter noise may result in a systematic difference between data and Monte Carlo. To decouple these effects, the taggability is introduced as the ratio between the number of taggable jets and the number of reconstructed jets. Here a “taggable” jet is a jet matched ($\Delta R < 0.5$) to a track-jet reconstructed with the following requirements:

- Tracks $p_T > 0.5$ GeV;

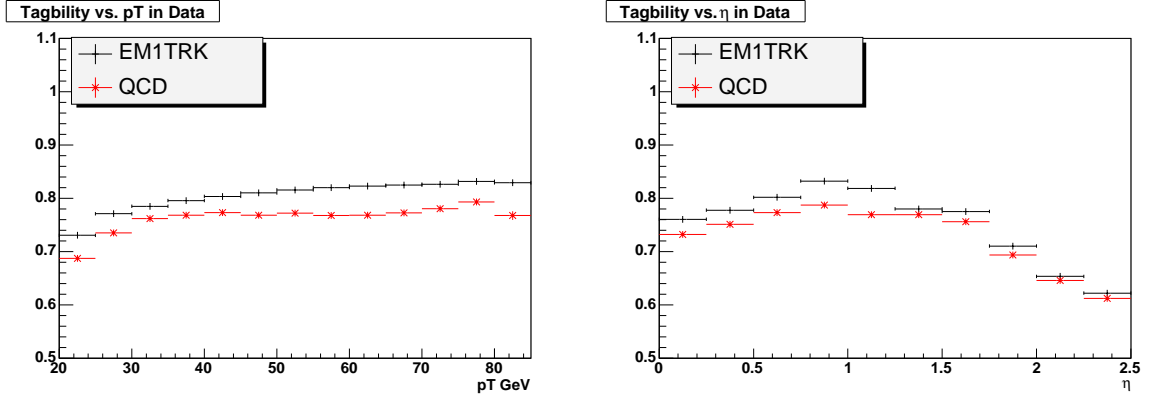


Figure 5.2: Taggability versus jet η (right) and jet p_T (left) for QCD and EM1TRK samples.

- Tracks with at least one SMT hit;
- At least one track with $p_T > 1$ GeV (track-jet seed p_T);
- Track-Jet cone size $\Delta R < 0.5$, $\Delta Z < 2$ cm;
- Track $dca_{xy} < 0.2$ cm;
- Track $dca_z < 0.4$ cm.

The "central", "ICR" and "forward" regions are defined in terms of calorimeter jets with detector $|\eta_{DET}| < 1.2$, $1.2 < |\eta_{DET}| < 1.8$, and $1.8 < |\eta_{DET}| < 2.5$ respectively. Taggability versus jet η and jet p_T for QCD and EM1TRK samples is shown in Figure 5.2.

5.2.3 V_0 Removal and γ -conversion Filter

As already discussed in Section 5.1.2 light-flavored long-living hadrons like K_S and Λ could be source of tracks with high dca significance. For this reason we examine the invariant mass of all track pairs in the event. All tracks are used without any p_T requirement. If the invariant mass of two tracks with opposite sign is within a mass window of 22 MeV centered about the nominal K_S mass or of 7 MeV around the Λ mass value

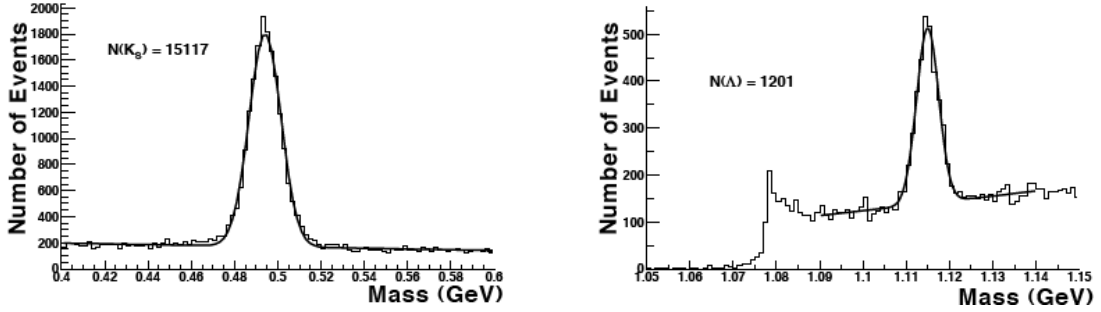


Figure 5.3: Two track invariant mass in QCD data, the left plot shows the K_s and the right plot the Λ peak [43].

both tracks are removed from the track list used by the SVT algorithm. Examples of reconstructed K_s and Λ 's and data are shown in Figure 5.3.

Another source of “fakes” is from a phenomenon called “ γ conversion”: when a photon interacts with the silicon detector it could shower and produce two electrons which are reconstructed as two tracks with high dca . These tracks are usually highly energetic and if they are not removed, they could be used as seed for the SVT algorithm; a γ conversion filter removes all tracks satisfying the following conditions:

- Pull of the angle between tracks in the $(r - z)$ plane less than 3;
- Distance between trajectories in $(r - \phi)$ plane less than 30 cm;
- Invariant mass of the two tracks should be less than 25 MeV.

An example of γ -conversion reconstructed in our detector is shown in Figures 5.4.

5.3 b -tagging Efficiency: SystemD

A system of 8 equations and 8 unknowns, called “SystemD” [72], is used in order to extract the data b -tagging efficiency from the “ μ +jets” sample. SystemD uses two data samples with different flavor compositions and two different b -tagging criteria. If the two different b -tagging algorithms are uncorrelated then their efficiencies factorize and the

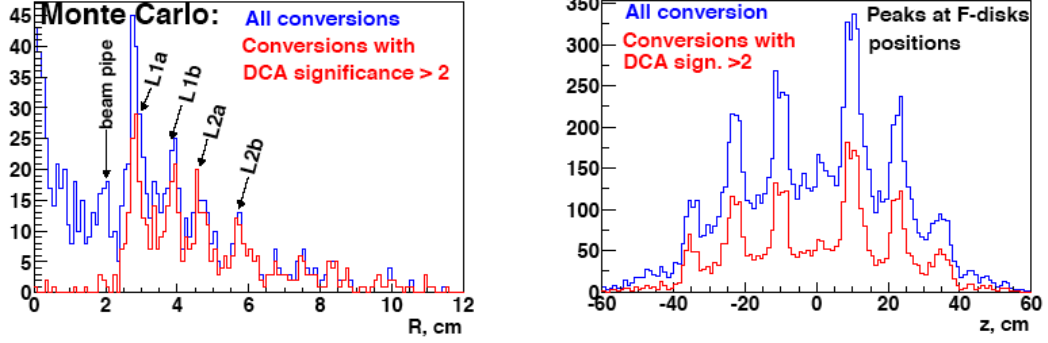


Figure 5.4: Reconstructed γ -conversion in MC vs. radius of the silicon layer (right) and in data vs. z -position of silicon F-disks (left) [43].

system becomes solvable. Note that calculating the efficiency for a b -tagging algorithm is equivalent to estimating the content of b -quarks in the same j sample before and after applying the tagging algorithm.

The most general case can be represented with one signal, f sources of background, t tagging algorithms and s data sample. Each sample j then gives $(f + 1)$ unknowns. The fraction of signal and background $n_{i=0,\dots,f}^{j=1,\dots,s}$ must satisfy the normalization relation:

$$\sum_{i=0}^f n_i^j = 1. \quad (5.1)$$

Each tagger k also gives $(1 + f)$ unknowns corresponding to the different efficiencies for each of the different flavors considered. After a tagger k is applied only a fraction q_j^k of the event survives:

$$q_j^k = \sum_{i=0}^f n_i^j \epsilon_i^k, \quad (5.2)$$

where ϵ_i^k is the efficiency of the k -th algorithm of tagging the j -th quark type. When two taggers k and ρ with correlation factor $\kappa_b^{k\rho}$ are applied, the fraction $q_j^{k\rho}$ becomes:

$$q_j^{k\rho} = \sum_{i=0}^f n_i^j \epsilon_i^k \epsilon_i^\rho \kappa_b^{k\rho}. \quad (5.3)$$

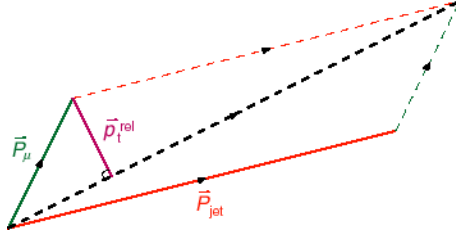


Figure 5.5: $p_T^{rel}(\mu)$: transverse momentum of muon measured with respect to the axis formed by the vectorial sum of the jet axis plus muon momentum [72].

The total number of equations that can be written is $2^t \cdot s$ which is equal to the total number of unknowns $(1 + f)(s + t)$ in the special case when $s = 2$, $t = 2$ and $f = 1$.

The two different data samples analyzed are both subset of the μ +jet sample and have as common requirement that for each event at least one “muon jet” is present. A muon jet is defined as a taggable jet associated with at least one muon having:

- $p_T > 4$ GeV;
- “medium” quality requirement;
- $\Delta R(\mu, jet) < 0.5$.

Restricting to evaluating the b -tagging efficiency in muon jets allows the possibility of using an uncorrelated tagging algorithm based on the muon momentum. The quantity used for discriminating signal and background is the $p_T^{rel}(\mu)$ defined as the transverse muon momentum with respect to the muon plus jet axis, i.e. the axis better representing the original b -quark direction (Figure 5.5). In general the higher B meson mass results in harder $p_T^{rel}(\mu)$ distributions with respect to light and c -flavored mesons.

The distribution for $p_T^{rel}(\mu)$ produced by the decays of different quarks is shown in Figure 5.6. By definition a muon jet passing the muon tag must have $p_T^{rel}(\mu) > 0.8$ GeV. The correlation factor κ_b for the muon and SVT taggers is measured from Monte Carlo and its value found to be very close to unity.

The two samples used by SystemD are:

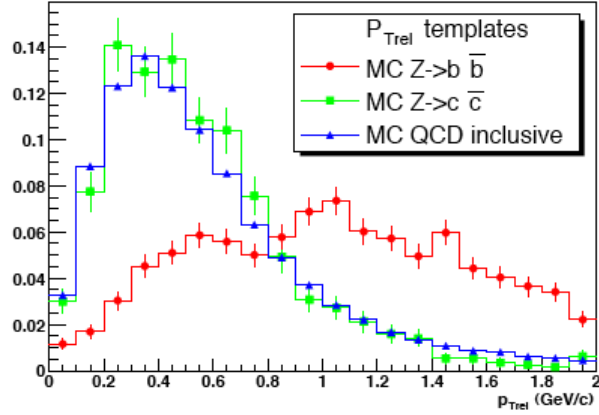


Figure 5.6: Normalized $p_T^{rel}(\mu)$ distributions in Monte Carlo simulation: muons from light-jets (blue triangles), c -jets (green squares) and b -jets (red dots) [72].

1. All events with at least one muon jet;
2. Events with two jets, one muon jet and another SVT tagged jet.

The second sample has greater b -quark contamination due to the presence of $qg \rightarrow g \rightarrow b\bar{b}$. If light and c -quark jets are considered together to be one individual source of background SystemD can be written as:

$$\begin{aligned}
 n &= n_b + n_{cl} \\
 p &= p_b + p_{cl} \\
 n^\mu &= \epsilon_p^\mu n_b^\mu + \epsilon_{cl}^\mu n_{cl}^\mu \\
 p^\mu &= \epsilon_p^\mu p_b^\mu + \epsilon_{cl}^\mu p_{cl}^\mu \\
 n^{SVT} &= \epsilon_b^{SVT} n_b^{SVT} + \epsilon_{cl}^{SVT} n_{cl}^{SVT} \\
 p^{SVT} &= \beta \epsilon_b^{SVT} p_b^{SVT} + \alpha \epsilon_{cl}^{SVT} p_{cl}^{SVT} \\
 n^{\mu,SVT} &= \epsilon_b^{SVT} \epsilon_p^\mu n_b^{\mu,SVT} + \epsilon_{cl}^{SVT} \epsilon_{cl}^\mu n_{cl}^{\mu,SVT} \\
 p^{\mu,SVT} &= \beta \kappa_b \epsilon_b^{SVT} \epsilon_p^\mu p_b^{\mu,SVT} + \alpha \kappa_{cl} \epsilon_{cl}^{SVT} \epsilon_{cl}^\mu p_{cl}^{\mu,SVT}.
 \end{aligned} \tag{5.4}$$

Where n and p are the number of muon jets in the two samples, n_b (n_{cl}) and p_b (p_{cl}) the fraction of b -quarks (light and c -quarks); n^μ , n^{SVT} and $n^{\mu,SVT}$ represent the same quantity for the sample of muon tagged jets, SVT tagged jets and jets tagged by both

algorithms respectively. The efficiency of tagging b -jets (light-jets) in the two samples is indicated as ϵ_b (ϵ_{cl}), and $\epsilon^{SVT(\mu)}$ indicates the SVT (muon tag) efficiency. Correlation factors are introduced, β for b -jets and α for light-jets, to take into account possible difference in the efficiency in the two samples. While κ_b and κ_{cl} express the correlation between the two algorithms when tagging b and light-quark respectively. Whenever possible these parameters are calculated using Monte Carlo simulation as discussed in Section 5.3.1.

The average secondary vertex tagger efficiency for the three vertex definitions in the μ +jets dataset, are given in Table 5.5. The uncertainties quoted are statistical only.

Efficiency per jet (%)		
LOOSE	MEDIUM	TIGHT
45.53 ± 0.26	42.85 ± 0.24	37.04 ± 0.18

Table 5.5: b -tagging efficiency in “ μ +jet” data derived using the SystemD method. Only statistical uncertainty is quoted.

The p_T and η dependence of the efficiencies are shown in Figures 5.7, 5.8, and 5.9. The η -dependence of the efficiency is found to be a third order polynomial for MEDIUM and LOOSE SVT and a fourth order polynomial for TIGHT SVT, while the functional form used to fit the p_T dependence of the efficiency is:

$$\epsilon(p_T) = \frac{p_2}{(1 + p_0 \cdot e^{-p_1 \cdot p_T})}. \quad (5.5)$$

SystemD has been tested on a Monte Carlo sample made of a mixture of b and c -jets from $Z \rightarrow q\bar{q}$, and light-jets from QCD processes. The comparison between the SystemD b -tagging efficiency and the “real” efficiency of tagging b -jet in $Z \rightarrow b\bar{b}$ events is shown in Figure 5.10.

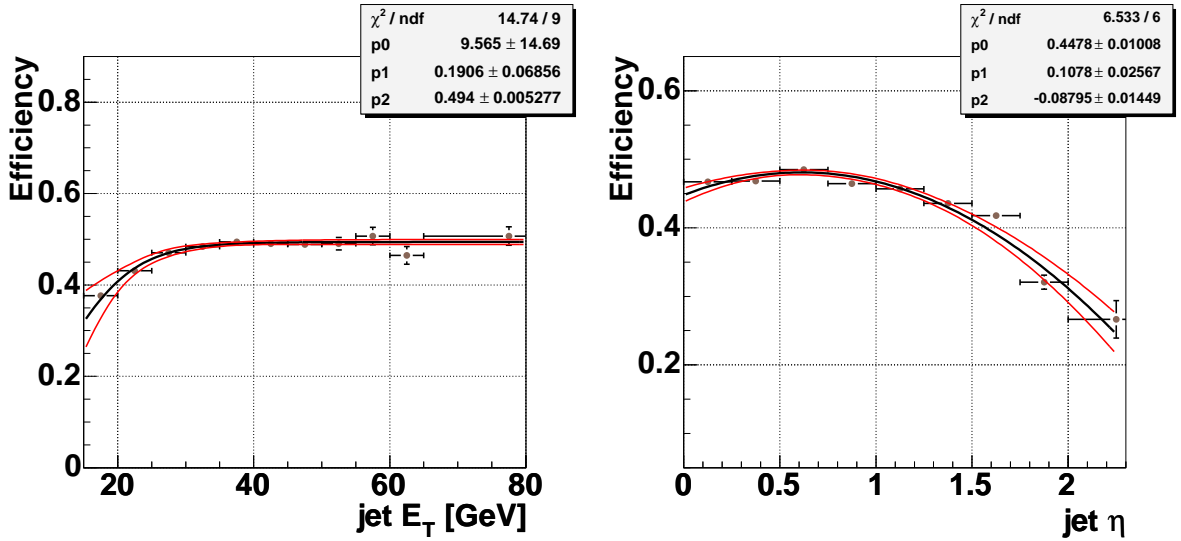


Figure 5.7: b -tagging efficiency determined from the “ μ +jet” data skim as a function of jet E_T and η for the LOOSE vertex criterion. The red curves represents the $\pm 1\sigma$ from the fit.

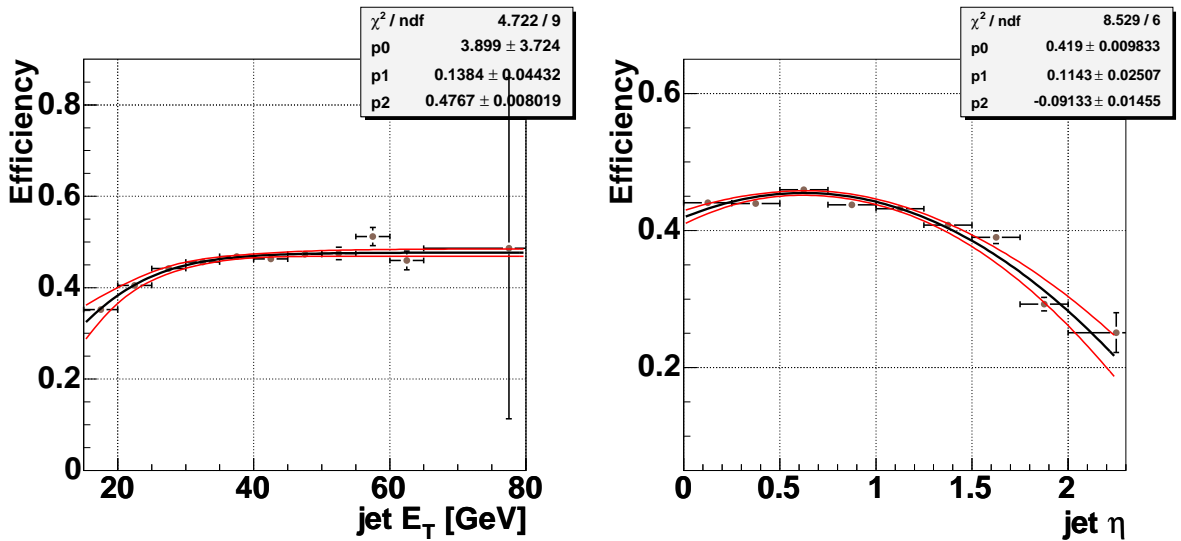


Figure 5.8: b -tagging efficiency determined from the “ μ +jet” data skim as a function of jet E_T and η for the MEDIUM vertex criterion. The red curves represents the $\pm 1\sigma$ from the fit.

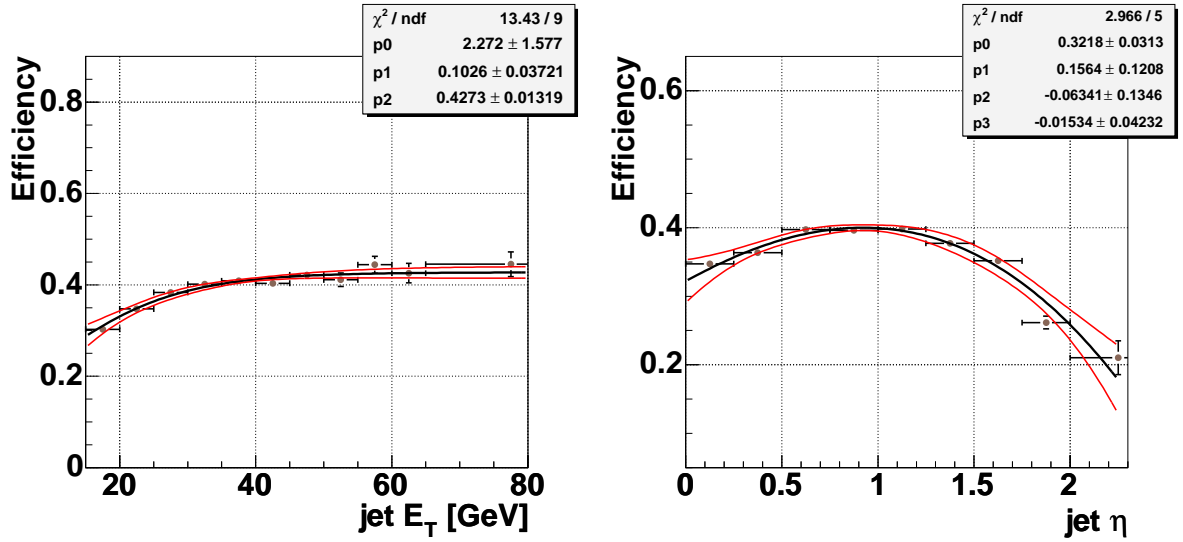


Figure 5.9: b -tagging efficiency determined from the “ μ +jet” data skim as a function of jet E_T and η for the TIGHT vertex criterion. The red curves represents the $\pm 1\sigma$ from the fit.

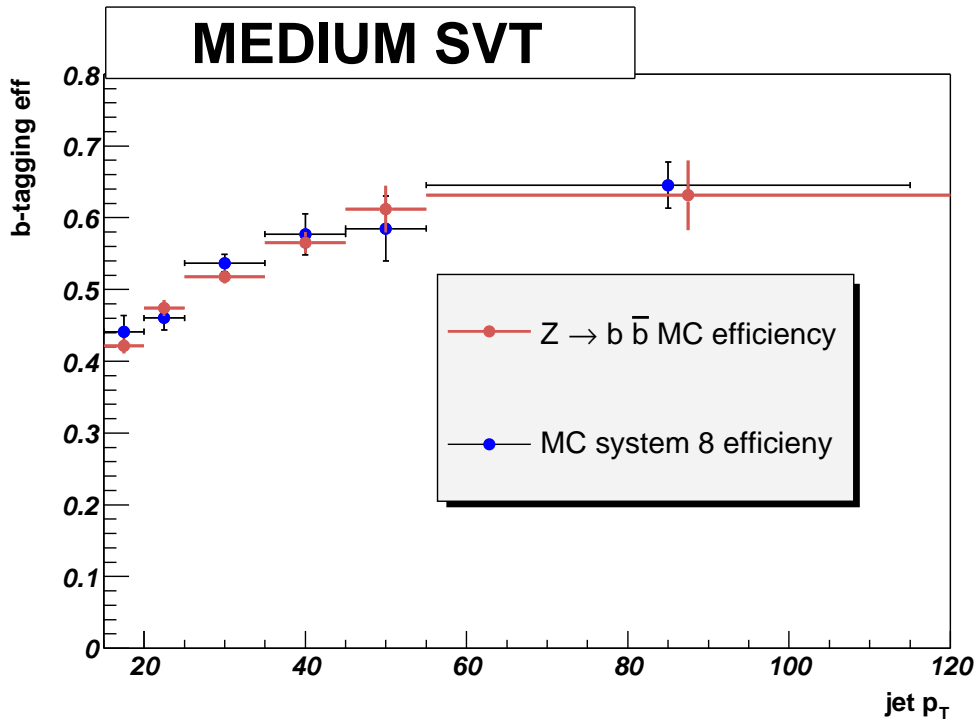


Figure 5.10: b -tagging efficiency in Monte Carlo simulated $Z \rightarrow b\bar{b}$ (red circles) and derived using SystemD in a mixtures of light and heavy-flavored jets.

5.3.1 SystemD Systematic Uncertainties

A Monte Carlo sample made of a mixture of $Z \rightarrow b\bar{b}$, $Z \rightarrow c\bar{c}$, $Z \rightarrow q\bar{q}$, qcd , $t\bar{t}$ is used to estimate the dependence of β and κ_b on the E_T of the jet as shown in Figures 5.11, 5.12 and 5.13. The values for the correlation parameters and their uncertainty are estimated by fitting the jet E_T dependencies; results are shown in Table 5.6.

	LOOSE	MEDIUM	TIGHT
β	1.000 ± 0.006	1.000 ± 0.006	0.999 ± 0.006
κ_b	0.993 ± 0.001	0.982 ± 0.001	0.978 ± 0.001
κ_{cl}	0.890 ± 0.013	0.840 ± 0.013	0.826 ± 0.014

Table 5.6: Correlation parameters derived from Monte Carlo.

In order to evaluate SystemD systematic uncertainty any correlation parameter values are individually changed inside the system of equations. With these different values the efficiency is then recalculated in order to assess how the indeterminacy on the knowledge of the correlation parameter affects the final b -tagging efficiency, i.e. the SystemD output; this will be then assumed to be the systematic uncertainty. SystemD parameters are changed either according to the uncertainty on the fit or by the differences observed in their values when derived using different Monte Carlo samples.

The variation for β is taken to be ± 0.006 corresponding to one standard deviation of the E_T fit. κ_{cl} is varied by ± 0.05 , about three standard deviations. The variation for κ_b of ± 0.004 is determined from the difference of the values obtained individually from $Z \rightarrow b\bar{b}$ and $t\bar{t}$ samples compared to the one obtained from the combined sample. The resulting variation in the b -tagging efficiency is defined as the systematic uncertainty. The parameter α can not be determined in Monte Carlo, is arbitrarily chosen to be 1 ± 0.8 .

Another source of systematic uncertainty is the p_T^{rel} cut chosen for the muon tagger. A cut value of 0.7 GeV is chosen in order to solve SystemD; the variation of the efficiency due to a change of this cut within an interval from 0.5 GeV to 0.9 GeV is shown in Table 5.7 together with all the other sources of systematics.

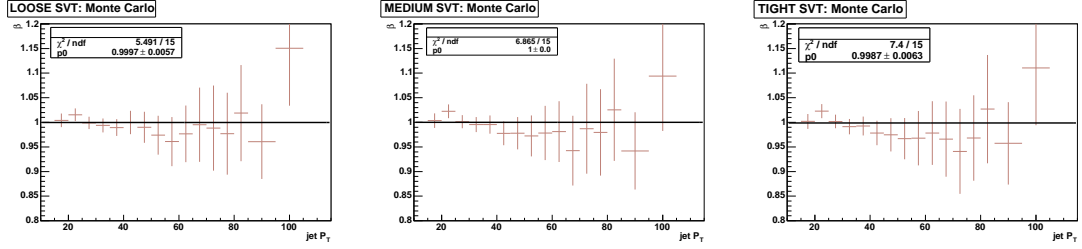


Figure 5.11: System8 variable β versus jet E_T for all SVT vertex definitions

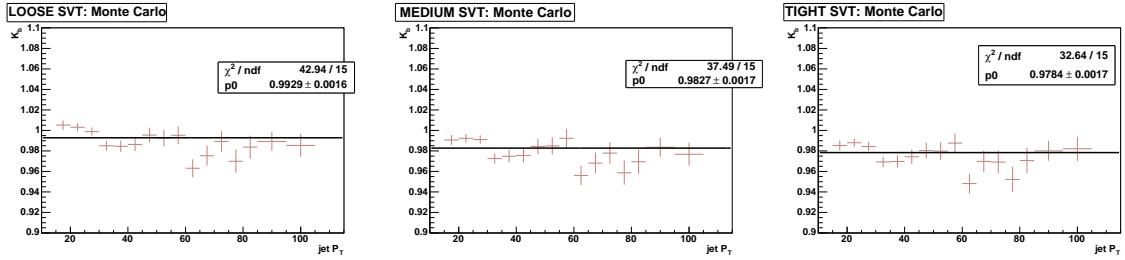


Figure 5.12: System8 variable κ_b versus jet E_T for all SVT vertex definitions

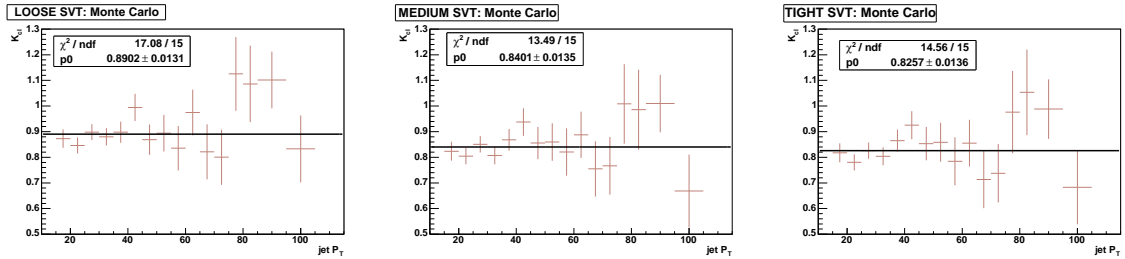


Figure 5.13: System8 variable κ_{cl} versus jet E_T for all SVT vertex definitions

	LOOSE	MEDIUM	TIGHT
κ_b	1.3 %	1.3 %	1.3 %
κ_{cl}	0.4 %	0.4 %	0.4 %
β	0.7 %	0.8 %	0.7 %
α	1.0 %	1.0 %	1.3 %
p_T^{rel}	1.0 %	1.0 %	1.0 %
Total	1.6 %	1.7 %	1.6 %

Table 5.7: Sources of systematic uncertainty for SystemD based b -tagging efficiency. Last line is the total systematic uncertainty from all contributions.

5.3.2 Tagging Efficiency in Monte Carlo Simulated Events

Even though the efficiency for tagging b -muon jets is estimated from data, Monte Carlo simulated events are still used to estimate the ratio between the efficiency of tagging jets formed by semileptonic hadron decay (muon-jets), and the efficiency of jets in which partons decayed fully hadronically. Also, Monte Carlo is used to calculate the ratio of b to c -tagging efficiency and in order to estimate the c -tagging efficiency for muon-jets and hadronic jets in data.

The samples used in this study are shown in Table 5.8:

Monte Carlo Sample	Number of Events
$b\bar{b}$	666,720
$Z \rightarrow b\bar{b}$	202,500
$Z \rightarrow c\bar{c}$	210,500
$Z \rightarrow b\bar{b} \rightarrow \mu + X$	96,488
$Z \rightarrow c\bar{c} \rightarrow \mu + X$	100,447
QCD	1,334,034

Table 5.8: Monte Carlo samples used for b -tagging efficiency and mistag rate estimation.

b -tagging Efficiency in Monte Carlo

The efficiency ϵ_b is defined as the fraction of the b -jet that are positively tagged, where a b -jet is a taggable jet matched to a b -quark is within a cone of radius 0.5 with respect to

the direction of the taggable jet. The b -tagging efficiency results are shown in Table 5.9.

Sample	Region	Efficiency per jet		
		LOOSE	MEDIUM	TIGHT
$Z \rightarrow bb$	ALL	$47.61 \pm 0.09\%$	$43.93 \pm 0.09\%$	$41.97 \pm 0.09\%$
	CC	$51.35 \pm 0.12\%$	$47.74 \pm 0.12\%$	$45.92 \pm 0.12\%$
	ICR	$46.5 \pm 0.19\%$	$42.79 \pm 0.18\%$	$40.59 \pm 0.18\%$
	EC	$36.95 \pm 0.20\%$	$33.1 \pm 0.19\%$	$30.89 \pm 0.19\%$
$Z \rightarrow bb \rightarrow \mu$	ALL	$49.66 \pm 0.13\%$	$45.9 \pm 0.13\%$	$43.97 \pm 0.13\%$
	CC	$52.79 \pm 0.16\%$	$49.12 \pm 0.16\%$	$47.37 \pm 0.16\%$
	ICR	$48.58 \pm 0.26\%$	$44.7 \pm 0.26\%$	$42.46 \pm 0.26\%$
	EC	$39.72 \pm 0.29\%$	$35.66 \pm 0.28\%$	$33.38 \pm 0.28\%$

Table 5.9: b -tagging efficiency in Monte Carlo.

Figure 5.14 shows dependence of the efficiencies on p_T , and η of the jet.

c -tagging Efficiencies in Monte Carlo

A c -jet is defined as matched to at least one c -quark and no b -quark. The SVT c -jet efficiency is significantly lower than the one for b -jets due to the smaller average c -flavored mesons decay length compared to B -mesons. The corresponding performance plots and results are shown in Figures 5.15 and Table 5.10.

Sample	Region	Efficiency per jet		
		LOOSE	MEDIUM	TIGHT
$Z \rightarrow c\bar{c}$	ALL	$12.52 \pm 0.06\%$	$10.24 \pm 0.05\%$	$9.224 \pm 0.05\%$
	CC	$14.29 \pm 0.08\%$	$11.76 \pm 0.07\%$	$10.66 \pm 0.07\%$
	ICR	$11.5 \pm 0.11\%$	$9.346 \pm 0.10\%$	$8.34 \pm 0.10\%$
	EC	$8.081 \pm 0.11\%$	$6.405 \pm 0.10\%$	$5.601 \pm 0.09\%$
$Z \rightarrow c\bar{c} \rightarrow \mu$	ALL	$13.97 \pm 0.09\%$	$11.35 \pm 0.08\%$	$10.34 \pm 0.08\%$
	CC	$15.64 \pm 0.11\%$	$12.8 \pm 0.10\%$	$11.75 \pm 0.10\%$
	ICR	$12.88 \pm 0.17\%$	$10.38 \pm 0.15\%$	$9.403 \pm 0.14\%$
	EC	$9.262 \pm 0.16\%$	$7.26 \pm 0.15\%$	$6.382 \pm 0.14\%$

Table 5.10: c -tagging Efficiency in Monte Carlo.

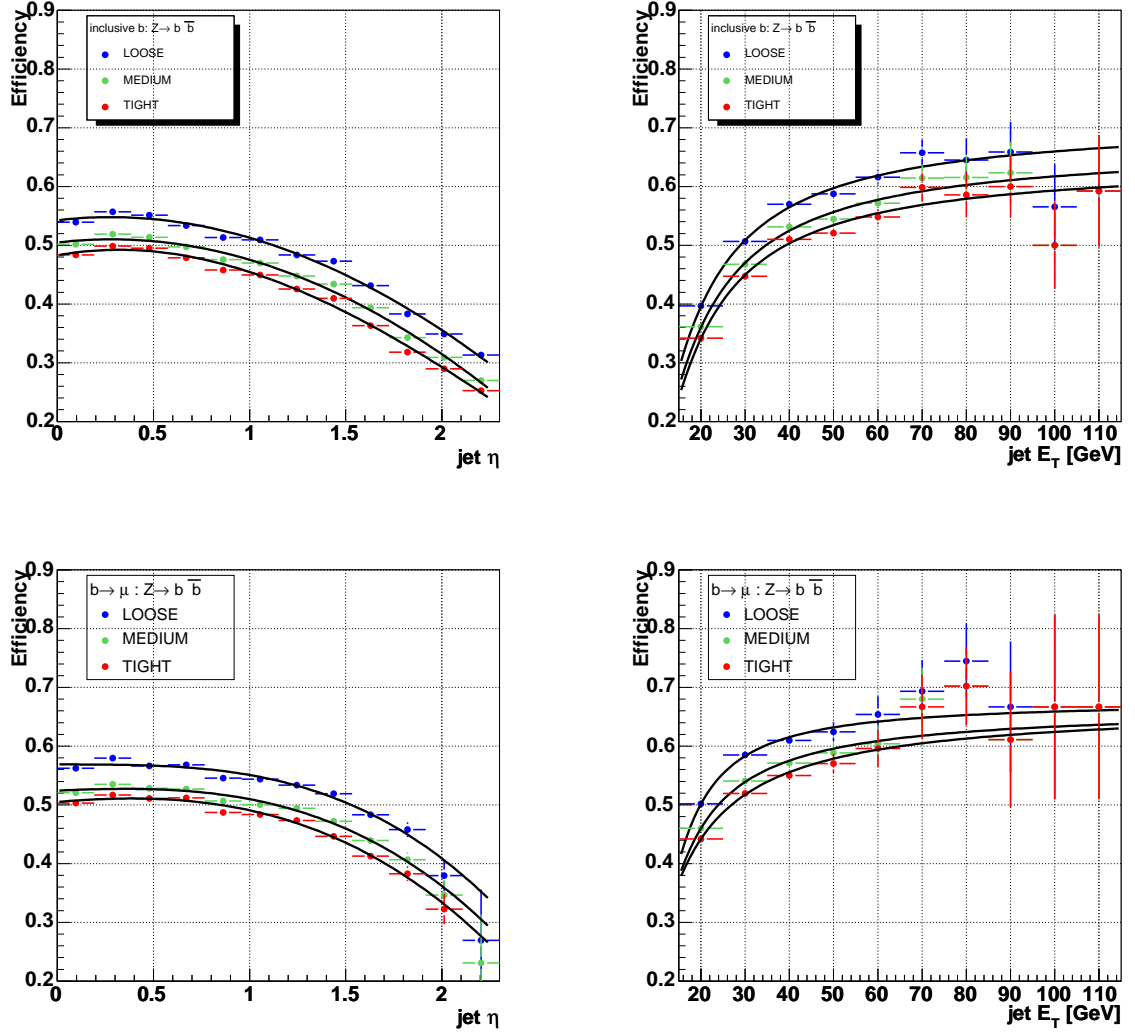


Figure 5.14: b -tagging efficiency in b -jets from $Z \rightarrow b\bar{b}$ events, both inclusive jets (top) and jets associated with a muon (bottom).

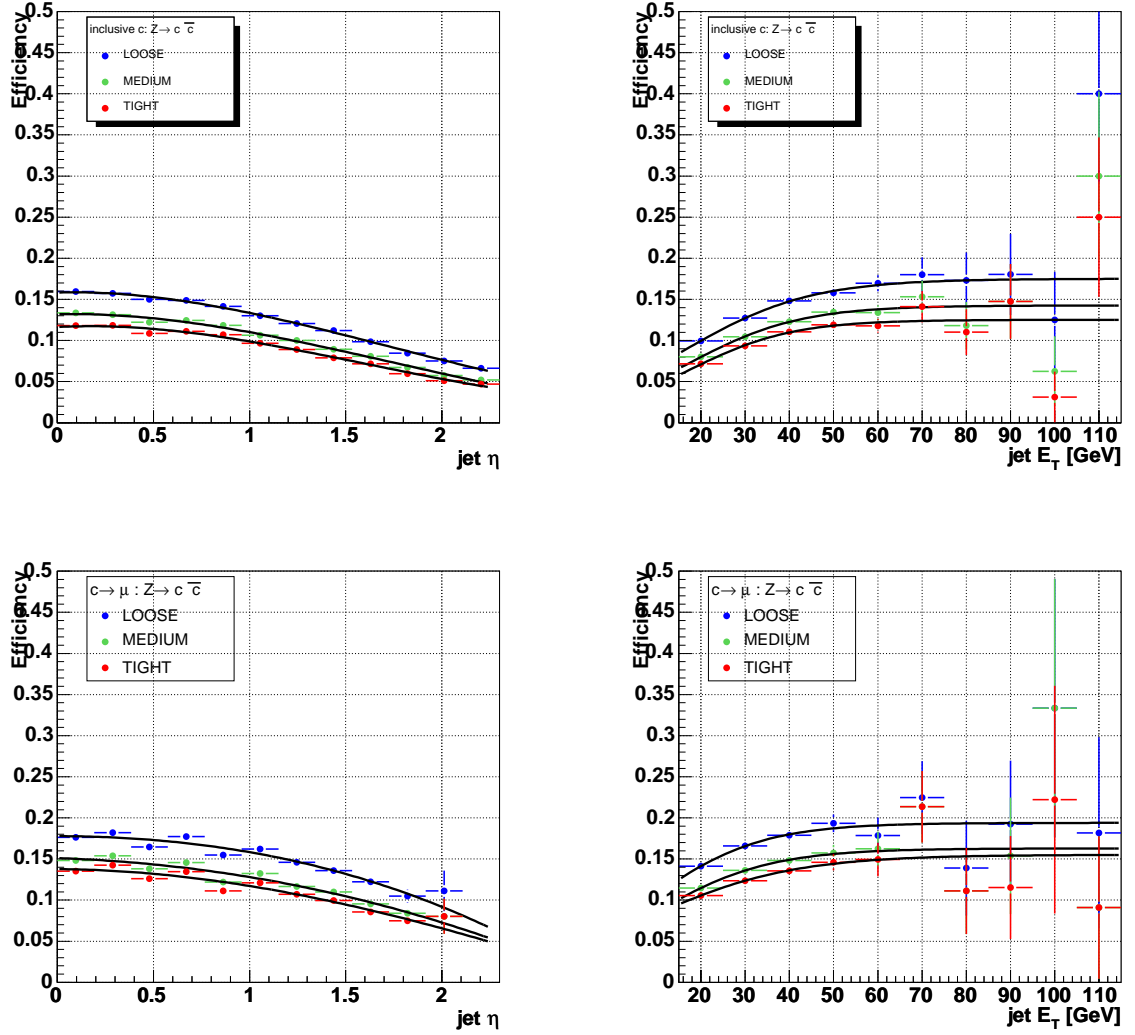


Figure 5.15: c -tagging efficiency in c -jets from $Z \rightarrow c\bar{c}$ events, both inclusive jets (top) and jets associated with a muon (bottom).

5.4 Light-jet tagging Efficiency a.k.a.. Mistag Rate

In the absence of long lived particles there is still a probability of having jets with a positive tag, as indicated in Figure 5.1, due to track misreconstruction and other detector effects. This represents the b -tagging fake rate and is often referred to “Mistag Rate” or simply “Mistag”. The main source of fake rate comes from the tracking detector resolution: either fake, badly reconstructed tracks or tracks that use spurious noisy hits could lead to an high value for their dca_{sig} . These tracks can be selected by the SVT algorithm.

Mistag rate for light-flavored jets in Monte Carlo have been studied in the qcd samples, results are summarized in Table 5.11.

Sample	Region	Mistag rate per jet		
		LOOSE	MEDIUM	TIGHT
qcd	ALL	$0.692 \pm 0.009\%$	$0.402 \pm 0.006\%$	$0.258 \pm 0.005\%$
	CC	$0.833 \pm 0.013\%$	$0.476 \pm 0.010\%$	$0.312 \pm 0.008\%$
	ICR	$0.613 \pm 0.019\%$	$0.373 \pm 0.015\%$	$0.234 \pm 0.012\%$
	EC	$0.473 \pm 0.014\%$	$0.279 \pm 0.011\%$	$0.171 \pm 0.008\%$

Table 5.11: Mistag rates for light quarks in the qcd Monte Carlo samples.

In general resolution effects, due to the randomness of their nature, contribute equally to form secondary vertices with positive and negative decay length significance. Nevertheless a slim preference towards positive tags is shown on Monte Carlo simulated light-jets. The reason for this, as illustrated in Figure 5.16, comes from several contributions:

- Inefficiencies in filtering K_s and Λ . In case only one track from the decay is reconstructed the invariant mass based filter fails;
- Inefficiencies in reconstructing both tracks coming from γ conversion;
- Interaction of particles with tracking detector resulting in decay in flight.

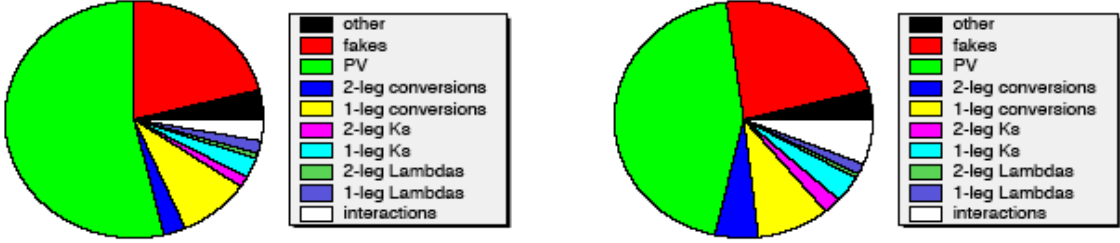


Figure 5.16: Origin of tracks contributing to negative tag (left) and positive tag (right) in Monte Carlo [73].

All contributions listed above have in common that the reconstructed track momentum points outward and therefore are more likely to contribute to the positive spectrum of the secondary vertices Decay Length Significance. On the other side, fake or badly reconstructed PV tracks contribute in equal measure to both the negative and positive tags.

Differences in tracking efficiency between real data and Monte Carlo simulated events as well as imperfect detector noise simulation do not allow to use results from Table 5.11 to estimate the real mistag from data.

5.4.1 Mistag rate for Data

Mistag is derived from Negative Tagging rate in two data samples: EM1TRK and QCD. Even though the negative tagging rate is not equivalent to the positive tagging rate even in a pure Monte Carlo sample, it is still the closest approximation to the detector resolution effects. Also, b and c quarks contribute to the positive as well as to the negative SVT tag rate.

Operationally the mistag rate is estimated by using the negative tagging rate function as obtained from the EM1TRK data, correcting it for the contribution to the negative tagging rate from the small fraction of the heavy flavor content, F_{hf} , and for the asymmetry between the positive and negative tags in light quarks $F_{\ell\ell}$. Both F_{hf} and $F_{\ell\ell}$ are derived from the qcd MC samples.

5.4.2 Monte Carlo based Correction to Negative Tag Rate

The distributions for F_{hf} , $F_{\ell\ell}$, and S_F as a function of jet p_T are shown in Figure 5.17.

The average values of the overall scale factors are shown in Table 5.12.

Vertex Type	F_{hf}	$F_{\ell\ell}$	$SF = F_{hf} \cdot F_{\ell\ell}$
LOOSE	0.665 ± 0.003	1.286 ± 0.005	0.856 ± 0.006
MEDIUM	0.583 ± 0.005	1.381 ± 0.008	0.809 ± 0.008
TIGHT	0.505 ± 0.006	1.463 ± 0.012	0.744 ± 0.010

Table 5.12: Average value of the heavy flavor correction factor F_{hf} , the positive vs negative tagging rate asymmetry correction factor $F_{\ell\ell}$, and the product of the two for different vertex definitions.

5.4.3 Parameterization of Light-quark Mistag Rate obtained in Data

Tables 5.13 and 5.14 summarize the average measured negative tagging rates and the light quark efficiency respectively in the data for both the EM1TRK and QCD trigger samples. Due to the large contamination of high em-fraction jets in the EM1TRK sample compared to the QCD sample, the average negative tagging rates for a low em-fraction sub-sample is also listed in the tables.

		Negative tagging rate per jet in data		
		LOOSE	MEDIUM	TIGHT
EM1TRK	ALL	$0.967 \pm 0.003\%$	$0.592 \pm 0.002\%$	$0.220 \pm 0.001\%$
	CC	$1.028 \pm 0.004\%$	$0.632 \pm 0.003\%$	$0.245 \pm 0.002\%$
	ICR	$0.956 \pm 0.007\%$	$0.597 \pm 0.006\%$	$0.204 \pm 0.003\%$
	EC	$0.678 \pm 0.007\%$	$0.393 \pm 0.005\%$	$0.108 \pm 0.003\%$
EM1TRK $EMF < 0.8$	ALL	$1.088 \pm 0.004\%$	$0.658 \pm 0.003\%$	$0.242 \pm 0.002\%$
	CC	$1.186 \pm 0.006\%$	$0.721 \pm 0.004\%$	$0.276 \pm 0.002\%$
	ICR	$1.022 \pm 0.009\%$	$0.630 \pm 0.007\%$	$0.219 \pm 0.004\%$
	EC	$0.729 \pm 0.009\%$	$0.414 \pm 0.007\%$	$0.115 \pm 0.003\%$

Table 5.13: Negative tagging efficiency and the statistical uncertainty in the EM1TRK data sample.

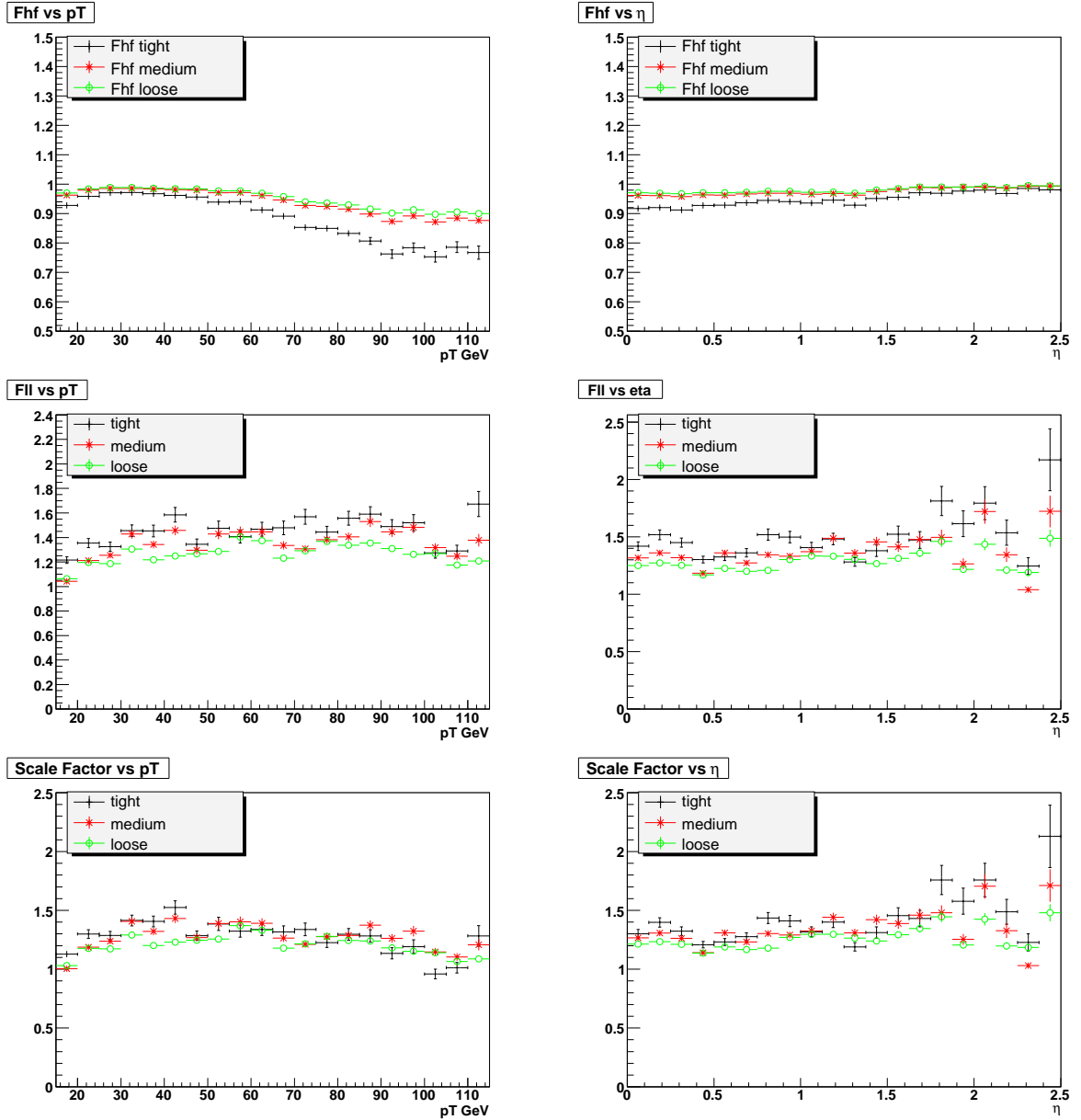


Figure 5.17: The light quark fraction F_{hf} (top plots) and the light quark positive/negative asymmetry F_{ll} (middle plots) and the combined quark scale factor $F_{hf} \cdot F_{ll}$ (bottom plots) as a function of jet E_T and η derived from qcd Monte Carlo for the different vertex types.

Sample	Region	Light quark mistag rate per jet in data		
		LOOSE	MEDIUM	TIGHT
EM1TRK	ALL	$0.811 \pm 0.002\%$	$0.427 \pm 0.001\%$	$0.140 \pm 0.001\%$
	CC	$0.862 \pm 0.003\%$	$0.456 \pm 0.002\%$	$0.156 \pm 0.001\%$
	ICR	$0.802 \pm 0.006\%$	$0.431 \pm 0.004\%$	$0.129 \pm 0.002\%$
	EC	$0.569 \pm 0.006\%$	$0.284 \pm 0.004\%$	$0.069 \pm 0.001\%$
EM1TRK <i>LowEMF</i>	ALL	$0.913 \pm 0.004\%$	$0.475 \pm 0.002\%$	$0.154 \pm 0.001\%$
	CC	$0.995 \pm 0.005\%$	$0.521 \pm 0.003\%$	$0.175 \pm 0.001\%$
	ICR	$0.857 \pm 0.008\%$	$0.455 \pm 0.005\%$	$0.139 \pm 0.002\%$
	EC	$0.612 \pm 0.008\%$	$0.299 \pm 0.005\%$	$0.073 \pm 0.002\%$

Table 5.14: Mistag rates for light quarks in the EM1TRK data sample.

The light-quark mistag rate is parameterized as a function of jet p_T , in the three calorimeter regions. The fact that the p_T shape is different in these regions, does not make it possible to provide a 2D parameterization assuming that p_T and η are independent variables. The mistag parameterization is based on three different data samples:

- *EM* parameterization is derived from the EM1TRK sample;
- *JET LowEMF* parameterization is computed using the QCD sample;
- *EM LowEMF* parameterization is derived from the EM1TRK sample using jets with em-fraction below 0.8.

Figure 5.18 (left plot) shows the negative tagging rate in the EM1TRK sample for the LOOSE tagger, as a function of jet p_T in for CC, ICR, and EC calorimeter regions. The jet p_T and η cannot be treated as uncorrelated variables since the slope of the p_T parameterization is different in the central and forward regions. Similar plots for the MEDIUM and TIGHT taggers are shown in Figures 5.19 and 5.20 respectively. The lower left plots in these figures show how the negative tagging rates in EM1TRK and QCD samples obtained using only the low em-fraction jets are very similar (their ratios are close to 1, apart from EC). Also, the low em-fraction jet selection does not change the rates in QCD data, as by design this sample is predominantly jets with large hadronic

fraction, and the bias due to EM trigger condition, as in EM1TRK sample, does not exist in this data set.

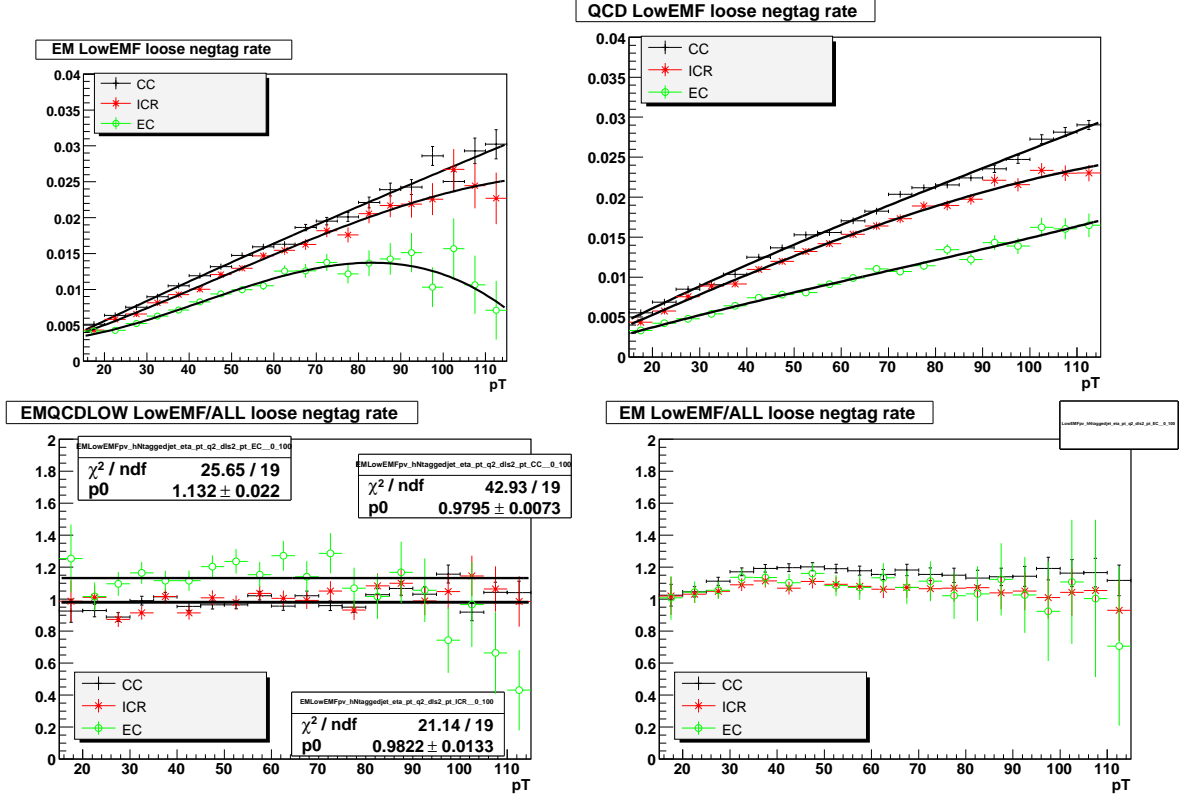


Figure 5.18: Negative Tagging rate as a function of jet p_T for the CC (black), ICR (red), and EC (green) calorimeters and for the LOOSE vertex types. The top plots are the negative tagging rates from the low em-fraction jets in the EM1TRK (left) and QCD multi-jet (right) data samples. Their ratio is plotted in the bottom left plot shows. The ratio of the negative tags rate obtained using low em-fraction jets in the EM1TRK data to that obtained in using all the jets in the EM1TRK sample is plotted on the bottom right.

5.4.4 Mistag Systematics

The systematic uncertainty on the light quark tag rate has two main components, the first is the negative tagging rate and the second comes from the scale factors.

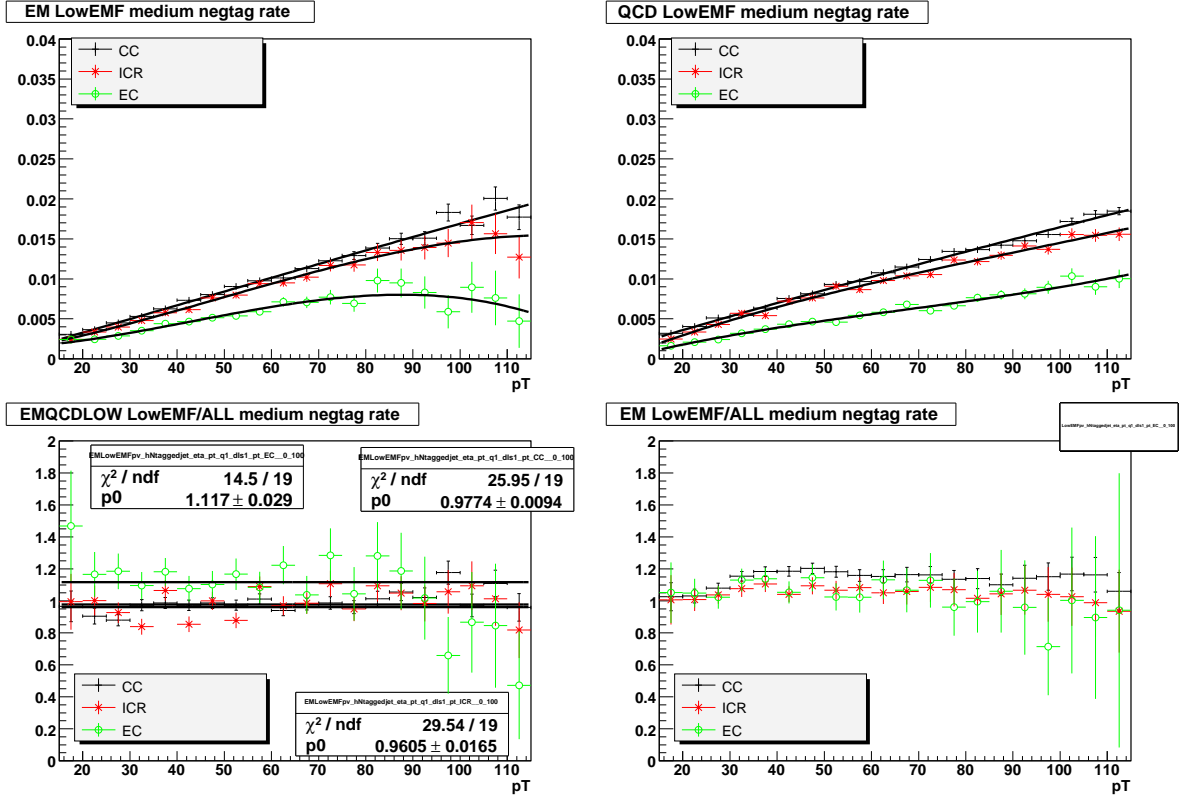


Figure 5.19: Negative Tagging rate as a function of jet p_T for the CC (black), ICR (red), and EC (green) calorimeters and for the MEDIUM vertex types. The top plots are the negative tagging rates from the low em-fraction jets in the EM1TRK (left) and QCD multi-jet (right) data samples. Their ratio is plotted in the bottom left plot shows. The ratio of the negative tags rate obtained using low em-fraction jets in the EM1TRK data to that obtained in using all the jets in the EM1TRK sample is plotted on the bottom right.

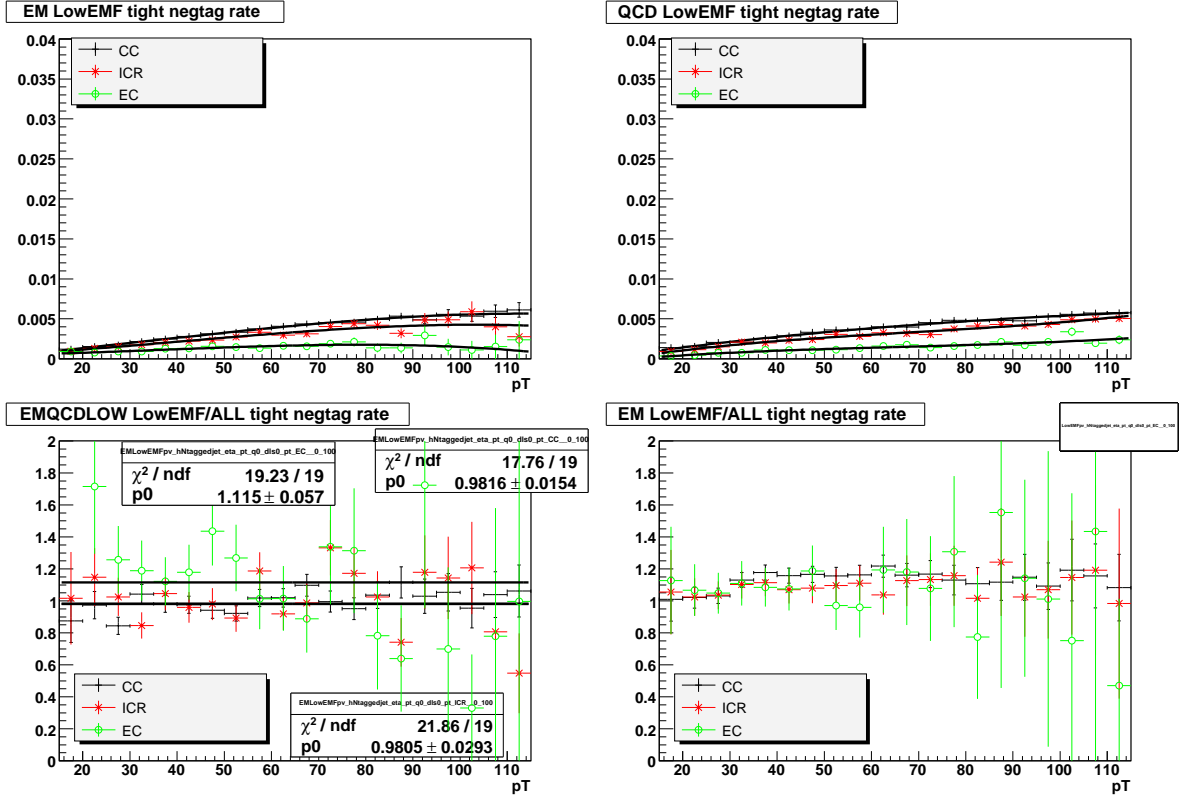


Figure 5.20: Negative Tagging rate as a function of jet p_T for the CC (black), ICR (red), and EC (green) calorimeters and for the TIGHT vertex types. The top plots are the negative tagging rates from the low em-fraction jets in the EM1TRK (left) and QCD multi-jet (right) data samples. Their ratio is plotted in the bottom left plot shows. The ratio of the negative tags rate obtained using low em-fraction jets in the EM1TRK data to that obtained in using all the jets in the EM1TRK sample is plotted on the bottom right.

Data parameterization		LOOSE	MEDIUM	TIGHT
EM1TRK	CC	0.06%	0.07%	0.05%
	ICR	0.57%	0.12%	0.10%
	EC	0.03%	0.35%	1.19%
QCD	CC	0.25%	0.26%	0.43%
	ICR	0.71%	1.07%	0.95%
	EC	10.37%	8.53%	7.95%

Table 5.15: Relative difference ($|\frac{predicted-observed}{observed}|$) between the number of observed tags using different *EM LowEMF* parameterization applied to EM1TRK and QCD data for the three vertex types.

Negative Tagging Systematics

Negative Tagging Rate parameterizations are tested in both low em-fraction EM1TRK and QCD using *EM LowEMF* mistag rate parameterization function. In order to derive a systematic uncertainty on the tag rate function, we look at the agreement between the predicted and observed negative tags both as a function of the p_T and integrated over p_T for the different detector regions, as shown in Table 5.15. We note that for the CC (ICR) these values scatter below 0.5% (1.1%). For the EC, the difference is below 1.5% in the EM1TRK sample and below 10% for the QCD sample .

The rms of these differences are tabulated in Table 5.16 and assigned as the systematic uncertainty on the negative tagging rate parameterizations.

Monte Carlo Scale Factor Systematics

The systematic uncertainty for the scale factors are derived by varying the b and c fractions in the *qcd* Monte Carlo by 20% and it is also shown in Table 5.17. Combining this source of uncertainty with the uncertainty on the negative tagging rate we determine the final systematic uncertainty on light quark mistag rate as shown in the bottom part of Table 5.17.

	LOOSE	MEDIUM	TIGHT
Negative Tagging Rate uncertainty (in %) from p_T dependence of closure test			
CC	2.3	2.7	2.2
ICR	3.3	3.3	7.3
EC	4.8	7.8	13.2
from closure test using EM $LowEMF$ parametrization on EM1TRK data			
CC	0.05	0.07	0.06
ICR	0.10	0.12	0.57
EC	0.03	0.35	1.19
from closure test of EM $LowEMF$ parametrization on QCD data			
CC	0.25	0.26	0.43
ICR	0.71	1.07	0.95
EC	10.37	8.53	7.95
Total uncertainty on Negative Tagging Rate (in %)			
CC	2.3	2.7	2.2
ICR	3.4	3.5	7.4
EC	11.4	11.6	15.5

Table 5.16: Systematic Uncertainties on the negative tagging rate.

	LOOSE	MEDIUM	TIGHT
Uncertainty on $SF = F_{hf} \cdot F_{\ell\ell}$ (in %) (vary b and c content in QCD MC by $\pm 20\%$)			
	4.3	4.9	5.6
Total uncertainty on Light Quark Tag Rate (in %)			
CC	4.8	5.5	6.1
ICR	5.5	6.0	9.3
EC	12.2	12.6	16.44

Table 5.17: Systematic Uncertainties for the Light Quark mistag rate.

5.5 SVT Optimization

The three SVT working points have been chosen in order to reach the highest efficiencies for fixed mistag rates of 1%, 0.5% and 0.25% respectively. Several SVT definitions have been analyzed and their efficiency versus negative tagging rate evaluated, before defining the LOOSE, MEDIUM and TIGHT definitions. For the process of optimizing cuts the Negative Tagging rate is used as an approximation of the mistag rate, Figure 5.21 show the dependence of the efficiency versus mistag curve as a function of track and vertex selection.

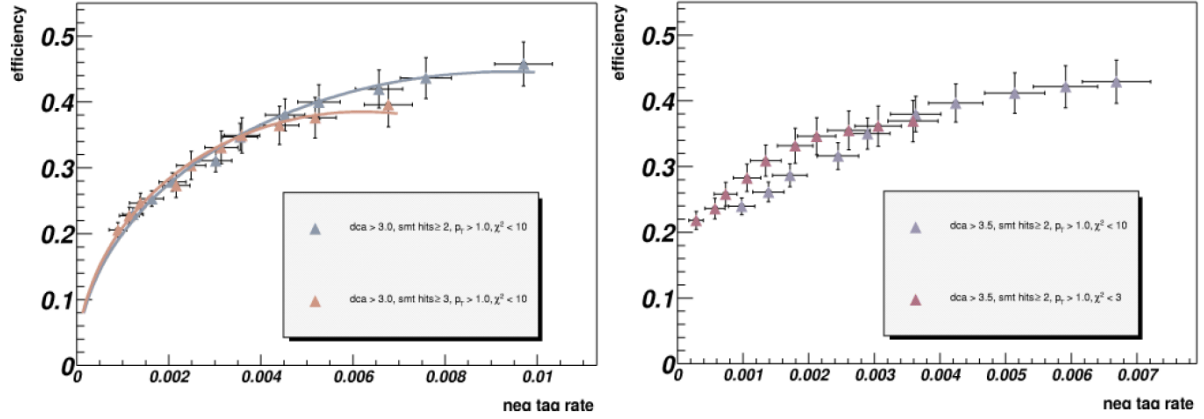


Figure 5.21: Efficiency versus Negative Tagging rate for different SVT definitions. The colored points indicate different cut on the vertex Decay Length Significance $1 \leq dl_{sig} \leq 10$. In the left plot SVT uses tracks with $dca_{sig} \geq 3.0$, $p_T \geq 1$ GeV, $\chi^2 < 10$ and 2 or more (red triangles, MEDIUM SVT) or 3 or more SMT hits (blue triangles). In the right plot SVT use tracks with $dca_{sig} \geq 3.5$, $p_T \geq 1$ GeV, 2 or more SMT hits and $\chi^2 < 3$ and (red triangles) or 3 or $\chi^2 < 10$ more (blue triangles).

A final plot showing the efficiency versus mistag rate together with their uncertainties for the three SVT definition is shown in Figure 5.22.

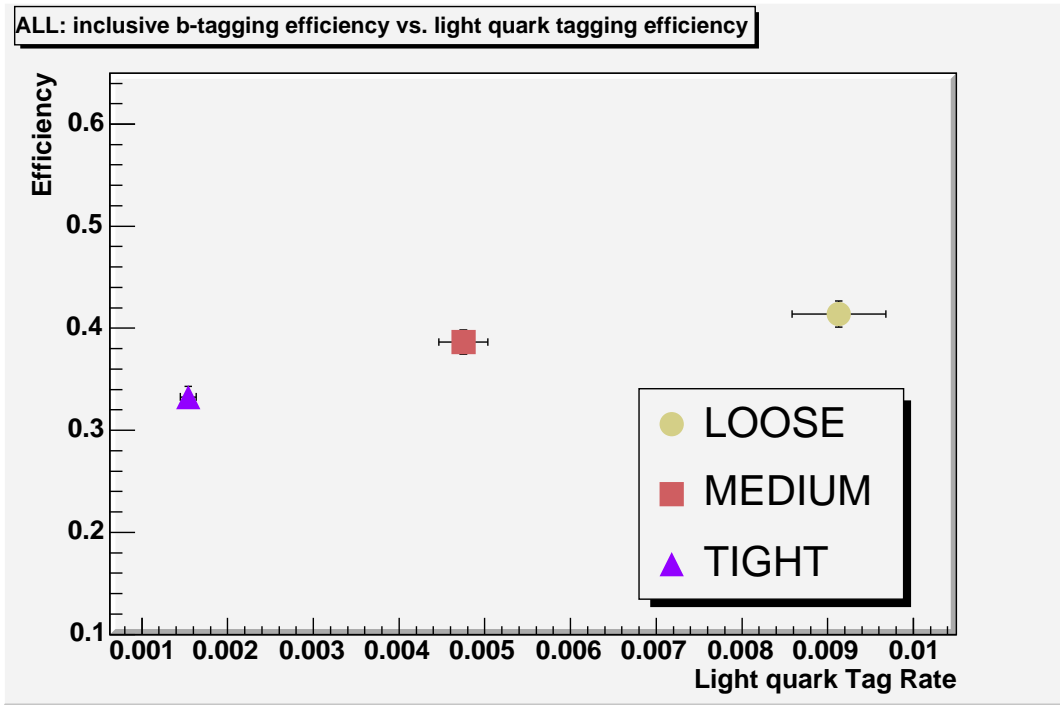


Figure 5.22: Performance of the SVT tagger.

Chapter 6

Event Selection

This chapter describes the search for $W\pi_T$ signal in the data collected by DØ from April 2002 until July 2004. The EM1TRK dataset, defined in Section 5.2.1, skimmed by DØ Common Sample Group (CGS) was analyzed [74]. This skim contains 64158721 events, 6.6% of the total events recorded in the same data taking period. These events were selected by requesting an electromagnetic cluster with $p_T > 8$ GeV and a track with $p_T > 5$ GeV within $\Delta\phi = 0.1$ of the EM cluster. All data events were processed using version p14 of DØ reconstruction software. From the event list we removed runs indicated as “bad” for the calorimeter, CFT and SMT sub-detectors in DØ run database, as these sub-detectors were not read out correctly by the data acquisition in these runs.

Almost all Monte Carlo samples are generated using the PYTHIA event generator. Only events where a W boson is produced together with hadronic jets (with no top-quarks) are generated with ALPGEN, as discussed in Section 4.7. All simulated events are processed via the full DØ Monte Carlo simulation, including DØGeant and the DØ reconstruction software version p14. A summary of the simulated physics processes is shown in Table 6.1.

process	generator	cross section (in pb)	# of events
$t\bar{t} \rightarrow \ell\nu b\bar{b} q\bar{q}$	pythia	2.95	26000
$t\bar{t} \rightarrow \ell^+\nu\ell^-\nu b\bar{b}$	pythia	0.695	46750
$W^* \rightarrow tb \rightarrow (e\nu + \tau\nu)bb$	pythia	0.115	32500
$qtb \rightarrow q (e\nu + \tau\nu)bb$	pythia	0.258	33000
$W(\rightarrow e\nu) + b\bar{b}$	alpgen	3.35	99500
$Wjj (+HFb - tag)$	alpgen	287.3	189500
$WZ \rightarrow \ell + \nu b\bar{b}$	pythia	0.0542	49000
$Z \rightarrow e^+e^-(m_{\ell\ell} = 15 - 60)$	pythia	528	19500
$Z \rightarrow e^+e^-(m_{\ell\ell} = 60 - 130)$	pythia	245.7	247000
$Z(\rightarrow e^+e^-) + b\bar{b}$	pythia	0.539	98000

Table 6.1: Physics Background Processes. We list their cross sections and number of events generated and processed through DØGeant.

6.1 Sample Luminosity

The Luminosity block is the fundamental unit of time for the luminosity measurement [75]. Each block is indexed with a luminosity block number (LBN). Each luminosity block accounts for about 60 seconds of data taking, an amount of time during which the instantaneous luminosity is constant within an acceptable approximation. The instantaneous luminosity is given by the expression:

$$\mathcal{L} = \frac{fBN_pN_{\bar{p}}}{2\pi(\sigma_p^2 + \sigma_{\bar{p}}^2)}F(\sigma_l/\beta^*) \quad (6.1)$$

where f is the revolution frequency (47.713 KHz), B is the number of bunches in the beam, N_p ($N_{\bar{p}}$) is the number of protons (anti-proton) per bunch, σ_p ($\sigma_{\bar{p}}$) the transverse size of the bunches and F a form factor depending on the longitudinal size of the bunches (σ_l) and on the beta function at the interaction point (β^*) [76].

For each luminosity block the Luminosity Monitor records the rate of coincidences in the scintillation counters located around the beam on the two end calorimeters. These counts are interpreted to be produced by non diffractive inelastic $p\bar{p}$ collisions, a process of known cross section ($\sigma = 60.7 \pm 2.4$ mb), and is used to calculate the integrated

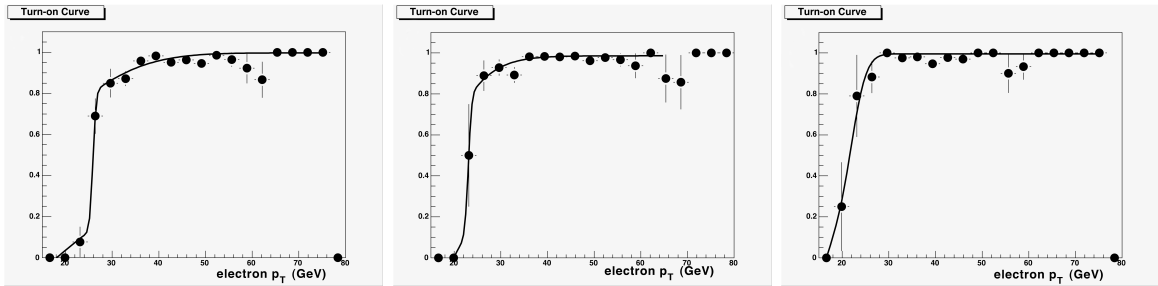


Figure 6.1: Turn-on curves versus electron p_T for trigger version v11 (left), v12 (center) and v13 (right) [77].

luminosity. The total integrated luminosity of the EM1TRK skim is 388 pb^{-1} with a relative uncertainty of 6.4%.

6.2 Trigger Selection

In order to pass the single EM trigger requirement, at least one of the triggers listed in Table 6.2 and Table 6.3 has to be fired by the event. Data events are categorized in three different trigger list versions: v11, v12 and v13. The efficiency “Turn-on” curves for the combination of the single EM triggers are derived for each trigger version as a function of electron p_T . These efficiencies as a function of the electron p_T , shown in Figure 6.1, are calculated in data by using a selected sample of $Z \rightarrow e^+e^-$ events, and are used to reproduce the trigger efficiency in Monte Carlo [77].

6.3 Electron Finding Efficiency

The electron finding efficiency is derived from $Z \rightarrow e^+e^-$ candidates in data and Monte Carlo events. The data sample consists of the entire EM1TRK, the Monte Carlo sample is the same $Z \rightarrow e^+e^- (m_{\ell\ell} = 60 - 130)$ sample listed in Table 6.1.

First we estimated the efficiency for finding a calorimeter electron, where a “calorimeter electron” is a Loose electron as defined in Section 4.4.1 without any requirement for

Version	Name	Requirements
V11	EM_HI	L1: NOT Cal unsuppressed readout and one EM trigger tower having $E_T > 10$ GeV. L2: One EM candidate with $E_T > 12$ GeV. L3: set the trigger bit true if an $ \eta < 3$ electron with $E_T > 30$ GeV meeting loose criteria is found.
	EM_MX	L1: NOT Cal unsuppressed readout and one EM trigger tower having $E_T > 15$ GeV. L3: set the trigger bit true if an $ \eta < 3$ electron with $E_T > 30$ GeV meeting loose criteria is found.
	EM_HI(MX)_FO	L1,L2 like EM_HI(MX). L3: set the trigger bit true if an $ \eta < 3$ electron with no em fraction cut and $E_T > 50$ GeV is found.
	EM_HI(MX)_SH	L1,L2 like EM_HI(MX). L3: set the trigger bit true if an $ \eta < 3$ electron is found with $E_T > 20$ GeV meeting loose criteria including a transverse shower shape requirement.
	EM_HI(MX)_TR	L1,L2 like EM_HI(MX). L3: one track is found by the GlobalTracker tool with $p_T > 25$ GeV.
	EM_HI(MX)_SH_TR	L1,L2 like EM_HI(MX). L3: one track is found by the GlobalTracker tool with $p_T > 12$ GeV and one loose calorimeter electron satisfying transverse shower shape requirements and $E_T > 12$ GeV.
	EM_HI(MX)_EMFR8	L1,L2 like EM_HI(MX). L3: set the trigger bit true if a $ \eta < 3$ electron with $E_T > 40$ GeV meeting very loose criteria ($emfraction > 0.8$) is found.

Table 6.2: Requirement at Level 1, Level 2 and Level 3 for the v11 single EM trigger list.

Version	Name	Requirements
V12/v13	E1_SHT20(30)	L1: Require one calorimeter EM object with $E_T > 11$ GeV. and NOT Calorimeter unsuppressed readout. L3: Requires an electron satisfying tight (loose) shower shape requirements with $E_T > 20(30)$ GeV.
	E1_SHT15_TK13	L1: like E1. L3: Require an electron with $E_T > 15$ GeV satisfying tight shower shape requirements. Also require one track with $p_T > 13$ GeV.
	E1_T13L15	L1: like E1. L3: Require an electron with $E_T > 15$ GeV satisfying loose requirement with a track match. Track must have $p_T > 13$ GeV.
	E4	L1: Require one calorimeter EM tower with $E_T > 9$ GeV plus one track with $p_T > 10$ GeV and NOT Calorimeter unsuppressed readout.
	E6	L1: One calorimeter EM trigger tower with $E_T > 6$ GeV. Also, the event must have one isolated CFT track with $p_T > 10$ GeV. Also, veto on cal unsuppressed trigger.

Table 6.3: Requirement at Level 1, Level 2 and Level 3 for the v12 and v13 single EM trigger list.

the value of the likelihood. For this purpose events with at least one calorimeter electron and one track are used to reconstruct the Z boson mass peak. Although in Monte Carlo the electron efficiency could be estimated directly by comparing the information at generator level and the reconstructed objects, for this analysis, data and Monte Carlo are treated in the same way in order to cancel out the systematic effects of this method.

6.3.1 Calorimeter Electron Reconstruction

The only differences in the requirements on data events compared to Monte Carlo are: a cut on transverse missing energy $MET < 10$ GeV and that analyzed runs are not listed in the Bad Run Database. Common requirements are:

- One or more calorimeter electrons;
- One track satisfying the following criteria, where e indicates the most energetic electron in the event:
 - $25 < p_T(trk) < 80$ GeV;
 - $\Delta R(e, trk) > 1$;
 - $|\eta_{DET}(trk)| < 1.1$;
 - Opposite sign between trk and e ;
 - $\Delta R(e, trk) < 5$ cm;
 - $Dca(trk) < 0.3$ cm;
 - $40 < M(e, trk) < 200$ GeV.

The invariant mass of the calorimeter electron plus track system, $M(e, trk)$, for the events passing the cuts above-mentioned is shown in Figure 6.2, for both data and Monte Carlo figures. The resulting distribution is fitted with the sum of two functions: a Gauss function convoluted with a Breit-Wigner for the signal plus an exponential to simulate the background. The six parameters for the fit are:

- p_0 : width (scale) of the Breit-Wigner;
- p_1 : most probable location for the Breit-Wigner mean;
- p_2 : total area;
- p_3 : width of the convoluted Gaussian function;
- p_4 : value of the exponential function at $x = 0$;
- p_5 : coefficient of the exponential.

In events where the track is within a ΔR of 0.1 with respect to a second calorimeter electron the invariant mass of the now dielectron system, $M(e, e)$, is re-calculated and then fitted again. A signal region is defined for value of the invariant mass between 80 and 100 GeV. The ratio of tracks from Z decays and the amount of these tracks matched to a calorimeter electron in the signal region is taken as the calorimeter electron reconstruction efficiency: ϵ_e .

In the $M(e, trk)$ distribution for data there are 10,153 events in the signal region, among these 9,401 are $Z \rightarrow e^+e^-$ events and 752 background events. The $M(e, e)$ distribution has 8,295 events in the signal region, 8,241 Z events and 55 background events, leading to a value $\epsilon_e^{data} = 83.9\%$.

For Monte Carlo, $M(e, trk)$ has 37,189 signal and 101 background events, while $M(e, e)$ has 31,649 signal and 17 background entries. The resulting efficiency is $\epsilon_e^{MC} = 85.1\%$ (Figure 6.2). The scale factor between Monte Carlo and data calorimeter electron efficiencies is computed to be $SF_e = 0.986$.

6.3.2 Electron ID Efficiency

In order to estimate the total electron finding efficiency in data and Monte Carlo the efficiencies for a calorimeter electron to pass the Loose and Tight requirements are cal-

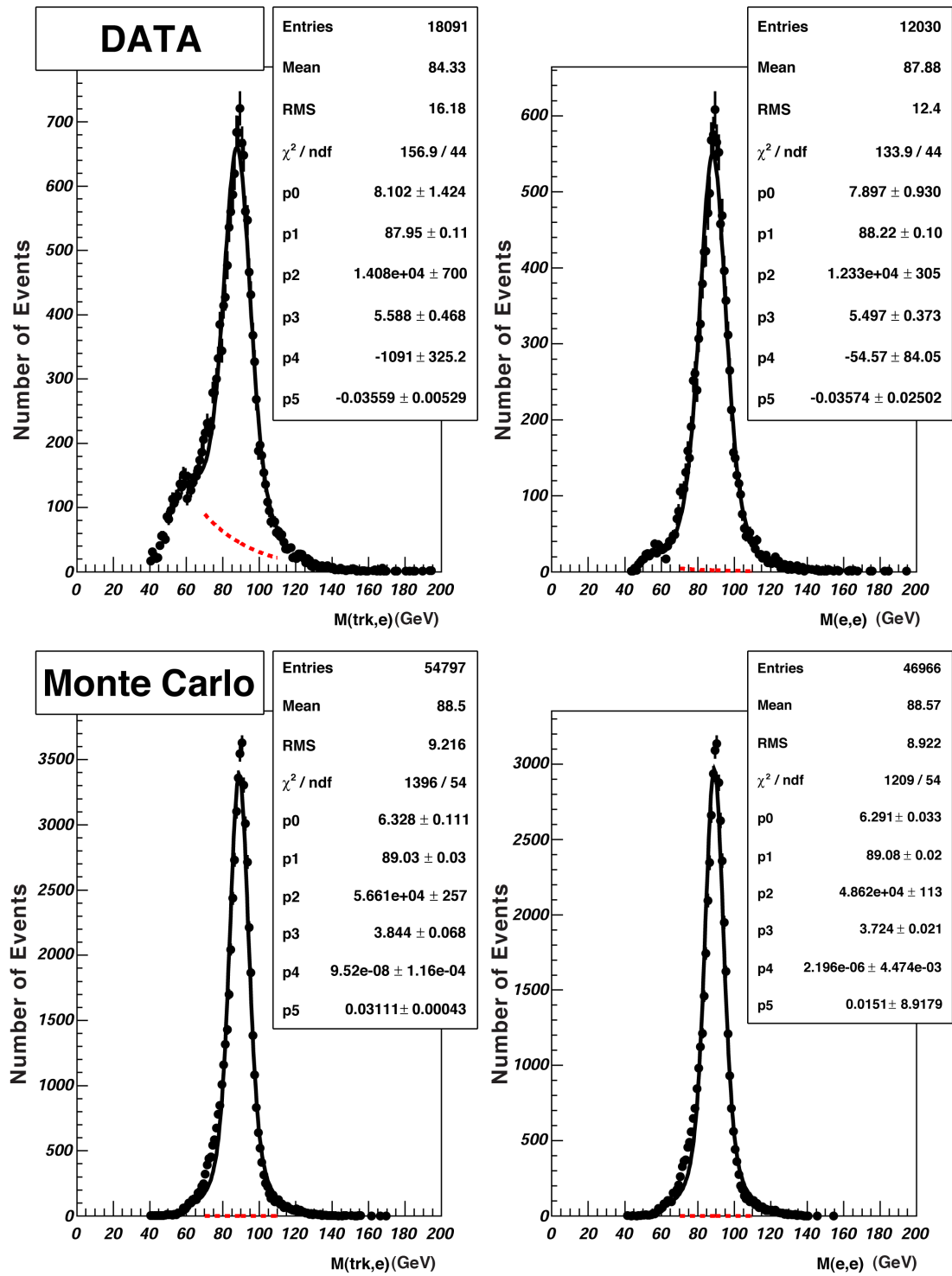


Figure 6.2: $M(e, trk)$ and $M(e, e)$ for EM1TRK data, two top plots, and Monte Carlo, two bottom plots.

culated independently. Similar to the previous case the procedure requires a sample of $Z \rightarrow e^+e^-$ events.

In the first sample the dielectron invariant mass is calculated for all calorimeter electron pairs with at least one electron passing the Loose electron likelihood cut, $M(e, Loose)$, and for all Loose electron pairs, $M(Loose, Loose)$. After fitting the Z mass peaks with the same combination of Gauss, Breit-Wigner and exponential functions and integrating between 80 and 100 GeV, the efficiency ϵ_l is given by the formula:

$$\epsilon_l = 2 \frac{N_L}{(N_L + N_e)}. \quad (6.2)$$

where N_L is the number of Z events with at least one Loose electron and N_e the number of Z events with two Loose electrons.

In data $M(e, Loose)$ has 14,444 events in the signal region, 12538 $Z \rightarrow e^+e^-$ events and 1905 background events. The $M(Loose, Loose)$ distribution has 11211 events in the signal region, 10871 Z events and 340 background events. In Monte Carlo there are 38863 $M(e, Loose)$ and 37502 $M(Loose, Loose)$ events in the signal region, with no background present as shown in Figure 6.3.

The corresponding efficiency value for data, Monte Carlo and the relative data-Monte Carlo scale factor are: $\epsilon_l^{data} = 92.9\%$, $\epsilon_l^{MC} = 98.1\%$ and $SF^l = 0.947$. At this point, we need to compute one more scale factor is then the efficiency for passing from Loose to Tight electron requirement. With the same criteria as before $M(Loose, Tight)$ and $M(Tight, Tight)$ are computed in data and Monte Carlo as shown in Figure 6.4. In data there are 10670 Z candidates and 181 background events populating the $M(Loose, Tight)$ distribution and 9282 Z candidates and 128 background events in the $M(Tight, Tight)$ spectrum. In Monte Carlo 38390 Z candidates and 422 background events in the $M(Loose, Tight)$ distribution while 37060 Z events and 395 background events make the signal region of $M(Tight, Tight)$. This results in the following values for efficien-

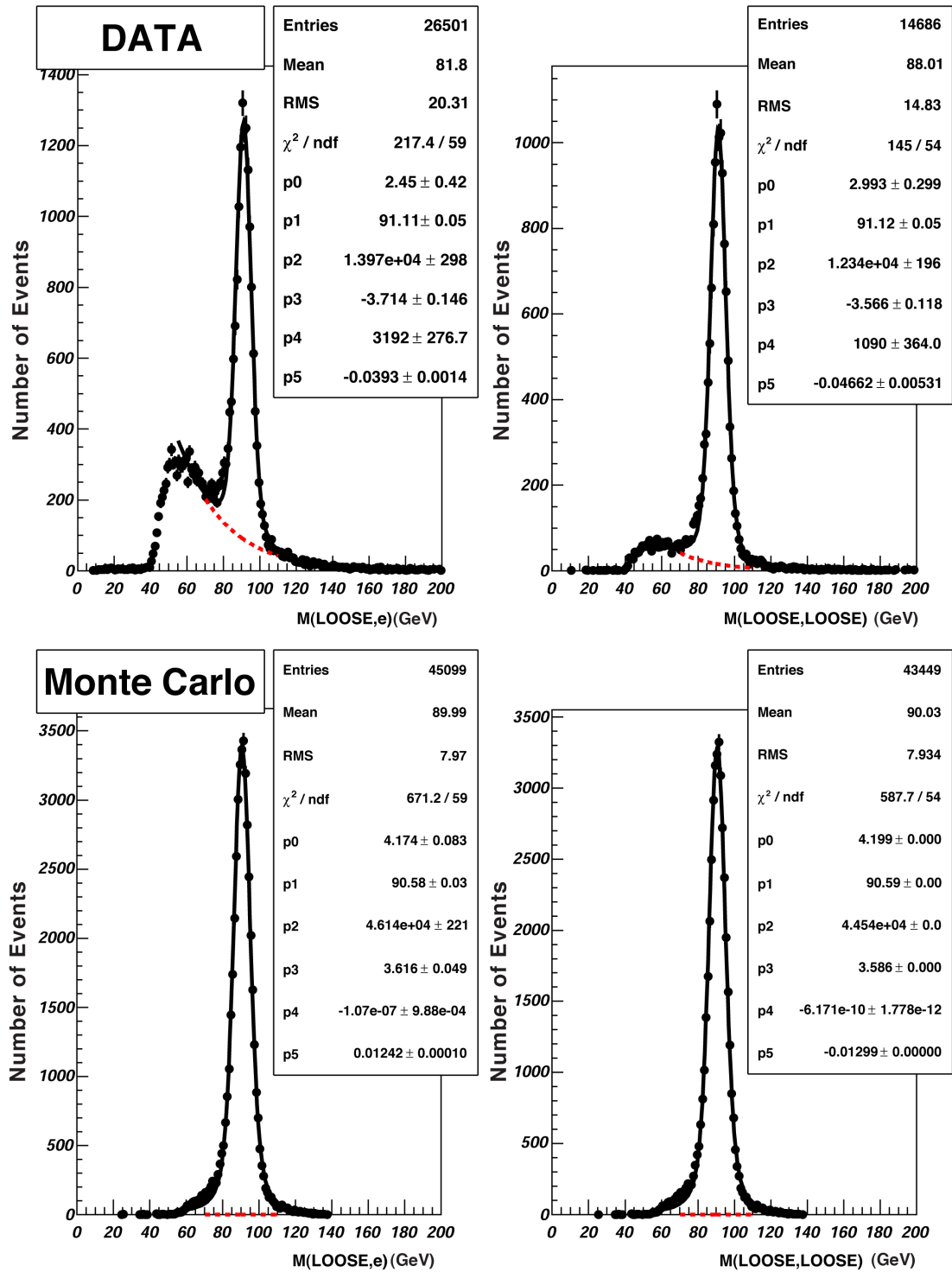


Figure 6.3: $M(e, Loose)$ and $M(Loose, Loose)$ for EM1TRK data (top plots) and Monte Carlo (bottom plots).

cies and background: $\epsilon_t^{data} = 93.0\%$, $\epsilon_t^{MC} = 98.2\%$ and $SF^t = 0.947$. The final total data-Monte Carlo scale factor $SF = SF_e \cdot SF_l \cdot SF_t = 0.884$.

6.3.3 Loose to Tight Fake Rate

The “Loose to Tight” electron fake rate is the rate by which the hadronic jets fake the Loose electron signature and pass the Tight electron identification criterion. In order to determine this fake rate in the EM1TRK sample, events with the following criteria are selected:

- low missing transverse energy ($MET < 10$ GeV),
- One hadronic jet with $\eta < 2.5$ and $p_T > 20$ GeV has to be present;
- One Loose electron back to back with the hadronic jet ($\Delta\phi(e, jet) > 2.8$);
- No other jets or electrons have to be in the event.

These events are interpreted as dijet events ($q\bar{q} \rightarrow g \rightarrow q'\bar{q}'$) with one of the jets faking the electron signature. The fake rate is the ratio of the events with one Tight electron divided by the total number of events with one jet back to back with a Loose electron. The fake rate $f(p_T(e))$ as a function of the p_T of the electron is shown in Figure 6.5.

6.4 $W + 2$ jets selection

The search for Technicolor $W\pi_T$ signal involves clearly distinguishing events where a W boson is produced together with two quarks from multijets events; the latter are also called “QCD-multijet” events since the Strong Force is responsible for their production. $W + 2$ jets events are selected by requesting two calorimeter jets with transverse momentum $p_T > 20$ GeV, one electron with $p_T > 20$ GeV and transverse missing energy

$MET > 20$ GeV. Jets are also requested to be inside a fiducial region of $|\eta_{DET}| < 2.5$ and electron are required to be in the central part of the calorimeter $|\eta_{DET}(e)| < 1.1$.

In addition to the calorimeter transverse missing energy, another quantity related to the presence of the undetected neutrino is used: the object-based missing transverse energy or MET^{obj} . MET^{obj} depends only on the momentum of the electron and the jets in the event and is defined as:

$$MET^{obj} = \sqrt{(p_x(j_1) + p_x(j_2) + p_x(e))^2 + (p_y(j_1) + p_y(j_2) + p_y(e))^2}, \quad (6.3)$$

where $p_{x(y)}(j_1)$, $p_{x(y)}(j_2)$ and $p_{x(y)}(e)$ are the x (y) component of the measured momentum for the first and second leading jet and for the electron.

The need for using this quantity will be clear later when the calibration of PMCS will be discussed. In this stage of the selection, we ask for events to pass a 20 GeV cut on object MET and a cut on 30 GeV on the transverse mass of the W boson, $M_T(W)$, reconstructed using object MET:

$$M_T(W) = \sqrt{(p_T(e) + MET^{obj})^2 - (p_x(e) + MET_x^{obj})^2 - (p_y(e) - MET_y^{obj})^2}, \quad (6.4)$$

where,

$$MET_{x(y)} = -p_{x(y)}(j_1) - p_{x(y)}(j_2) - p_{x(y)}(e). \quad (6.5)$$

6.4.1 Physics Background

The physics background is listed in Table 6.1, trigger turn-on curves, shown in Figure 6.1, are applied to each event in the correct proportion: 33% of the EM1TRK was processed with v11 version of the trigger, 19% with v12 and the rest with v13. Also, to each simulated event the data to Monte Carlo scale factor due to the difference in electron finding efficiency, as calculated in Section 6.3, is applied.

6.4.2 QCD-multijet Background

The QCD-multijet background is due to multi-jet events where one or more jets are badly reconstructed, giving rise to a substantial amount of missing energy, and another jet fakes the electron signature. The expected background from QCD-multijet is estimated with the “matrix method” which consists on two linear equations:

$$N_{loose} = N_{qcd} + N_{W+jets} \quad (6.6)$$

$$N_{tight} = f(p_T(e)) \cdot N_{qcd} + \epsilon_t N_{W+jets} \quad (6.7)$$

where N_{loose} and N_{tight} are the number of events with one Loose and one Tight electron, $f(p_T(e))$ and ϵ_t are the “Loose to Tight” fake rate and efficiency as discussed in Sections 6.3.2 and 6.3.3. The quantity of QCD-multijet contamination in the Tight sample is given by $f(p_T(e)) \cdot N_{qcd}$.

6.4.3 Data Yield and Background Estimate

Table 6.4 shows the data and background yield at this stage of the selection. Distributions of fundamental kinematic quantities after $W + 2$ jets selection are shown in Figures 6.6, 6.7 and 6.8.

6.5 $W + 2$ jets and 1 b -tag selection

As shown in the $W\pi_T$ Feynman diagram in Figure 6.9, Technicolor events are associated with the production of heavy-flavored jets: charged technipions, $\pi_T^{+(-)}$, are expected to decay predominantly into $\bar{b}c$ ($b\bar{c}$) quarks, while the neutral technipions decays most of the times to $b\bar{b}$ quarks. In order to reduce the presence of events where light-flavored jets are produced, we only keep those events in which at least one jet is b -tagged with the TIGHT SVT tagging algorithm.

	Number of events
	$W + 2$ jets
DATA:	4664
Physics Backgrounds:	
$t\bar{t} \rightarrow \ell\nu b\bar{b} q\bar{q}$	18.9
$t\bar{t} \rightarrow \ell^+\nu\ell^-\nu b\bar{b}$	25.8
$W^* \rightarrow tb \rightarrow (e\nu + \tau\nu)bb$	6.3
$qtb \rightarrow q (e\nu + \tau\nu)bb$	12.1
$W(\rightarrow e\nu) + b\bar{b}$	52.1
Wjj	3901
WZ	2.4
$Z(\rightarrow e^+e^-)$	39.2
$Z(\rightarrow e^+e^-) + b\bar{b}$	1.4
Total Physics Backgrounds	4059
Instrumental Backgrounds:	
QCD-multijet	447
Total Background:	4506

Table 6.4: Data Sample and Background Estimates after $W + 2$ jets selection.

6.5.1 Physics Background

Physics processes contributions to the background, after 1 b -tag selection are listed in Table 6.5:

- top -quark production: generally events where a top -quark is produced can pass the $W + 2$ jets and 1 b -tag selection. In fact, $t\bar{t}$ events, when both W decay into an electron and electron neutrino and one of the electrons is not reconstructed, have a signature similar to $W\pi_T^0$ events. The same happens when the W boson decays into hadrons and more than one jet are not reconstructed. Single top events, in both production channel (s and t), are more likely to pass the $W + 2$ jets and 1 b -tag selection but have smaller cross section. In general top -quark events are more energetic than Technicolor events resulting in an efficient rejection when topological variable are used, as discussed in Section 6.5.3;
- Events where a W boson is produced together with two or more jets and at least

one *heavy flavored*-jet are an irreducible source of background in this analysis. Among these processes are: W boson produced together with two b -jets ($Wb\bar{b}$) and W plus at least one c -jet ($Wc\bar{c}$, Wc , $Wcj, Wccj$). Apart from the first process, which is generated separately, all other contributions are grouped under the name of $W + \text{HF}$;

- Another source of physics background are events where a Z boson, produced together with *heavy flavored*-jets decays to two electrons and diboson events where a W boson decays into electron and electron neutrino and a Z boson into $c\bar{c}$ or $b\bar{b}$ pairs.

Contributions from these processes are estimated using a flavor dependent tagging parameterization applied after the $W + 2$ jets selection. The only physics process that has a special treatment is $W + \text{heavy flavor}$ production. To determine this contribution we use the ALPGEN Wjj sample, choosing events with at least one b or c quark (excluding events with two b -quarks that are generated separately). The contribution of W boson plus light jets is derived from data and detailed in the next section.

Monte Carlo b -tagging Scale Factor

Due to the differences in b -tagging efficiency between data and Monte Carlo the SVT tagging algorithm is not applied directly to simulated events used to estimate the physics background. Instead, each Monte Carlo event passing the $W + 2$ jets selection is weighted with respect to the probability of having at least one jet tagged by the SVT. This probability, w , depends upon the efficiency of tagging each jet in the event and is function of the jet p_T , η and *flavor*. This efficiency is the data derived parameterization of the b and c -tagging efficiency and mistag rate as described in Sections 5.3 and 5.4.

To every jet in the event a *flavor* is associated depending upon the generated partons within a cone of radius $\Delta R = 0.5$ with respect to the jet axis:

- A b -jet is associated to at least one b -quark;
- A c -jet is associated to at least one c -quark, and not b -quark;
- A $light$ -jet is not associated to any b or c -quark.

The weight w has the form:

$$w = 1 - (1 - \epsilon_i(p_T, \eta))(1 - \epsilon_j(p_T, \eta)), \quad i, j = b, c, light, \quad (6.8)$$

where $\epsilon_b(p_T, \eta)$ is a two dimensional efficiency parameterization (top left plot in Figure 6.10). This efficiency is made of two components: the efficiency derived in the $\mu + jets$ data sample, $\epsilon_b^{mj\ data}(p_T, \eta)$, times a Monte Carlo derived scale factor taking into account the higher efficiency for tagging Muon Jets, $\epsilon_b^{mj\ MC}(p_T, \eta)$, with respect to jets coming from a fully hadronic parton decay (Hadronic Jets), $\epsilon_b^{hj\ MC}(p_T, \eta)$:

$$\epsilon_b(p_T, \eta) = \epsilon_b^{mj\ data}(p_T, \eta) \frac{\epsilon_b^{hj\ MC}(p_T, \eta)}{\epsilon_b^{mj\ MC}(p_T, \eta)}. \quad (6.9)$$

The c -tagging two dimensional parametrization $\epsilon_c(p_T, \eta)$ is also based on b -tagging efficiency derived from the $\mu + jets$ sample and then scaled to the Monte Carlo derived ratio of c to b -tagging.

$$\epsilon_c(p_T, \eta) = \epsilon_b(p_T, \eta) \frac{\epsilon_c^{MC}(p_T, \eta)}{\epsilon_b^{MC}(p_T, \eta)}. \quad (6.10)$$

And finally $\epsilon_{light}(p_T, \eta)$ is derived from negatively tagged jets in the EM1TRK data sample as discussed in Section 5.4. In general given N the number of simulated events passing a series of cuts *except* the b -tagging requirement, the predicted number N_{tag} of events with at least one jet b -tagged is:

$$N_{tag} = \sum_{i=1}^N w_i, \quad (6.11)$$

where w is defined in Equation 6.8.

6.5.2 W +jets mistag background:

The W +jets background originates from events in which a jet from light quark is falsely identified as a b -jet because of a wrongly reconstructed secondary vertex. This contribution is directly estimated from the untagged W +jets data sample.

Starting from the untagged W +jets, sample the probability of the event to have at least one tag is estimated using the weight from Equation 6.8 and considering all jets to be light-flavored. About 5% of the events passing the W +jets selection is made of QCD-multijet background. In the process of estimating the W +light-jets from data the multijet contribution has to be eliminated in order to avoid double counting: once when it's estimated with the matrix method in the tagged sample, and the second time when it's weighted as part of the W +light-jets estimation. From the final W +light-jets estimation the matrix method is used again to subtract the QCD-multijet. In summary the matrix method is used twice, in order to establish the QCD-multijet contamination in the $W + 2$ jets and 1 b -tag sample and the second time to remove the contamination to the W +light-jets derived from data. Both these contribution are part of the instrumental background in Table 6.5.

6.5.3 $W + 2$ jets ≥ 1 b -tag: event topology

In order to optimize the technipion signal over background after the b -tagging requirement, several topological variables are considered. As the Technicolor particles are expected to have narrow widths (~ 1 GeV/ c^2), in addition to correlations between the two jets from the technipion decay, these particles are expected to be seen in the distributions of dijet invariant mass, $M(jj)$ and the invariant mass of the W +dijets, $M(Wjj)$.

In particular, we optimize the following variables:

	Number of events $W + 2 \text{ jets} \geq 1 \text{ } b\text{-tag}$
DATA:	125
Physics Backgrounds:	
$t\bar{t} \rightarrow \ell\nu \bar{b}\bar{b} q\bar{q}$	13.7
$t\bar{t} \rightarrow \ell^+\nu\ell^-\nu \bar{b}\bar{b}$	7.6
$W^* \rightarrow tb \rightarrow (e\nu + \tau\nu)bb$	3.3
$qtb \rightarrow q (e\nu + \tau\nu)bb$	4.3
$W(\rightarrow e\nu) + \bar{b}\bar{b}$	22.9
Wjj (+HF)	31.8
WZ	1.1
$Z(\rightarrow e^+e^-)$	0.5
$Z(\rightarrow e^+e^-) + \bar{b}\bar{b}$	0.5
Total Physics Backgrounds	85.7
Instrumental Backgrounds:	
QCD-multijet	16.5
$W + \text{jets mistag}$	11.5
Total Background:	113.7

Table 6.5: Data Sample and Background Estimates after $W + 2 \text{ jets} \geq 1 \text{ } b\text{-tag}$ selection.

- $\Delta\phi(jj)$ is the difference in ϕ between the two jets present in the event, i.e. the dijet system;
- $\Delta\phi(e, MET)$ the ϕ difference in between the electron and the missing transverse momentum;
- $p_T(jj)$ is the transverse momentum for the same dijet system;
- H_T^e is the scalar sum of p_T of the electron and the two jets in the event;
- $M(jj)$ is the invariant mass of the dijet system. The $M(jj)$ distribution corresponds to the reconstructed π_T invariant mass;
- $M(Wjj)$ is the invariant mass of the dijet system combined with the W (reconstructed from the electron and missing p_T in the event). This is equivalent to reconstructing the mass of the technirho resonance (ρ_T). While computing $M(Wjj)$, we reconstruct the W boson four vectors from the electron and the missing p_T using

the W mass constraint to solve for the p_z of the neutrino. Out of the two possible solutions for the neutrino p_z , we take the smaller value, and if in case of a complex solution, we take the real part of the solution.

Figures 6.11, 6.12, 6.13, 6.14 and 6.15 show distributions for electron, MET and jet quantities together with topological variables like $\Delta\phi$, $p_T(jj)$, $M(jj)$, and $M(Wjj)$ for events with 2 jets and at least one tagged jet. The event counts are listed in Table 6.5.

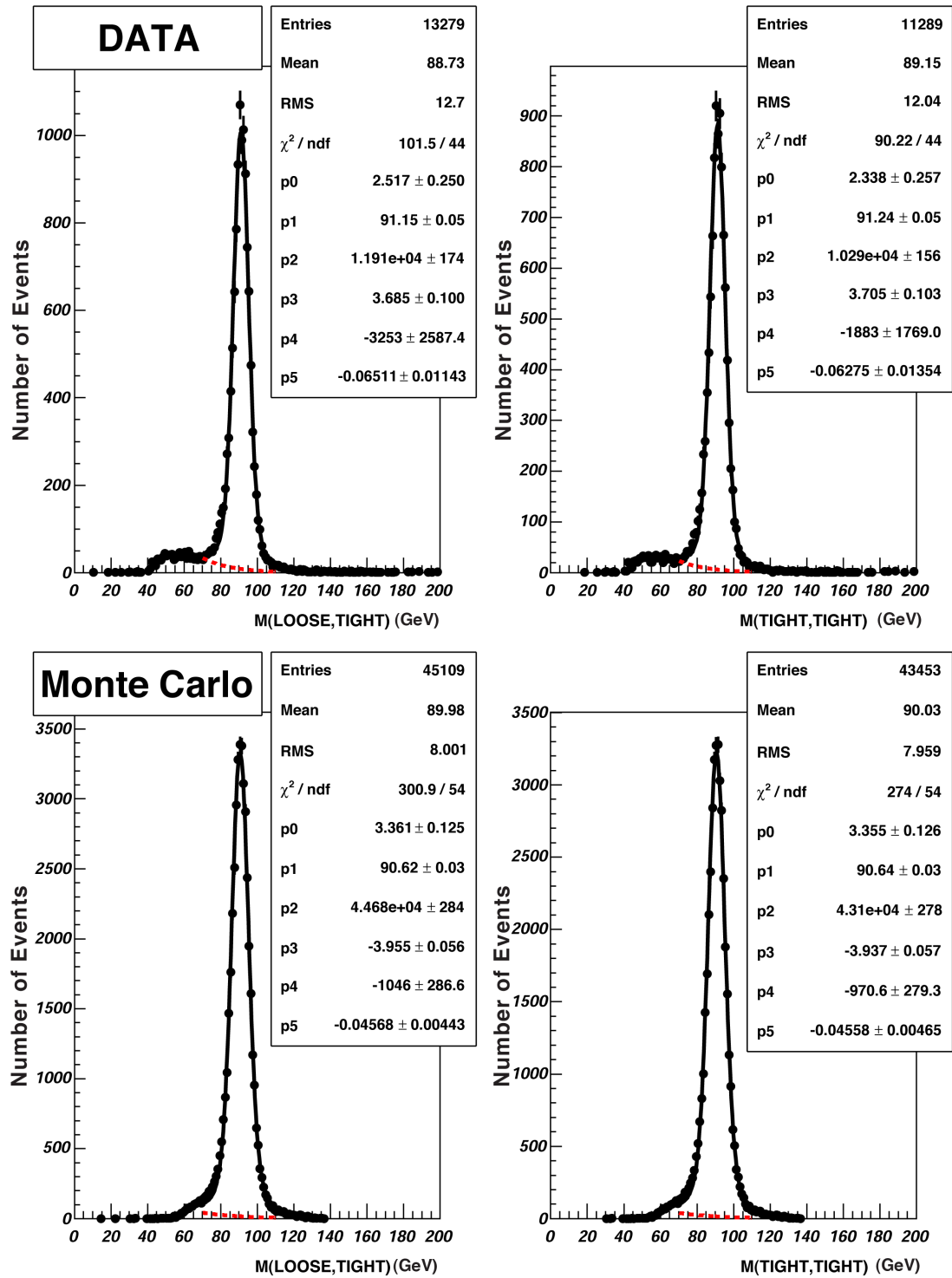


Figure 6.4: $M(\text{Loose}, \text{Tight})$ and $M(\text{Tight}, \text{Tight})$ for EM1TRK data (top plots) and Monte Carlo (bottom plots).

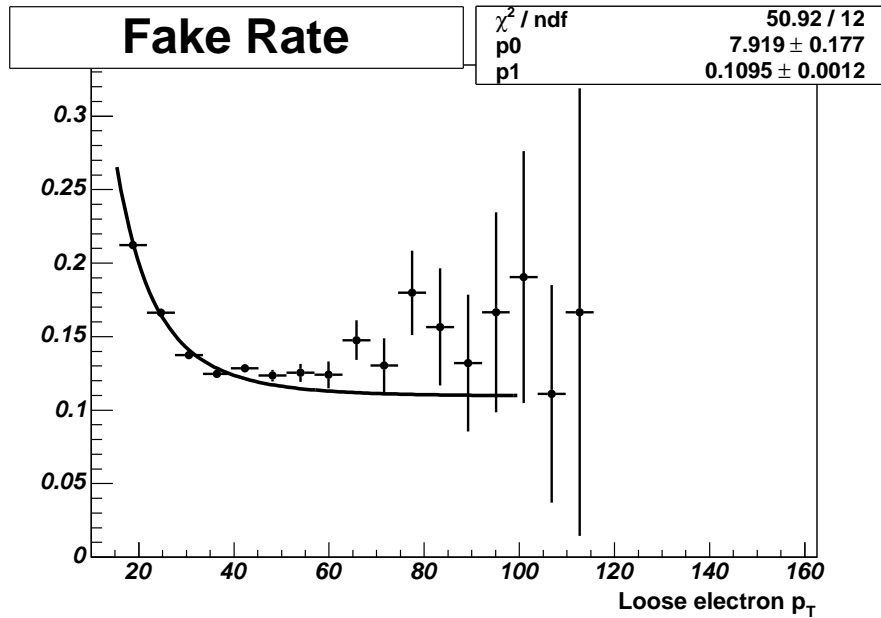


Figure 6.5: Electron fake rate versus p_T estimated in EM1TRK data. The function used for the fit is $f(p_T(e)) = p_0 \exp(-\sqrt{x}) + p_1$.

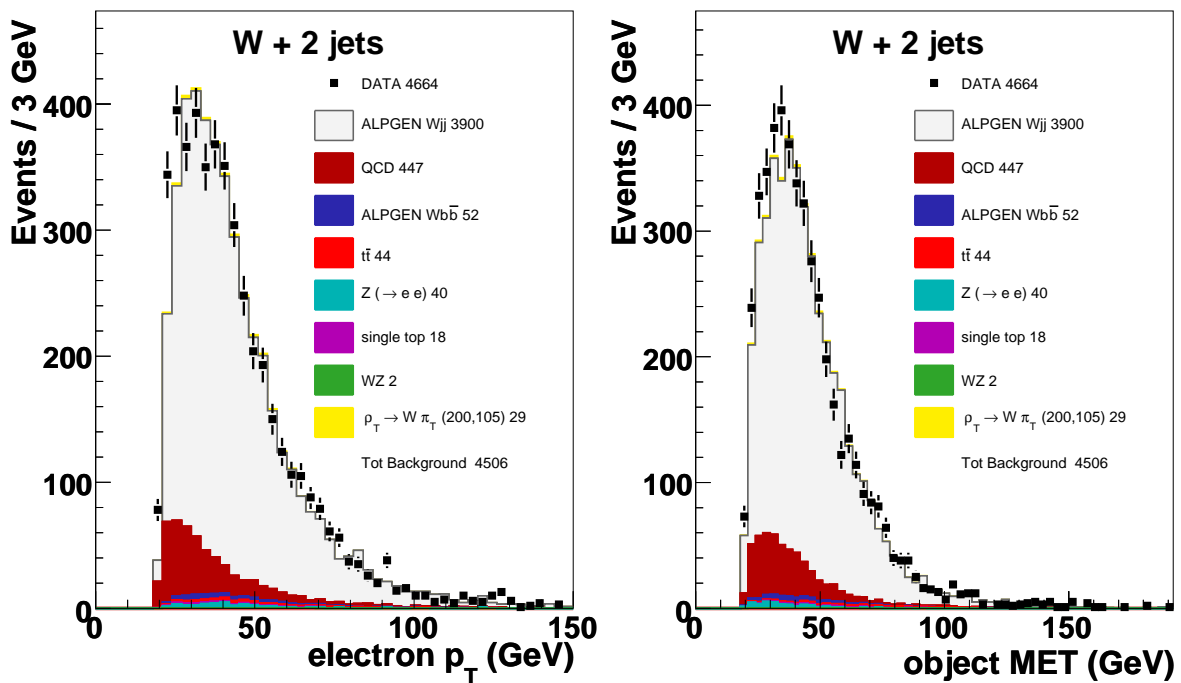


Figure 6.6: Distributions for electron p_T (left) and object missing energy (right), after $W + 2$ jets selection.

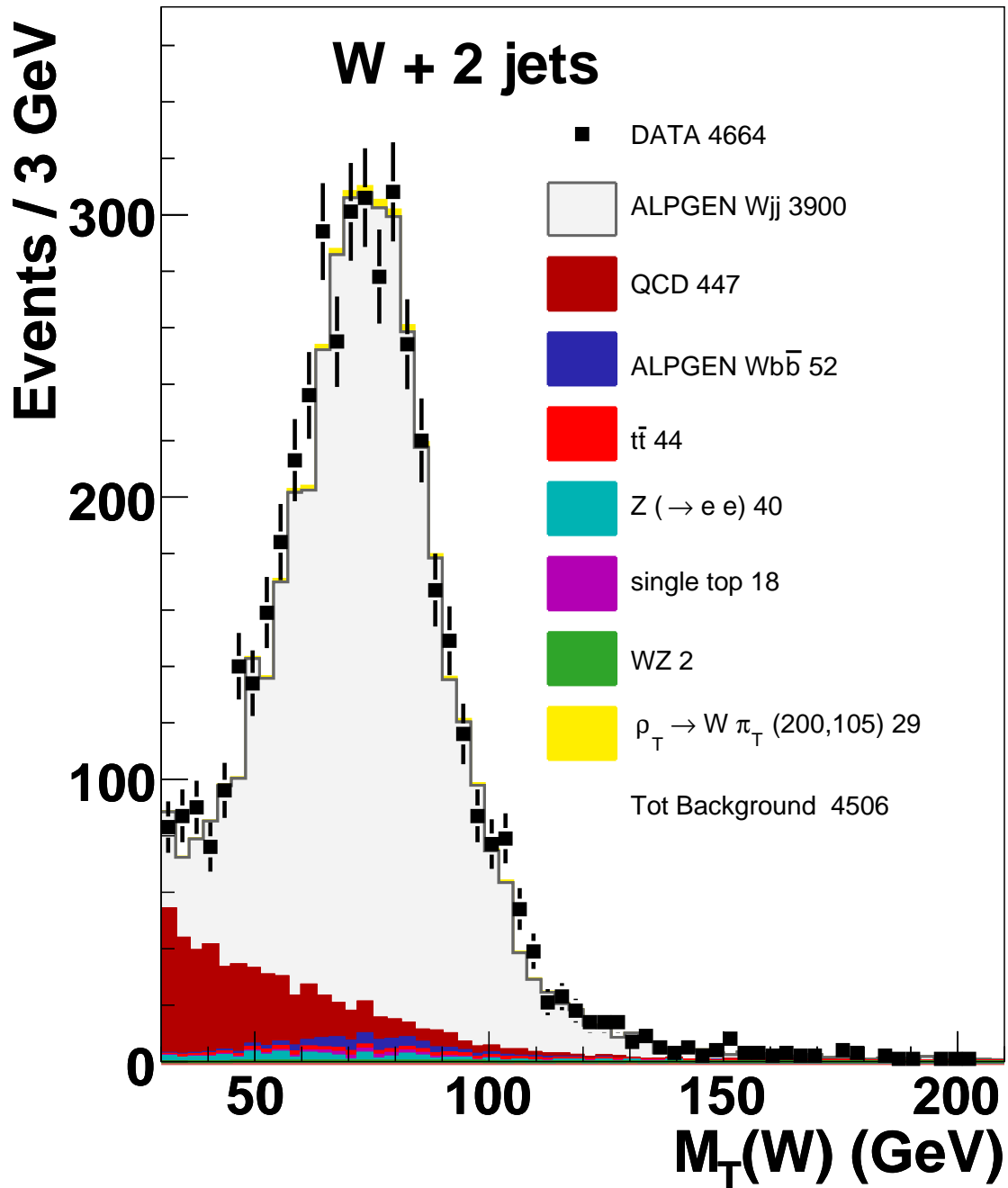


Figure 6.7: Distribution for W boson transverse mass after $W + 2$ jets selection. Object missing energy is used in order to compute $M_T(W)$.

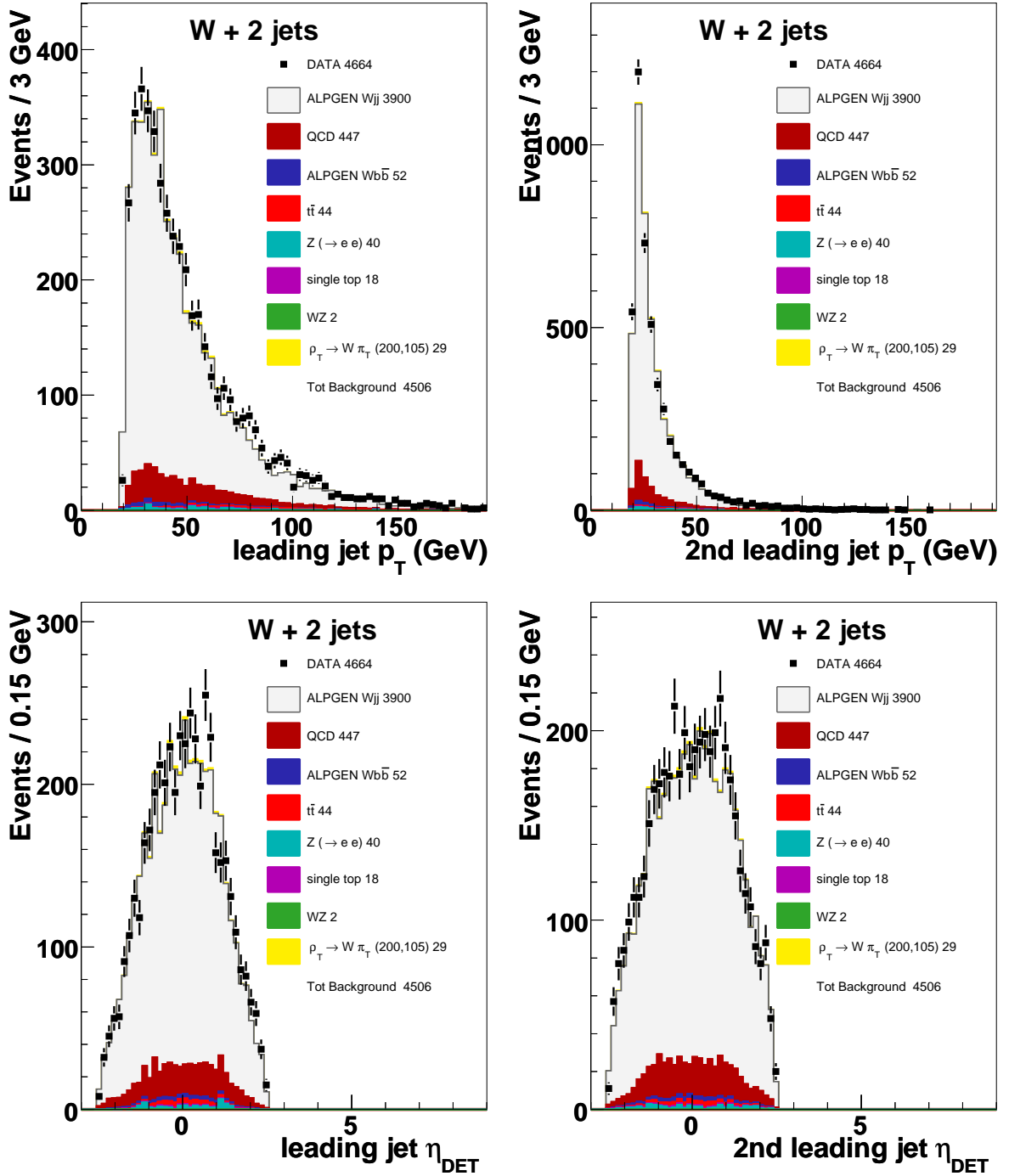


Figure 6.8: Distributions for first and second leading jet p_T (top row), and detector η (bottom row) after $W + 2$ jets selection.

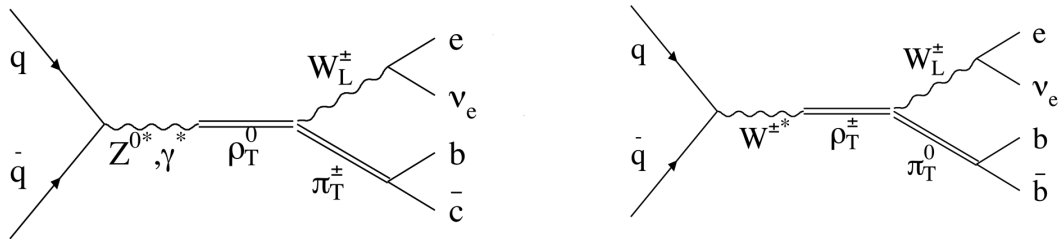
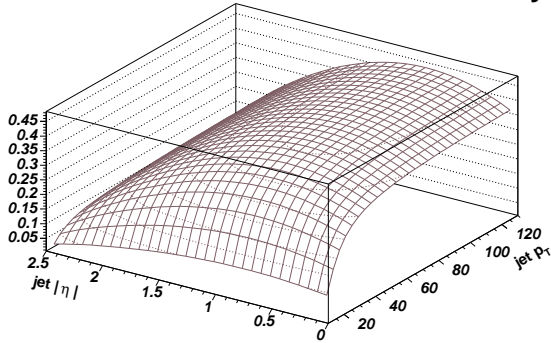
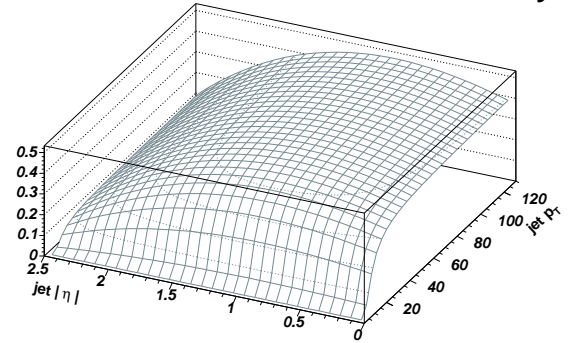


Figure 6.9: Feynman Diagram for the technipion production and decay.

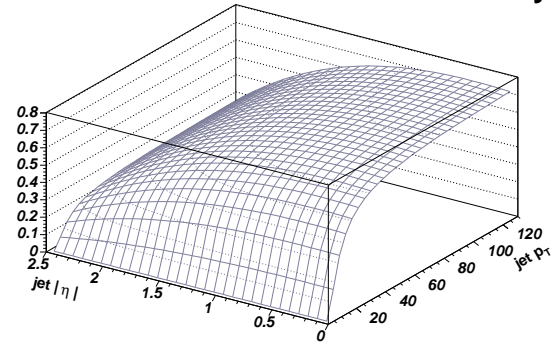
SVT TIGHT DATA Inclusive Efficiency



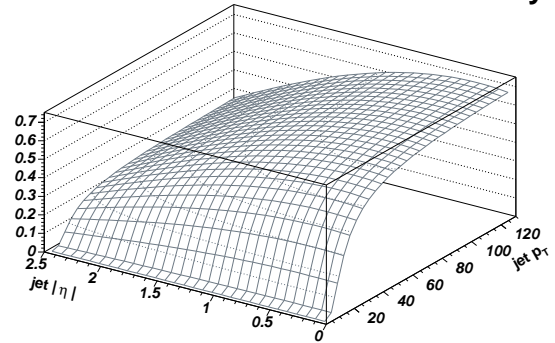
SVT TIGHT Muon Jets DATA Efficiency



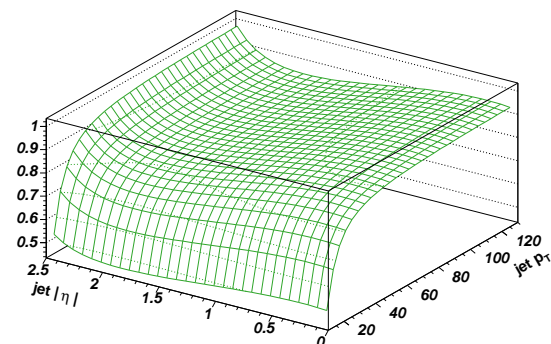
SVT TIGHT Muon Jets MC b-Efficiency



SVT TIGHT Inclusive MC b-Efficiency



SVT TIGHT Inclusive / Muon Jets Scale Factor



SVT TIGHT Inclusive MC c-Efficiency

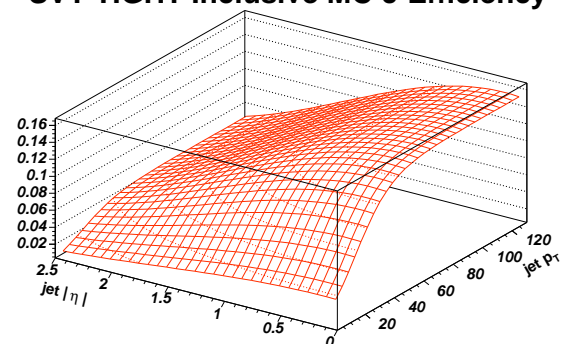


Figure 6.10: b -tagging efficiency two-dimensional parametrization (top left) comes from the data derived Muon Jets efficiency times a Monte Carlo derived scale factor (bottom left) which takes into account the different efficiency in pure Muon Jet sample (center left) with respect to the inclusive sample (center right). The bottom right plot shows the Monte Carlo c -tagging needed to derived the c -tagging efficiency parameterization.

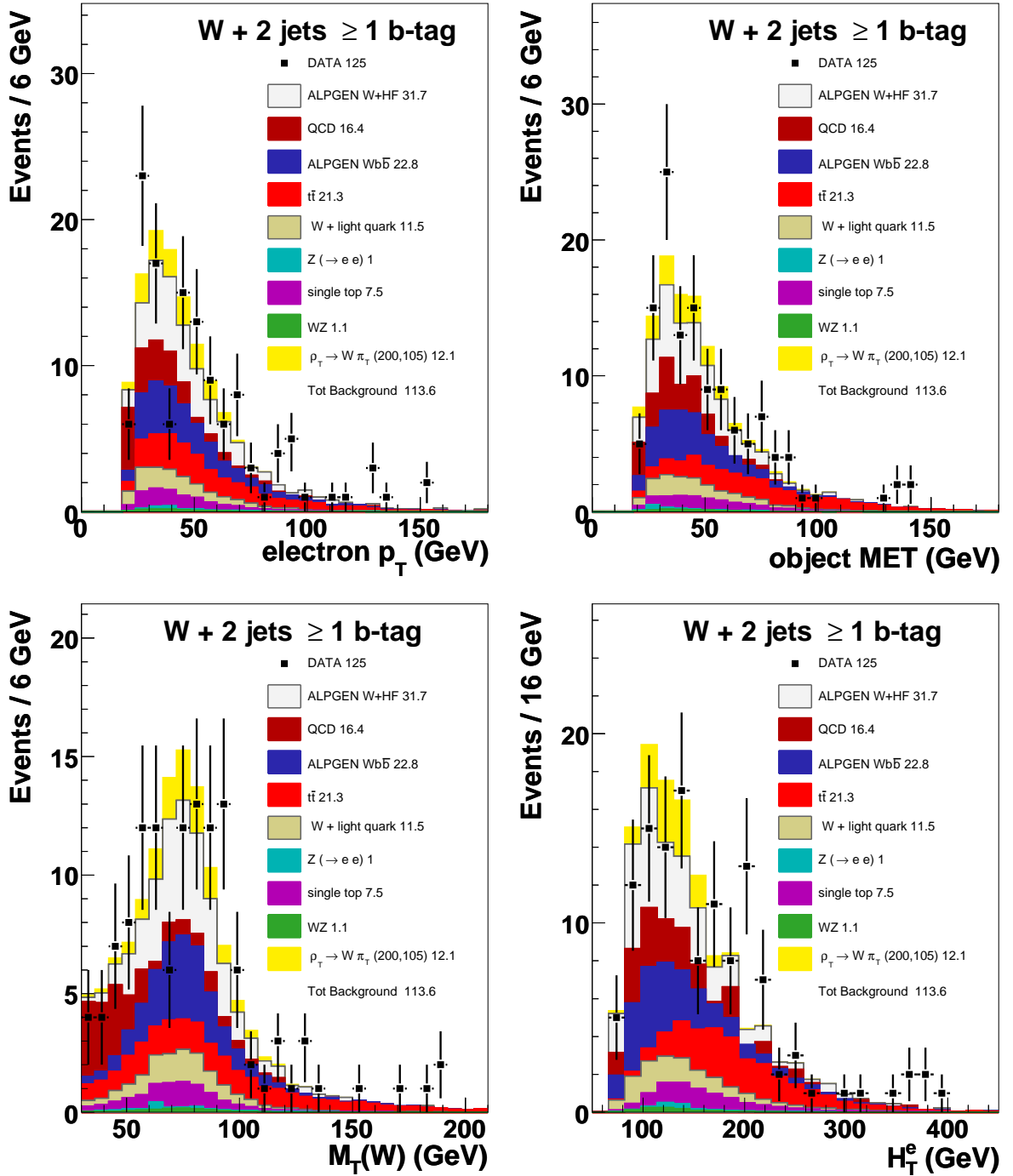


Figure 6.11: Distributions for electron p_T , object missing energy (top row), W boson transverse mass and H_T^e (bottom row) after $W + 2 jets \geq 1b$ - tag selection. The yellow histogram represents $W\pi_T$ for $M(\rho_T) = 200$ GeV, $M(\pi_T) = 105$ GeV and $M_V = 100$ GeV. Object missing energy is used in order to compute $M_T(W)$ and H_T^e .

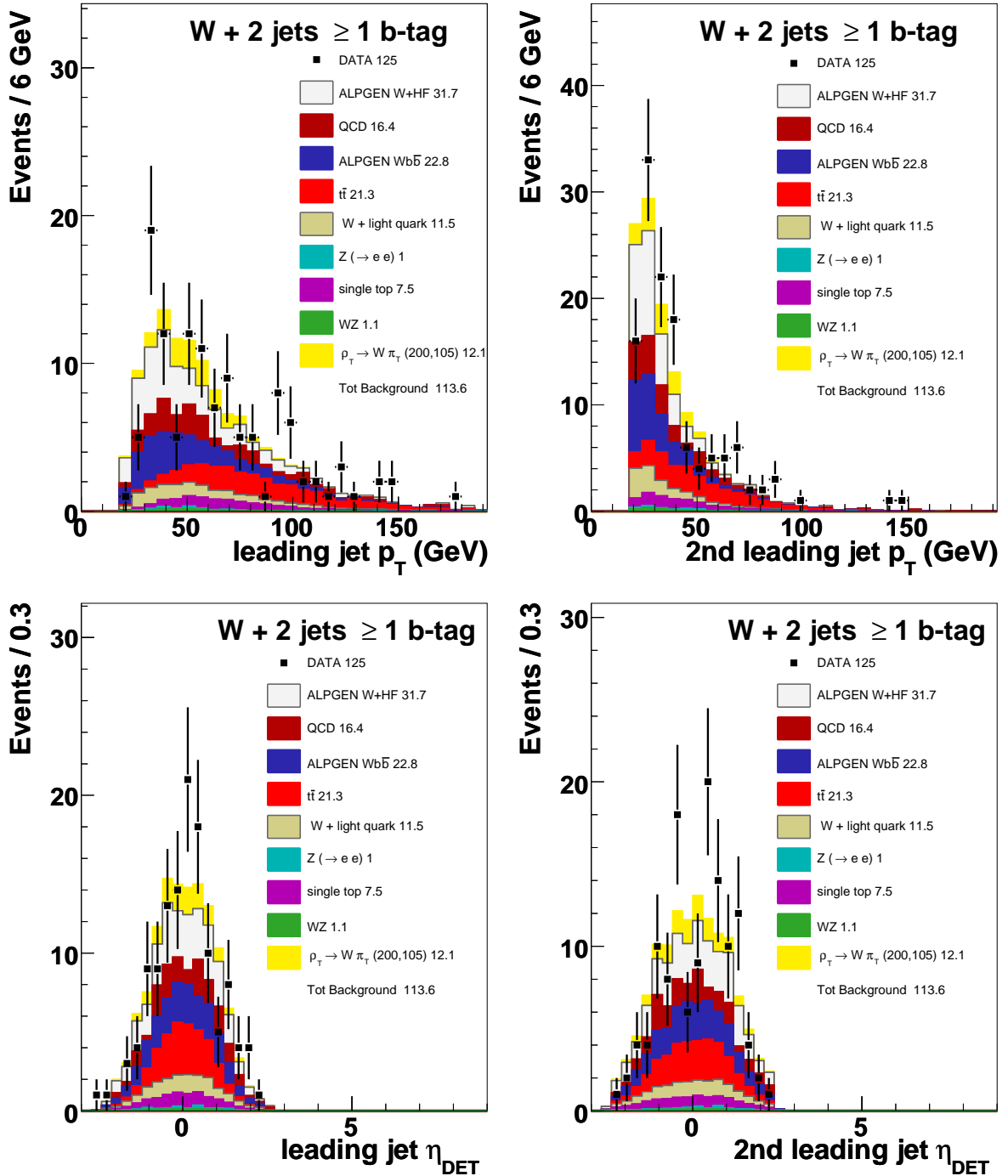


Figure 6.12: Distributions for first and second leading jet p_T (top row), and detector η (bottom row) after $W + 2 jets \geq 1b\text{-tag}$ selection. The yellow histogram represents $W\pi_T$ for $M(\rho_T) = 200$ GeV, $M(\pi_T) = 105$ GeV and $M_V = 100$ GeV.

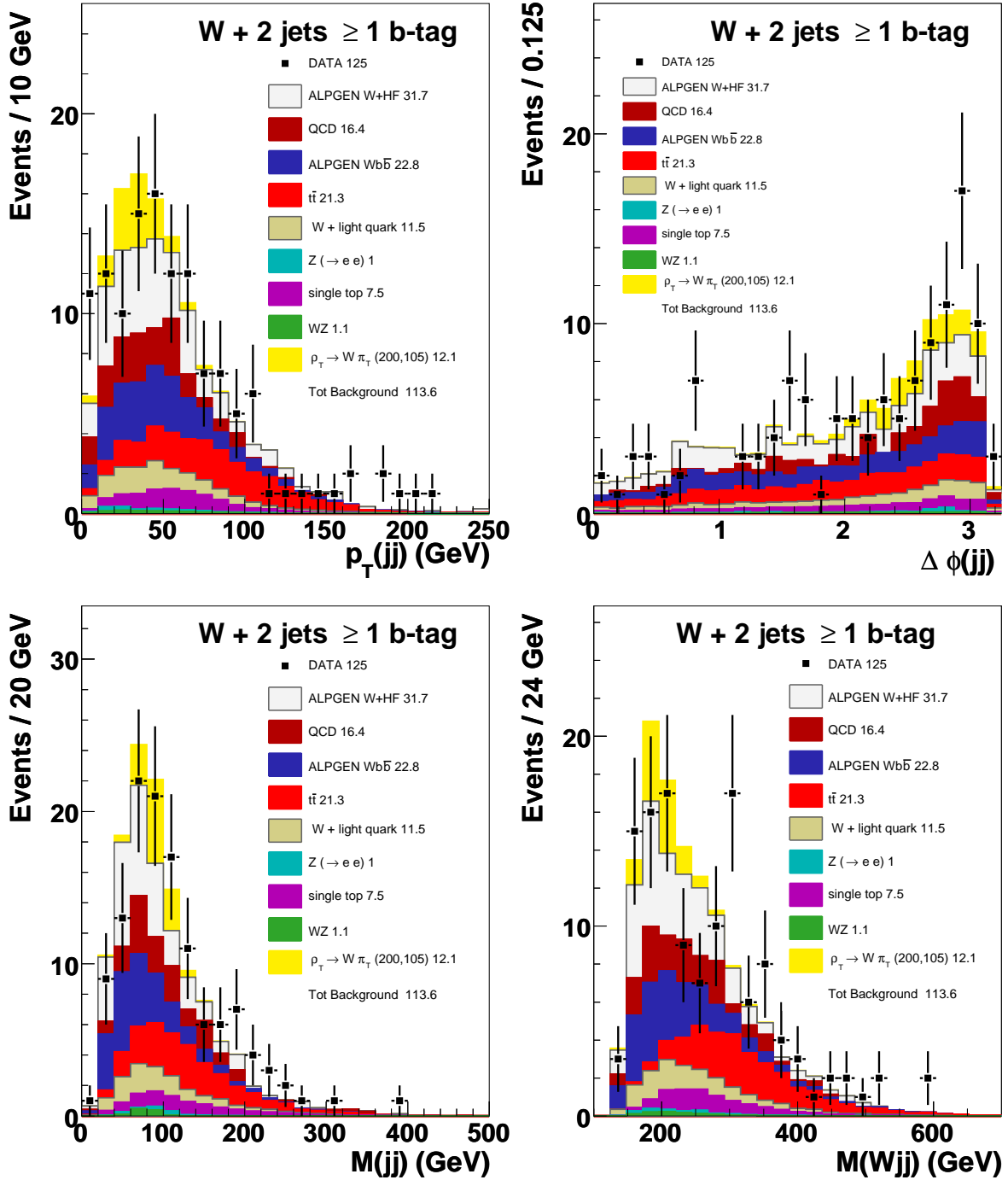


Figure 6.13: Distributions for p_T and $\Delta\phi$ of the dijet system (top row), dijet and W plus dijet invariant mass (bottom row) after $W + 2$ jets $\geq 1b$ -tag selection. The yellow histogram represents $W\pi_T$ for $M(\rho_T) = 200$ GeV, $M(\pi_T) = 105$ GeV and $M_V = 100$ GeV. Object missing energy is used in order to compute $M(Wjj)$.

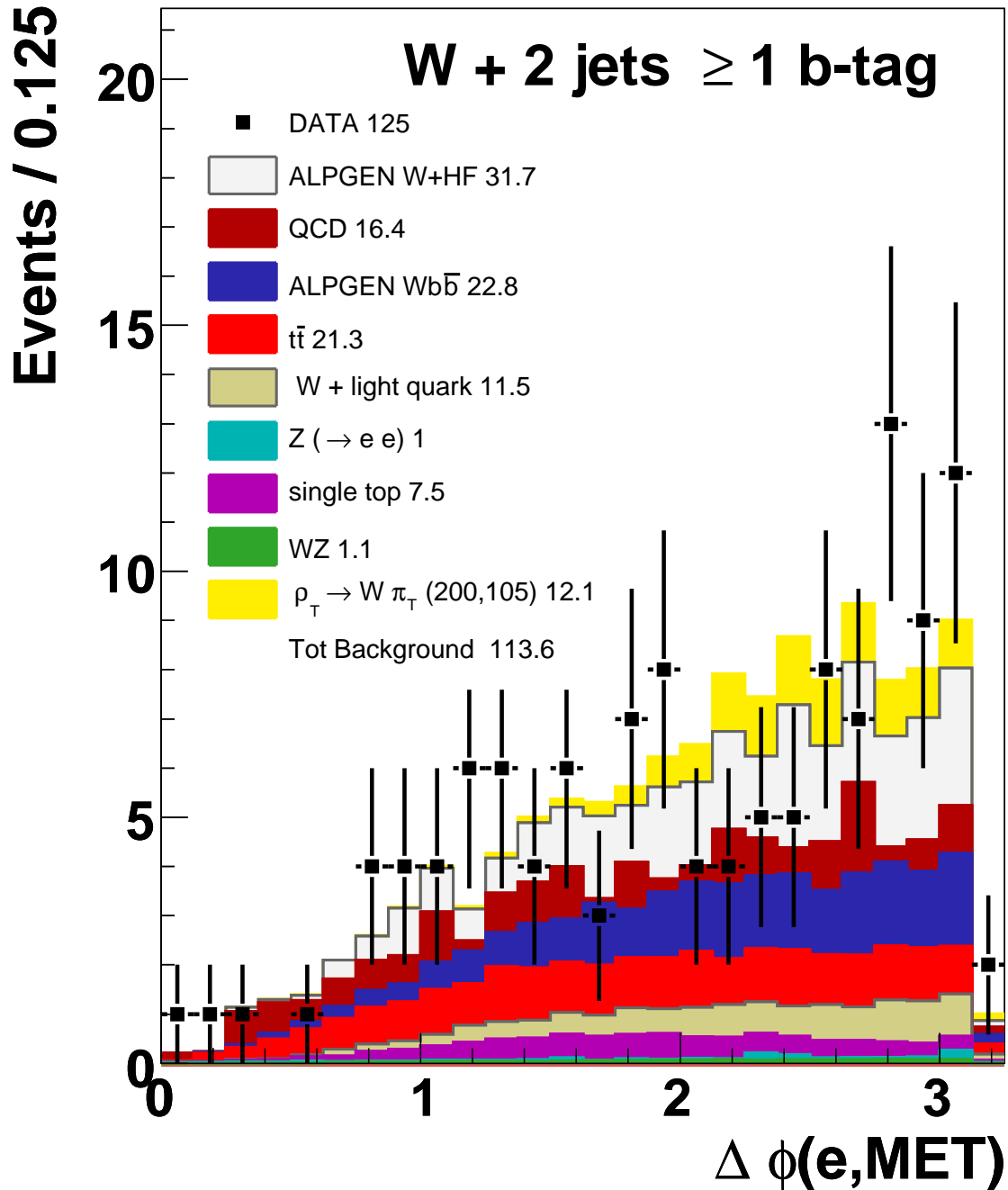


Figure 6.14: Distributions for $\Delta\phi$ between the electron and the object missing transverse momentum direction, after $W + 2 \text{ jets} \geq 1b\text{-tag}$ selection. The yellow histogram represents $W\pi_T$ for $M(\rho_T) = 200$ GeV, $M(\pi_T) = 105$ GeV and $M_V = 100$ GeV.

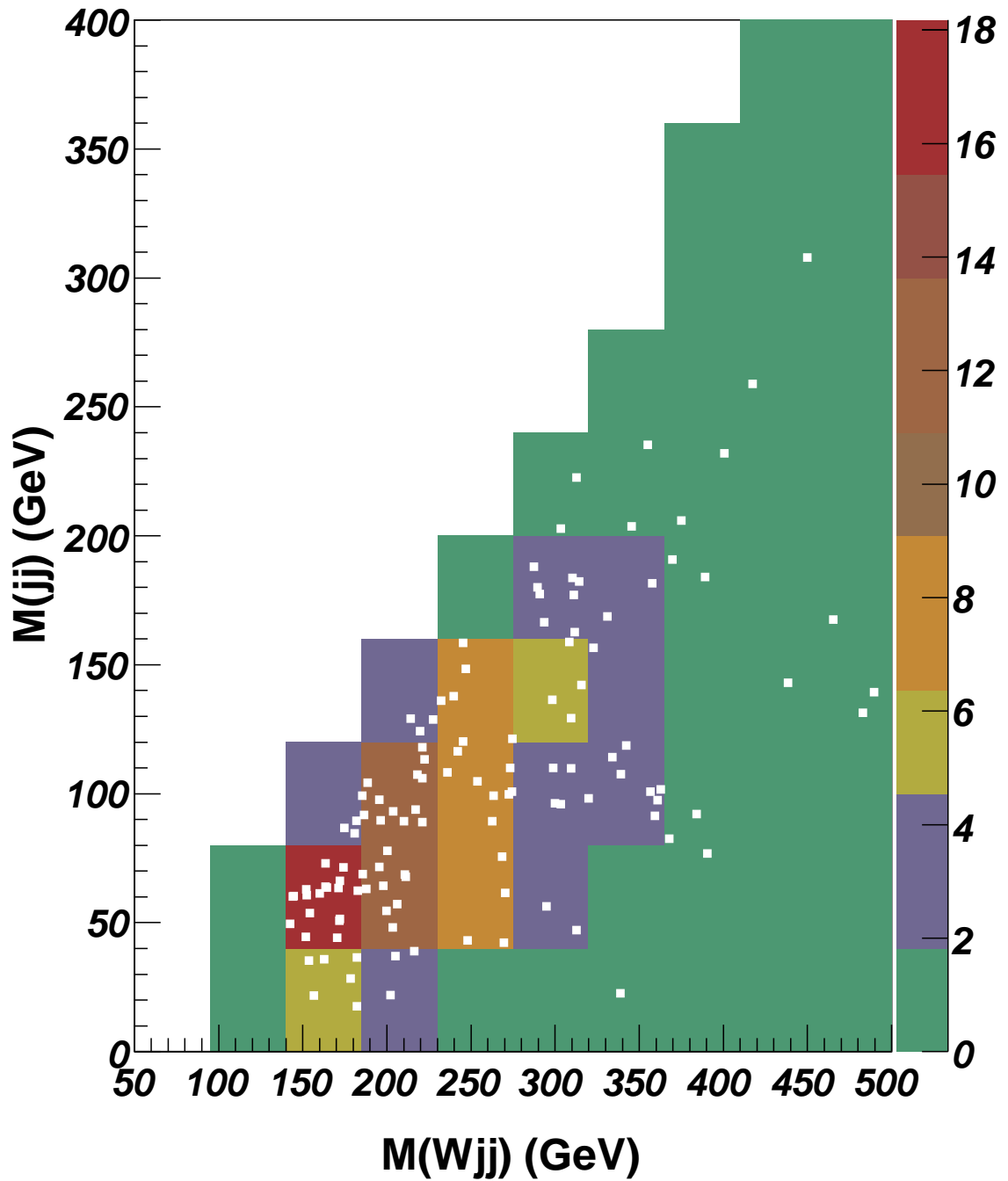


Figure 6.15: Distributions for $M(jj)$ versus $M(Wjj)$. The colored 2D histogram represents the expected SM background, white squares represent data after $W + 2 \text{ jets} \geq 1b\text{-tag}$ selection.

Chapter 7

Calibration of Parametrized Monte Carlo

As discussed in Section 4.7, PMCS does not directly simulate the interaction between the detector material and the particles produced in the $p\bar{p}$ collision; PMCS simulation consists on applying pre-determined parameterized detector acceptances and resolution curves to the particles generated by PYTHIA or other Monte Carlo generators. By doing so, PMCS allows a much faster event simulation when compared to the full detector simulation (DØGeant). The goal of this section is to show how the calibration for $W\pi_T$ events is determined from DØGeant, and the level of agreement reached between DØGeant and PMCS at the end of this procedure.

For the purpose of calibrating and comparing the two simulations, three samples, with different mass values of charged and neutral ρ_T and π_T , have been processed with DØGeant and PMCS. Looking at exactly same set of events ensures that eventual differences are due to differences in simulation responses.

Mass values for ρ_T and π_T used for this study are shown in Table 7.1.

$M(\rho_T)$ (GeV)	$M(\pi_T)$ (GeV)
210	110
190	100
200	105

Table 7.1: Mass points generated with full detector simulation and used for PMCS calibration.

7.1 Electron Calibration

For all mass points, events with one reconstructed central electron and two jets are selected in the DØGeant sample, as discussed in Section 6.4. The reconstruction efficiency is derived by looking at how many generated electrons are matched to a reconstructed EM cluster within a ΔR cone of 0.1. Because of the boundaries of the calorimeter cells, reconstruction inefficiencies can be geometrically localized in the azimuthal ϕ direction. For convenience a local variable, ϕ_{loc} is introduced:

$$\phi_{loc} = MOD(\phi, \pi/16) - \pi/32. \quad (7.1)$$

Figure 7.1 shows the efficiency of the electron reconstruction as a function of ϕ_{loc} , notice the loss in efficiency in the proximity of the detector cell boundaries at $1 < |\phi_{loc}| < 0.8$. Therefore the efficiency for reconstructing central electron is chosen to be parameterized as function of the “local ϕ ” and then applied back to generated electrons in PMCS.

7.1.1 Electron Resolution

Tight electrons are used in order to estimate the resolution and offset of the energy measurement. Electrons are binned according to their generated energy, for each bin the resolution defined as the difference between the generated and the reconstructed energy is fitted with a Gaussian function as shown in Figure 7.2.

For all energy bins σ/E_{GEN} is computed, where σ is the width of the fitted Gaussian

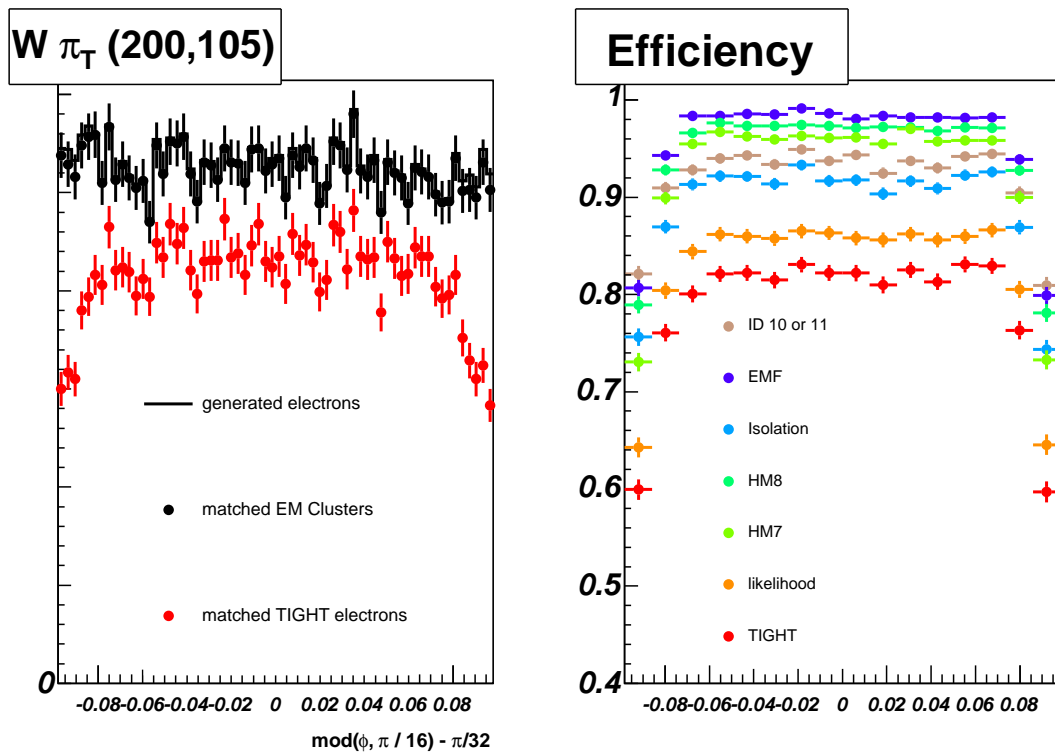
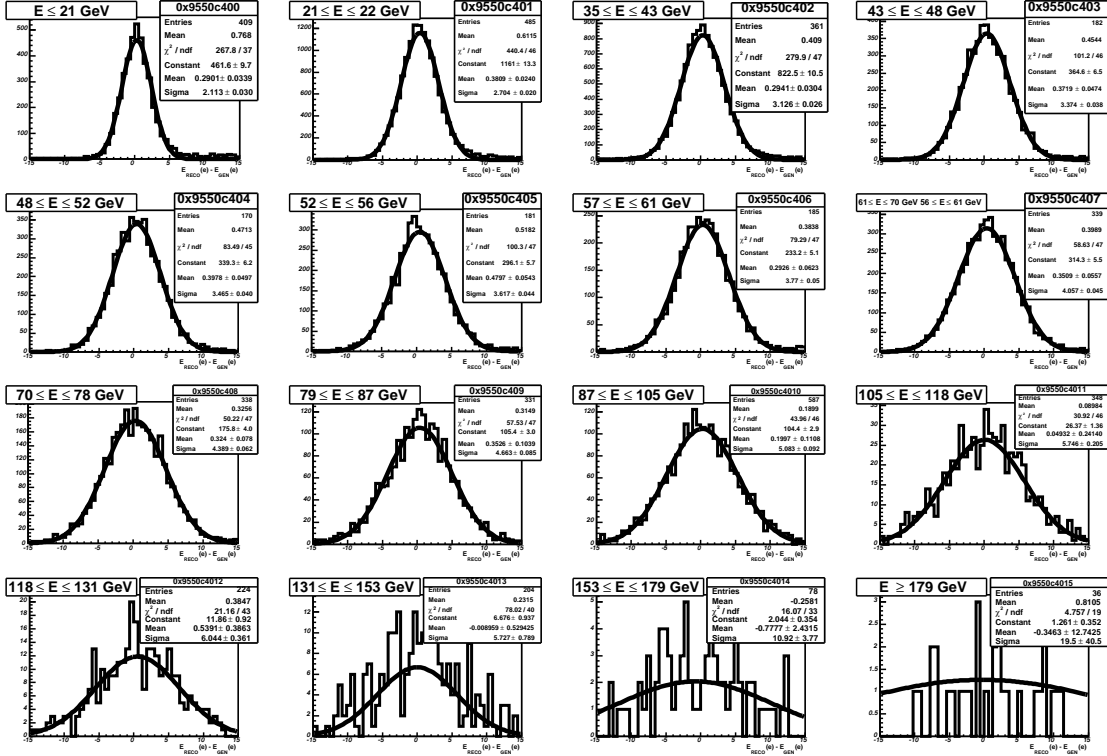


Figure 7.1: Efficiency versus ϕ_{loc} for the mass point (200,105). Right plot: black solid histograms represents ϕ_{loc} for the generated electrons, overlaid with the ϕ_{loc} distributions for the generated electrons matched to a reconstructed EM cluster (black circles). In the same plot the red dots represent the generated electrons matched to a TIGHT electron. Left plot: Efficiency for a generated electron to pass several quality cuts as function of ϕ_{loc} .



and E_{GEN} is the mean of the electron generated energy for each energy interval; the result is plotted in Figure 7.3. σ/E_{GEN} is then fitted with a resolution function $Res(e)$ defined as:

$$Res(e) = \sqrt{C^2 + \frac{S^2}{E_{GEN}} + \frac{N^2}{E_{GEN}^2}}. \quad (7.2)$$

N is called “noise” term, S is the “sampling” term, and C the “constant term”.

The p_T distributions for event with one electron in fast Monte Carlo and PMCS, after the ϕ_{loc} -dependent efficiency and smearing are applied to PMCS, are shown in Figure 7.4. The agreement in acceptance are shown in Table 7.2.

7.2 Jet Calibration

In DØGeant the jet reconstruction algorithm input GeV consists of the simulation of the interaction between the generated particles and the calorimeter material. This involves

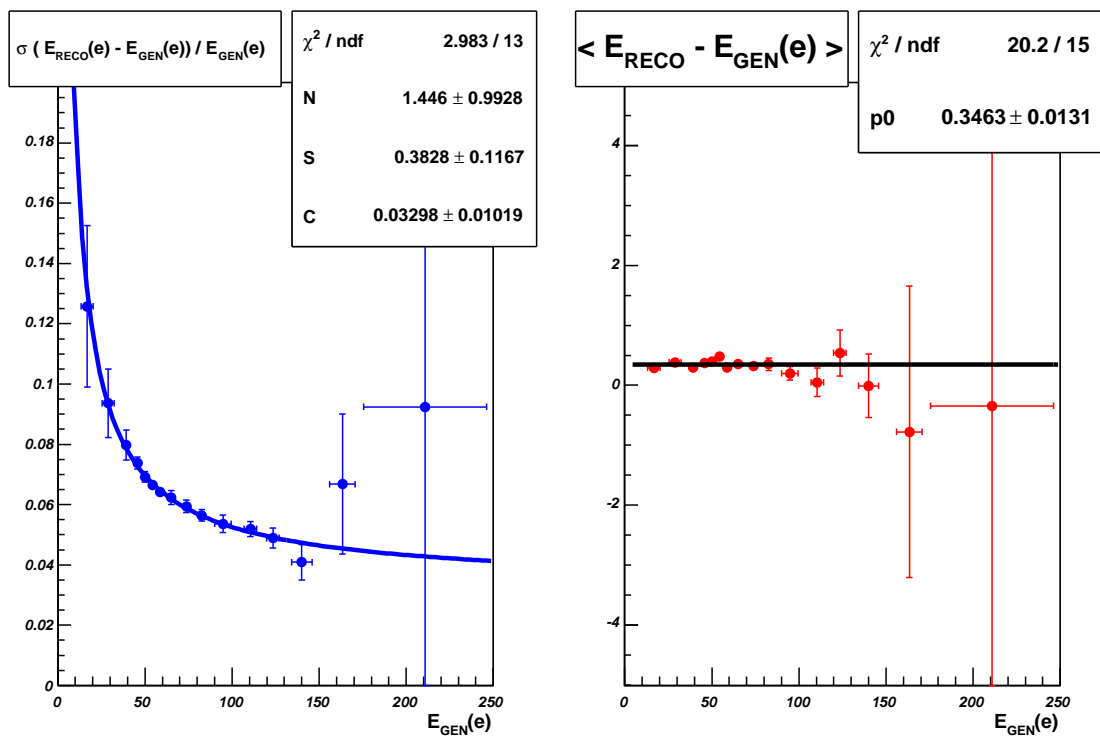


Figure 7.3: Electron Resolution (left) and Offset (right) estimated from fully simulated events.

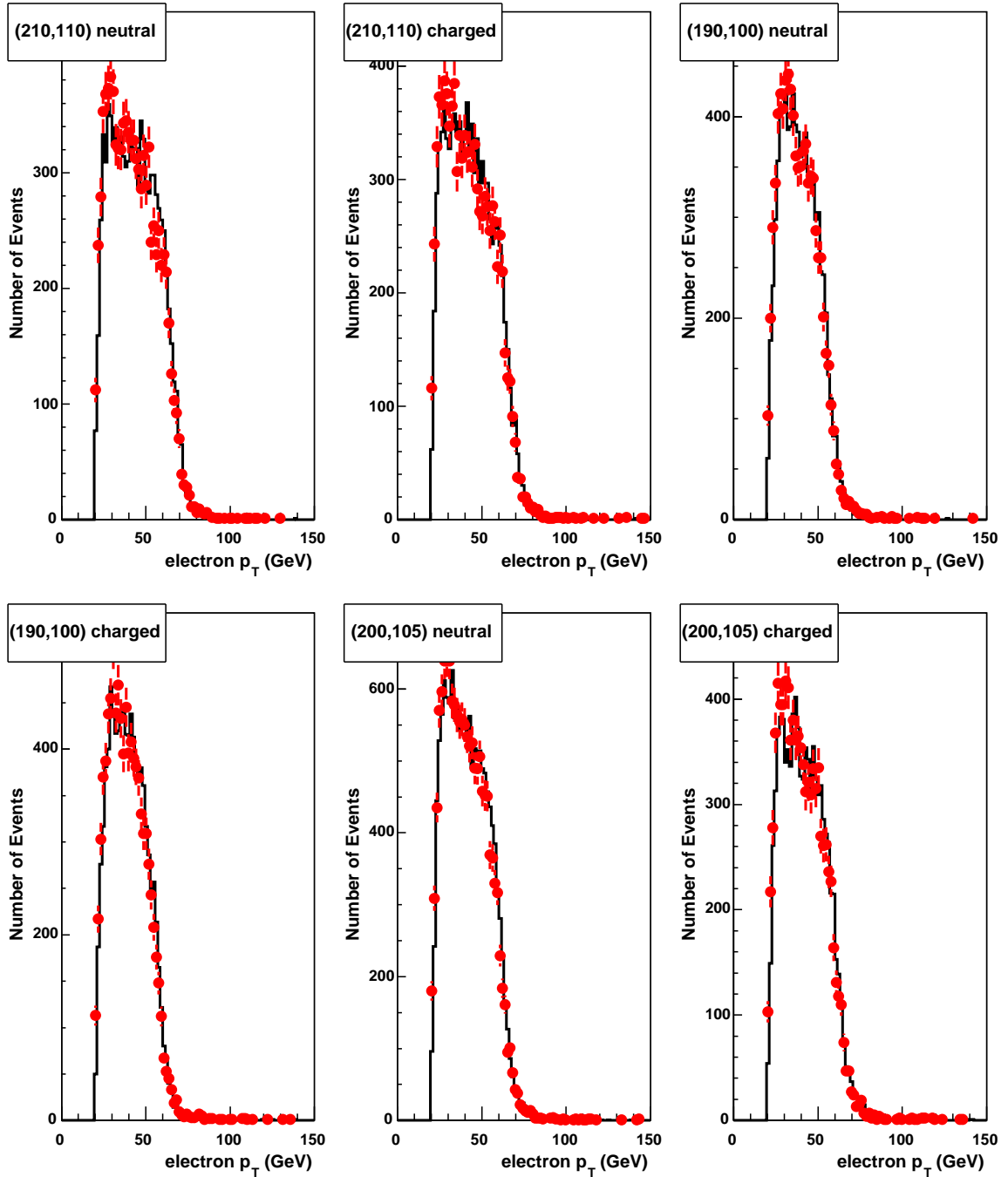


Figure 7.4: Selected events with one reconstructed electron, distributions of the electron transverse momentum for DØGeant (black histogram) and PMCS (red dots).

$(M(\rho_T), M(\pi_T))$ (GeV)	electron		
	DØGeant	PMCS	r
(210,110) neutral	0.373	0.373	1.00
(210,110) charged	0.380	0.380	1.00
(190,100) neutral	0.336	0.339	0.99
(190,100) charged	0.374	0.373	1.00
(200,105) neutral	0.444	0.442	1.00
(200,105) charged	0.438	0.442	0.99

Table 7.2: Acceptance for all tuning mass points after requesting one central electron to be present in the event in both PMCS and DØGeant; r is the ratio of the acceptances in DØGeant and PMCS.

the simulation of particle energy deposition in the calorimeter and indirectly leads to reproducing both the detector geometric acceptance and the calorimeter energy resolution. PMCS starts with only information about hadrons originated during the fragmentation of the quarks produced in the $p\bar{p}$ interaction. From these hadrons “particle jets” are formed. The same jet finding algorithm is used as for calorimeter jets. PMCS categorizes jets in five different regions depending on their η_{DET} . For each category it smears the particle jet energy with a resolution function with different sampling, noise and constant terms [78] (Table 7.3). It also has the capability of adjusting the slope and offset for the reconstructed energy scale, which are set to 1 and 0 in the PMCS version used for this analysis.

	$\eta \leq 0.5$	$0.5 \leq \eta \leq 1.0$	$1.0 \leq \eta \leq 1.5$	$1.5 \leq \eta \leq 2.0$	$\eta \geq 2.0$
noise	3.0	2.6	0.	4.9	4.5
sampling	0.942	1.1	1.2	0.001	0.001
constant	0.057	0.059	0.085	0.091	0.045
offset	0.	0.	0.	0.	0.
slope	1.	1.	1.	1.	1.

Table 7.3: Resolution parameters for the PMCS jet categories.

The agreement between the acceptances in PMCS and DØGeant after requesting one electron and 2 jets with $p_T > 20$ GeV and $|\eta_{DET}| < 2.5$ is shown in Table 7.4, p_T distributions for the two jets are shown in Figures 7.5 and 7.6.

$(M(\rho_T), M(\pi_T))$ (GeV)	electron and 2 jets		
	DØGeant	PMCS	r
(210,110) neutral	0.190	0.188	1.01
(210,110) charged	0.205	0.203	1.01
(190,100) neutral	0.162	0.162	1.00
(190,100) charged	0.188	0.188	1.00
(200,105) neutral	0.225	0.221	1.02
(200,105) charged	0.225	0.194	0.97

Table 7.4: Acceptance for all tuning mass points after requesting one central electron and two jets to be present in the event in both PMCS and DØGeant; r is the ratio of the acceptances in DØGeant and PMCS.

The flavor content of the first and second leading jet is the same, as shown in Figure 7.7. This is an important check in order to ensure the same performances in the two simulation when the data-derived b -tagging efficiencies are applied.

7.3 Object Missing Energy

In general the unbalance of the momentum in the event is the signature for neutrino production. The missing transverse energy is a quantity that can be detected with the DØ detector. In order to compute it RECO not only makes use of the sum of the momentum of electrons and jets in the event but also uses unclustered calorimeter energy. This is fully simulated in DØGeant but not in PMCS where there is no simulation for the energy deposition. For this reason MET_{obj} as defined in Equations 6.3 and 6.5 is introduced: MET_{obj} makes use of the agreement reached between PMCS and (DØGeant) to reproduce electron and jet momentum distributions and propagate this agreement to the missing energy. MET_{obj} distribution for events with two jets and one electron in both simulations is shown in Figure 7.8. The agreement after cutting on:

1. $MET_{obj} > 20$ GeV;
2. W transverse mass calculated with MET_{obj} , $M_T(W) > 30$ GeV;

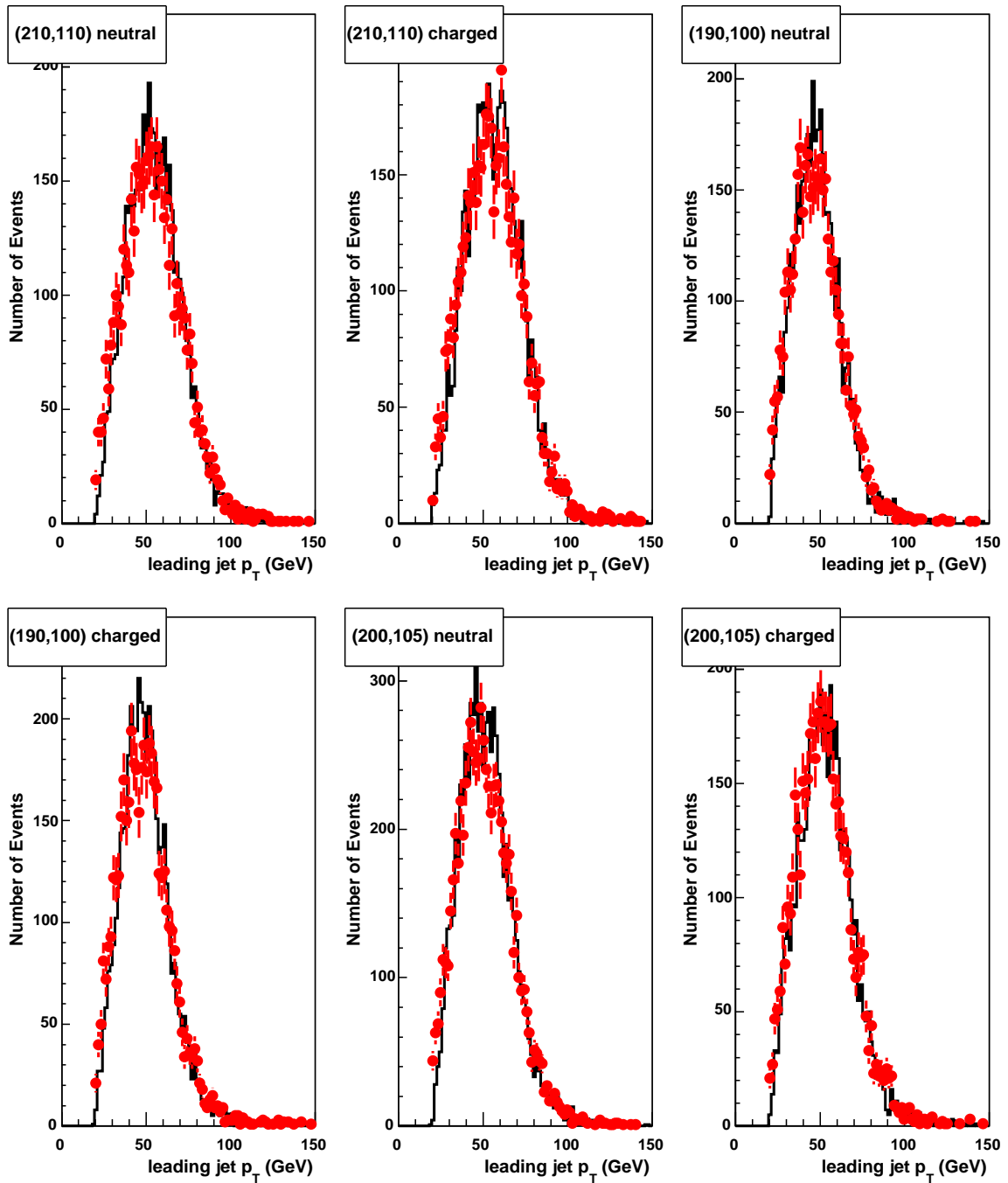


Figure 7.5: Selected events with one reconstructed electron and two jets, distributions of the transverse momentum for the leading jet DØGeant (black histogram) and PMCS (red dots).

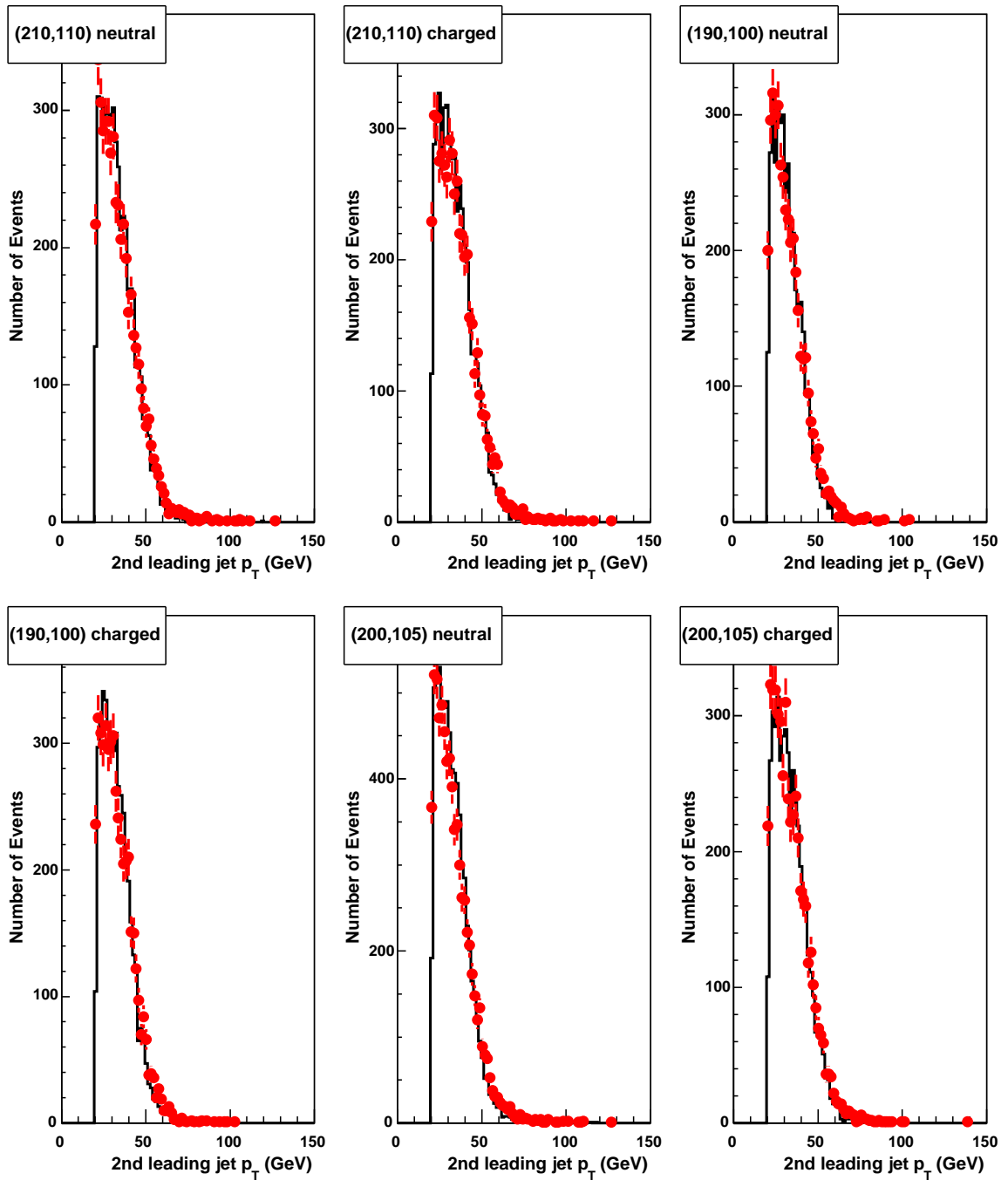


Figure 7.6: Selected events with one reconstructed electron and two jets, distributions of the transverse momentum for the second leading jet DØGeant (black histogram) and PMCS (red dots).

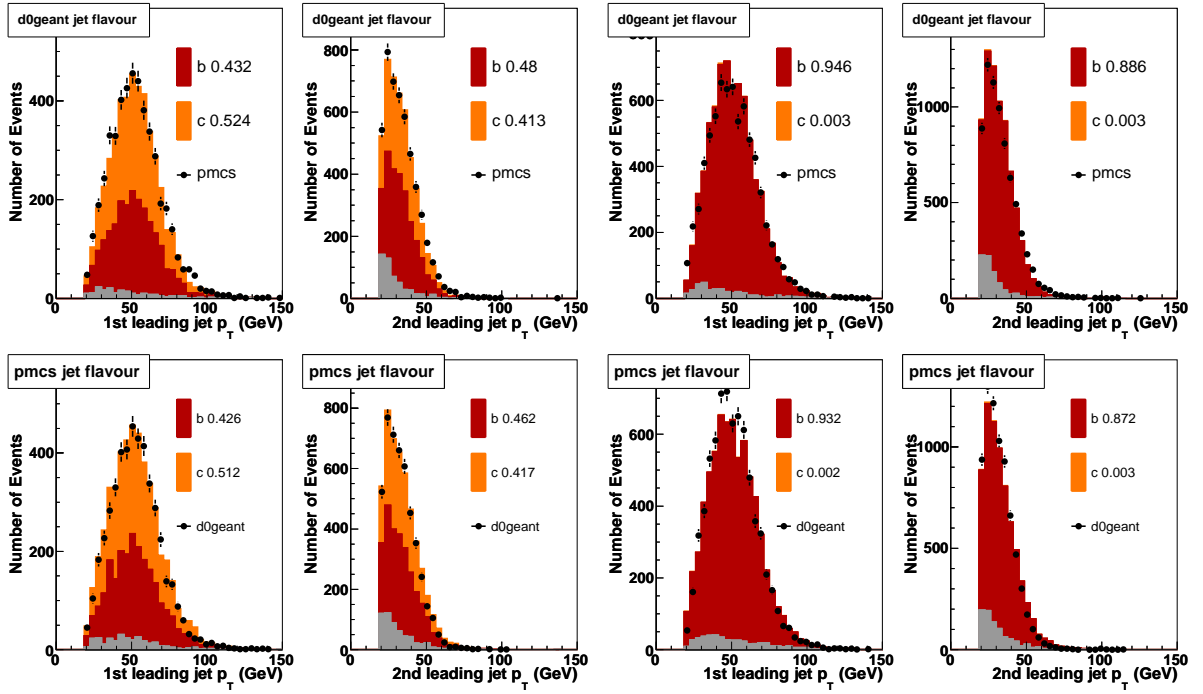


Figure 7.7: Flavour content for jet in events with two jets and one electron for the mass point (200,105) in both charged (left) and neutral state (right). In the upper (lower) plots the first and second leading jet for D0Geant (PMCS) are the solid histogram, red is the b -content, yellow the c -content and grey the $light$ -content. Black dots represent PMCS (D0Geant).

3. at least one jet b -tagged.

is shown in Tables 7.5, 7.6 and 7.7.

7.4 $W\pi_T$ Search Optimization

In order to enhance the sensitivity for Technicolor signal over the background several cuts on kinematic quantities are performed. To identify the region of maximum sensitivity for each quantity, the ratio of the signal, S , and the square root of the background $S/\sqrt{B}(t)$ is plotted as a function of the cut value t . The value t_{max} where $S/\sqrt{B}(t)$ reaches a maximum indicates where the cut is applied. All kinematic quantities have distributions which are heavily dependent on the mass of the generated technihadrons. Therefore, for all quantities t_{max} has a different value for different generated masses. In this section the optimization for the six mass points is performed with both PMCS and DØGeant.

After cutting on missing energy and requesting one b -tagged jet, distributions for H_T^e , $\Delta\phi(jj)$, $\Delta\phi(e, MET)$, $p_T(jj)$ and $M(jj)$ together with $M(Wjj)$ are shown in Figures 7.9, 7.10, 7.11, 7.12, 7.13, 7.14 and 7.15. For all these quantities a sensitivity region is estimated using $S/\sqrt{B}(t)$. A window cut is performed on the H_T^e variable, $S/\sqrt{B}(t)$ as function of a lower and upper cut is plotted in Figures 7.9 and 7.10. The signal distributions is also superimposed in the same figures. The background distribution used for optimization is plotted in Figure 6.11. The lower cuts on $\Delta\phi(jj)$ and $\Delta\phi(e, MET)$ are shown in Figures 7.11 and 7.12, the upper cut on $p_T(jj)$ in Figure 7.13. Finally the window cuts on $M(jj)$ and $M(Wjj)$ are shown in Figures 7.16, 7.17, 7.18 and 7.19 respectively.

7.4.1 Systematic Uncertainties

In order to estimate the systematic difference between PMCS and DØGeant a series of optimized cuts are applied separately to both simulated events. The agreement after

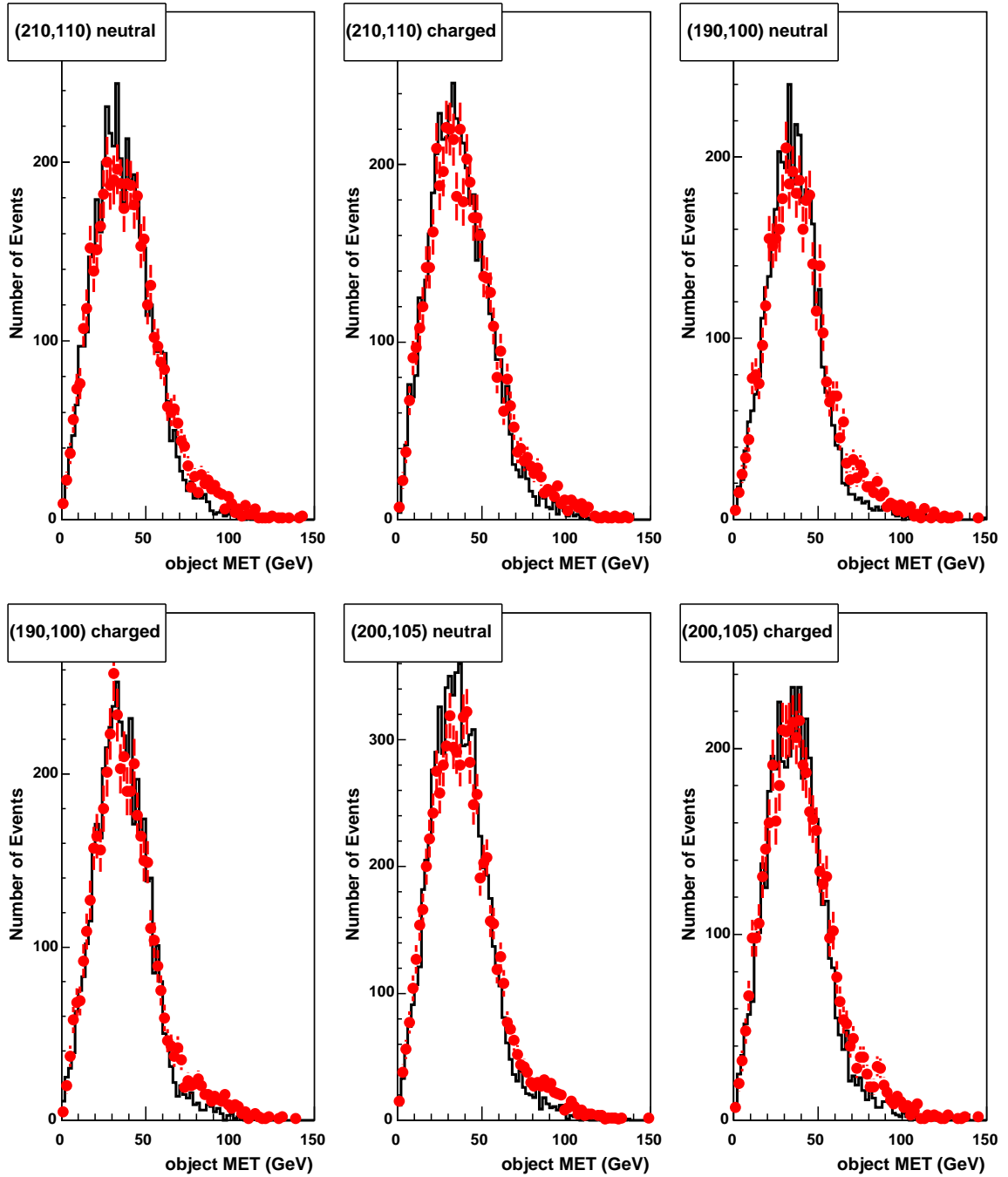


Figure 7.8: Selected events with one reconstructed electron and two jets, distributions of object missing transverse energy in DØGeant (black histogram) and PMCS (red dots).

each cut is shown in Table 7.8.

In the baseline present in Section 6.4, a cut on the calorimeter MET of 20 GeV is applied. While this quantity is available in full detector simulated events it is not available in PMCS. The effect of cutting on this quantity at the end of all other cuts is shown in Table 7.9. The average ratio between PMCS and DØGeant acceptances is 0.905. After folding this ratio in PMCS acceptances the average difference between PMCS and DØGeant is 5.4%, which is taken as the systematic uncertainty introduced by using fast simulated Monte Carlo instead of the full simulation.

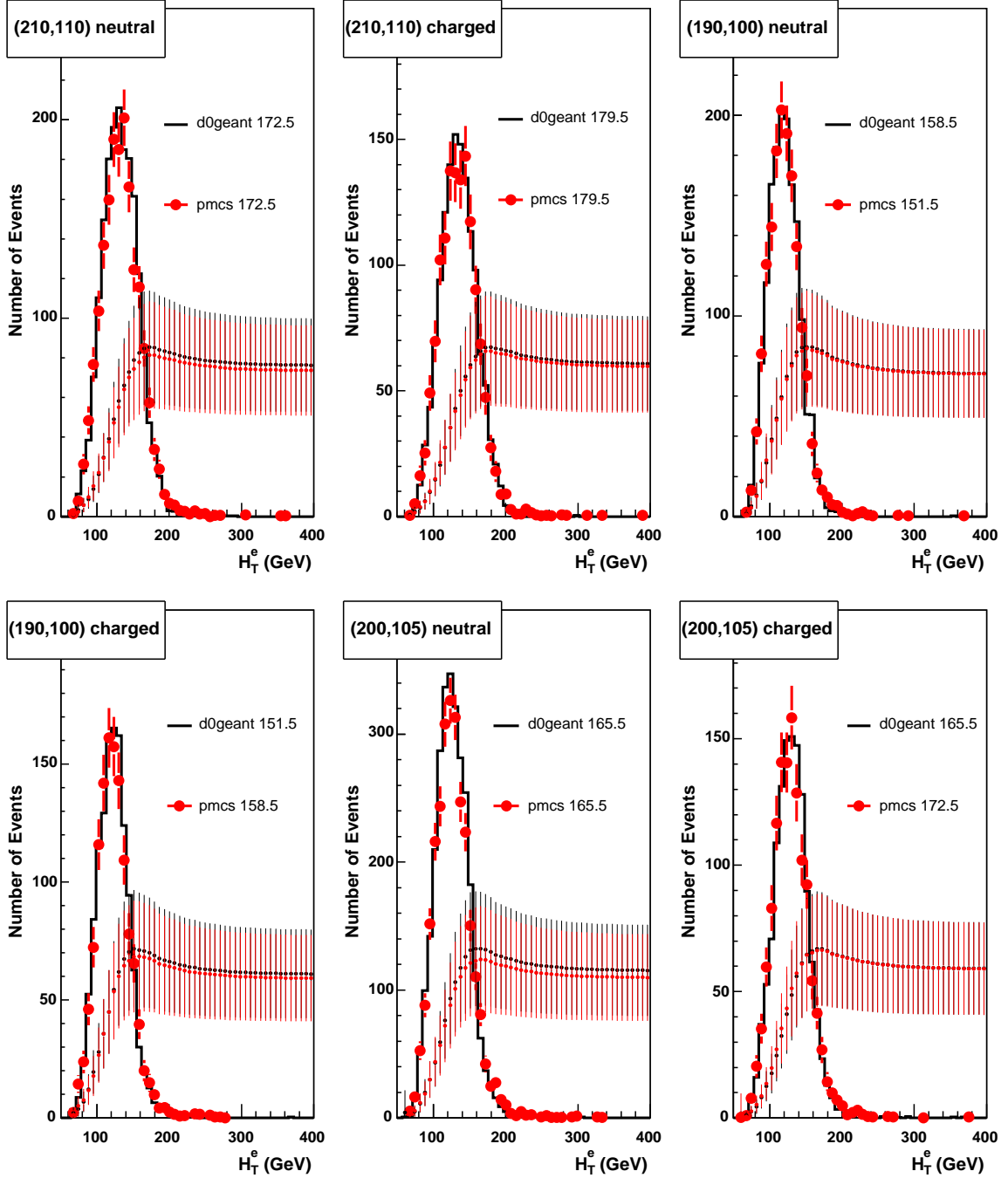


Figure 7.9: H_T^e distributions for events passing the cuts listed in Table 7.7, for DØGeant (solid black histogram), and PMCS (red dots) in arbitrary units. The same distributions are used together with the background in Figure 6.11 to calculate the upper cut on H_T^e maximizing S/\sqrt{B} for (shown in the superimposed curve for both simulations). Optimized cut values are shown in the legend.

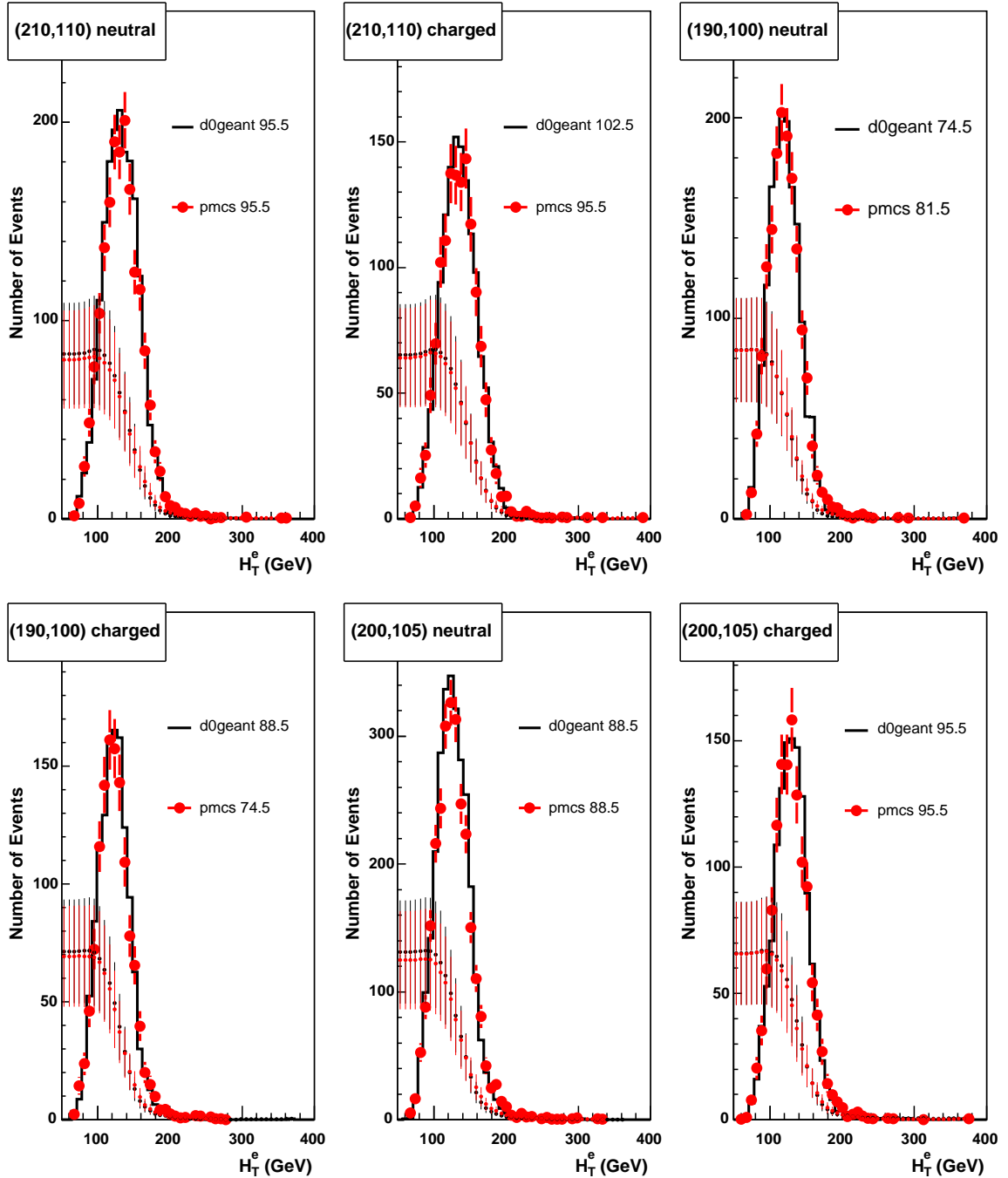


Figure 7.10: H_T^e distributions for events passing the cuts listed in Table 7.7, for DØGeant (solid black histogram), and PMCS (red dots) in arbitrary units. The same distributions are used together with the background in Figure 6.11 to calculate the lower cut on H_T^e maximizing S/\sqrt{B} for (shown in the superimposed curve for both simulations). Optimized cut values are shown in the legend.

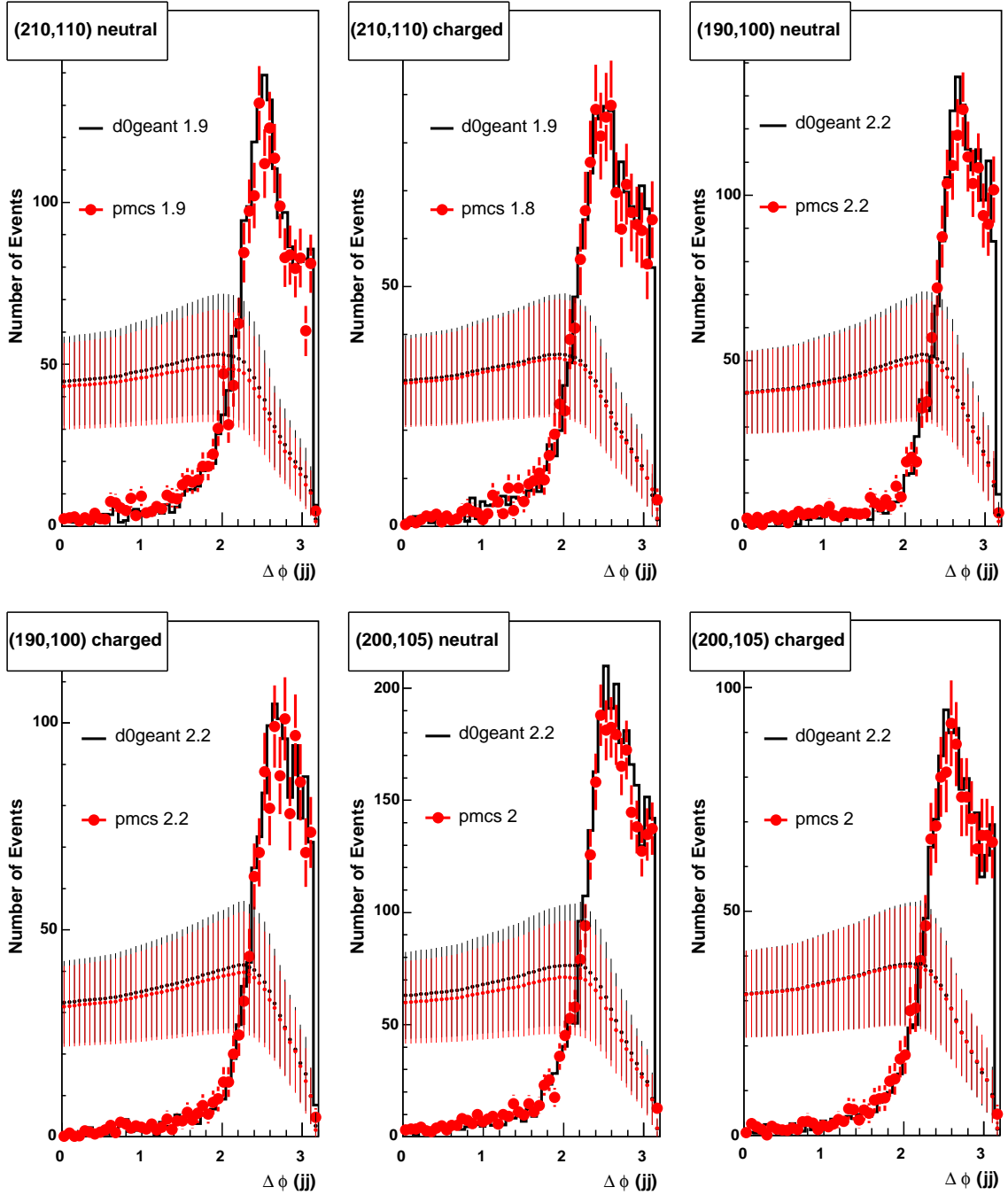


Figure 7.11: $\Delta\phi(jj)$ distributions for events passing the cuts listed in Table 7.7, for D0Geant (solid black histogram), and PMCS (red dots) in arbitrary units. The same distributions are used together with the background in Figure 6.13 to calculate the lower cut on $\Delta\phi(jj)$ maximizing S/\sqrt{B} for (shown in the superimposed curve for both simulations). Optimized cut values are shown in the legend.

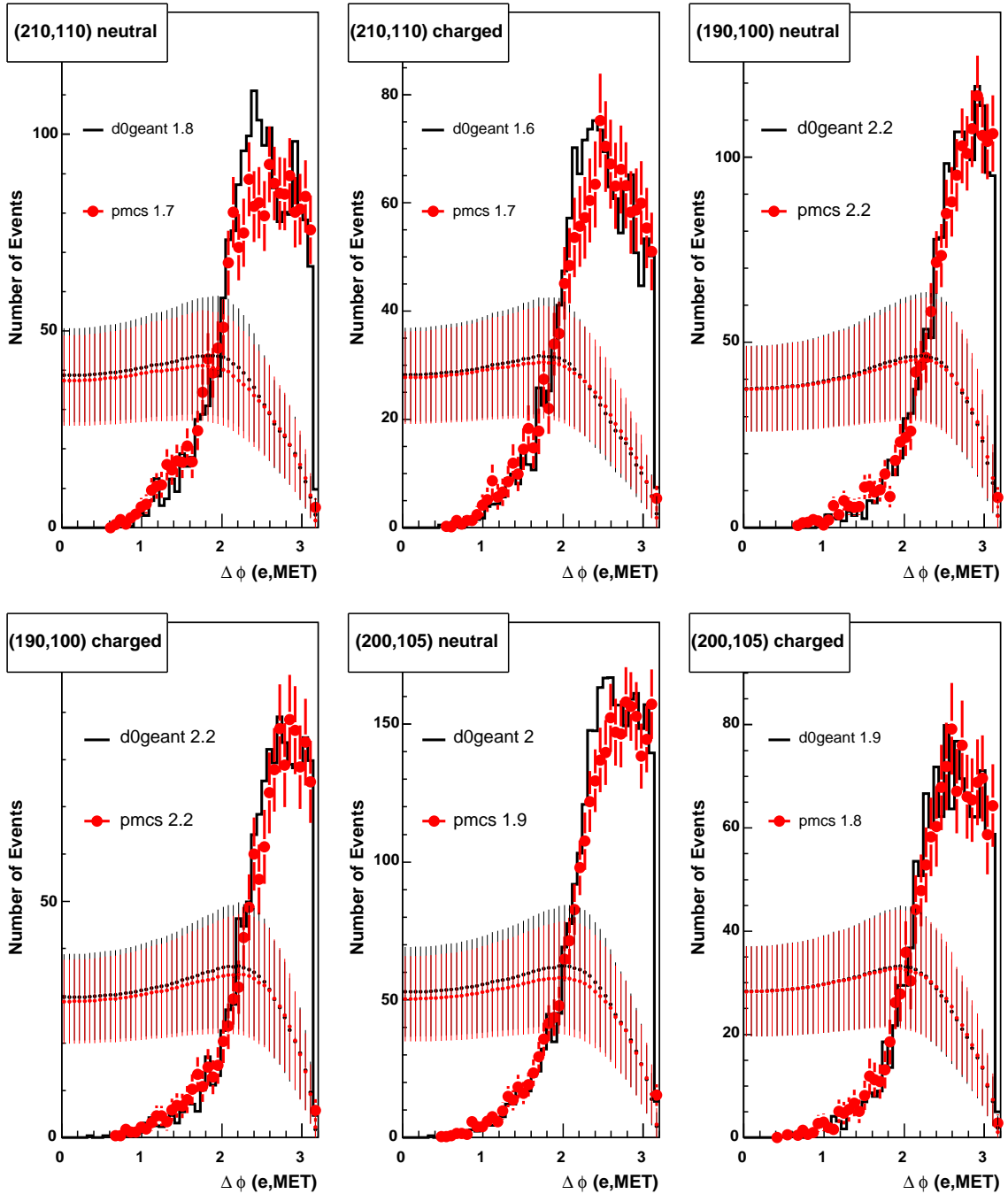


Figure 7.12: $\Delta\phi(e, MET)$ distributions for events passing the cuts listed in Table 7.7, for DØGeant (solid black histogram), and PMCS (red dots) in arbitrary units. The same distributions are used together with the background in Figure 6.14 to calculate the lower cut on $\Delta\phi(e, MET)$ maximizing S/\sqrt{B} for (shown in the superimposed curve for both simulations). Optimized cut values are shown in the legend.

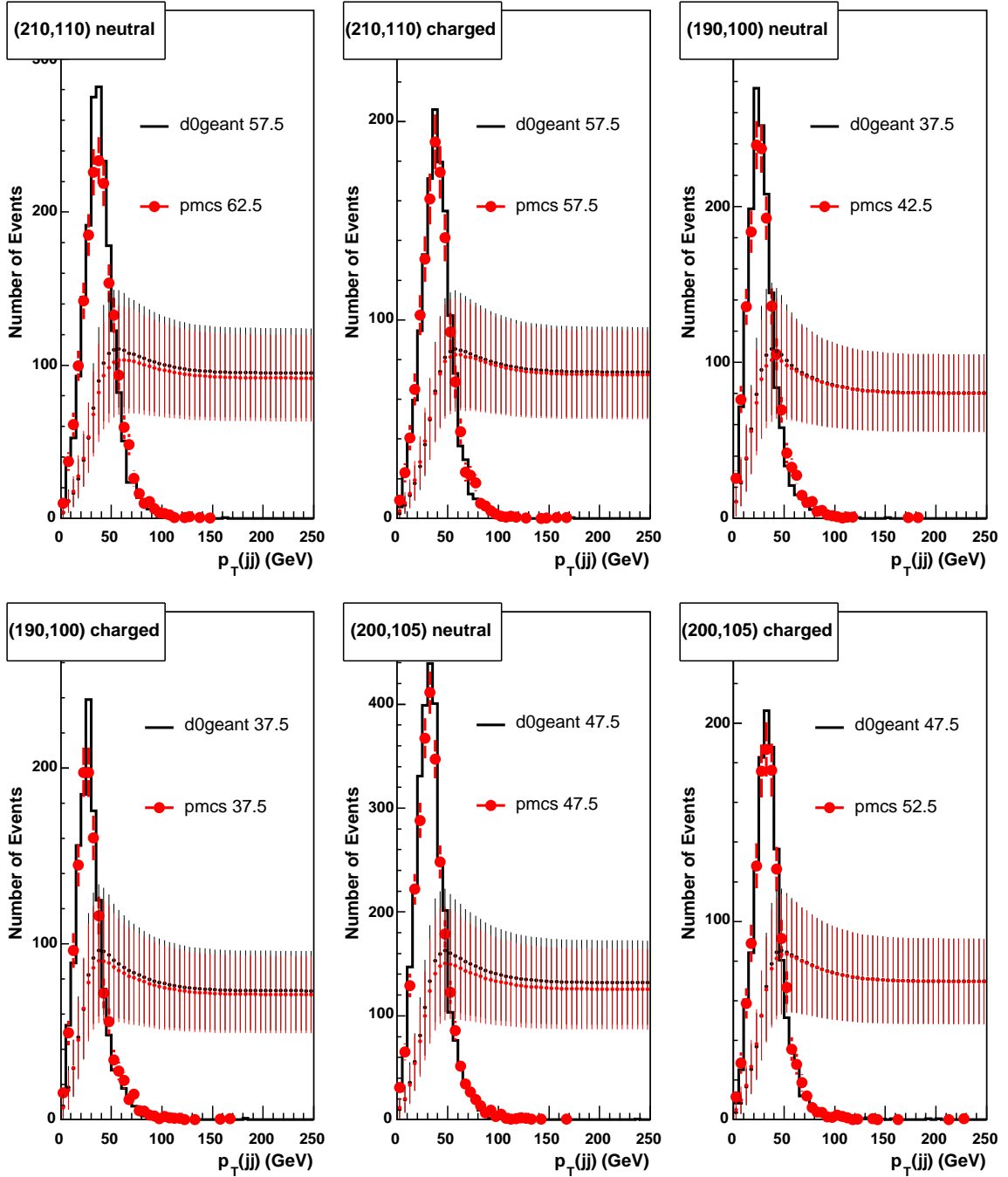


Figure 7.13: $p_T(jj)$ distributions for events passing the cuts listed in Table 7.7, for D0Geant (solid black histogram), and PMCS (red dots) in arbitrary units. The same distributions are used together with the background in Figure 6.13 to calculate the upper cut on $p_T(jj)$ maximizing S/\sqrt{B} for (shown in the superimposed curve for both simulations). Optimized cut values are shown in the legend.

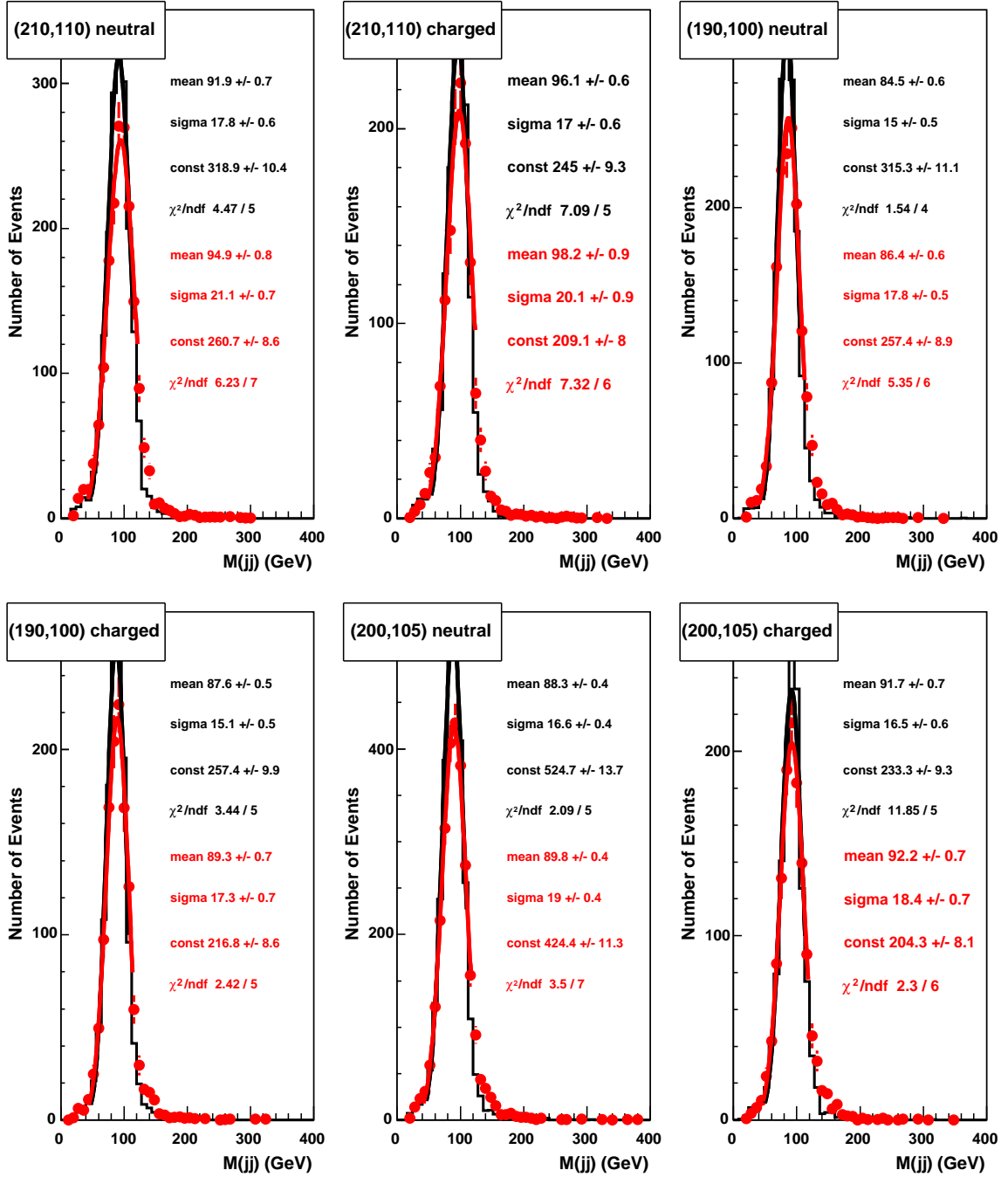


Figure 7.14: $M(jj)$ distributions for events passing the cuts listed in Table 7.7, for DØGeant (solid black histogram), and PMCS (red dots) in arbitrary units. The π_T resonance is fitted with a Gaussian in both simulations.

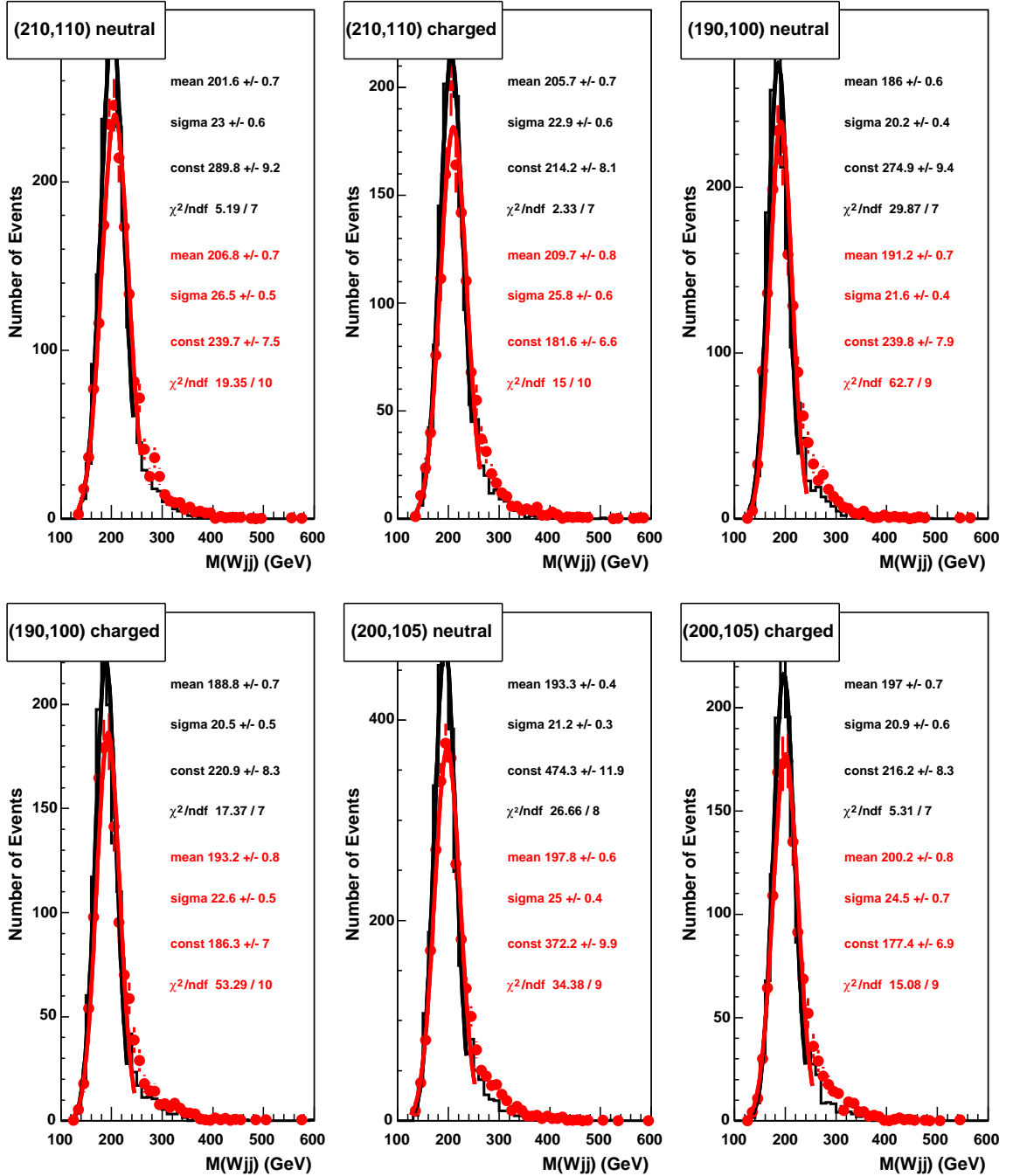


Figure 7.15: $M(W_{jj})$ distributions for events passing the cuts listed in Table 7.7, for DØGeant (solid black histogram), and PMCS (red dots) in arbitrary units. The ρ_T resonance is fitted with a Gaussian in both simulations.

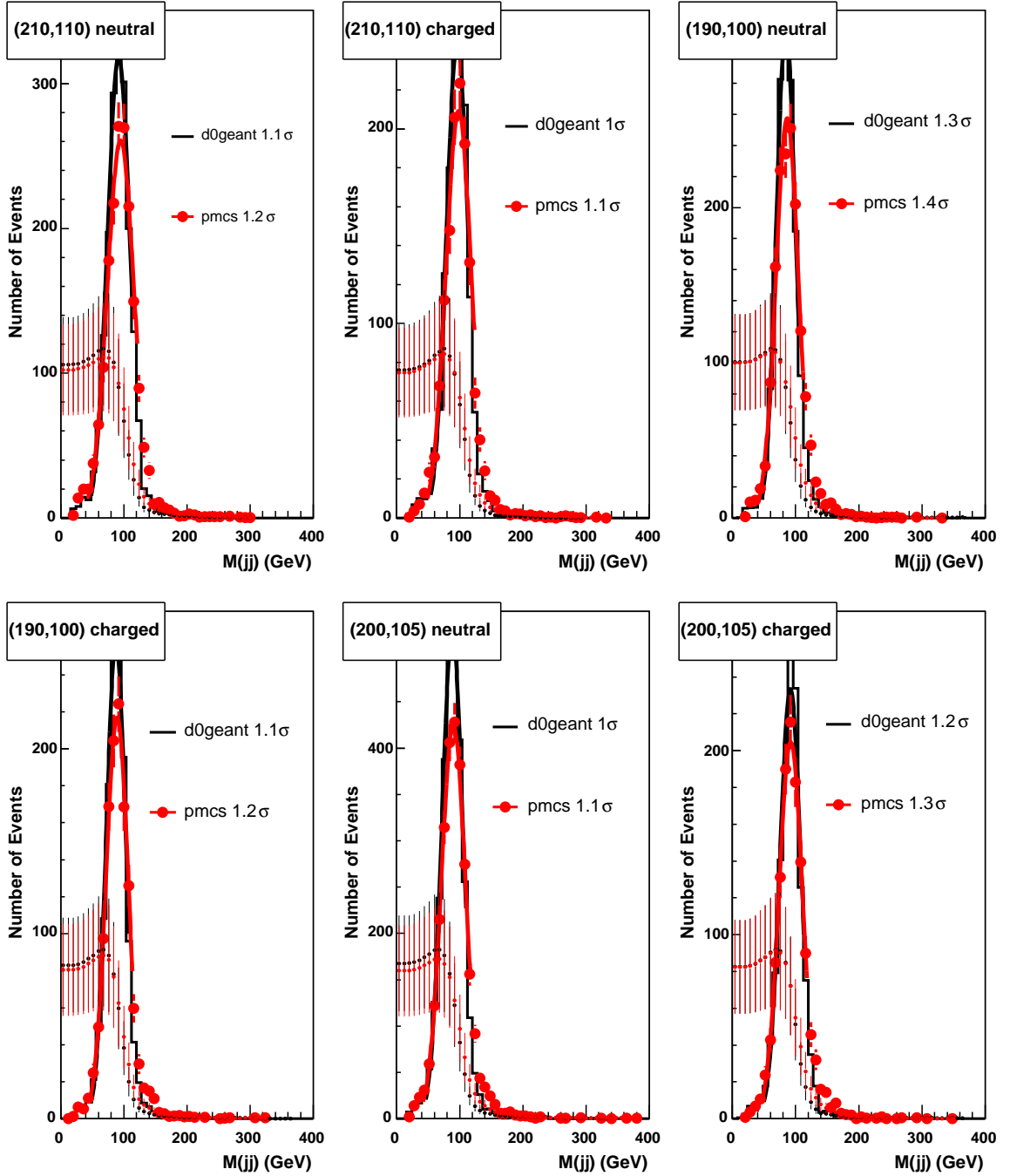


Figure 7.16: $M(jj)$ distributions for events passing the cuts listed in Table 7.7, for D0Geant (solid black histogram), and PMCS (red dots) in arbitrary units. The same distributions are used together with the background in Figure 6.13 to calculate the lower cut on $M(jj)$ maximizing S/\sqrt{B} for (shown in the superimposed curve for both simulations). Optimized cut values are shown in the legend.

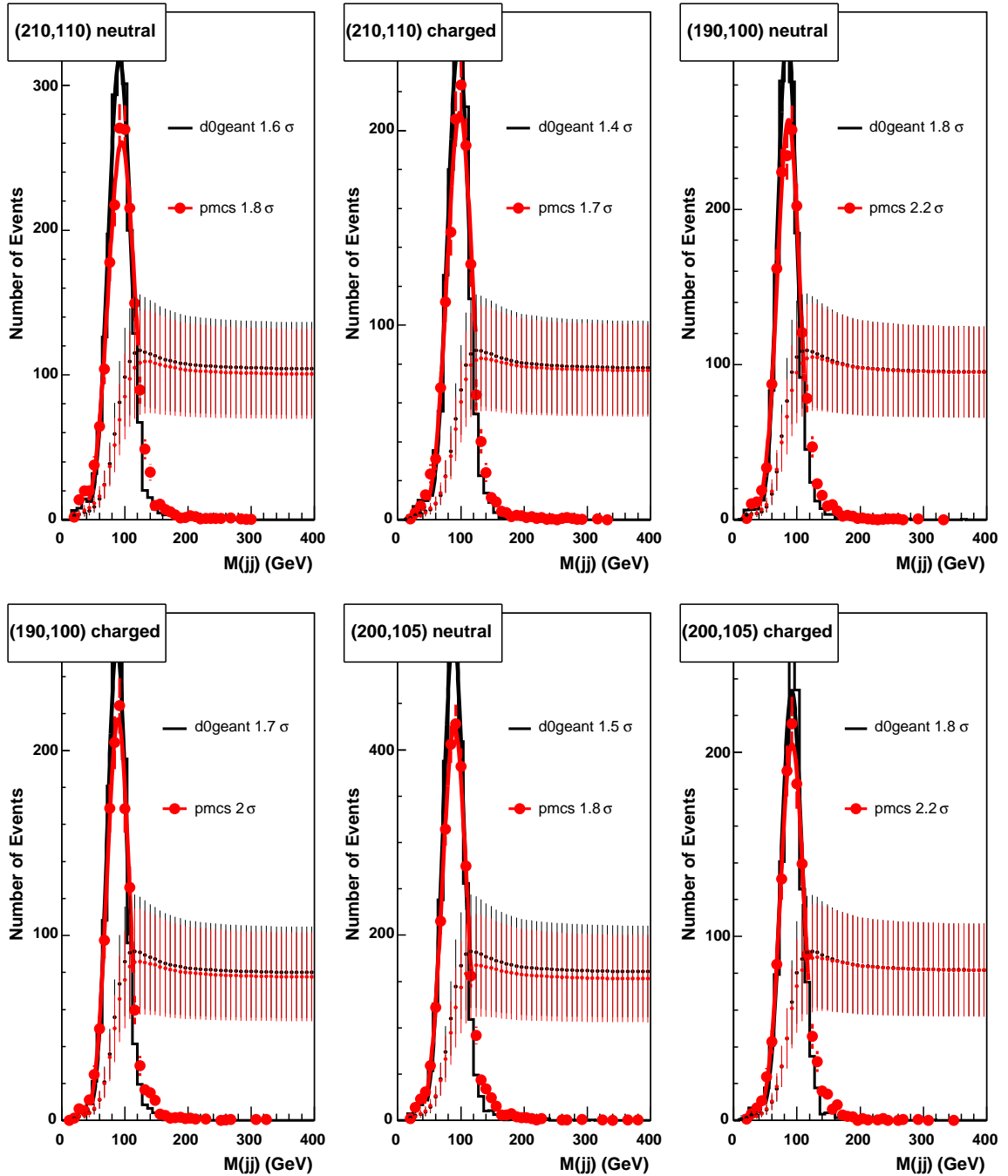


Figure 7.17: $M(jj)$ distributions for events passing the cuts listed in Table 7.7, for D0Geant (solid black histogram), and PMCS (red dots) in arbitrary units. The same distributions are used together with the background in Figure 6.13 to calculate the upper cut on $M(jj)$ maximizing S/\sqrt{B} for (shown in the superimposed curve for both simulations). Optimized cut values are shown in the legend.

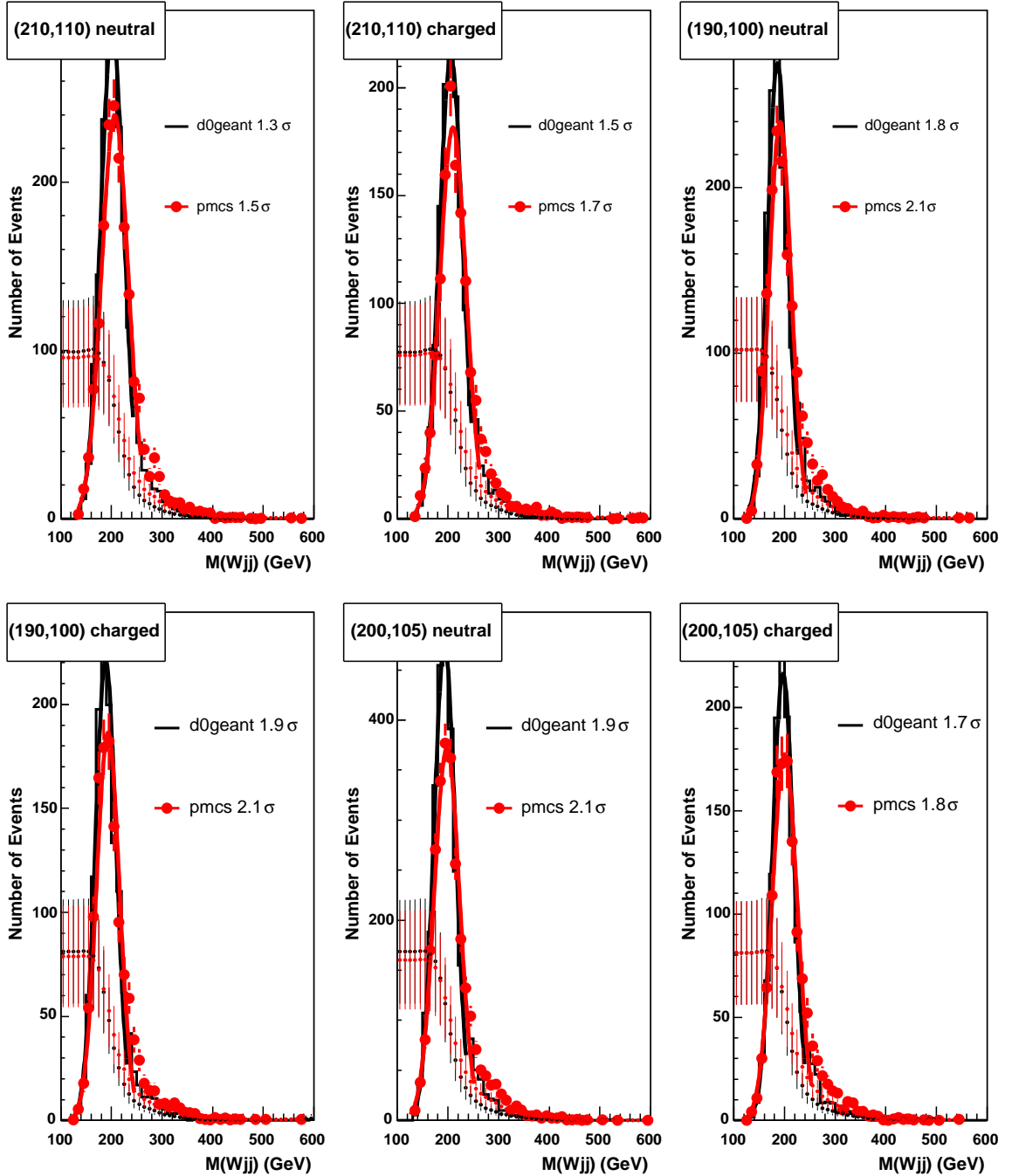


Figure 7.18: $M(W_{jj})$ distributions for events passing the cuts listed in Table 7.7, for D0Geant (solid black histogram), and PMCS (red dots) in arbitrary units. The same distributions are used together with the background in Figure 6.13 to calculate the lower cut on $M(W_{jj})$ maximizing S/\sqrt{B} for (shown in the superimposed curve for both simulations). Optimized cut values are shown in the legend.

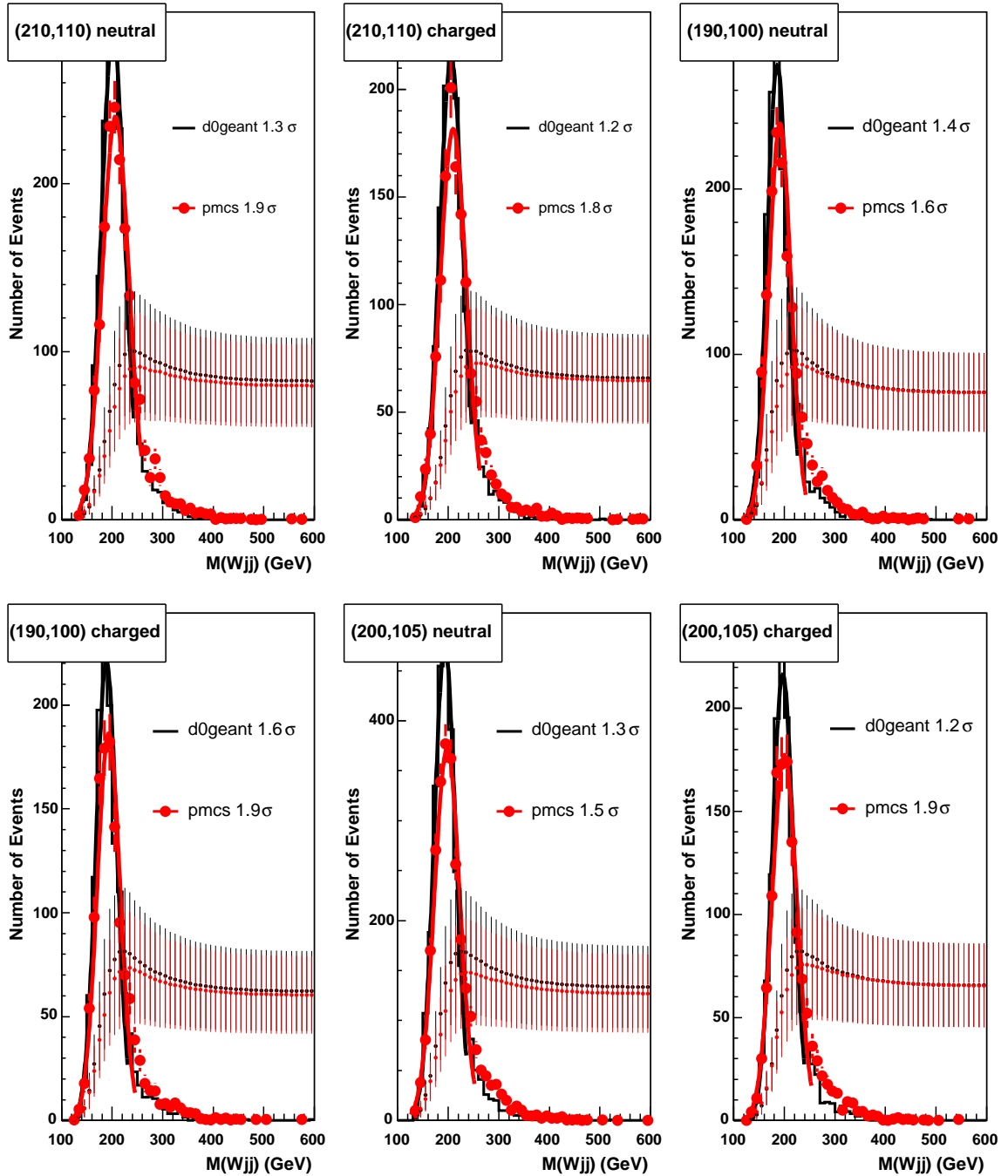


Figure 7.19: $M(W_{jj})$ distributions for events passing the cuts listed in Table 7.7, for D0Geant (solid black histogram), and PMCS (red dots) in arbitrary units. The same distributions are used together with the background in Figure 6.13 to calculate the upper cut on $M(W_{jj})$ maximizing S/\sqrt{B} for (shown in the superimposed curve for both simulations). Optimized cut values are shown in the legend.

$(M(\rho_T), M(\pi_T))$ (GeV)	electron and 2 jets $MET_{obj} > 20$ GeV		
	DØGeant	PMCS	r
(210,110) neutral	0.159	0.157	1.01
(210,110) charged	0.171	0.170	1.00
(190,100) neutral	0.138	0.139	0.99
(190,100) charged	0.160	0.159	1.00
(200,105) neutral	0.190	0.185	1.03
(200,105) charged	0.191	0.197	0.97

Table 7.5: Acceptance for all tuning mass points after requesting one central electron, two jets, $MET_{obj} > 20$ GeV in both PMCS and DØGeant; r is the ratio of the acceptances in DØGeant and PMCS.

$(M(\rho_T), M(\pi_T))$ (GeV)	electron, 2 jets, $MET_{obj} > 20$ GeV $M_T(W) > 30$ GeV		
	DØGeant	PMCS	r
(210,110) neutral	0.155	0.150	1.03
(210,110) charged	0.164	0.162	1.02
(190,100) neutral	0.135	0.135	0.99
(190,100) charged	0.157	0.152	1.03
(200,105) neutral	0.186	0.178	1.04
(200,105) charged	0.186	0.189	0.99

Table 7.6: Acceptance for all tuning mass points after requesting one central electron, two jets, $MET_{obj} > 20$ GeV, $M_T(W) > 30$ GeV, in both PMCS and DØGeant; r is the ratio of the acceptances in DØGeant and PMCS.

$(M(\rho_T), M(\pi_T))$ (GeV)	electron, 2 jets, $MET_{obj} > 20$ GeV $M_T(W) > 30$ GeV $\geq 1b$ -tag		
	DØGeant	PMCS	r
(210,110) neutral	0.077	0.071	1.04
(210,110) charged	0.054	0.053	1.02
(190,100) neutral	0.062	0.062	1.00
(190,100) charged	0.051	0.049	1.03
(200,105) neutral	0.087	0.083	1.05
(200,105) charged	0.061	0.061	1.00

Table 7.7: Acceptance for all tuning mass points after requesting one central electron, two jets, $MET_{obj} > 20$ GeV, $M_T(W) > 30$ GeV and at least one b -tagged jet in both PMCS and DØGeant; r is the ratio of the acceptances in DØGeant and PMCS.

Cuts		$(M(\rho_T), M(\pi_T))$ (GeV)					
		(210,110)		(190,100)		(200,105)	
		neutral	charged	neutral	charged	neutral	charged
H_T^e	G	0.066	0.047	0.059	0.044	0.080	0.053
	P	0.062	0.048	0.056	0.046	0.074	0.53
	r	1.07	0.98	1.07	0.096	1.08	0.99
$\Delta\phi(jj)$	G	0.060	0.044	0.053	0.040	0.069	0.045
	P	0.055	0.045	0.048	0.040	0.066	0.048
	r	1.10	0.98	1.10	0.99	1.03	0.94
$p_T(jj)$	G	0.054	0.039	0.044	0.033	0.060	0.040
	P	0.050	0.039	0.041	0.036	0.057	0.043
	r	1.07	1.00	1.08	0.95	1.05	0.93
$\Delta\phi(e, MET)$	G	0.054	0.039	0.044	0.033	0.060	0.040
	P	0.050	0.039	0.041	0.036	0.057	0.043
	r	1.07	1.00	1.08	0.95	1.05	0.93
Mass Window	G	0.043	0.030	0.037	0.028	0.048	0.034
	P	0.042	0.032	0.036	0.029	0.045	0.037
	r	1.01	0.96	1.06	0.97	1.07	0.91

Table 7.8: Acceptance for all tuning mass points after subsequent cuts on H_T^e , $\Delta\phi(jj)$, $\Delta\phi(e, MET)$, $p_T(jj)$ and $M(jj)$ together with $M(Wjj)$ (mass window cut) in both PMCS (P) and DØGeant (G); r is the ratio of the acceptances in DØGeant and PMCS.

Cuts		$(M(\rho_T), M(\pi_T))$ (GeV)					
		(210,110)		(190,100)		(200,105)	
		neutral	charged	neutral	charged	neutral	charged
$MET > 20$ GeV	G	0.038	0.027	0.034	0.025	0.044	0.030
	P	0.042	0.032	0.036	0.029	0.045	0.037
	r	0.91	0.85	0.98	0.89	0.97	0.82
scaled PMCS	G	0.038	0.027	0.034	0.025	0.044	0.030
	P	0.029	0.029	0.032	0.026	0.041	0.033
	r	1.01	0.94	1.08	0.98	1.07	0.91

Table 7.9: Acceptance after optimization in PMCS (P) and DØGeant (G). The first row shows the effect of cutting on the calorimeter missing energy in DØGeant. A scale factor of 0.905 is applied to PMCS to correct for this cut. The agreement between PMCS and DØGeant after this scale factor is applied, is shown in the last row. The average difference between the two simulations is 5.4%.

Chapter 8

Final Event Selection and Upper Limits on $W\pi_T$ Production Cross Section

8.1 Acceptance for Technicolor signal mass grid

A mass grid of Technicolor signal events has been generated with PMCS. For each mass point, 100,000 events are generated for both charged and neutral states. The ρ_T mass value for generated Technicolor processes start at 190 GeV up to a maximum of 220 GeV. The π_T mass values start from the kinematic threshold for $W\pi_T$ production ($M(W) + M(\pi_T)$) up to twice the π_T mass, when the decay channel $\rho_T^{\pm(0)} \rightarrow \pi_T^{\pm,(0,\pm)} \pi_T^{0,(0,\mp)}$ becomes accessible with the consequence of reducing $\rho_T^{\pm(0)} \rightarrow W\pi_T$ branching ratio. Each PMCS set is generated according to the procedures discussed in Sections 7.1.1 and 7.2. The acceptances for each generated mass point, after baseline cuts as defined in Section 7.3, is shown in Figure 8.1.

For each mass point, distributions for the kinematic quantities after baseline cuts are used together with the background in order to optimize S/\sqrt{B} -based cuts as discussed

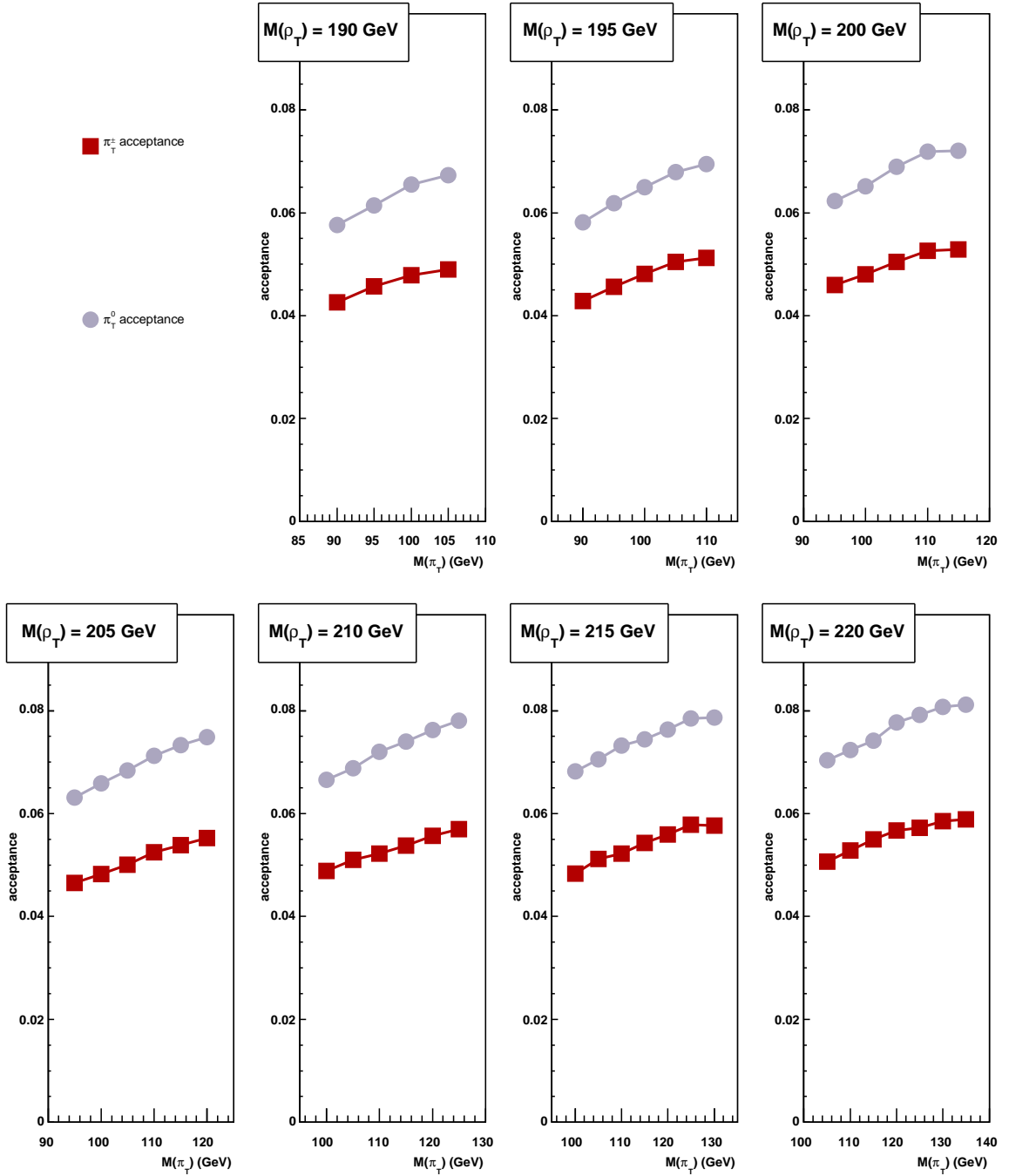


Figure 8.1: Acceptance after baseline cuts for the $190 \leq M(\rho_T) \leq 220$ GeV mass grid region produced with PMCS. Red squares (grey circles) indicate the acceptance for $W\pi_T^{\pm(0)}$.

in Section 7.4. The optimized window cut for H_T^e as function of ρ_T and π_T masses is shown in Figure 8.2, the upper cut on $p_T(jj)$ in Figure 8.3, the two cuts on the angular difference between the two jets and between the electron and the reconstructed neutrino direction are shown in Figures 8.4 and 8.5 respectively. Lastly, the mass window cut for the technirho and technipion resonances, $M(Wjj)$ and $M(jj)$, as function of the fitted mass peak width are shown in Figures 8.6 and 8.7. For each mass point, a single valued cut, t_{cut} , for each topological quantity is defined as:

$$t_{cut} = \frac{\omega_n t_n + \omega_c t_c}{\omega_n + \omega_c}, \quad (8.1)$$

where $t_{n(c)}$ is the value for the cut on any variable obtained using the charged (neutral) Technicolor state, and the weight ω is the cross section times branching ratio for that particular process. All topological variable cuts are listed in Tables 8.1, 8.2, 8.3, 8.4, 8.5 and 8.6.

For one particular mass point, $M(\rho_T) = 210$ GeV and $M(\pi_T) = 110$ GeV, the cut flow is shown extensively. After baseline cuts the distribution for H_T^e for signal, SM prediction and data is shown in Figure 8.8. After cutting on the optimized window cut on the H_T^e variable, the distribution for $\Delta\phi(e, MET)$ is shown in Figure 8.9, and after additional cuts on $\Delta\phi(e, MET)$ and $\Delta\phi(jj)$ the $p_T(jj)$ distribution is shown in Figure 8.10. Distributions for $M(Wjj)$ and $M(jj)$ for $W\pi_T$ signal, background and data after all cuts except the mass windows cut are shown in Figures 8.11, 8.12 and 8.13.

After all cuts the acceptance for the mass grid is shown in Figure 8.14 (for the high mass points), and listed in Tables 8.7 , 8.8 and 8.9.

$M(\rho_T)$ (GeV)	$M(\pi_T)$ (GeV)	Topological Cuts				
		H_T^e		$\Delta\phi(jj)$	$\Delta\phi(e, MET)$	$p_T(jj)$
		Lower (GeV)	Upper (GeV)	rad	rad	(GeV)
155	70	56	123	1.7	2.4	29
	75	60	123	1.8	2.4	37
160	75	53	123	2.1	2.4	29
	80	53	123	1.9	2.4	37
165	75	53	134	1.9	2.2	37
	80	67	127	2.2	2.4	27
	85	60	134	2	2.3	37
170	80	65	137	1.9	2.2	37
	85	67	137	2.2	2.4	32
	90	74	137	2.1	2.2	37
175	80	66	141	1.7	1.9	47
	85	65	137	2	2.2	37
	90	74	137	2.2	2.4	29
	95	64	144	2.2	2.3	37
180	85	74	144	1.8	1.9	47
	90	74	144	2.1	2.2	37
	95	74	144	2.2	2.4	32
	100	74	148	2.2	2.3	37
185	85	74	151	1.6	1.7	52
	90	78	151	1.9	1.9	47
	95	74	151	2.2	2.2	39
	100	77	147	2.2	2.4	32
	105	74	158	2.2	2.2	40

Table 8.1: Values of optimized cuts using S/\sqrt{B} for topological variable as function of $M(\pi_T)$ and $M(\rho_T)$.

$M(\rho_T)$ (GeV)	$M(\pi_T)$ (GeV)	H_T^e		Topological Cuts		
		Lower (GeV)	Upper (GeV)	$\Delta\phi(jj)$ rad	$\Delta\phi(e, MET)$ rad	$p_T(jj)$ (GeV)
190	90	82	155	1.7	1.7	52
	95	78	151	1.9	1.9	47
	100	81	155	2.2	2.2	42
	105	78	151	2.4	2.3	37
195	90	83	165	1.6	1.5	62
	95	85	165	1.8	1.7	57
	100	89	162	2	1.9	47
	105	81	165	2.2	2.2	42
	110	84	165	2.4	2.3	37
200	95	92	172	1.6	1.6	62
	100	92	169	1.8	1.7	57
	105	92	165	2	1.9	47
	110	92	169	2.2	2.1	42
	115	88	172	2.4	2.3	37
205	95	95	172	1.5	1.5	72
	100	95	172	1.7	1.6	62
	105	95	172	1.8	1.7	57
	110	95	172	2.1	1.9	50
	115	95	172	2.2	2.1	42
	120	92	172	2.5	2.3	37

Table 8.2: Values of optimized cuts using S/\sqrt{B} for topological variable as function of $M(\pi_T)$ and $M(\rho_T)$.

$M(\rho_T)$ (GeV)	$M(\pi_T)$ (GeV)	H_T^e		Topological Cuts		
		Lower (GeV)	Upper (GeV)	$\Delta\phi(jj)$ rad	$\Delta\phi(e, MET)$ rad	$p_T(jj)$ (GeV)
210	100	95	179	1.5	1.5	72
	105	95	176	1.7	1.6	65
	110	95	176	1.9	1.6	57
	115	95	179	2.2	1.9	50
	120	95	176	2.2	2.1	42
	125	95	179	2.4	2.3	37
215	100	100	179	1.3	1.1	77
	105	99	179	1.5	1.5	72
	110	99	179	1.8	1.5	70
	115	99	179	1.9	1.7	60
	120	99	179	2.2	1.9	52
	125	99	179	2.2	2	45
	130	95	187	2.5	2.3	37
220	105	102	193	1.5	1.1	77
	110	102	187	1.6	1.2	72
	115	102	191	1.8	1.5	70
	120	102	187	1.9	1.7	62
	125	99	187	2.2	1.9	52
	130	99	190	2.2	2	47
	135	99	204	2.5	2.2	37

Table 8.3: Values of optimized cuts using S/\sqrt{B} for topological variable as function of $M(\pi_T)$ and $M(\rho_T)$.

$M(\rho_T)$ (GeV)	$M(\pi_T)$ (GeV)	Mass Window Cut			
		$M(\pi_T)$		(W_{jj})	
		Lower (GeV)	Upper (GeV)	Lower (GeV)	Upper (GeV)
155	70	47	84	125	175
	75	51	92	113	185
160	75	51	92	105	189
	80	55	92	113	199
165	75	51	92	125	205
	80	55	92	125	195
	85	55	104	105	210
170	80	55	92	125	205
	85	55	103	125	195
	90	59	112	113	215
175	80	51	92	131	215
	85	59	100	125	210
	90	63	116	105	209
	95	63	116	125	220
180	85	55	104	136	225
	90	59	111	135	215
	95	63	116	129	219
	100	67	124	120	225
185	85	60	108	141	225
	90	59	112	140	225
	95	63	116	134	225
	100	66	119	139	225
	105	71	128	145	230

Table 8.4: Values of optimized cuts using S/\sqrt{B} for $M(\pi_T)$, $M(\rho_T)$ mass window as function of $M(\pi_T)$ and $M(\rho_T)$.

$M(\rho_T)$ (GeV)	$M(\pi_T)$ (GeV)	Mass Window Cut			
		$M(\pi_T)$		(W_{jj})	
		Lower (GeV)	Upper (GeV)	Lower (GeV)	Upper (GeV)
190	90	66	108	145	230
	95	70	116	145	230
	100	74	124	145	230
	105	78	128	145	225
195	90	56	112	145	235
	95	60	116	150	235
	100	64	124	150	235
	105	68	132	145	235
	110	71	132	145	235
200	95	60	116	155	241
	100	64	120	150	235
	105	68	128	150	235
	110	72	132	150	235
	115	76	144	150	235
205	95	60	116	161	255
	100	64	120	160	250
	105	68	124	160	245
	110	72	132	160	250
	115	76	140	160	245
	120	80	148	160	250

Table 8.5: Values of optimized cuts using S/\sqrt{B} for $M(\pi_T)$, $M(\rho_T)$ mass window as function of $M(\pi_T)$ and $M(\rho_T)$.

$M(\rho_T)$ (GeV)	$M(\pi_T)$ (GeV)	Mass Window Cut			
		$M(\pi_T)$		(Wjj)	
		Lower (GeV)	Upper (GeV)	Lower (GeV)	Upper (GeV)
210	100	64	120	165	255
	105	64	124	165	255
	110	72	132	165	255
	115	76	140	165	255
	120	80	148	160	255
	125	80	160	165	255
215	100	65	116	171	265
	105	68	128	165	265
	110	72	132	170	265
	115	76	136	170	260
	120	80	148	170	265
	125	80	156	170	260
	130	84	168	170	265
220	105	78	124	171	271
	110	82	132	175	265
	115	86	140	170	265
	120	90	144	175	265
	125	84	152	175	265
	130	94	164	175	270
	135	98	180	175	270

Table 8.6: Values of optimized cuts using S/\sqrt{B} for $M(\pi_T)$, $M(\rho_T)$ mass window as function of $M(\pi_T)$ and $M(\rho_T)$.

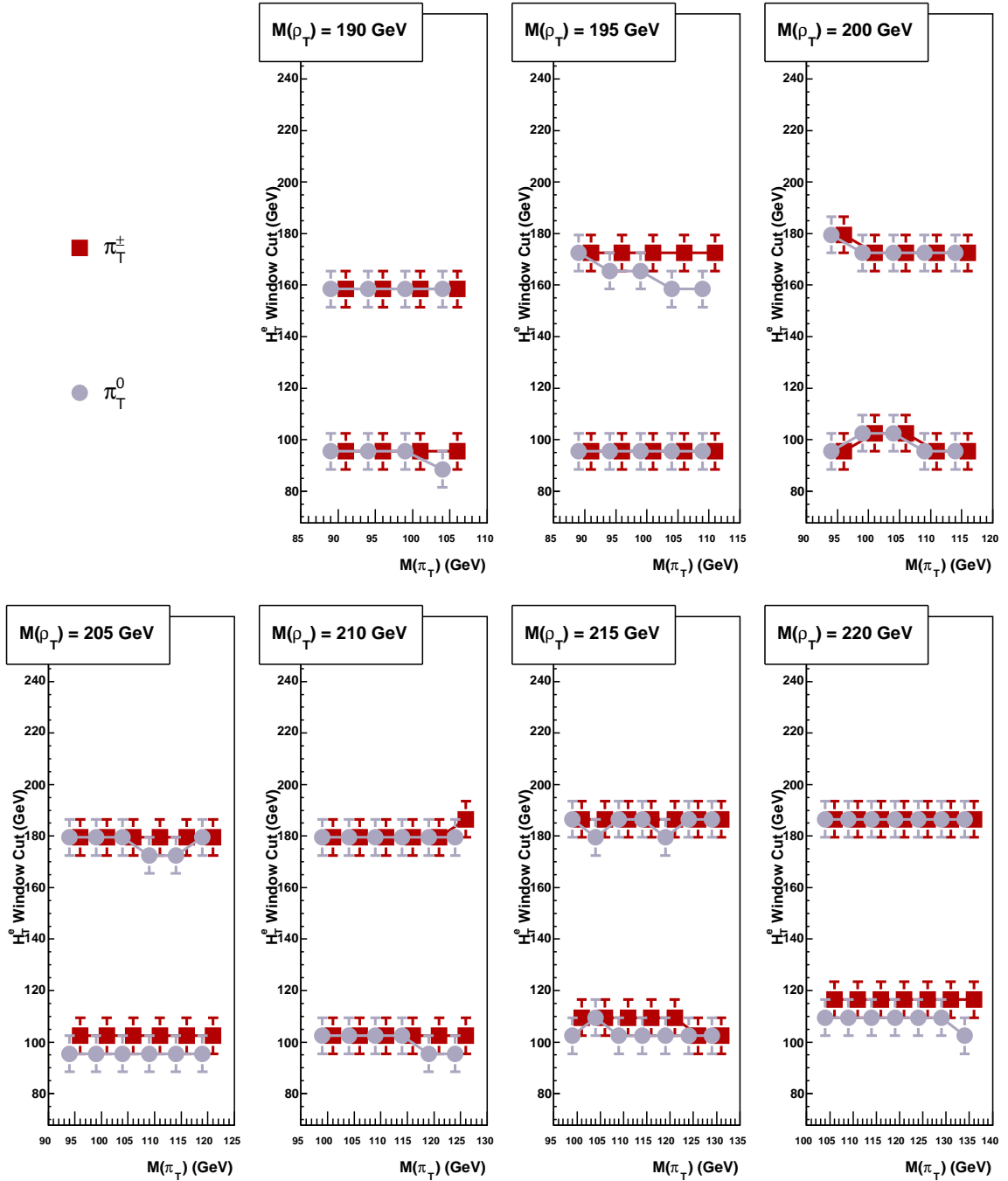


Figure 8.2: Cut values for the H_T^e window for the $190 \leq M(\rho_T) \leq 220$ GeV mass grid region produced with PMCS. Red squares (grey circles) indicate the cut optimized using $W\pi_T^{\pm(0)}$.

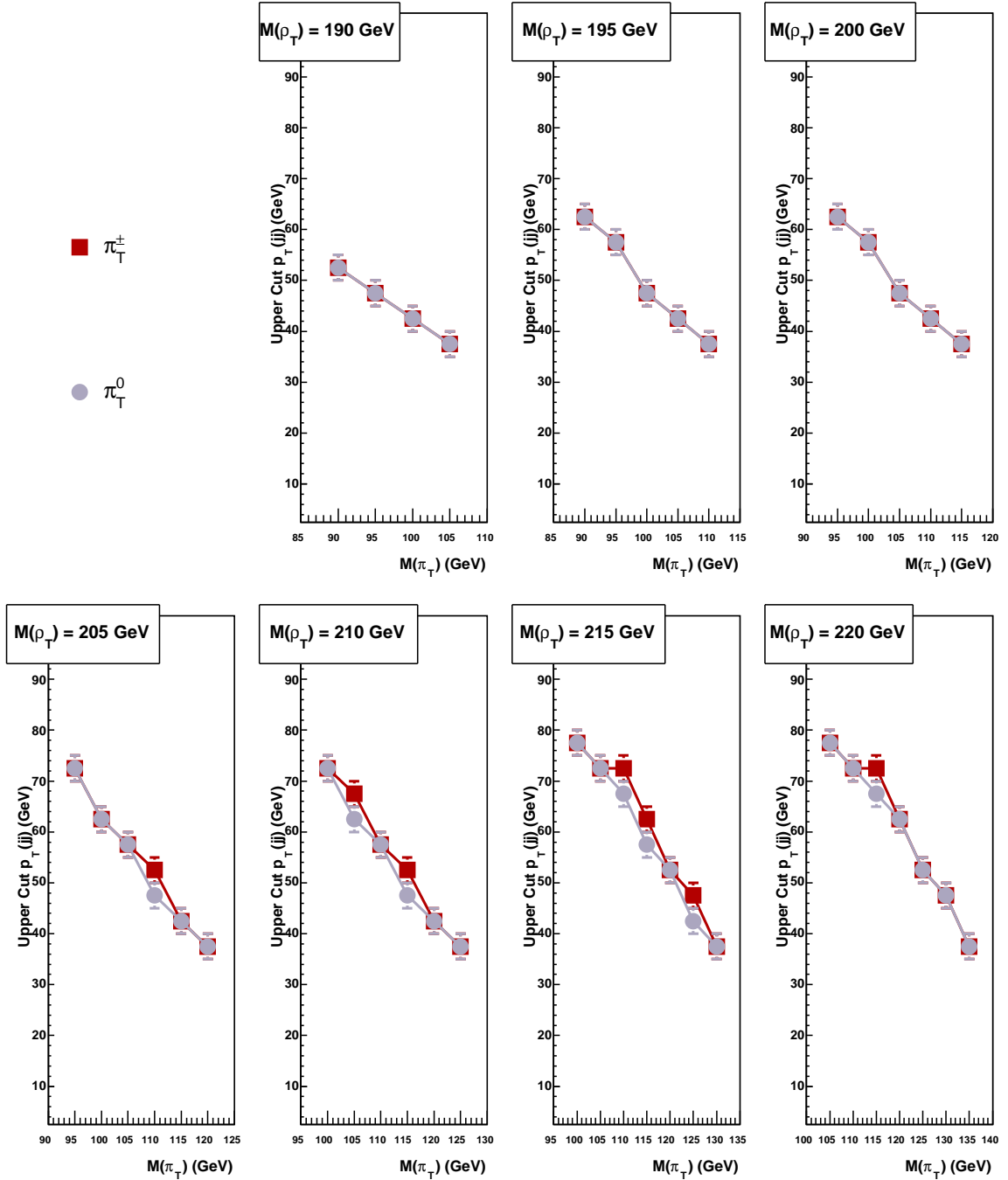


Figure 8.3: Cut values for $p_T(jj)$ for the $190 \leq M(\rho_T) \leq 220$ GeV mass grid region produced with PMCS. Red squares (grey circles) indicate the cut optimized using $W\pi_T^{\pm(0)}$.

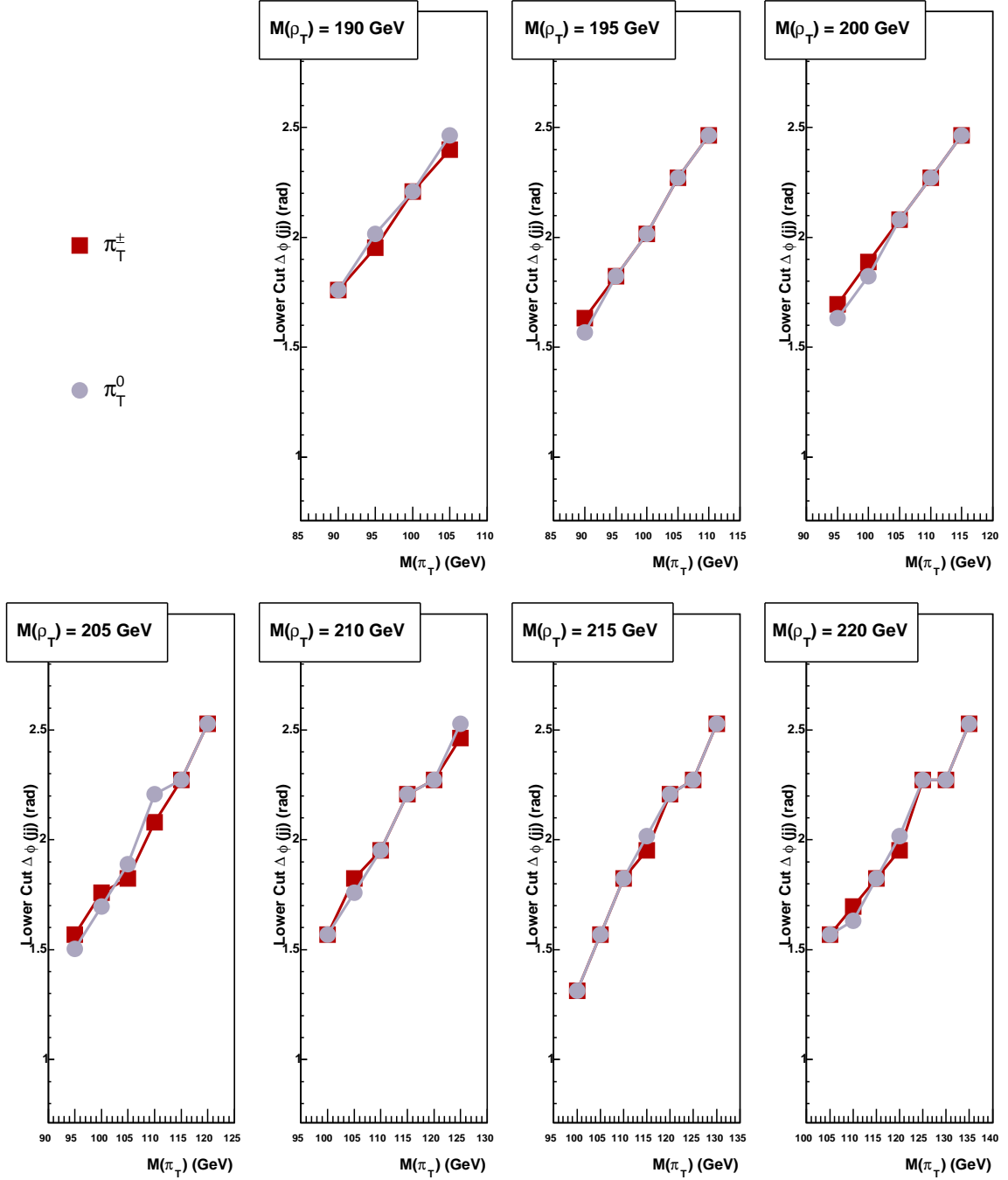


Figure 8.4: Cut values for $\Delta\phi(jj)$ for the $190 \leq M(\rho_T) \leq 220$ GeV mass grid region produced with PMCS. Red squares (grey circles) indicate the cut optimized using $W\pi_T^{\pm(0)}$.

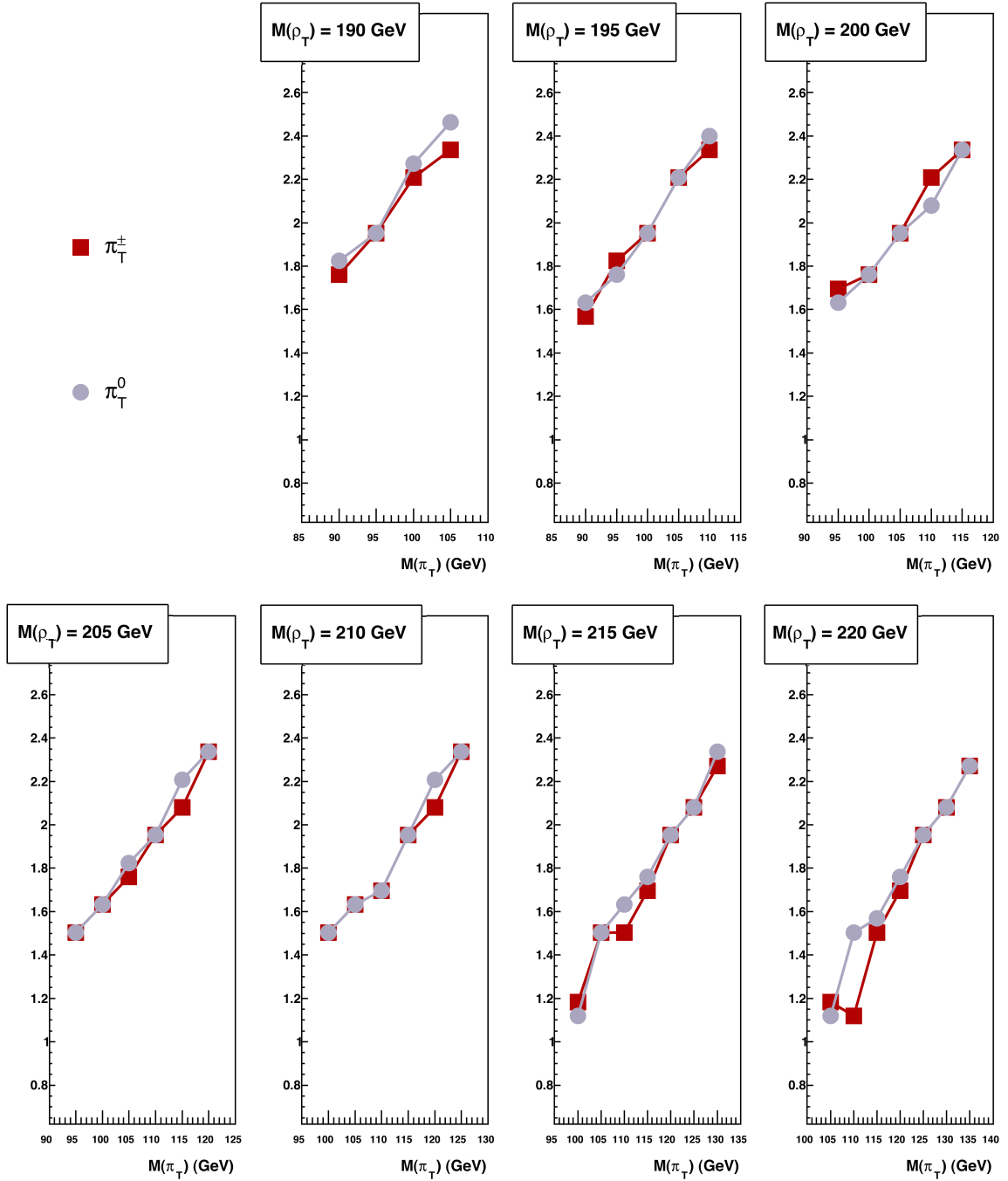


Figure 8.5: Cut values for $\Delta\phi(e, MET)$ for the $190 \leq M(\rho_T) \leq 220$ GeV mass grid region produced with PMCS. Red squares (grey circles) indicate the cut optimized using $W\pi_T^{\pm(0)}$.

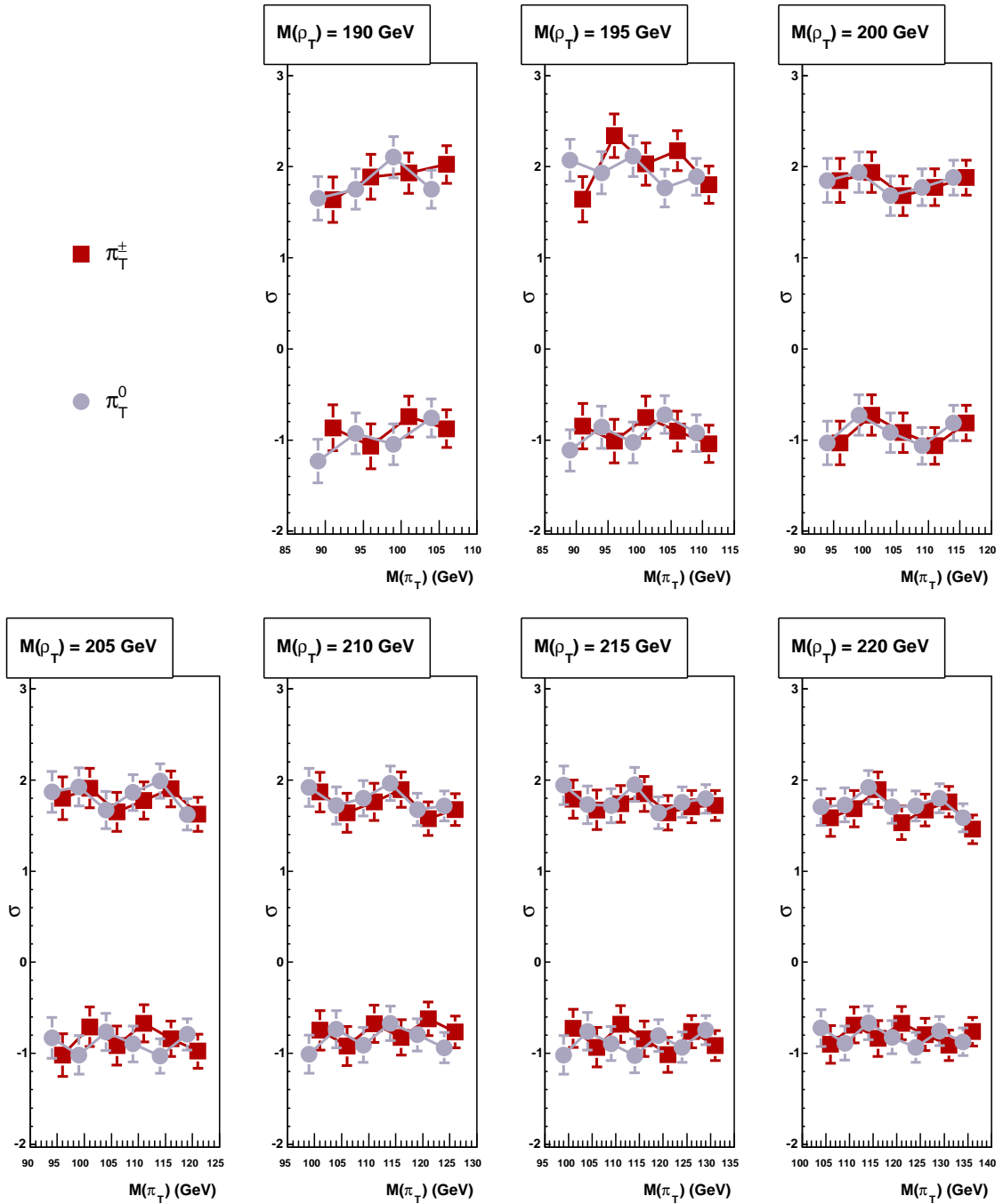


Figure 8.6: Cut values for the $M(jj)$ window for the $190 \leq M(\rho_T) \leq 220$ GeV mass grid region produced with PMCS. Red squares (grey circles) indicate the cut optimized using $W\pi_T^{\pm(0)}$.

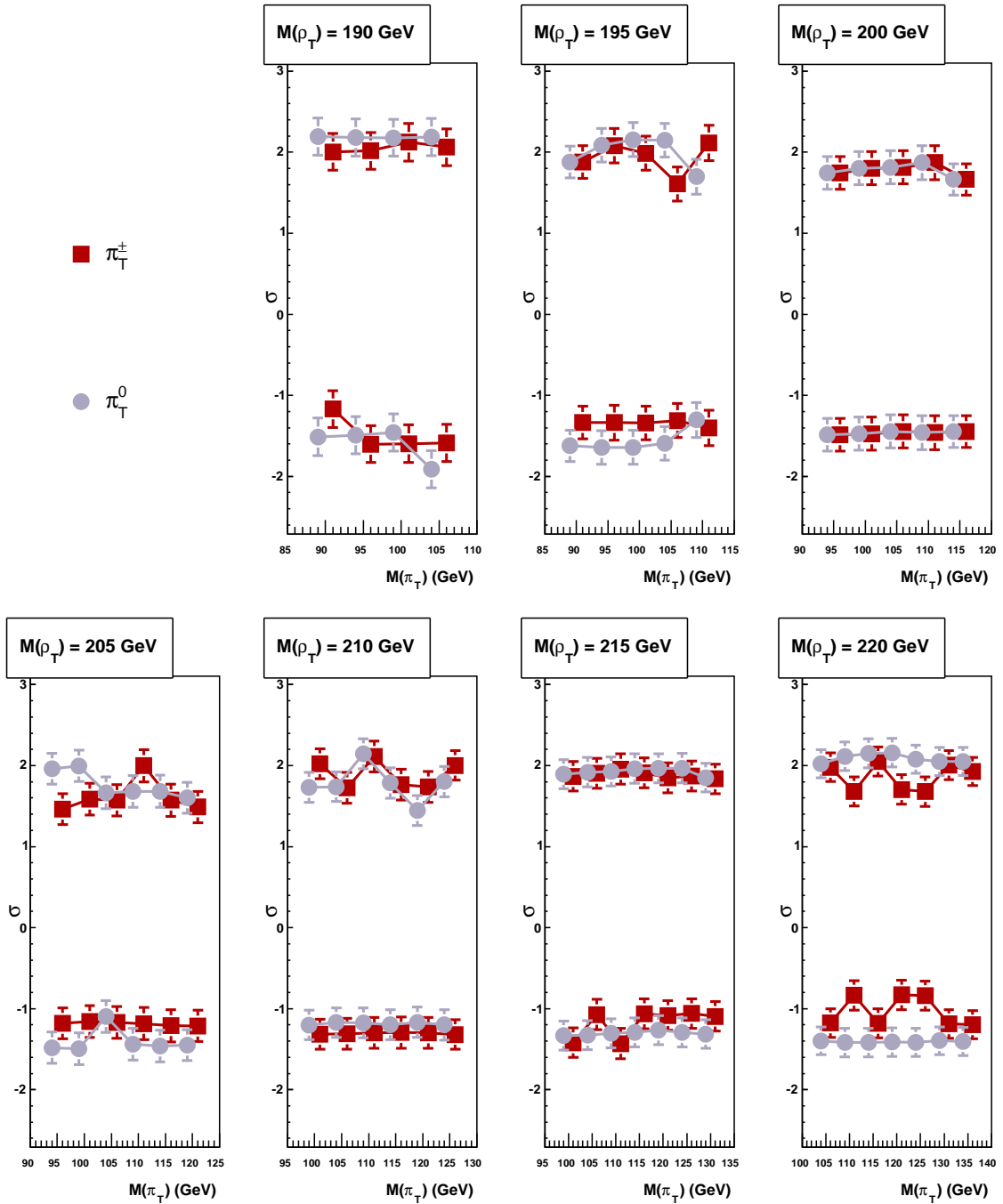


Figure 8.7: Cut values for the $M(Wjj)$ window for the $190 \leq M(\rho_T) \leq 220$ GeV mass grid region produced with PMCS. Red squares (grey circles) indicate the cut optimized using $W\pi_T^{\pm(0)}$.

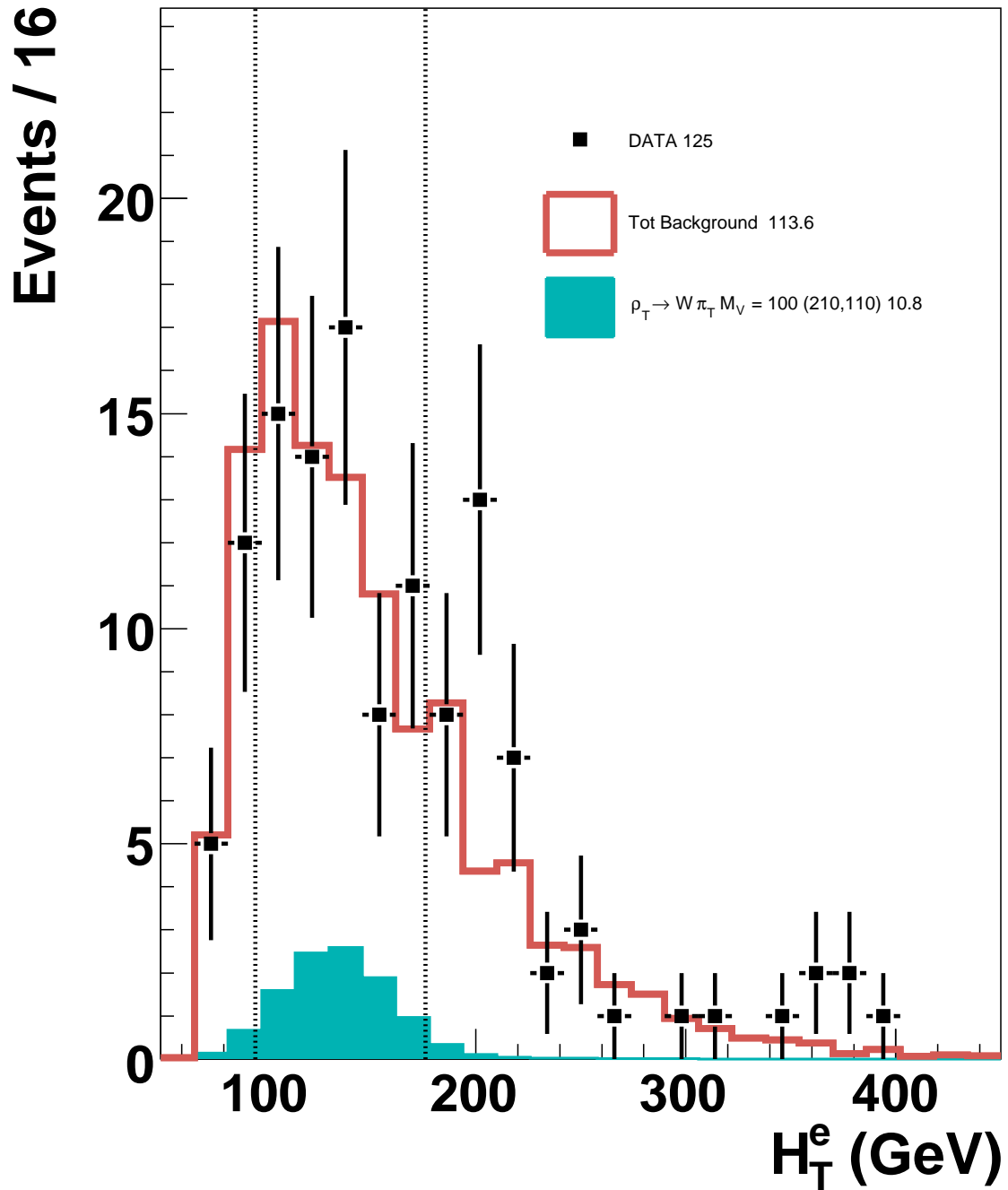


Figure 8.8: Distribution for H_T^e for $W\pi_T$ produced with $M(\rho_T) = 210$ GeV and $M(\pi_T) = 110$ GeV (azure histogram), SM predicted background (red histogram) and data (black squares) after baseline cuts. The optimized mass window cuts, at $H_T^e = 95$ GeV and $H_T^e = 176$ GeV, are represented with a dotted line.

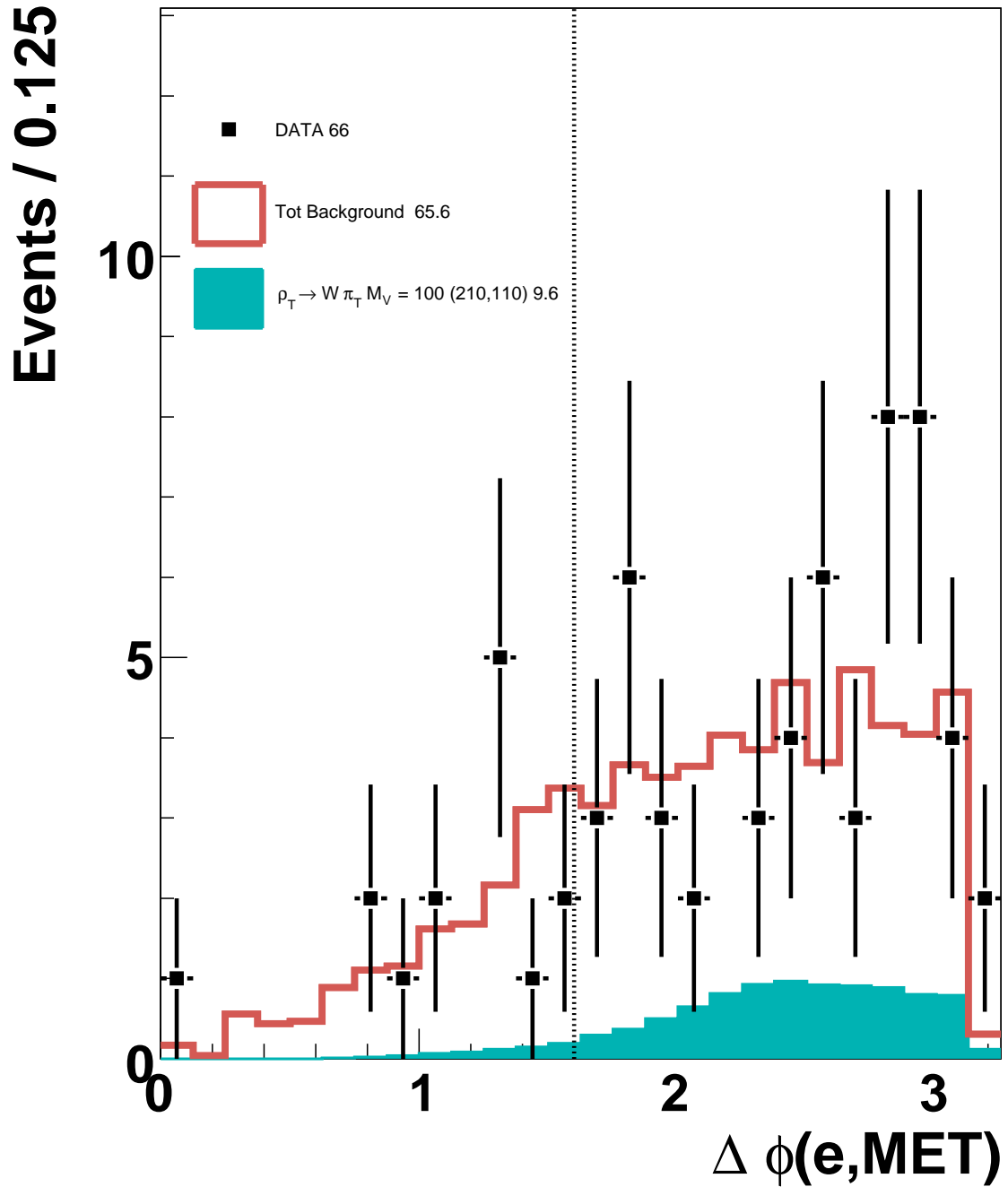


Figure 8.9: Distribution for $\Delta\phi(e, MET)$ for $W\pi_T$ produced with $M(\rho_T) = 210$ GeV and $M(\pi_T) = 110$ GeV (azure histogram), SM predicted background (red histogram) and data (black squares) after baseline and H_T^e cuts. The optimized lower cut at $\Delta\phi(e, MET) = 1.6$ is represented with a dotted line.

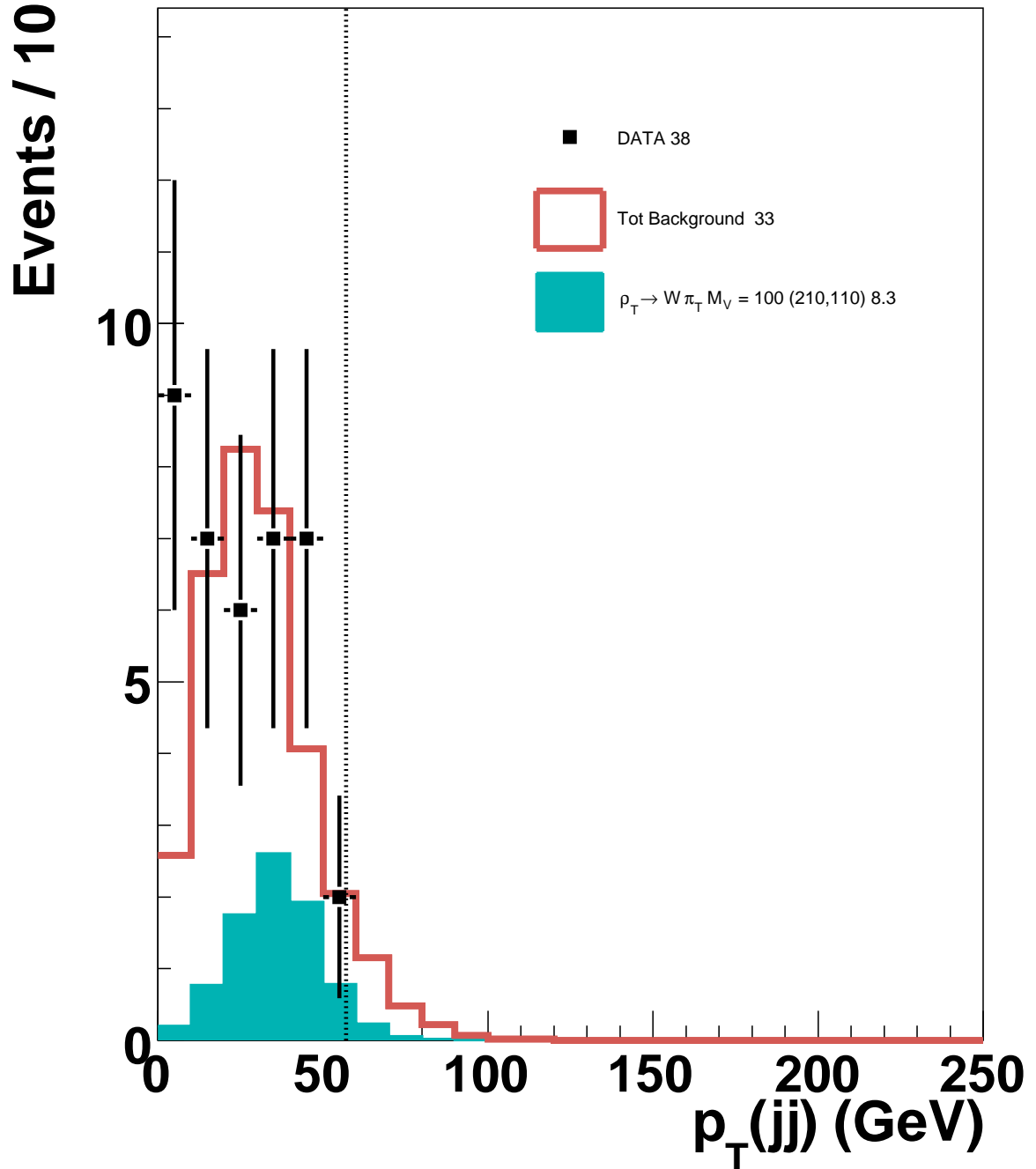


Figure 8.10: Distribution for $p_T(jj)$ for $W\pi_T$ produced with $M(\rho_T) = 210$ GeV and $M(\pi_T) = 110$ GeV (azure histogram), SM predicted background (red histogram) and data (black squares) after baseline, H_T^e , $\Delta\phi(e, MET)$ and $\Delta\phi(jj)$ cuts. The optimized upper cut at $p_T(jj) = 57$ GeV is represented with a dotted line.

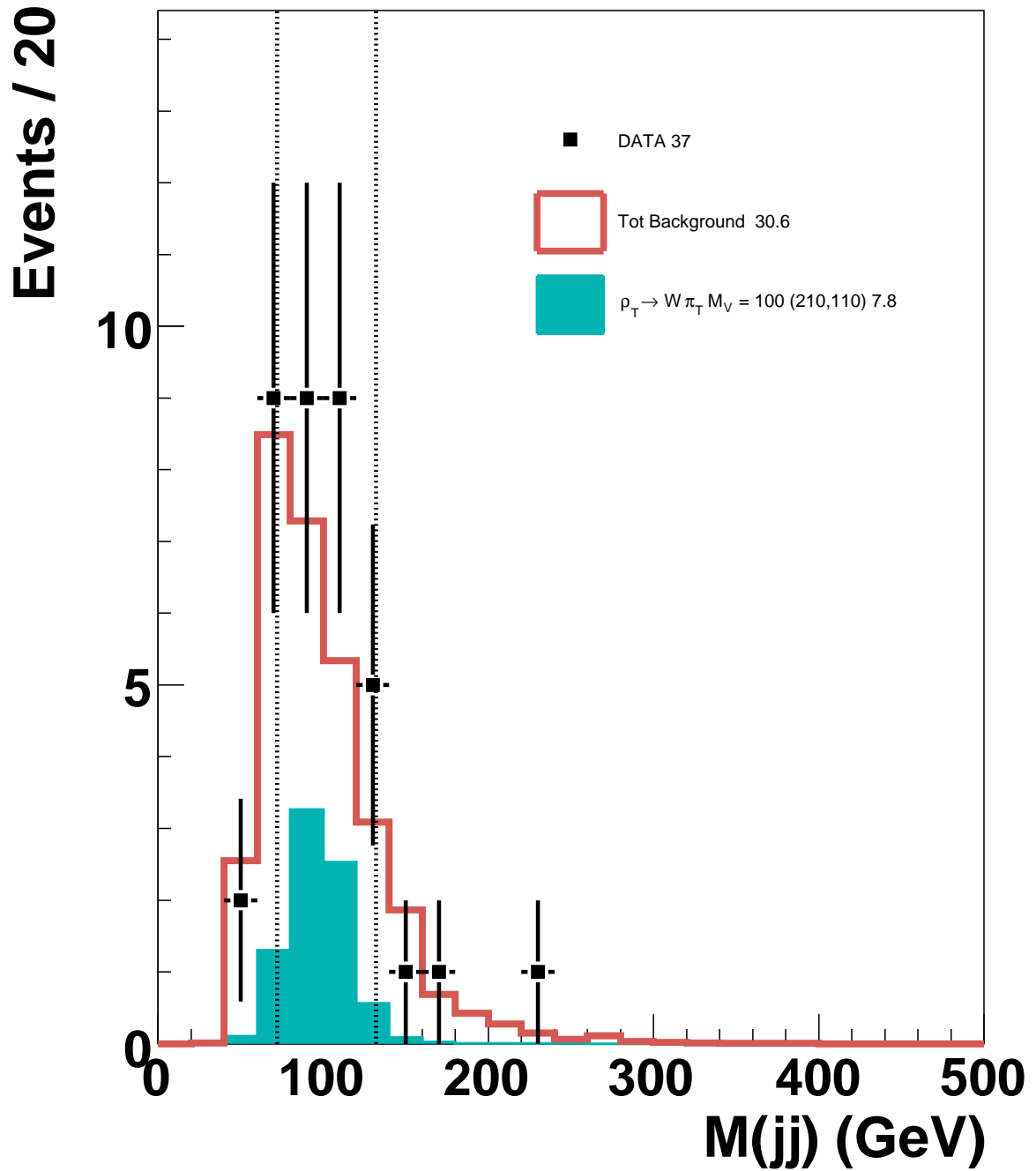


Figure 8.11: Distribution for $M(jj)$ for $W\pi_T$ produced with $M(\rho_T) = 210$ GeV and $M(\pi_T) = 110$ GeV (azure histogram), SM predicted background (red histogram) and data (black squares) after baseline, H_T^e , $\Delta\phi(e, MET)$, $\Delta\phi(jj)$ and $p_T(jj)$ cuts. The optimized window cuts at $M(jj) = 72$ GeV and $M(jj) = 132$ GeV are represented with a dotted line.

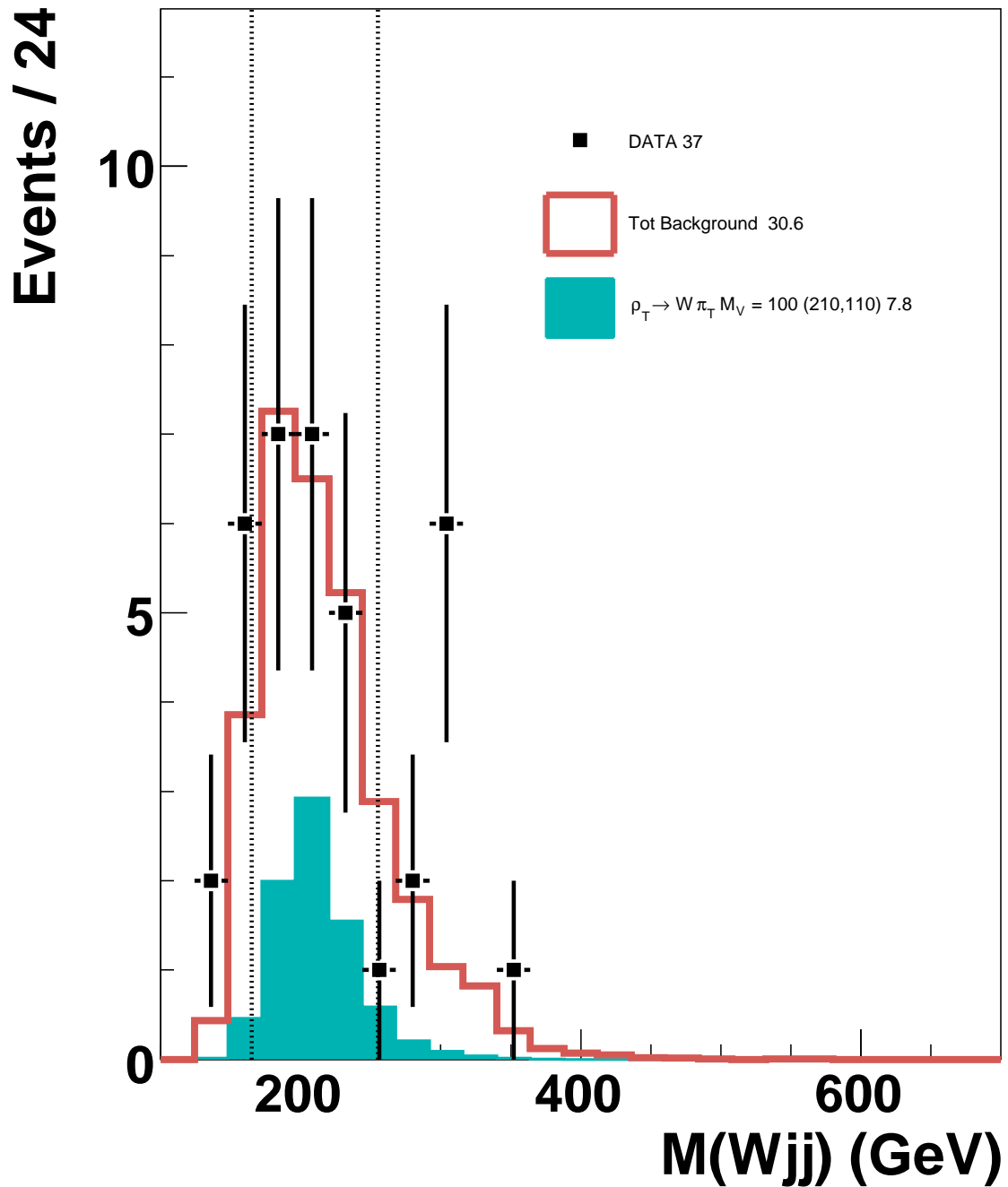


Figure 8.12: Distribution for $M(Wjj)$ for $W\pi_T$ produced with $M(\rho_T) = 210$ GeV and $M(\pi_T) = 110$ GeV (azure histogram), SM predicted background (red histogram) and data (black squares) after baseline, H_T^e , $\Delta\phi(e, MET)$, $\Delta\phi(jj)$ and $p_T(jj)$ cuts. The optimized window cuts at $M(Wjj) = 165$ GeV and $M(Wjj) = 255$ GeV are represented with a dotted line.

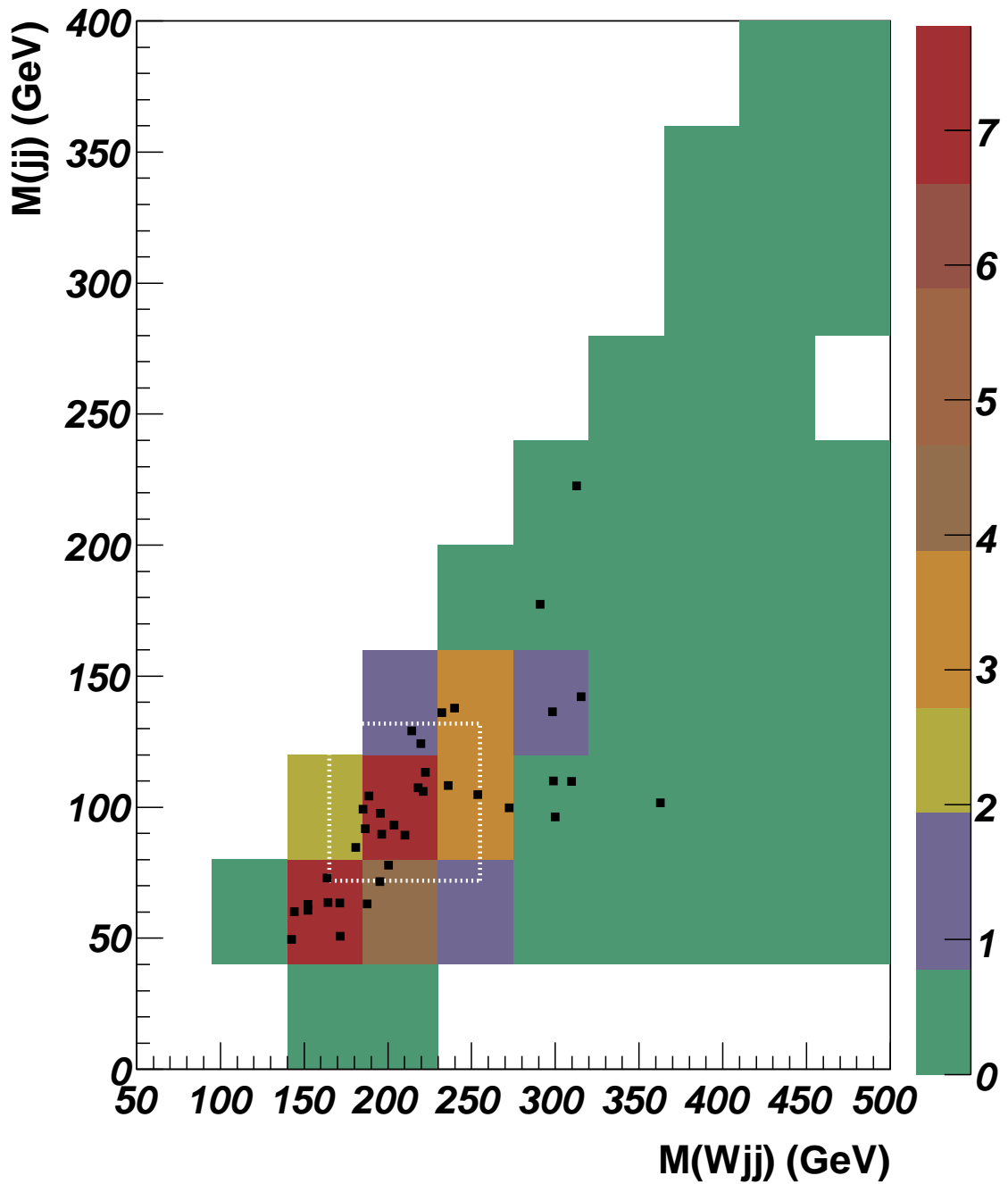


Figure 8.13: Distribution of $M(Wjj)$ versus $M(jj)$ for the SM predicted (colored histogram) and data (black dots), after baseline, H_T^e , $\Delta\phi(e, MET)$, $\Delta\phi(jj)$ and $p_T(jj)$ cuts optimized for $W\pi_T$ produced with $M(\rho_T) = 210$ GeV and $M(\pi_T) = 110$ GeV. The optimized mass window cuts are represented with a white dotted line.

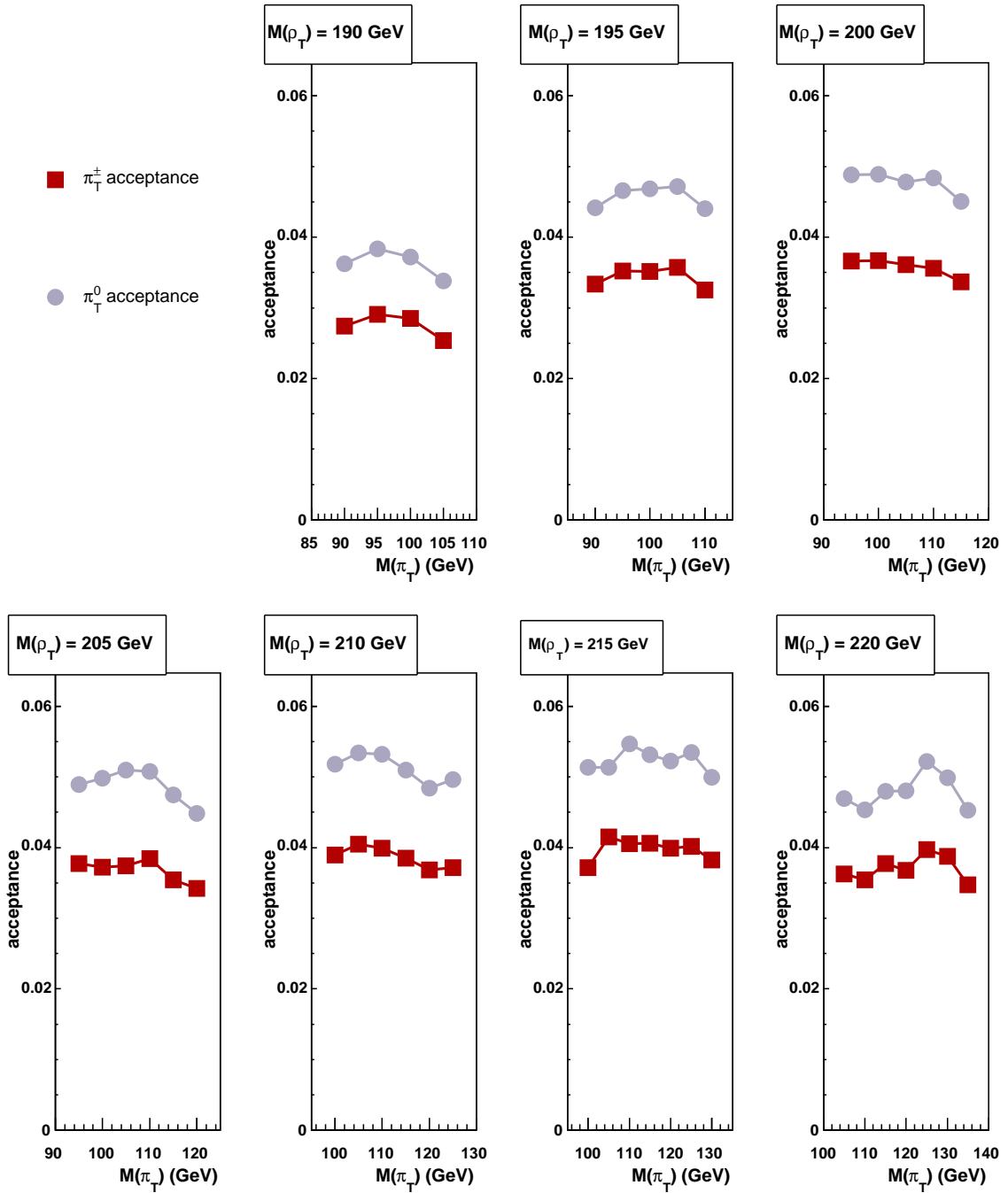


Figure 8.14: Acceptance after all optimized cuts for the $190 \leq M(\rho_T) \leq 220$ GeV mass grid region produced with PMCS. Red squares (grey circles) indicate the acceptance for $W\pi_T^{\pm(0)}$.

$M(\rho_T)$ (GeV)	$M(\pi_T)$ (GeV)	$W\pi_T \rightarrow e\nu_e b\bar{b}(b\bar{c})$ Acceptance		
		neutral	charged	combined
155	70	0.0146	0.0112	0.0125 ± 0.0001
	75	0.0153	0.0114	0.013 ± 0.0001
160	75	0.0187	0.0142	0.0161 ± 0.0002
	80	0.0169	0.0127	0.0145 ± 0.0002
165	75	0.0246	0.0184	0.0207 ± 0.0002
	80	0.0222	0.0163	0.0188 ± 0.0002
	85	0.0246	0.018	0.0209 ± 0.0002
170	80	0.0264	0.0199	0.0227 ± 0.0002
	85	0.0253	0.0184	0.022 ± 0.0002
	90	0.0262	0.0192	0.0223 ± 0.0002
175	80	0.0296	0.0218	0.0249 ± 0.0002
	85	0.0291	0.0209	0.0245 ± 0.0002
	90	0.0264	0.0188	0.0227 ± 0.0002
	95	0.0274	0.0204	0.0236 ± 0.0002
180	85	0.0352	0.0256	0.0296 ± 0.0002
	90	0.0296	0.0214	0.0257 ± 0.0002
	95	0.0303	0.022	0.0264 ± 0.0003
	100	0.0262	0.0196	0.0228 ± 0.0002
185	85	0.0323	0.024	0.0269 ± 0.0002
	90	0.0363	0.0275	0.0312 ± 0.0003
	95	0.0352	0.0257	0.0306 ± 0.0003
	100	0.0279	0.02	0.0242 ± 0.0002
	105	0.0298	0.0224	0.026 ± 0.0002

Table 8.7: Acceptances for $\rho_T \rightarrow W\pi_T \rightarrow e\nu b\bar{b}(b\bar{c})$ production as a function of $M(\pi_T)$, $M(\rho_T)$ and M_V . Only statistical uncertainties are reported.

8.2 Systematic Uncertainty

Apart from the uncertainty due to use of fast Monte Carlo techniques (discussed in the previous section), several other sources of indeterminacy affect both background and signal predictions:

- Heavy flavor tags: the systematic uncertainty on the b , c and *light*-tagging efficiency is estimated by varying the efficiencies up and down one σ_{syst} and calculating

$M(\rho_T)$ (GeV)	$M(\pi_T)$ (GeV)	$W\pi_T \rightarrow e\nu_e b\bar{b}(b\bar{c})$ Acceptance		
		neutral	charged	combined
190	90	0.029	0.0219	0.0247 ± 0.0002
	95	0.0306	0.0232	0.0267 ± 0.0002
	100	0.0297	0.0227	0.0262 ± 0.0002
	105	0.027	0.0203	0.0236 ± 0.0002
195	90	0.0353	0.0266	0.0299 ± 0.0002
	95	0.0372	0.0281	0.0322 ± 0.0003
	100	0.0374	0.0281	0.0321 ± 0.0003
	105	0.0377	0.0285	0.0331 ± 0.0003
	110	0.0352	0.026	0.0308 ± 0.0003
200	95	0.039	0.0292	0.0329 ± 0.0003
	100	0.0391	0.0293	0.0336 ± 0.0003
	105	0.0382	0.0288	0.0329 ± 0.0003
	110	0.0386	0.0284	0.0335 ± 0.0003
	115	0.036	0.0269	0.0313 ± 0.0003
205	95	0.0391	0.0301	0.0332 ± 0.0003
	100	0.0398	0.0297	0.0341 ± 0.0003
	105	0.0407	0.0299	0.0346 ± 0.0003
	110	0.0406	0.0307	0.0351 ± 0.0003
	115	0.0379	0.0283	0.0329 ± 0.0003
	120	0.0358	0.0273	0.0314 ± 0.0003

Table 8.8: Acceptances for $\rho_T \rightarrow W\pi_T \rightarrow e\nu b\bar{b}(b\bar{c})$ production as a function of $M(\pi_T)$, $M(\rho_T)$ and M_V . Only statistical uncertainties are reported.

the difference in the predicted signal and background;

- Jet Energy Scale: the systematic uncertainty due to the Jet Energy Scale estimation is also evaluated by varying the correction to the reconstructed jet energy plus or minus one σ_{syst} ;
- Jet Resolution: after jets are corrected a smearing is applied to Monte Carlo only to take into account the difference in resolutions with respect to data. The effect of this correction in the systematic uncertainties is estimated by switching off the smearing itself and evaluate the difference in the predicted signal and background;
- QCD-multijet: for the signal only it is considered a 20% uncertainty on the amount

$M(\rho_T)$ (GeV)	$M(\pi_T)$ (GeV)	$W\pi_T \rightarrow e\nu_e b\bar{b}(b\bar{c})$ Acceptance		
		neutral	charged	combined
210	100	0.0414	0.0311	0.0352 ± 0.0003
	105	0.0427	0.0323	0.0366 ± 0.0003
	110	0.0425	0.0319	0.0363 ± 0.0003
	115	0.0407	0.0308	0.0353 ± 0.0003
	120	0.0387	0.0294	0.0339 ± 0.0003
	125	0.0397	0.0297	0.0343 ± 0.0003
215	100	0.0411	0.0297	0.0335 ± 0.0003
	105	0.0411	0.0332	0.0363 ± 0.0003
	110	0.0437	0.0324	0.0369 ± 0.0003
	115	0.0425	0.0324	0.0368 ± 0.0003
	120	0.0417	0.0319	0.036 ± 0.0003
	125	0.0427	0.0321	0.0373 ± 0.0003
	130	0.0399	0.0306	0.0347 ± 0.0003
220	110	0.0362	0.0283	0.0318 ± 0.0003
	115	0.0383	0.0301	0.0335 ± 0.0003
	120	0.0384	0.0294	0.0332 ± 0.0003
	125	0.0417	0.0317	0.0359 ± 0.0003
	130	0.0399	0.0309	0.0351 ± 0.0003
	135	0.0362	0.0278	0.0315 ± 0.0003

Table 8.9: Acceptances for $\rho_T \rightarrow W\pi_T \rightarrow e\nu_e b\bar{b}(b\bar{c})$ production as a function of $M(\pi_T)$, $M(\rho_T)$ and M_V . Only statistical uncertainties are reported.

of QCD predicted with the matrix method.

To evaluate the systematic uncertainties three mass points are randomly chosen, with the constraint that they have to be different from the tuning mass points used in the previous section. These mass points are listed in Table 8.10.

The acceptance and background estimation is evaluated after individual and combined cuts on the kinematic variables. The ratio between the expected background and the expected background when no smearing is applied to the jet energy, as a function of applied cuts, is shown in Table 8.11. The same quantity for the signal is shown in Table 8.12. The ratio for expected background and signal when the jet energy scale is varied is shown in Tables 8.13 and 8.14 for a positive correction of σ_{syst} and Tables 8.15 and 8.16

for a negative correction. For b -tagging efficiency Tables 8.17, 8.18, 8.19 and 8.20. For each variation, the average deviation from the unity is taken to be the contribution to the systematic uncertainty.

A summary of all contributions is shown in Table 8.21. In Figure 8.15 systematic uncertainties after all cuts is plotted as a function of technihadron masses for the $190 \leq M(\rho_T) \leq 220$ GeV mass grid region; in the same figure the QCD-multijet contribution is shown together with the statistical uncertainty, mainly due to the $W + \text{heavy flavor}$ sample. In Figure 8.16 and 8.17, the number of data, background and signal events are shown after all cuts on the kinematic variables.

8.3 Upper Limits on $W\pi_T$ Production Cross Section

In order to set limits on $W\pi_T$ production cross section a Bayesian limits-setting procedure is used [79]. For a discrete stochastic variable A , $P(A|B)$ represents the probability of A given that B is true. Bayes's theorem states that:

$$P(A|BC) = \frac{P(B|AC)P(A|C)}{P(B|C)} \quad (8.2)$$

A reflects the probability that the cross section for $W\pi_T$ production is between σ and $\sigma + d\sigma$, the integrated luminosity between \mathcal{L} and $\mathcal{L} + d\mathcal{L}$, the signal acceptance between ϵ and $\epsilon + d\epsilon$, and the background between b and $b + db$. B reflects the k events observed in data, and C contains all relevant prior knowledge, including the descriptions of the knowledge of the parameters σ , \mathcal{L} , ϵ and b . Given that the probability for the outcome of a counting experiment being k when $\mu = b + \mathcal{L}\epsilon\sigma$ is given by the Poisson probability distribution:

$$P(B|AC) = P(k|b, \mathcal{L}, \epsilon, \sigma, I) = \frac{e^{-(b+\mathcal{L}\epsilon\sigma)}(b + \mathcal{L}\epsilon\sigma)^k}{k!} \quad (8.3)$$

where I represents any relevant information used to build μ . In most cases, the prior

probability can be factorized:

$$P(A|C) = P(b, \mathcal{L}, \epsilon, \sigma|I) = P(\theta|I)P(\sigma|I), \quad (8.4)$$

where θ represents all parameters but σ . In general once the value and the uncertainty is estimated for a given quantity, the relative prior distribution can be considered a Gaussian. A flat prior probability is used for the cross section $\rho(\sigma|I) = 1/\sigma_{max}$ for $0 \leq \sigma \leq \sigma_{max}$ and $\rho(\sigma|I) = 0$ otherwise; σ_{max} is chosen sufficiently large so that the likelihood function for $\sigma > \sigma_{max}$ is negligible. Equation 8.2 can be written as:

$$P(b, \mathcal{L}, \epsilon, \sigma|k, I) \propto \frac{e^{(b+\mathcal{L}\epsilon\sigma)}(b+\mathcal{L}\epsilon\sigma)^k}{k!} P(\sigma|I)P(b, \mathcal{L}, \epsilon|I), \quad (8.5)$$

where the constant of proportionality is determined by the condition:

$$\int_0^\infty d\sigma \int_0^\infty d\mathcal{L} \int_0^1 d\epsilon \int_0^\infty db \rho(b, \mathcal{L}, \epsilon, \sigma|k, I) = 1. \quad (8.6)$$

The posterior distribution for σ is calculated by integrating over all other parameters:

$$\rho(\sigma|k, I) = \int_0^\infty d\mathcal{L} \int_0^1 d\epsilon \int_0^\infty db \rho(b, \mathcal{L}, \epsilon, \sigma|k, I) \quad (8.7)$$

and the 95% confidence level (C.L.) upper limit (U.L.) on the cross section (σ_{UL}) is defined by the formula:

$$0.95 = \int_0^{\sigma_{UL}} \rho(\sigma|k, I). \quad (8.8)$$

With the data and background listed in Tables 8.22, 8.23 and 8.24 and shown in Figures 8.16 and 8.17, the systematic uncertainty shown in Table 8.21 and the signal acceptance listed in Tables 8.7, 8.8 and 8.9, the final 95% C.L. U.L. on $\rho_T \rightarrow W\pi_T \rightarrow e\nu b\bar{b}(\bar{c})$ production cross section, the expected 95% C.L. U.L. on the cross section using the predicted SM background, the cross section times branching ratio for $\rho_T \rightarrow W\pi_T \rightarrow$

$e\nu b\bar{b}(\bar{c})$ production in the two case, $M_V = 100$ GeV and $M_V = 500$ GeV (listed in Tables 2.4, 2.5 and 2.6), are shown in Figures 8.18 and 8.19. The excluded region at 95% C.L. in the $(M(\rho_T), M(\pi_T))$ plane is illustrated in Table 8.25.

$M(\rho_T)$ (GeV)	$M(\pi_T)$ (GeV)
190	100
200	120
205	115

Table 8.10: Mass points used for the evaluation of the systematic uncertainties.

Cuts	$(M(\rho_T), M(\pi_T))$ (GeV)					
	(190,100)		(205,120)		(220,115)	
	charged	neutral	charged	neutral	charged	neutral
baseline	1.018	1.018	1.018	1.018	1.018	1.018
H_T^e	1.035	1.027	1.035	1.027	1.029	1.029
$\Delta\phi$	1.012	1.011	1.007	1.011	1.009	1.009
$p_T(jj)$	1.014	1.021	1.014	1.021	1.023	1.023
$H_T^e + \Delta\phi$	1.024	1.010	1.016	1.010	1.016	1.016
$H_T^e + \Delta\phi + p_T(jj)$	1.019	1.012	1.011	1.012	1.019	1.019
Mass Window	1.014	1.021	1.008	1.020	1.023	1.017
$H_T^e + \Delta\phi + p_T(jj) +$ Mass Window	1.017	1.043	1.006	1.045	1.026	1.029

Table 8.11: Ratio between the number of expected background events and the number of expected background events when no jet smearing is applied. The rows represent different series of mass dependent cuts on topological variables. Different columns represent the three different mass points (190,100), (200,115), (220,115) chosen for the evaluation of the systematic uncertainty.

Cuts	$(M(\rho_T), M(\pi_T))$ (GeV)					
	(190,100)		(205,120)		(220,115)	
	charged	neutral	charged	neutral	charged	neutral
baseline	1.015	1.019	1.019	0.985	1.019	1.009
H_T^e	1.031	1.036	1.030	0.997	1.032	1.020
$\Delta\phi$	1.020	1.021	1.024	0.994	1.017	1.012
$p_T(jj)$	1.056	1.057	1.054	1.0199	1.040	1.034
$H_T^e + \Delta\phi$	1.040	1.042	1.036	1.0069	1.031	1.025
$H_T^e + \Delta\phi + p_T(jj)$	1.067	1.075	1.057	1.0337	1.043	1.040
Mass Window	1.076	1.077	1.077	1.0316	1.079	1.073
$H_T^e + \Delta\phi + p_T(jj) +$ Mass Window	1.116	1.120	1.110	1.0713	1.097	1.084

Table 8.12: Ratio between the number of expected signal events and the number of expected signal events when no jet smearing is applied. The rows represent different series of mass dependent cuts on topological variables. Different columns represent the three different mass points (190,100), (200,115), (220,115) chosen for the evaluation of the systematic uncertainty.

Cuts	$(M(\rho_T), M(\pi_T))$ (GeV)					
	(190,100)		(205,120)		(220,115)	
	charged	neutral	charged	neutral	charged	neutral
baseline	1.029	1.029	1.029	1.029	1.029	1.029
H_T^e	1.046	1.038	1.046	1.038	1.037	1.037
$\Delta\phi$	1.020	1.019	1.018	1.019	1.021	1.021
$p_T(jj)$	1.027	1.021	1.027	1.021	1.029	1.029
$H_T^e + \Delta\phi$	1.030	1.020	1.027	1.020	1.022	1.022
$H_T^e + \Delta\phi + p_T(jj)$	1.031	1.019	1.027	1.019	1.018	1.018
Mass Window	1.034	1.048	1.037	1.043	1.041	1.034
$H_T^e + \Delta\phi + p_T(jj) +$ Mass Window	1.022	1.044	1.012	1.043	1.026	1.035

Table 8.13: Ratio between the number of expected background events and the number of expected background events when jet energy scale is increased by σ_{syst} . The rows represent different series of mass dependent cuts on topological variables. Different columns represent the three different mass points (190,100), (200,115), (220,115) chosen for the evaluation of the systematic uncertainty.

Cuts	$(M(\rho_T), M(\pi_T))$ (GeV)					
	(190,100)		(205,120)		(220,115)	
	charged	neutral	charged	neutral	charged	neutral
baseline	1.025	1.050	0.997	1.020	1.006	1.025
H_T^e	0.945	0.977	0.938	0.960	0.933	0.964
$\Delta\phi$	1.010	1.046	0.987	1.008	1.000	1.020
$p_T(jj)$	0.927	0.961	0.908	0.933	0.939	0.963
$H_T^e + \Delta\phi$	0.918	0.963	0.924	0.945	0.918	0.951
$H_T^e + \Delta\phi + p_T(jj)$	0.870	0.918	0.882	0.895	0.880	0.918
Mass Window	0.983	0.989	0.951	0.990	0.980	1.007
$H_T^e + \Delta\phi + p_T(jj) +$ Mass Window	0.890	0.911	0.901	0.929	0.913	0.956

Table 8.14: Ratio between the number of expected signal events and the number of expected signal events when jet energy scale is increased by σ_{syst} . The rows represent different series of mass dependent cuts on topological variables. Different columns represent the three different mass points (190,100), (200,115), (220,115) chosen for the evaluation of the systematic uncertainty.

Cuts	$(M(\rho_T), M(\pi_T))$ (GeV)					
	(190,100)		(205,120)		(220,115)	
	charged	neutral	charged	neutral	charged	neutral
baseline	0.993	0.993	0.993	0.993	0.993	0.993
H_T^e	0.993	0.991	0.993	0.991	0.991	0.991
$\Delta\phi$	0.991	0.997	0.992	0.998	0.994	0.994
$p_T(jj)$	0.983	0.980	0.983	0.980	0.987	0.987
$H_T^e + \Delta\phi$	0.977	0.988	0.977	0.988	0.985	0.985
$H_T^e + \Delta\phi + p_T(jj)$	0.985	0.986	0.988	0.986	0.983	0.983
Mass Window	0.977	1.019	0.984	1.024	1.006	1.013
$H_T^e + \Delta\phi + p_T(jj) +$ Mass Window	0.960	1.011	0.967	1.017	0.988	0.989

Table 8.15: Ratio between the number of expected background events and the number of expected background events when jet energy scale is decreased by σ_{syst} . The rows represent different series of mass dependent cuts on topological variables. Different columns represent the three different mass points (190,100), (200,115), (220,115) chosen for the evaluation of the systematic uncertainty.

Cuts	$(M(\rho_T), M(\pi_T))$ (GeV)					
	(190,100)		(205,120)		(220,115)	
	charged	neutral	charged	neutral	charged	neutral
baseline	0.908	0.887	0.951	0.971	0.944	0.955
H_T^e	0.953	0.924	0.985	1.001	0.985	0.987
$\Delta\phi$	0.915	0.903	0.964	0.976	0.959	0.966
$p_T(jj)$	0.972	0.946	1.030	1.042	0.985	0.992
$H_T^e + \Delta\phi$	0.964	0.944	0.999	1.009	1.006	1.008
$H_T^e + \Delta\phi + p_T(jj)$	0.999	0.968	1.052	1.048	1.029	1.025
Mass Window	0.843	0.862	0.887	0.895	0.843	0.842
$H_T^e + \Delta\phi + p_T(jj) +$ Mass Window	0.897	0.909	0.926	0.920	0.888	0.885

Table 8.16: Ratio between the number of expected signal events and the number of expected signal events when jet energy scale is decreased by σ_{syst} . The rows represent different series of mass dependent cuts on topological variables. Different columns represent the three different mass points (190,100), (200,115), (220,115) chosen for the evaluation of the systematic uncertainty.

Cuts	$(M(\rho_T), M(\pi_T))$ (GeV)					
	(190,100)		(205,120)		(220,115)	
	charged	neutral	charged	neutral	charged	neutral
baseline	1.031	1.031	1.031	1.031	1.031	1.031
H_T^e	1.036	1.034	1.036	1.034	1.034	1.034
$\Delta\phi$	1.031	1.032	1.031	1.032	1.031	1.031
$p_T(jj)$	1.024	1.020	1.024	1.020	1.028	1.028
$H_T^e + \Delta\phi$	1.030	1.031	1.031	1.031	1.032	1.032
$H_T^e + \Delta\phi + p_T(jj)$	1.026	1.027	1.027	1.027	1.030	1.031
Mass Window	1.026	1.026	1.024	1.024	1.025	1.035
$H_T^e + \Delta\phi + p_T(jj) +$ Mass Window	1.029	1.034	1.027	1.032	1.020	1.036

Table 8.17: Ratio between the number of expected background events and the number of expected background events when b , c and $light$ -tagging efficiencies are increased by σ_{syst} . The rows represent different series of mass dependent cuts on topological variables. Different columns represent the three different mass points (190,100), (200,115), (220,115) chosen for the evaluation of the systematic uncertainty.

Cuts	$(M(\rho_T), M(\pi_T))$ (GeV)					
	(190,100)		(205,120)		(220,115)	
	charged	neutral	charged	neutral	charged	neutral
baseline	0.997	0.997	0.997	0.997	0.997	0.997
H_T^e	0.998	0.998	0.998	0.998	0.998	0.998
$\Delta\phi$	0.997	0.997	0.997	0.997	0.997	0.997
$p_T(jj)$	0.988	0.985	0.988	0.985	0.992	0.992
$H_T^e + \Delta\phi$	0.994	0.994	0.994	0.994	0.996	0.996
$H_T^e + \Delta\phi + p_T(jj)$	0.990	0.992	0.990	0.991	0.995	0.995
Mass Window	0.990	0.988	0.988	0.987	0.988	0.998
$H_T^e + \Delta\phi + p_T(jj) +$ Mass Window	0.993	0.995	0.991	0.992	0.982	0.998

Table 8.18: Ratio between the number of expected background events and the number of expected background events when b , c and $light$ -tagging efficiencies are decreased by σ_{syst} . The rows represent different series of mass dependent cuts on topological variables. Different columns represent the three different mass points (190,100), (200,115), (220,115) chosen for the evaluation of the systematic uncertainty.

Cuts	$(M(\rho_T), M(\pi_T))$ (GeV)					
	(190,100)		(205,120)		(220,115)	
	charged	neutral	charged	neutral	charged	neutral
baseline	1.013	1.007	1.012	1.013	1.007	1.008
H_T^e	1.011	1.004	1.010	1.012	1.007	1.007
$\Delta\phi$	1.010	1.016	1.011	1.010	1.009	1.010
$p_T(jj)$	1.006	1.008	1.006	1.011	1.009	1.009
$H_T^e + \Delta\phi$	1.009	1.010	1.008	1.009	1.008	1.010
$H_T^e + \Delta\phi + p_T(jj)$	1.004	0.999	1.005	1.008	1.007	1.008
Mass Window	1.014	1.009	1.000	1.019	1.011	1.015
$H_T^e + \Delta\phi + p_T(jj) +$ Mass Window	1.009	0.997	0.994	1.003	1.009	1.018

Table 8.19: Ratio between the number of expected signal events and the number of expected signal events when b , c and $light$ -tagging efficiencies are increased by σ_{syst} . The rows represent different series of mass dependent cuts on topological variables. Different columns represent the three different mass points (190,100), (200,115), (220,115) chosen for the evaluation of the systematic uncertainty.

Cuts	$(M(\rho_T), M(\pi_T))$ (GeV)					
	(190,100)		(205,120)		(220,115)	
	charged	neutral	charged	neutral	charged	neutral
baseline	0.983	0.980	0.982	0.986	0.977	0.981
H_T^e	0.982	0.977	0.980	0.985	0.978	0.980
$\Delta\phi$	0.980	0.989	0.982	0.983	0.979	0.984
$p_T(jj)$	0.976	0.981	0.976	0.984	0.979	0.983
$H_T^e + \Delta\phi$	0.979	0.983	0.978	0.982	0.978	0.983
$H_T^e + \Delta\phi + p_T(jj)$	0.975	0.973	0.976	0.982	0.977	0.981
Mass Window	0.984	0.982	0.971	0.984	0.982	0.989
$H_T^e + \Delta\phi + p_T(jj) +$ Mass Window	0.980	0.971	0.965	0.977	0.980	0.991

Table 8.20: Ratio between the number of expected signal events and the number of expected signal events when b , c and $light$ -tagging efficiencies are decreased by σ_{syst} . The rows represent different series of mass dependent cuts on topological variables. Different columns represent the three different mass points (190,100), (200,115), (220,115) chosen for the evaluation of the systematic uncertainty.

Uncertainty Source	Signal	Background
resolution	4.0%	1.9%
JES	4.5%	1.8%
b -tag	1.6%	1.5%
PMCS	5.4%	

Table 8.21: Summary of systematic uncertainties for signal and background.

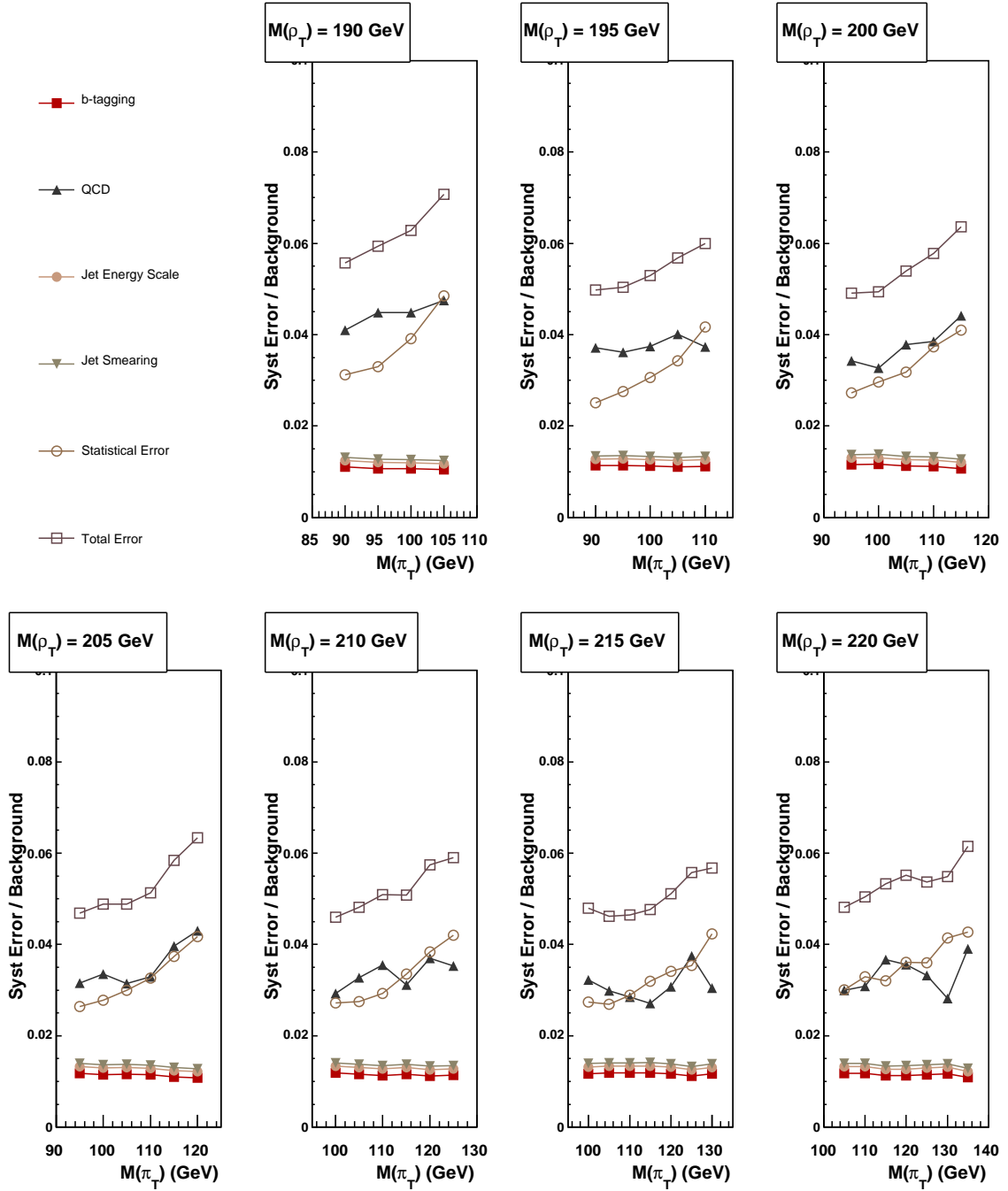


Figure 8.15: Summary of relative uncertainties for the background evaluated at the end of the optimization chain for the $190 \leq M(\rho_T) \leq 220$ GeV mass grid region.

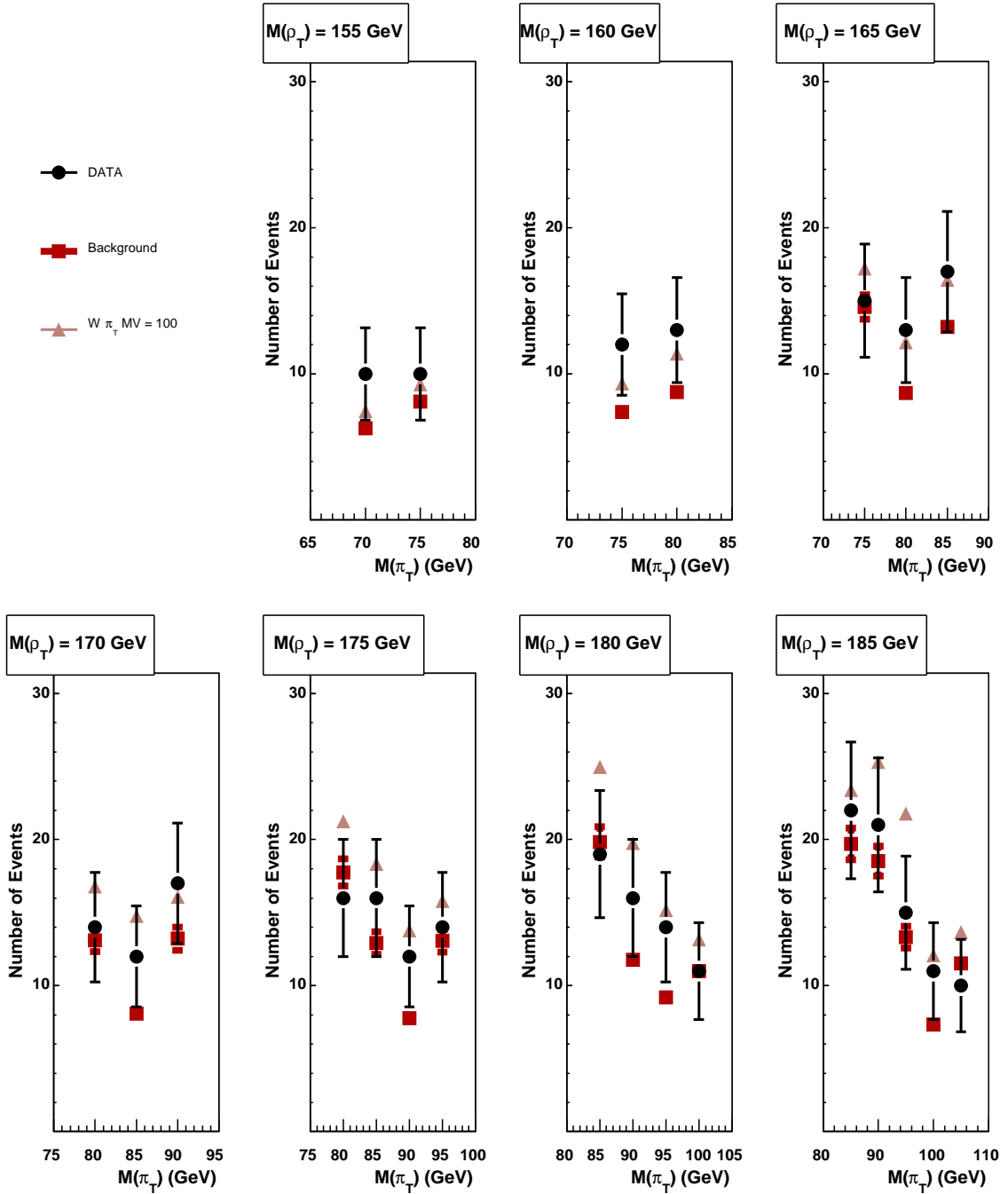


Figure 8.16: Comparison of data events (black dots) and background events (red squares) after all mass-dependent optimized cuts applied. Also shown is the expected $\rho_T \rightarrow W\pi_T \rightarrow e\nu b\bar{b}(\bar{c})$ signal events for $M_V = 100$ GeV (yellow triangles).

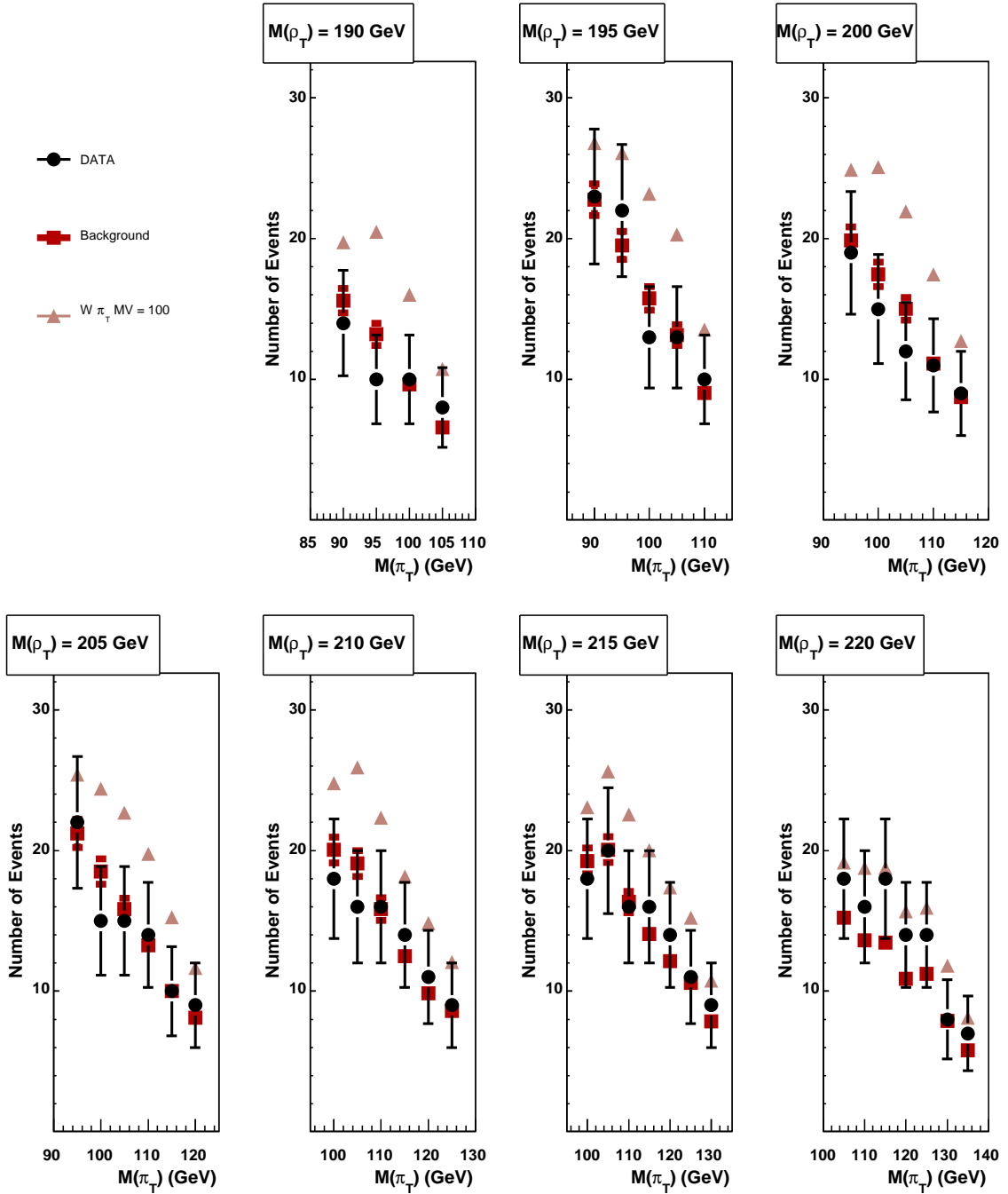


Figure 8.17: Comparison of data events (black dots) and background events (red squares) after all mass-dependent optimized cuts applied. Also shown is the expected $\rho_T \rightarrow W\pi_T \rightarrow e\nu b\bar{b}(\bar{c})$ signal events for $M_V = 100$ GeV (yellow triangles).

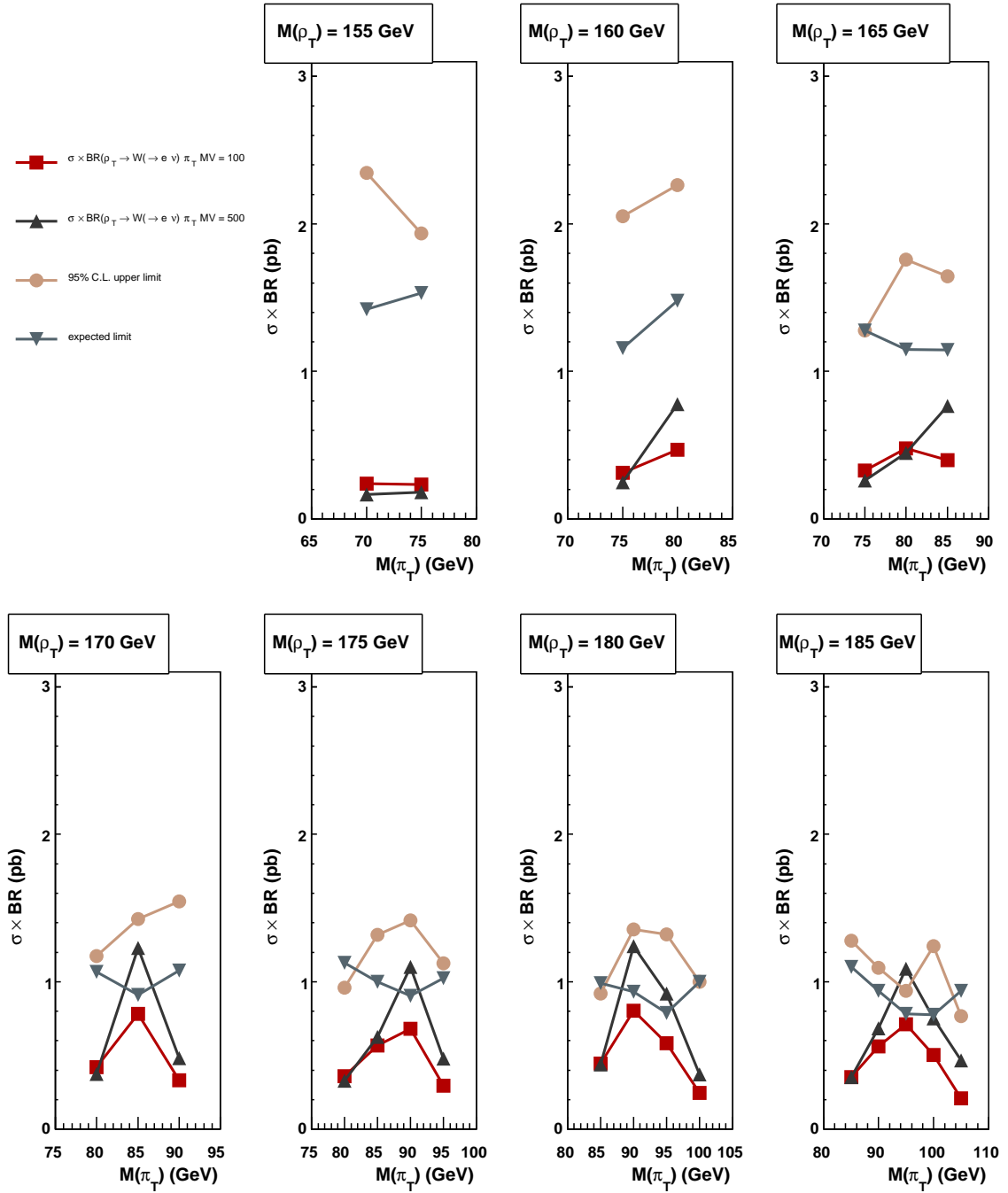


Figure 8.18: 95% C.L. U.L. on $\rho_{\tau} \rightarrow W\pi_{\tau} \rightarrow e\nu b\bar{b}(\bar{c})$ production cross section for the $155 \leq M(\rho_{\tau}) \leq 185$ GeV mass grid region. Red squares (blue triangles) represent $W\pi_{\tau}$ cross section times branching ratio with $M_V = 100$ ($M_V = 500$). Grey reverse triangles represent the expected 95% C.L. U.L. on the cross section, the yellow circles represent the 95% C.L. U.L. on the cross section with 388 pb^{-1} integrated luminosity of D0 data.

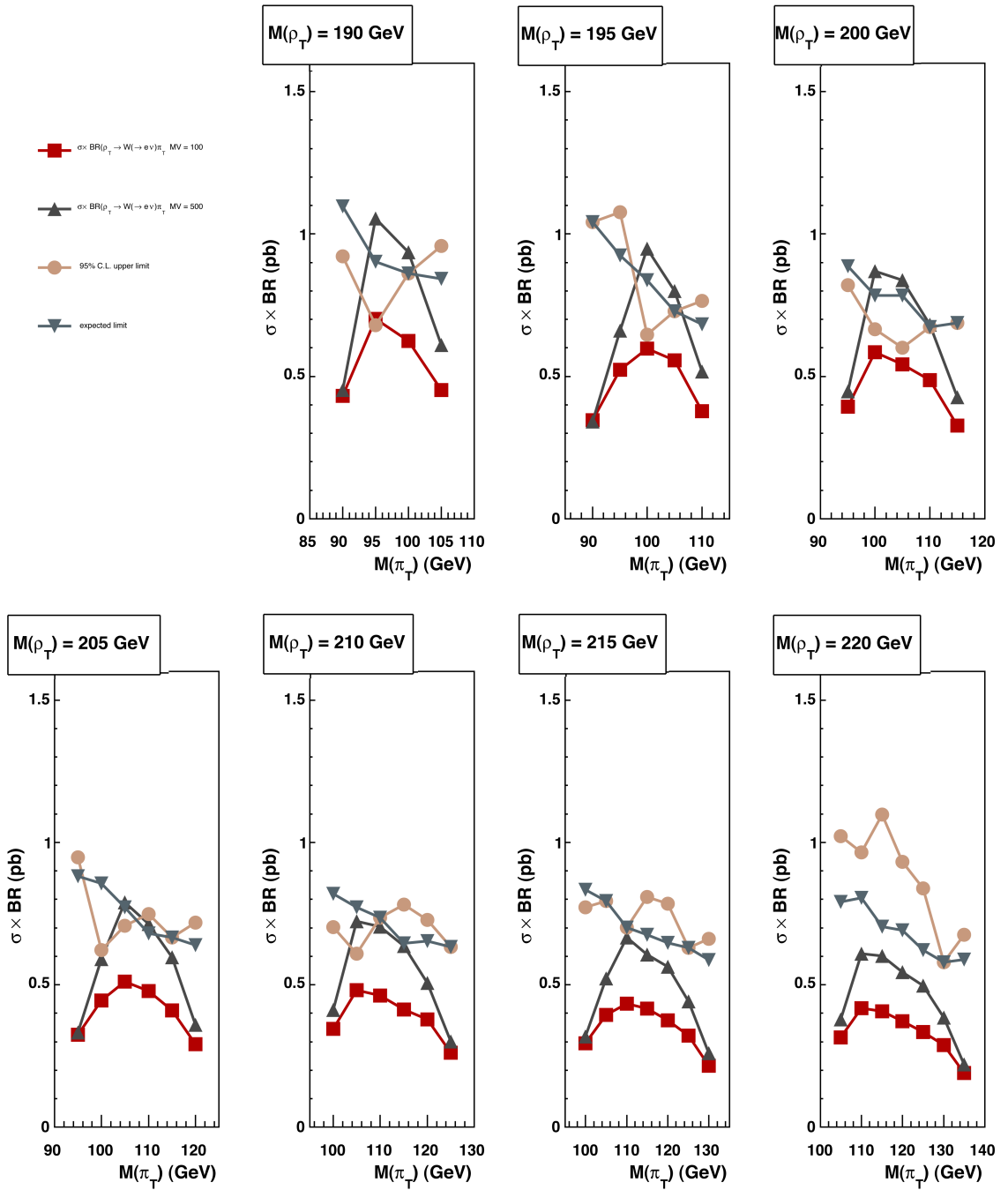


Figure 8.19: 95% C.L. U.L. on $\rho_T \rightarrow W\pi_T \rightarrow e\nu b\bar{b}(\bar{c})$ production cross section for the $190 \leq M(\rho_T) \leq 220$ GeV mass grid region. Red squares (blue triangles) represent $W\pi_T$ cross section times branching ratio with $M_V = 100$ ($M_V = 500$). Grey reverse triangles represent the expected 95% C.L. U.L. on the cross section, the yellow circles represent the 95% C.L. U.L. on the cross section with 388 pb^{-1} integrated luminosity of DØ data.

$M(\rho_T)$ (GeV)	$M(\pi_T)$ (GeV)	Data	Number of Events		95% C.L. U.L. on cross section	
			Background	Signal	Expected (pb)	Calculated (pb)
155	70	10	6.2 ± 0.2	1.1 ± 0.1	1.42	2.34
	75	10	8 ± 0.2	1.1 ± 0.1	1.53	1.93
160	75	12	7.3 ± 0.2	1.9 ± 0.1	1.15	2.05
	80	13	8.7 ± 0.3	2.6 ± 0.2	1.47	2.26
165	75	15	14.5 ± 0.6	2.6 ± 0.2	1.27	1.27
	80	13	8.6 ± 0.4	3.4 ± 0.2	1.14	1.75
	85	17	13.2 ± 0.5	3.2 ± 0.2	1.14	1.64
170	80	14	13.1 ± 0.6	3.6 ± 0.3	1.06	1.17
	85	12	8 ± 0.3	6.6 ± 0.5	0.91	1.42
	90	17	13.2 ± 0.6	2.8 ± 0.2	1.07	1.54
175	80	13	8.6 ± 0.4	3.4 ± 0.2	1.14	1.75
	85	16	12.9 ± 0.6	5.4 ± 0.4	1	1.31
	90	12	7.7 ± 0.3	6 ± 0.4	0.9	1.41
	95	14	13 ± 0.6	2.7 ± 0.2	1.02	1.12
180	85	19	19.8 ± 0.8	5.1 ± 0.4	0.99	0.91
	90	16	11.7 ± 0.4	8 ± 0.6	0.93	1.35
	95	14	9.2 ± 0.3	5.9 ± 0.4	0.78	1.32
	100	11	10.9 ± 0.4	2.1 ± 0.1	0.99	0.99
185	85	22	19.7 ± 0.9	3.6 ± 0.3	1.09	1.27
	90	21	18.5 ± 0.8	6.8 ± 0.5	0.93	1.09
	95	15	13.3 ± 0.5	8.4 ± 0.6	0.78	0.93
	100	11	7.3 ± 0.2	4.7 ± 0.3	0.77	1.24
	105	10	11.5 ± 0.5	2.1 ± 0.1	0.93	0.76

Table 8.22: Data yield, background and signal expectation, expected 95% C.L. U.L. and calculated 95% C.L. U.L. on $\rho_T \rightarrow W\pi_T \rightarrow e\nu b\bar{b}(\bar{c})$ cross section using 388 pb^{-1} of $D\bar{D}$ data after cuts on topological variable as listed in Tables 8.2, 8.3, 8.5 and 8.6 as function of $M(\pi_T)$ and $M(\rho_T)$.

$M(\rho_T)$ (GeV)	$M(\pi_T)$ (GeV)	Number of Events			95% C.L. U.L. on cross section	
		Data	Background	Signal	Expected (pb)	Calculated (pb)
190	90	14	15.5 ± 0.7	4.1 ± 0.3	1.09	0.92
	95	10	13.2 ± 0.6	7.2 ± 0.5	0.9	0.67
	100	10	9.6 ± 0.4	6.3 ± 0.5	0.86	0.86
	105	8	6.5 ± 0.3	4.1 ± 0.3	0.84	0.95
195	90	23	22.7 ± 0.9	4 ± 0.3	1.04	1.04
	95	22	19.5 ± 0.8	6.5 ± 0.5	0.92	1.07
	100	13	15.7 ± 0.6	7.4 ± 0.6	0.83	0.64
	105	13	13.1 ± 0.5	7.1 ± 0.5	0.72	0.72
	110	10	9 ± 0.3	4.5 ± 0.3	0.68	0.76
200	95	19	19.8 ± 0.8	5 ± 0.4	0.88	0.82
	100	15	17.4 ± 0.6	7.6 ± 0.6	0.78	0.66
	105	12	15 ± 0.6	6.9 ± 0.5	0.78	0.6
	110	11	11.1 ± 0.4	6.3 ± 0.5	0.67	0.67
	115	9	8.7 ± 0.4	3.9 ± 0.3	0.68	0.68
205	95	22	21.2 ± 0.8	4.1 ± 0.3	0.88	0.94
	100	15	18.5 ± 0.7	5.8 ± 0.4	0.85	0.62
	105	15	15.8 ± 0.6	6.8 ± 0.5	0.77	0.7
	110	14	13.2 ± 0.5	6.5 ± 0.5	0.68	0.74
	115	10	10 ± 0.4	5.2 ± 0.4	0.66	0.66
	120	9	8 ± 0.3	3.5 ± 0.2	0.63	0.71

Table 8.23: Data yield, background and signal expectation, expected 95% C.L. U.L. and calculated 95% C.L. U.L. on $\rho_T \rightarrow W\pi_T \rightarrow e\nu b\bar{b}(\bar{c})$ cross section using 388 pb^{-1} of $D\bar{D}$ data after cuts on topological variable as listed in Tables 8.2, 8.3, 8.5 and 8.6 as function of $M(\pi_T)$ and $M(\rho_T)$.

$M(\rho_T)$ (GeV)	$M(\pi_T)$ (GeV)	Number of Events			95% C.L. U.L. on cross section	
		Data	Background	Signal	Expected (pb)	Calculated (pb)
210	100	18	20 ± 0.7	4.7 ± 0.3	0.81	0.7
	105	16	19 ± 0.7	6.8 ± 0.5	0.77	0.6
	110	16	15.8 ± 0.6	6.5 ± 0.5	0.73	0.73
	115	14	12.4 ± 0.4	5.6 ± 0.4	0.64	0.78
	120	11	9.8 ± 0.4	4.9 ± 0.4	0.65	0.72
	125	9	8.5 ± 0.3	3.4 ± 0.2	0.63	0.63
215	100	18	19.2 ± 0.7	3.8 ± 0.3	0.83	0.77
	105	20	20 ± 0.7	5.5 ± 0.4	0.79	0.79
	110	16	16.3 ± 0.5	6.2 ± 0.5	0.7	0.7
	115	16	14 ± 0.4	5.9 ± 0.4	0.67	0.8
	120	14	12.1 ± 0.4	5.2 ± 0.4	0.64	0.78
	125	11	10.5 ± 0.4	4.6 ± 0.3	0.62	0.62
	130	9	7.8 ± 0.2	2.9 ± 0.2	0.58	0.66
220	105	18	15.2 ± 0.5	3.9 ± 0.3	0.79	1.02
	110	16	13.6 ± 0.5	5.1 ± 0.4	0.8	0.96
	115	18	13.4 ± 0.5	5.2 ± 0.4	0.7	1.09
	120	14	10.8 ± 0.4	4.7 ± 0.3	0.69	0.93
	125	14	11.2 ± 0.4	4.6 ± 0.3	0.62	0.83
	130	8	7.8 ± 0.2	3.9 ± 0.3	0.57	0.57
	135	7	5.7 ± 0.2	2.3 ± 0.1	0.58	0.67

Table 8.24: Data yield, background and signal expectation, expected 95% C.L. U.L. and calculated 95% C.L. U.L. on $\rho_T \rightarrow W\pi_T \rightarrow e\nu b\bar{b}(\bar{c})$ cross section using 388 pb^{-1} of $D\bar{O}$ data after cuts on topological variable as listed in Tables 8.2, 8.3, 8.5 and 8.6 as function of $M(\pi_T)$ and $M(\rho_T)$.

$M(\rho_T)$	$M(\pi_T)$ excluded at 95% C.L. $M_V = 500 \text{ GeV}$
185 GeV	$M(\pi_T) \neq 95 \text{ GeV}$
190 GeV	$92 \leq M(\pi_T) \leq 100 \text{ GeV}$
195 GeV	$98 \leq M(\pi_T) \leq 105 \text{ GeV}$
200 GeV	$98 \leq M(\pi_T) \leq 110 \text{ GeV}$
205 GeV	$101 \leq M(\pi_T) \leq 109 \text{ GeV}$
210 GeV	$104 \leq M(\pi_T) \leq 108 \text{ GeV}$

Table 8.25: Excluded region at 95% C.L. in the $(M(\rho_T), M(\pi_T))$ plane for $\rho_T \rightarrow W\pi_T \rightarrow e\nu b\bar{b}(\bar{c})$ production with $M_V = 500 \text{ GeV}$ calculated using 388 pb^{-1} of $D\bar{O}$ data.

Chapter 9

Conclusion and Outlook

9.1 Summary

In this thesis, the search for $W\pi_T$ in the production decay chain $q\bar{q} \rightarrow \rho_T \rightarrow W\pi_T \rightarrow e\nu_e b\bar{b}(b\bar{c})$ has been presented. For this analysis we used 388 pb^{-1} data collected from April 2002 to July 2004 with the DØ detector. The search consisted in performing a topological analysis aimed to isolate $W\pi_T$ signal from the SM background by cutting on relevant kinematic quantities.

The result of this analysis has been interpreted in terms of upper limits for the $W\pi_T$ cross section. In the explored TCSM parameter space region, as a function of the technihadron masses $M(\rho_T)$ and $M(\pi_T)$, the absence of a clear excess over the Standard Model expectation led to an excluded region at 95% confidence level for $M_V = 500 \text{ GeV}$.

9.2 Outlook

In the short term the result of this analysis is going to be improved by using a Neural Network to maximize the discrimination power of the topological variables and improving the limits. DØ is expected to collect as much as 8 fb^{-1} of data delivered by the Tevatron

accelerator by the end of Run II. Scaling the result of this topological analysis to 8 fb^{-1} shows that even without improvement in detector performances, this would result in excluding most of the parameter space presented here. Better prospects are foreseen when the expected improvement in jet energy scale, b -tagging performances, and better understanding of the Monte Carlo simulation are included.

Of course, when the Large Hadron Collider at CERN will begin to take data another frontier in high energy physics is going to be open. In particular, the higher center of mass energy and the higher luminosity involved will be a true probe for the strong dynamical models of the Electroweak Symmetry Breaking.

Bibliography

- [1] A. A. Michelson and E.W. Morley, On the Relative Motion of the Earth and the Lumineferous Ether, *American Journal of Science* **1**(34), 333 (1887)
- [2] O. Lummer and E. Pringsheim, Die Vertheilung der Energie im Spectrum des schwarzen Körpers und des blanken Platins, *Verhandlungen der Physikalischen Gesellschaft* (10), 232 (1899)
- [3] A. Einstein, Zur Elektrodynamik bewegter Körper, *Annalen der Physik* (17), 891 (1905)
- [4] M. Plank, Über das Gesetz der Energieverteilung im Normalspektrum, *Annalen der Physik* **4**, 553 (1901)
- [5] S. L. Glashow, *Nuclear Physics* **22**, 579 (1961)
- [6] S. Weinberg, *Physical Review Letters* **19**, 1264 (1967)
- [7] A. Salam, Herausgeber. *Elementary Particle Theory: Relativistic Groups and Analyticity*. Almqvist Wiksell, 1968.
- [8] G.E. Uhlenbeck and S. Goudsmit, *Naturwissenschaften* **47**, 953 (1925)
- [9] (<http://www.fnal.gov/pub/inquiring/matter/madeof/>)
- [10] J. C. Street and E. C. Stevenson, New Evidence for the Existence of a Particle Intermediate Between the Proton and Electron, *Physical Review* **52**, 1003 (1937)

- [11] M. L. Perl *et al.*, Evidence for Anomalous Lepton Production in e^+e^- Annihilation, *Physical Review Letters* **35**, 1489 (1975)
- [12] M. L. Perl *et al.*, Properties of Anomalous $e\mu$ events Events Produced in e^+e^- Annihilation, *Physical Review Letters* **63B**, 466 (1975)
- [13] M. L. Perl *et al.*, Properties of the Proposed τ Charged Lepton, *Physical Review Letters* **70B**, 487 (1975)
- [14] S. Eidelmann *et al.*, Particle Data Group, *Physics Letters B* **592**, 1 (2004)
- [15] S. Abachi *et al.*, *Physical Review Letters* **74**, 2632 (1995)
- [16] F. Abe *et al.*, *Physical Review Letters* **74**, 2626 (1995)
- [17] C. N. Yang and R. L. Mills, *Physical Review* **96**, 191 (1954)
- [18] S. L. Glashow, *Nuclear Physics* **22**, 579 (1961)
- [19] C. Quigg, *Gauge Theories of the Strong, Weak and Electromagnetic Interactions*, Addison Wesley, 1983
- [20] *Technicolor Evolution*, Snowmass, CO, 2001.
- [21] S. Weinberg, Implication of Dynamical Symmetry Breaking, *Physical Review* **D13**, 974–996 (1976)
- [22] L. Susskind, Dynamics of Spontaneous Symmetry Breaking in the Weinberg-Salam Theory, *Physical Review* **D20**, 2619 (1979)
- [23] *The origin of mass in QCD*, 2004.
- [24] S. Dimopoulos and L. Susskind, *Nuclear Physics* **B(155)**, 237 (1979)
- [25] E. Eichten and K. Lane, *Physics Letters* **B(90)**, 125 (1980)

- [26] B. Holdom, *Physical Review D* **24**, 1441 (1981)
- [27] C. T. Hill, *Physics Letters B* **345**, 483 (1995)
- [28] E. Eichten, K. Lane and J. Womersley, Finding Low-Scale Technicolor at Hadron Colliders, *Physics Letters B* **405**, 305 (1997)
- [29] T. Affolder *et al.*, *Physical Review Letters* **84**, 1110 (2000)
- [30] T. Affolder *et al.*, *Physical Review Letters* **83**, 3124 (1999)
- [31] *Technicolor 2000*, Frascati, RM Italy, 2000.
- [32] V. M. Abazov *et al.*, *Physical Review Letters* **87**, 1110 (2001)
- [33] S. Mrenna K. Lane, The Collider Phenomenology of Technihadrons in the Technicolor Straw Man Model, *Physical Review D* **67**, 115011 (2003)
- [34] T. Handa. *Search for Technicolor Particles in $p\bar{p}$ collision at $\sqrt{1.8}$ GeV*. PhD thesis, 1999.
- [35] Fermilab Beam Division, (<http://www-bd.fnal.gov>)
- [36] V. M. Abazov *et al.*, (The Upgraded DØ Detector, hep-physics/0507191, Fermilab-Pub-05/341-E.)
- [37] Run II Luminosity Performance Review Committee Report. Technical report, Department of Energy, 2002.
- [38] Central Fiber Tracker, (http://d0server1.fnal.gov/projects/SciFi/cft_home.html)
- [39] B. Baldin *et al.*, Technical Design of the Central Muon System (March 1997)
- [40] (<http://www-d0.fnal.gov/runcoor/>)

- [41] DØ Run II Computing Planning Board. Technical report, January 31, 1997. Run II Computer and Software Plan for the DØ Experiment.
- [42] A. Kanohv, HTF: Histogramming Method For Finding Tracks. The algorithm description, DØ note 3778 (September 2000)
- [43] P.V.C. Hough, Machine Analysis of Bubble Chamber Pictures, in *International Conference on High Energy Accelerators and Instrumentation*, CERN, 1959
- [44] A. Garcia-Bellido *et al.*, Primary Vertex Certification in p14, DØ note 4320 (January 2004)
- [45] A. Schwartzman and M. Narain, Probabilistic Vertex Selection, DØ note 4042 (November 2002)
- [46] G. Sterman and S. Weinberg, *Physycal Review Letters* **39**, 1436 (1977)
- [47] G. C. Blazey *et al.*, (Run II Jet Physics, hep-ex/0005012)
- [48] B. Andrieu, Jet Finding Algorithms at Tevatron, *ACTA PHISICA POLONICA B* **36**(3) (2005)
- [49] E. Busato and B. Andrieu, Jet Algorithms in DØ Run II Software: Description and User's Guide, DØ note 4457 (April 2004)
- [50] B. Olivier *et al.*, NADA: A New Event by Event Hot Cell Killer, DØ note 3687 (July 2000)
- [51] J.R. Vlimant *et al.*, Technical Description of the T42 Algorithm for the Calorimeter Noise Suppression, DØ note 4146 (December 2003)
- [52] R. Akers *et al.*, QCD Studies Using a Cone Based Jet Finding Algorithm for e+ e- Collisions at LEP, *Z. Phys. C* **63**, 197 (1994)

- [53] D. Gillbert. A study of the jet response in the $d\phi$ calorimeter. Master's thesis, Lund Institute of Technology, 2004.
- [54] J. Agram *et al.*, Jet Energy Scale at DØ Run II, DØ note 4720 (February 2005)
- [55] Georg Steinbrueck. PhD thesis, University of Oklahoma, 1999.
- [56] Daniel Whiteson and Lukas Phaf, Electron Likelihood, DØ note 4449 (July 2003)
- [57] Joseph Kozminski *et al.*, Electron Likelihood in p14, DØ note 4449 (April 2004)
- [58] L. Sayewr and A. Stone, Missing ET Reconstruction: Variables and Methods, DØ note 3957 (July 2003)
- [59] S. Trincaz-Duvoid and P. Verdier, Missing ET Reconstruction in p17, DØ note 4474 (June 2004)
- [60] T Sjöstrand *et al.*, *Computer Physics Communications* **135**, 238 (2001)
- [61] M. L. Mangano *et al.*, (ALPGEN, A Generator for Hard Multiparton Processes in Hadronic Collisions, hep-ex/020693)
- [62] (<http://www-d0.fnal.gov/d0dist/dist/packages/d0gstar/devel/docs/html/d0gstar.html>)
- [63] S. Agostinelli *et al.*, Geant4: A Simulation Toolkit, *Nuclear Instruments and Methods A* **506**, 250–303 (2003)
- [64] G. Graham *et al.*, Status of the Fast Simulation, DØ note 4059 (December 2002)
- [65] A. Djouadi *et al.*, (HDECAY: A Program for Higgs Boson Decays in the Standard Model and its Supersymmetric Extension, hep-ph/9704448)
- [66] A. Schwartzman and M. Narain, b -quark Jet Identification via Secondary Vertex Reconstruction, DØ note 4080 (January 2003)

- [67] A. Schwartzman *et al.*, An Object-Oriented Framework for Physics Analysis from ROOT ples, DØ note 3887 (July 2001)
- [68] (<http://root.cern.ch>)
- [69] R. Frühwirth, Application of Kalman Filtering to Track and Vertex Fitting, *Nuclear Instruments and Methods in Physics Research* **A**(262), 444–450 (1987)
- [70] R. Luchsinger and C. Graab, Vertex Reconstruction by Means of the Method of Kalman Filtering, *Computer Physics Communications* (76), 263 (1993)
- [71] L. Feligioni *et al.*, Update on b-quark Jet Identification with Secondary Vertex Reconstruction using DØReco version p14, DØ note 4414 (March 2004)
- [72] B. Clement *et al.*, SystemD or How to Get Signal, Background and their Efficiencies with Real Data oOnly, DØ note 4159 (June 2003)
- [73] R. Demina *et al.*, Measurement of b-tagging efficiency and mis-tagging rates with CSIP method, DØ note 4432 (April 2004)
- [74] (<http://www-d0.fnal.gov/Run2Physics/cs/index.html>)
- [75] P. K. Mal *et al.*, DØ Luminosity in Run II: Reconstructed, DØ note 4438 (April 2004)
- [76] M. Begel *et al.*, DØ Luminosity in Run II: Delivered, DØ note 3970 (May 2003)
- [77] H. Kim and J. Yu, A Search for $Wb\bar{b}$ and WH Production in $p\bar{p}$ Collisions at $\sqrt{s} = 1.96$ TeV with Full Data Set of Pass2, DØ note 4706 (February 2006)
- [78] G. Graham *et al.*, Status of the Fast Simulation PMCS, DØ note 4059 (December 2002)
- [79] I. Bertran *et al.*, A Recipe for the Constructions of Confidence Limits, DØ note 3476 (September 1999)

Curriculum Vitae

LORENZO FELIGIONI

E-mail: lorenzo@fnal.gov

Work: 630-840-2931

Home: 630-353-6027

Education:

Ph.D., Physics, Boston University (2006).

Laurea, Università degli Studi di Perugia (1999).

Fellowships:

2000–2005 Research Assistant, Department of Physics, Boston University

Awards:

2002 Goldhaber Prize for Achievements by a First Year Graduate Student, Boston University

Research Experience:

Installation and maintenance of $D\bar{O}$ software.

Study of fast fitting technique (Discrete Kalman Filter) used to determine proton antiproton beam direction by using $D\bar{O}$ tracking detector. This work produced a software package used by the $D\bar{O}$ on line data acquisition system to monitor detector performance.

Statistical data analysis for beam emittance growth monitoring with Fermilab Main Injector accelerator data.

http://www-bd.fnal.gov/sdahomepage/osda/main_injector.html

Study of $D\bar{O}$ b-tagging capability using data collected during RunII.

Study of Technicolor production in the W boson plus heavy flavors channel.

Calibration of fast Monte Carlo for W boson plus jet production.

Contributions to conferences:

A.P.S. Meeting, Albuquerque, NM, 2002. *Search for Technicolor at DØ RunII.*

XXI International Symposium on Lepton and Photon Interaction at High Energies, Fermilab, Batavia, IL 2003. *Wb \bar{b} production at DØ. Poster.*

D.P.F., Riverside, CA, 2004. *Search for Technicolor at DØ RunII.*

<http://physics.ucr.edu/~billdbrk/talks/talk120.pdf>

Publications:

“b-jet Identification in the DØ Detector”, D. Bloch *et al.*, DØ Note 004590 (2004).

“A search for Techniparticle production at DØ RunII in the mode, $\rho_T \rightarrow W(\rightarrow e\nu) + \pi_T(\rightarrow bb)$ with b-quark jet identification using Secondary Vertex”, L. Feligioni, M. Narain, DØ Note 4590 (2004).

“Update on b-quark jet identification with Secondary Vertex reconstruction using DØ Reco version p14”, L. Feligioni, M. Narain, , P. Schieferdecker, A. Schwartzman DØ Note 4414 (2004).

“Update on the b-quark Jet Identification with Secondary Vertex Reconstruction using DØ Reco version p13”, L. Feligioni, A. Schwartzman, L. Sonnenschein, M. narain DØ Note 4182 (2003).

“Two-Time Correlation Functions: Bohm Theory and Conventional Quantum Mechanics”, L. Feligioni, O. Panella, Y.N. Srivastava, A. Widom (2002); [quant-ph/0202045](http://arxiv.org/abs/quant-ph/0202045).

DØ Publications:

“Search for Doubly-charged Higgs Boson Production in the Decay $H^{++}H^{--} \rightarrow \mu^+\mu^+\mu^-\mu^-$ with the DØ Detector at $\sqrt{s} = 1.96$ TeV”, V. M. Abazov *et al.*, Phys. Rev. Lett **93**, 141801 (2004); [hep-ex/040415](http://arxiv.org/abs/hep-ex/040415); FERMILAB-PUB-04/045-E.

“Observation and Properties of the X(3872) Decaying to $J/\psi\pi^+\pi^-$ in $p\bar{p}$ Collisions at $\sqrt{s} = 1.96$ TeV”, V. M. Abazov *et al.*, Phys. Rev. Lett. **93**, 162004 (2004); [hep-ex/0405004](http://arxiv.org/abs/hep-ex/0405004), Fermilab-Pub-04/061-E.

“Search for Supersymmetry with Gauge-Mediated Breaking in Diphoton Events at DØ”, V. M. Abazov *et al.*, Phys. Rev. Lett. **94**, 041801 (2005); [hep-ex/0408146](http://arxiv.org/abs/hep-ex/0408146); FERMILAB-Pub-04/198-E.

“Measurement of Dijet Azimuthal Decorrelations at Central Rapidities in $p\bar{p}$ Collisions at $\sqrt{s} = 1.96$ TeV”, V. M. Abazov *et al.*, Phys. Rev. Lett. **94**, 221801 (2005); hep-ex/0409040; FERMILAB-Pub-04/217-E.

“Measurement of the B_s^0 Lifetime in the Exclusive Decay Channel $B_s^0 \rightarrow J/\psi\phi$ ”, V. M. Abazov *et al.*, Phys. Rev. Lett. **94**, 042001 (2005); hep-ex/0409043; FERMILAB-Pub-04-225-E.

“A Search for the Flavor-Changing Neutral Current Decay $B_s^0 \rightarrow \mu^+\mu^-$ in $p\bar{p}$ Collisions at $\sqrt{s} = 1.96$ TeV”, V. M. Abazov *et al.*, Phys. Rev. Lett. **94**, 071802 (2005); hep-ex/0410039; FERMILAB-Pub-04-215-E.

“Measurement of the Ratio of B^+ and B_0 Lifetimes”, V. M. Abazov *et al.*, Phys. Rev. Lett. **94**, 182001 (2005); hep-ex/0410052; FERMILAB-Pub-04-284-E.

“Measurement of the Λ_b Lifetime in the Decay $\Lambda_b \rightarrow J/\psi\Lambda$ with the DØ Detector”, V. M. Abazov *et al.*, Phys. Rev. Lett. **94** 102001 (2005); hep-ex/0410054; FERMILAB-Pub-04-286-E.

“A Search for $Wb\bar{b}$ and WH Production in $p\bar{p}$ Collisions at $\sqrt{s} = 1.96$ TeV”, V. M. Abazov *et al.*, Phys. Rev. Lett. **94** 091802 (2005); hep-ex/0410062; FERMILAB-Pub-04-288-E.

“Measurement of the WW Production Cross Section in $p\bar{p}$ Collisions at $\sqrt{s} = 1.96$ TeV”, V. M. Abazov *et al.*, Phys. Rev. Lett. **94**, 151801 (2005); hep-ex/0410066; FERMILAB-Pub-04-293-E.

“A Measurement of the Ratio of Inclusive Cross Sections $p\bar{p} \rightarrow Zb/p\bar{p} \rightarrow Zj$ at $\sqrt{s} = 1.96$ TeV”, V. M. Abazov *et al.*, Phys. Rev. Lett. **94**, 161801 (2005); hep-ex/0410078; FERMILAB-Pub-04-297-E.

“A search for Anomalous Heavy-Flavor Quark Production in Association with W bosons”, V. M. Abazov *et al.*, Phys. Rev. Lett. **94**, 152002 (2005); hep-ex/0411084; FERMILAB-Pub-04-359-E.

“First Measurement of $\sigma(p\bar{p} \rightarrow Z) \times \text{Br}(Z \rightarrow \tau\tau)$ at $\sqrt{s} = 1.96$ TeV”, V. M. Abazov *et al.*, Phys. Rev. D **71**, 072004 (2005); hep-ex/0412020; FERMILAB-Pub-04-381-E.

“Search for First-Generation Scalar Leptoquarks in $p\bar{p}$ collisions at $\sqrt{s} = 1.96$ TeV”, V. M. Abazov *et al.*, Phys. Rev. D Rap. Comm. **71**, 071104(R)(2005); hep-ex/0412029; FERMILAB-Pub-04-389-E.

“Study of $Z\gamma$ Events and Limits on Anomalous $ZZ\gamma$ and $Z\gamma\gamma$ Couplings in $p\bar{p}$ Collisions at $\sqrt{s} = 1.96$ TeV”, V. M. Abazov *et al.*, Phys. Rev. Lett. **95**, 051802 (2005); hep-ex/0502036; FERMI-PUB-05-023-E.

“Measurement of Inclusive Differential Cross Sections for $\Upsilon(1S)$ Production in $p\bar{p}$ Collisions at $\sqrt{s} = 1.96$ TeV”, V. M. Abazov *et al.*, Phys. Rev. Lett., **232001** (2005); hep-ex/0502030; FERMI-PUB-05-020-E.

“Measurement of the $p\bar{p} \rightarrow W\gamma + X$ Cross Section and Limits on Anomalous $WW\gamma$ Couplings at $\sqrt{s} = 1.96$ TeV”, V. M. Abazov *et al.*, Phys. Rev. D Rap. Comm. **71**, 091108 (2005); hep-ex/0503048; Fermilab-Pub-05/046-E.

“Production of WZ Events in $p\bar{p}$ Collisions at $\sqrt{s} = 1.96$ TeV and Limits on Anomalous WWZ Couplings”, V. M. Abazov *et al.*, Phys. Rev. Lett. **95** 141802, (2005); hep-ex/0504019, Fermilab-Pub-05/061-E.

“Search for Neutral Supersymmetric Higgs Boson in Multijet Events at $\sqrt{s} = 1.96$ TeV”, V. M. Abazov *et al.*, accepted for publication in Phys. Rev. Lett. (2005); hep-ex/0504018, Fermilab-Pub-05/058-E.

“Measurement of the $t\bar{t}$ Cross Section in $p\bar{p}$ Collisions at $\sqrt{s} = 1.96$ TeV Using Kinematic Characteristics of Lepton plus Jet Events”, V. M. Abazov *et al.*, accepted by Phys. Lett. B (2005); hep-ex/0504043, Fermilab-Pub-05/079-E.

“Measurement of the $t\bar{t}$ Cross Section in $p\bar{p}$ Collisions at $\sqrt{s} = 1.96$ TeV Using Lepton plus Jets Events with Lifetime b -tagging”, V. M. Abazov *et al.*, accepted by Phys. Lett. B (2005); hep-ex/0504058, Fermilab-Pub-05/087-E.

“Search for Supersymmetry via Associated Production of Charginos and Neutralinos Using Tripleton Final States”, V. M. Abazov *et al.*, accepted for publication in Phys. Rev. Lett. (2005); hep-ex/0504032, Fermilab-Pub-05/075-E.

“Search for Randall-Sundrum Gravitons in Dilepton and Diphoton Final States”, V. M. Abazov *et al.*, Phys. Rev. Lett. **95**, 091801 (2005); hep-ex/0505018, Fermilab-Pub-05/126-E.

“Search for Right-Handed W Bosons in Top Quark Decay”, V. M. Abazov *et al.*, Phys. Rev. D Rap. Comm **72**, 011104 (R) (2005); hep-ex/0505031, Fermilab-Pub-05/187-E.

“Search for Single Top Quark Production in $p\bar{p}$ Collisions at $\sqrt{s} = 1.96$ TeV”, V. M. Abazov *et al.*, Phys. Lett. B **622** 265-276 (2005); hep-ex/0505063, Fermilab-Pub-05/207-E.

“Measurement of the $t\bar{t}$ Production Cross Section in $p\bar{p}$ Collisions at $\sqrt{s} = 1.96$ TeV in Dilepton Final States”, V. M. Abazov *et al.*, accepted by Phys. Lett. B (2005); hep-ex/0505082, Fermilab-Pub-05/217-E.

“Search for Large Extra Spatial Dimensions in Dimuon Production at $D\bar{D}$ ”, V. M. Abazov *et al.*, accepted by Phys. Rev. Lett. (2005); hep-ex/0506063; Fermilab-Pub-05/250-E.

“Measurement of Semileptonic Branching Fractions of B Mesons to Narrow D^{**} States”, V. M. Abazov *et al.*, accepted by Phys. Rev. Lett. (2005); hep-ex/0507046; Fermilab-Pub-05/313-E.

“Measurement of the Lifetime Difference in the B_s System, V. M. Abazov *et al.*, accepted by Phys. Rev. Lett.; hep-ex/0507084, Fermilab-Pub-05/324-E.

“The Upgraded DØ Detector”, V. M. Abazov *et al.*, submitted to Nucl. Instr. and Methods, hep-physics/0507191, Fermilab-Pub-05/341-E.

“Search for the Higgs Boson in $H \rightarrow WW^{(*)}$ Decays in $p\bar{p}$ Collisions at $\sqrt{s} = 1.96$ TeV”, submitted to Phys. Rev. Lett.; hep-ex/0508054; Fermilab-Pub-05/377-E.